# Towards High Performance Nanostructured Thermoelectric Materials. A Bottom-Up Approach

Doris Cadavid

# Towards High Performance Nanostructured Thermoelectric Materials

## A Bottom-Up Approach


Thesis by
***Doris Cadavid***


In Partial Fulfilment of the Requirements for the Degree of Doctor of Philosophy


Supervisor
***Prof. Dr. Andreu Cabot***
Tutor
***Prof. Dr. Atilá Herms***

Department of Electronics
University of Barcelona




**Doctorado en Física – Universidad de Barcelona – 2014**

# Contents

# Acknowledgements

Undertaking a PhD research is a journey that requires the collaboration of many people. First of all, I would like to express my sincere thanks to my supervisor Andreu Cabot, who believed in me as a researcher from the beginning, giving me the opportunity to be part of his research group. He had confidence in my skills and allowed me to work with independence and, at the same time, supported my ideas. I am deeply grateful to him also for introducing me to the fantastic world of colloidal nanocrystals and for encouraging me to communicate and present my work at the highest level in national and international academic events which helped me to grow as a researcher.

I would like to express my gratitude to my workmates of Functional Nanomaterials group: Maria, who helped me in the first colloidal synthesis that I did, and also share with me the fascination for thermoelectricity; Raquel who made me laugh and supported me in many ways; Alex who shared with me all those long days in the lab doing ligand exchange; Alexey who always helped me with chemistry issues throughout these years, explained and answered with patience all my questions; Wenhua and Fan for their help in the lab and their friendship during these years. Thanks also to Silvia, Alejandro, Zhishan, Xuelian and Gihan for sharing with me great moments inside and outside the lab. All of you have become a special part of my life.

Special thanks to all the collaborators that teamed up with me during this thesis: Oscar Juan Durá from the Universidad de Castilla-La Mancha and Stéphane Gorsse from the Université de Bordeaux for the thermal diffusivity measurements. Umberto Anselmi-Tamburini from the Universita di Pavia for having me over in his group and letting me to consolidate my samples with his SPS. Also to Jordi Arbiol and Reza Zamani for their amazing TEM work and to Dani Prades and Sergio Illera for their theoretical work.

Many thanks to Professor George S. Nolas for letting me stay in his research group, and for his kindness in taking care of me and my research projects. He is amazing professor and gave me important lessons. Also I would like to thank to all the members of his lab, for making me feel part of the group and share with me their knowledge.

I would like to thank also to the people in IREC for these years of nice work, especially to Diouldé who helped me so many times and shared with me a lot of weekends in the lab. Also, thanks to Cristian and Marta for their friendship.

Last but not the least, I would like to express my infinite gratitude to my family as they are the motor of my life. Without their love and support I could not have reached this point. During these years I really missed their company but in spite of the distance all their support helped me to arrive to this moment. Infinite thanks to my parents Dora and Euclides who sacrifice all for my benefit, to my sisters Paty and Stella that truly are my best friends and to my beloved nephews Diego, Camilo and Julian for being so nice to me. Finally, thanks to Omar, my partner in this adventure, for his unconditional support that has been my strength during these years. "Esto es por ustedes mi hermosa familia, que han hecho posible mi camino hasta aquí. Nunca serán suficientes las palabras para agradecerles su amor incondicional y su apoyo en todo momento"

Moltes gràcies als meus amics catalans!

# Preface

This work is devoted to search and develop different strategies to use colloidal nanocrystals (NCs) as building blocks for efficient nanostructured thermoelectric materials.

The thesis is organized in six chapters, in the first chapter, a general background of the thermoelectric field is presented as well as the framework and important features of the bottom-up approach followed in this thesis. Chapter two includes experimental details of the specific techniques used during this work. Chapters three to six are dedicated to the results and discussions of the experimental work. Chapter three starts with the production of binary heterostructured material using the $Ag_2Te$-PbTe system as a model. I point out the advantages of the solution processing and I give an approach to tune the structure of the nanocomposites, with the control of the different crystallographic phases and their compositions. In chapter four and five I address the surfactants issue, using $Ag_2Te$ and PbSe as the model systems. Ligand displacement strategies are developed in order to increase the electrical conductivity of the final nanocomposite and to tune the carrier concentration by means of controlling NCs surface composition. Chapter six addresses the consolidation stage. I used SPS to obtain bulk nanostructured materials and I discuss the importance of producing high density solids to optimize their transport properties using a novel synthesis to obtain $Cu_2SnSe_3$ NCs. I also detail the effect of the consolidation technique in grain size growth. Finally I summarises the general conclusion of the work and I include some recommendations for future work in this area.

# List of publications

1. **Doris Cadavid**, Maria Ibáñez, Stéphane Gorsse, Antonio M. López, Albert Cirera, Joan Ramon Morante, and Andreu Cabot. Bottom-up processing of thermoelectric nanocomposites from colloidal nanocrystal building blocks: the case of $Ag_2Te$–PbTe. *J. Nanopart. Res., 2012, 14, 1328*.

2. **Doris Cadavid**, Maria Ibáñez, Alexey Shavel, Oscar Juan Durá, M.A. López de la Torre, and Andreu Cabot. Organic ligand displacement by metal salts to enhance nanoparticle functionality: Thermoelectric properties of $Ag_2Te$. *J. Mater. Chem. A, 2013, 1, 4864-4870*.

3. María Ibáñez, **Doris Cadavid**, Umberto Anselmi-Tamburini, Reza Zamani, Stéphane Gorsse, Wenhua Li, Antonio M. López, Joan Ramon Morante, Jordi Arbiol, and Andreu Cabot. Colloidal synthesis and thermoelectric properties of $Cu_2SnSe_3$ nanocrystals. *J. Mater. Chem. A, 2013, 1, 1421-1426*

4. **Doris Cadavid**, Sergio Illera, Kaya Wey, Oscar Juan Durá, Maria Ibáñez, Alexey Shavel, M. A. López de la Torre, Joan Daniel Prades, George S. Nolas and Andreu Cabot. Thermoelectric properties of bottom-up assembled bulk nanomaterials: Surface ligand influence on PbSe. *Submitted*

In addition to the work done in direct relation to my Ph.D. project, I have participated in several other projects that have resulted in publications and are not part of this thesis. These are listed below.

1. **Doris Cadavid**, Maria Ibáñez, Umberto Anselmi-Tamburini, Oscar Juan Durá, M.A. López de la Torre, and Andreu Cabot. Thermoelectric properties of bottom-up assembled $Bi_2S_{3-x}Te_x$ nanocomposites. *Int. J. Nanotechnol. 2014, Accepted*.

2. Wenhua Li, Reza Zamani, Pilar Rivera Gil, Beatriz Pelaz, Maria Ibáñez, **Doris Cadavid**, Alexey Shavel, Ramon A. Alvarez-Puebla,

Wolfgang J. Parak, Jordi Arbiol, and Andreu Cabot. CuTe Nanocrystals: Shape and size control, plasmonic properties, and use as SERS probes and photothermal agents. *J. Am. Chem. Soc., 2013, 135 (19), 7098-7101.*

3. Wenhua Li, Reza Zamani, Maria Ibáñez, **Doris Cadavid**, Alexey Shavel, Joan Ramon Morante, Jordi Arbiol, and Andreu Cabot. Metal ions to control the morphology of semiconductor nanoparticles: Copper Selenide Nanocubes. *J. Am. Chem. Soc., 2013, 135 (12), 4664-4667.*

4. Maria Ibáñez, Reza Zamani, Stéphane Gorsse, Jiandong Fan, Silvia Ortega, **Doris Cadavid**, Joan Ramon Morante, Jordi Arbiol, and Andreu Cabot. Core–Shell Nanoparticles as Building Blocks for the Bottom-Up Production of Functional Nanocomposites: PbTe–PbS Thermoelectric Properties. *ACS Nano, 2013, 7 (3), 2573-2586.*

5. Alexey Shavel, **Doris Cadavid**, Maria Ibáñez, Alex Carrete, and Andreu Cabot. Continuous Production of $Cu_2ZnSnS_4$ Nanocrystals in a Flow Reactor. *J. Am. Chem. Soc., 2012, 134 (3), 1438-1441.*

6. Maria Ibáñez, Reza Zamani, Wenhua Li, **Doris Cadavid**, Stéphane Gorsse, Nebil A. Katcho, Alexey Shavel, Antonio M. López, Joan Ramon Morante, Jordi Arbiol, and Andreu Cabot. Crystallographic control at the nanoscale to enhance functionality: polytypic Cu2GeSe3 nanoparticles as thermoelectric materials. *Chem. Mater., 2012, 24 (23), 4615-4622.*

7. Maria Ibáñez, **Doris Cadavid**, Reza Zamani, Nuria García-Castelló, Victor Izquierdo-Roca, Wenhua Li, Andrew Fairbrother, Joan Daniel Prades, Alexey Shavel, Jordi Arbiol, Alejandro Pérez-Rodriguez, Joan Ramon Morante, and Andreu Cabot. Composition Control and Thermoelectric Properties of Quaternary Chalcogenide Nanocrystals: The Case of Stannite $Cu_2CdSnSe_4$. *Chem. Mater., 2012, 24 (3), 562-570.*

8. Maria Ibáñez, Reza Zamani, Aaron LaLonde, **Doris Cadavid**, Wenhua Li, Alexey Shavel, Jordi Arbiol, Joan Ramon Morante,

Stéphane Gorsse, G. Jeffrey Snyder, and Andreu Cabot. $Cu_2ZnGeSe_4$ Nanocrystals: Synthesis and Thermoelectric Properties. *J. Am. Chem. Soc., 2012, 134 (9), 4060-4063.*

9. Maria Ibáñez, Pablo Guardia, Alexey Shavel, **Doris Cadavid**, Jordi Arbiol, Joan Ramon Morante, and Andreu Cabot. Growth Kinetics of Asymmetric $Bi_2S_3$ Nanocrystals: Size Distribution Focusing in Nanorods. *J. Phys Chem. C., 2011, 115 (16), 7947-7955.*

10. Wenhua Li, Alexey Shavel, Roger Guzman, Javier Rubio-Garcia, Cristina Flox, Jiandong Fan, **Doris Cadavid**, Maria Ibáñez, Jordi Arbiol, Joan Ramon Morante, and Andreu Cabot. Morphology evolution of $Cu_{2-x}S$ nanoparticles: from spheres to dodecahedrons. *Chem. Commun., 2011, 47, 10332-10334.*

# Summary of results

Thanks to the fine control in size, shape and the composition of the nanocrystals (NCs) provided by solution synthesis routes. The bottom-up approach to produce nanostructured thermoelectric (TE) materials gives a wide range of possibilities to increase their efficiency.

Colloidal NCs are excellent building blocks to produce nanostructured materials. Additionally, different possibilities to combine or grow NCs allow obtaining heterostructures with enhanced electronic properties. However, in spite of the multiple advantages of colloidal synthesis to produce nanostructure materials, they have also some intrinsic limitations. First, the capping surfactants that bond to the NCs surface form isolating barriers affecting the charge carrier transport. Second, the control of charge carrier density is difficult due to both, a self-purification process that avoids the introduction of impurities, and the large concentration of dangling bonds in the surface of the NCs that controls the charge carrier density.

This thesis aims to develop high efficiency thermoelectric nanostructured materials from the bottom-up assembly of NCs. To achieve this, first of all, I optimized colloidal synthesis routes to produce nanocrystals with the desired size, shape and composition at the gram scale. Then, I developed different approaches with the purpose to enhance the transport properties of the materials and to overcome the limitations of solution processed NCs. The materials I used were silver, lead, bismuth and copper chalcogenides, due to their intrinsic useful properties to obtain efficient thermoelectric materials

This thesis is divided in fourth parts. The first part is the background. The second part is related with the production of nanocomposites by using two types of colloidal NCs (chap. 3). In

the third part I board the organic ligand effect in the transport properties (chaps. 4, 5). Finally, I discuss the process of consolidation of the nanostructured material (chap. 6):

The chapter 1 consist in the Introduction of the thesis. Chapter two details the experimental techniques used for the TE characterization of the bulk nanostructured materials. In chapter 3, I explore the production of binary nanocomposite materials. The combination of different stoichiometry and crystallographic structure provides effective phonon blocking which allows enhancing the TE afficiency. PbTe and $Ag_2Te$ colloidal NCs were assembled into $Ag_2Te$-PbTe nanocomposites with homogeneous phase distributions and adjustable composition. The thermoelectric properties of these nanocomposites were analyzed in the temperature range from 300 K to 700 K. The evolution of their electrical conductivity and Seebeck coefficient is discussed in terms of the blend composition and the characteristics of the constituent materials. Undoped $(Ag_2Te)_{0.75}(PbTe)_{0.25}$ nanocomposites displayed best power factor ($PF=S^2\sigma$) among the different nanocomposites tested and reached ZT values up to 0.38 at 670 K. The results of this work were published in*: J. Nanopart. Res., 2012, 14, 1328*

Since the presence of organic ligands (OL) on the surface of colloidal NCs strongly limits their performance in technological applications, where charge carrier transfer/transport plays an important role, I developed strategies to replace the OL from the NCs surface. The first strategy was to use metal salts matched with the NCs composition to eliminate the surface OL without introducing extrinsic impurities in the final nanomaterial (chap. 4). The potential of this simple, general and scalable process was demonstrated by characterizing the thermoelectric properties of nanostructured bulk $Ag_2Te$ produced by the bottom up assembly of $Ag_2Te$ NCs. A 6-fold increase of the $Ag_2Te$ thermoelectric figure of merit was obtained when displacing organic ligands by $AgNO_3$. These results were published in *J. Mater. Chem. A, 2013,1, 4864-4870*

In a second approach, I used sodium salts to carry out the OL replacement, with PbSe NCs (chap. 5). I tested salts including sodium azide, sodium nitrate and sodium amide with the aim of tuning the carrier concentration of the NCs. The electrical conductivity of the bulk nanocrystalline material, treated with sodium amide, increased more than one order of magnitude, and the resultant figure of merit at 600 K was 0.6. Additionally I discussed the effect that the scattering at the grain interfaces has in electronic transport using a model that takes into account the energy barrier at the NCs boundaries. The results of this work have been submitted for publication.

Additionally to the OLs another challenge in the preparation of bulk nanostructured materials is to obtain a dense solid. The process of consolidation of the NCs into a dense solid plays a crucial role in obtaining a bulk nanomaterial with high thermoelectric properties, because the porosity strongly affects the charge carrier and phonon transport. In order to obtain the dense solids, I started using the cold press (CP) technique, chap. 3. Later, I was able to use the hot press (HP) technique, and carried out the adjustment of the parameters like temperature and time, in order to avoid a high increase of the grain size (chaps. 4 and 5). Another technique that has shown outstanding results in the thermoelectric field is spark plasma sintering (SPS). Thus I analyzed the transport properties of the nanomaterials obtained by the consolidation of colloid NCs-based powder into dense pellets by SPS (chap. 6).

Also, in chapter 6, a novel colloidal synthesis route to prepare $Cu_2SnSe_3$ NCs with controlled size, shape and composition is presented. The high yield of the developed procedure allowed scaling it up to the production of grams of colloidal $Cu_2SnSe_3$ NCs. These NCs were used as building blocks for the production of $Cu_2SnSe_3$ bulk nanostructured materials by SPS. The thermoelectric properties of the prepared nanocrystalline $Cu_2SnSe_3$ pellets were characterized in the temperature range from 300 to 720 K. These results were published in *J. Mater. Chem. A, 2013, 1, 1421-1426*.

My results show the bottom-up production of nanocrystalline materials from solution-processed NCs to be a potentially advantageous alternative to conventional methods in the production of efficient thermoelectric materials. At the same time, the progress achieved here allows to overcome some of the main difficulties in the production of bulk nanomaterials with high thermoelectric efficiency from the bottom-up assembly of colloidal NCs.

# Resumen

La estrategia de “Bottom-up” para la producción de materiales termoeléctricos nano-estructurados da un amplio rango de posibilidades para aumentar la eficiencia de los materiales termoeléctricos, porque permite aumentar los valores de la figura de mérito *ZT* (parámetro que mide la eficiencia del material termoeléctrico). Lo anterior, gracias al fino control del tamaño, la forma y la composición de los nanocristales (NCs) que proporciona la síntesis en solución, de tal manera que los NCs se convierten en los componentes básicos del material nanoestructurado. Además, existen diferentes posibilidades de combinar y/o de sintetizar los NCs, a fin de obtener heteroestructuras, con mejores propiedades electrónicas.

Sin embargo, a pesar de las múltiples ventajas de la síntesis coloidal para la producción de materiales nanoestructurados, también hay algunas limitaciones intrínsecas en la producción de materiales nanoestructurados procesados desde soluciones: Una de las mayores dificultades son los ligandos orgánicos (OL) que se usan en las síntesis, estos se pegan a los NCs y forman barreras aislantes que afectan el transporte de los portadores de carga. Otra dificultad es el control de la concentración de portadores, debido a la gran cantidad de “enlaces libres” en la superficie de los NCs, así como las limitaciones para colocar impurezas en los NCs.

Por lo tanto, esta tesis tiene como objetivo el desarrollo de materiales nanoestructurados de alta eficiencia termoeléctrica con NCs coloidales como los elementos constituyentes. Para ello, he seguido diferentes estrategias, con el propósito de mejorar las propiedades de transporte de los materiales. Primero, he utilizado y optimizado la síntesis coloidal para producir NCs con el tamaño, forma, composición deseada y a escala del gramo. Así mismo, he desarrollado varias técnicas para superar las limitaciones que tienen los NCs en solución en la formación de los materiales

nanoestructurados. Los materiales seleccionados fueron calcogenuros de plata, plomo, bismuto y cobre, debido a sus propiedades intrínsecas útiles para conseguir materiales termoeléctricos eficientes.

Esta tesis de divide en cuatro partes, la primera es la introducción al campo de la termoelectricidad y los NCs coloidales. La segunda se relaciona con el desarrollo de nanocompositos o heteroestructuras, usando dos tipos de NCs coloidales. En la tercera parte se ataca el problema de los ligandos orgánicos, que quedan atados a los nanocristales, para la formación de materiales nanoestructurados en bloque o nanocompositos. En la parte final se aborda el problema de la consolidación de los materiales nanoestructurados, mediante la utilización de diferentes técnicas de consolidación.

En el capítulo 3, se explora la posibilidad de mejorar las propiedades térmicas a través de la producción de nanocompositos-heteroestructuras, que son materiales muy prometedores para mejorar la eficiencia de los dispositivos termoeléctricos actuales. Su importancia radica en el bloqueo fonónico por la alta densidad de interfaces en los nano-granos y la diferencia de estructura cristalográfica que se obtiene al usar dos tipos diferentes de nanocristales de partida.

Los NCs en solución fueron ensamblados para obtener distribuciones de fase homogénea y composición ajustable, mezclando NCs de PbTe y $Ag_2Te$ para formar nanocompositos de $Ag_2Te$-PbTe. Las propiedades termoeléctricas de estos nanocompositos se analizaron en el intervalo de temperatura de 300 K a 700 K. La evolución de su conductividad eléctrica y el coeficiente de Seebeck se discute en términos de la composición de la mezcla y de las características de los materiales constituyentes. Entre los distintos nanocompositos que se probaron, el $(Ag2Te)_{0.75}(PbTe)_{0.25}$ sin dopar mostró los mejores valores de PF (factor de potencia $PF=\sigma S^2$) y se alcanzaron valores de figura de mérito ($ZT$) de 0.38 a 670 K. Los resultados de este trabajo fueron publicados en*: J. Nanopart. Res., 2012, 14, 1328*

Dado que la presencia de OL en la superficie de las nanopartículas coloidales limita en gran medida su rendimiento en aplicaciones tecnológicas donde la transferencia/transporte de portadores de carga juega un papel importante. Se desarrolló una estrategia para reemplazar los OL de los NCs. El primer enfoque es utilizar sales metálicas que coincidan con la composición de los NCs, para eliminar los OL superficiales sin introducir impurezas extrínsecas en el nanomaterial final (Capítulo 4). El potencial de este proceso simple, general y escalable se demostró mediante la caracterización de las propiedades termoeléctricas del nanocomposito de $Ag_2Te$ producido a partir de los NCs coloidales de $Ag_2Te$. Se obtuvo un aumento de 6 veces en los valores de la figura de Mérito (*ZT*) termoeléctrica al desplazar los OL usando $AgNO_3$ .Los resultados de este trabajo fueron publicados en: *J. Mater. Chem. A, 2013,1, 4864-4870*

El segundo enfoque consiste en utilizar sales de sodio con el fin de llevar a cabo la sustitución de ligandos en NCs de PbSe (capítulo 5), diferentes sales fueron probadas, incluidos azida de sodio, nitrato de sodio y amida de sodio con el fin de ajustar la concentración de portadores de la NCs mediante el simple procedimiento de sustitución del OL. La conductividad eléctrica del material nanocristalino, tratado con amida de sodio, aumenta más de un orden de magnitud, y la figura de mérito resultante a 600 K es 0.6. Además se discute el efecto que tiene la dispersión de los portadores de carga en las interfaces de los granos, en el transporte electrónico; usando un modelo que tiene en cuenta la barrera de energía en los límites de los NCs. Los resultados de este trabajo están sometidos para su publicación.

Además de la inconveniencia de tener los NCs cubiertos con OL, otro desafío importante en la preparación de los materiales nano-estructurados en bloque, es la obtención de un sólido denso. El proceso de consolidación tiene un papel crucial en la obtención de los nano-materiales con altos valores de figura de mérito (ZT), debido a que la porosidad afecta el transporte de portadores y por lo tanto las propiedades de transporte, como la conductividad eléctrica

y térmica. Al inicio (capítulo 3) se utiliza el prensado en frio (CP), mientras que en los capítulos 4 y 5, se utilizó el prensado en caliente y se realizó el ajusté de los parámetros, como tiempo y temperatura, de prensado. En el capítulo 6, se utiliza la técnica de "spark plasma sintering" (SPS), la cual ha demostrado ser una de las técnicas más eficientes para obtener materiales con alta eficiencia termoeléctrica. Se expone una nueva ruta sintética para preparar NCs coloidales $Cu_2SnSe_3$ controlando el tamaño, la forma y la composición. El alto rendimiento del procedimiento desarrollado permitió la producción de gramos de NCs de $Cu_2SnSe_3$. Estos NCs se utilizan como los bloques básicos para la construcción de materiales nanoestructurados de $Cu_2SnSe_3$ consolidados por SPS. Las propiedades termoeléctricas de las pastillas nanocristalinas de $Cu_2SnSe_3$ se caracterizaron en el rango de temperatura de 300 a 720 K, la figura de mérito (ZT) obtenida es comparable a los materiales en bloque obtenidos a partir de síntesis de estado sólido. Los resultados de este trabajo fueron publicados en *J. Mater. Chem. A, 2013, 1, 1421-1426*

Estos resultados muestran que la producción de materiales nanoestructurados usando como unidades fundamentales los NCs obtenidos en solución, es decir, la estrategia del "Bottom-up", es un método muy ventajoso con respecto a los métodos convencionales de producción de materiales termoeléctricos, puesto que da gran flexibilidad para la ingeniería de las nanoestructuras y así permite obtener materiales eficientes para usarlos en dispositivos termoeléctricos. De la misma manera se presentan estrategias que permiten superar las dificultades de los NCs coloidales en la producción de los materiales nanoestructurados, demostrando que se puede aumentar la eficiencia termoeléctrica.

# Chapter 1 Introduction

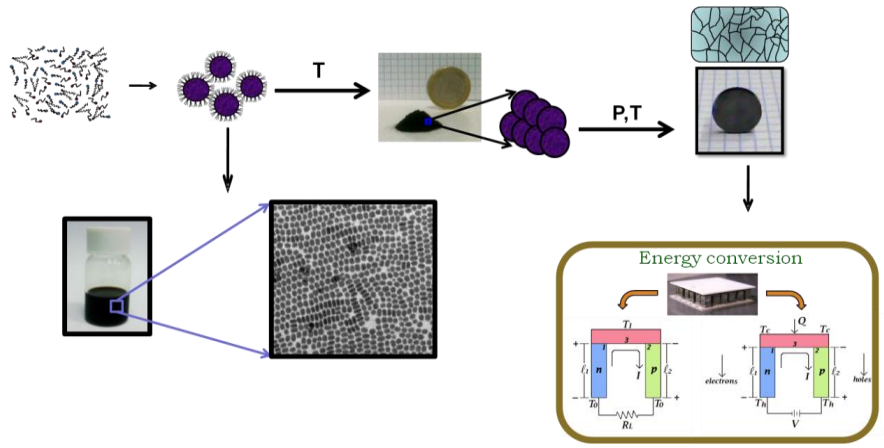


Energy production and consumption, as well as their environmental sustainability are some of the most important issues that our world has to face in the XXI century. The excessive dependence on the combustion of non-renewable fossil fuels and the huge increases on the global energy consumption, produce negative impact in the environment.[1–4] This situation, demand for alternative, low cost, efficient and environmental friendly energy technologies, which is driving the increasing development of solar, wind, geothermal and TE energy conversion devices.[5–8]

The fact that in most energy conversion processes over 60 % of the energy is lost as heat opens up opportunities for the development of TE devices that can directly convert waste heat into electricity.[9,10] Solid state TE devices can be used in a wide range of applications from temperature measurement, waste heat recovery, air conditioning, refrigeration and to power autonomous systems.[3,11,12] They have several advantages like no moving parts, lack of noise, high reliability, and operation in hostile environments without maintenance.[3,13] However, the low efficiency of TE devices has limited their spread in commercial applications. A significant increase in their efficiency, which still remains below 5 %, is required to be competitive with current technologies, both in electric generation and refrigeration.[10] Nevertheless, TE devices find their place in niche market in which their features can be more suitable and efficient. Nowadays, novel applications are being explored: TE generators to use the wasted heat from radiators and exhaust systems in order to increase fuel efficiency;[14] seat temperature control for comfort; TE refrigeration for biological specimens and samples; and also localized cooling in optoelectronic devices and infrared detector are currently in use. The cooling in computers still needs improvement and it is predicted that the resulting of cool computing could produce speed gains of 30 % to 200 %.[15,16] Additionally to these niche applications there is an important potential for distribution of electric power in development countries. TE devices in cooking stoves or solar thermal systems, will allow improving the quality of life in many places.[17,18]

According to the above discussion it is necessary to improve the efficiency of TE devices, which requires not only more efficient materials, but also the development of lower cost TE devices.[19] The efficiency of a TE device is given in terms of the temperature difference between the cold and the hot side and its figure of merit ($ZT$) which is a direct function of the transport properties of the TE materials within the device. The figure of merit is given by $ZT=(S^2\sigma/\kappa)T$, where $S$, $\sigma$, $\kappa$ and $T$ are the Seebeck coefficient, electrical conductivity, thermal conductivity, and temperature, respectively.[3,20] The thermal conductivity is the sum of two

contributions $\kappa = \kappa_e + \kappa_l$ where $\kappa_e$ and $\kappa_l$ are the electronic and lattice thermal conductivity, respectively. Therefore, a good TE material has to have high power factor ($PF=S^2\sigma$) but low $\kappa$.[21–25] Normally the *ZT* maximization is based on increasing the *PF* by optimizing the carrier concentration and on decreasing $\kappa_l$ by phonon blocking. Nevertheless, the improvement of *ZT* becomes difficult because of the interconnection among all these properties through more fundamental physical parameters, such as, carrier concentration *n*, carrier effective mass *m**, and carrier mobility $\mu$.[26] For instance *S* and $\sigma$ are coupled through *n*. An increase in *n* decreases *S*, but $\sigma$ increases with *n*.[27–29] Also $\sigma$ and $\kappa_e$ are directly related through the Wiedeman-Franz equation, so an increases of $\sigma$ will causes an increase of $\kappa$.[3,30–36]

The best materials that optimized the *ZT* according to the conditions describes above, are highly doped semiconductors (Figure 1.1).[37] Even though, today TE materials include semimetals, semiconductors and ceramic systems with a variety of crystalline forms, single crystals, polycrystalline and even nanocomposite materials.[38,39]

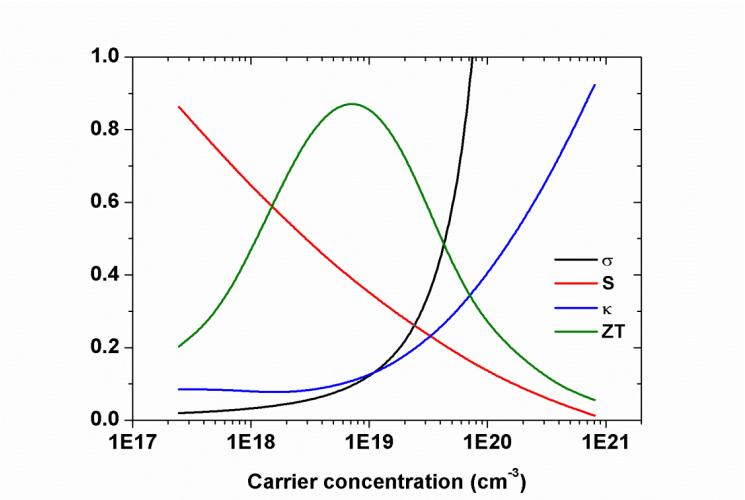


**Figure 1.1** Dependence of the different transport properties with the carrier concentration and resulting *ZT*.

Since the 90s, the field of thermoelectrics has been advancing rapidly, due to new scientific ideas together with investment from the governments and private companies.[28] Two main research approaches have been followed during these years: the development of new families of advanced bulk materials, and the use of low dimensional materials[19] The development of bulk materials with complex crystal structures came from the idea that an ideal thermoelectric material should combine the low thermal conductivity of a glass with the electronic properties of a single crystal. This idea is known as "phonon-glass electron-crystal" (PGEC).[40] In this kind of materials, the presence of voids (vacancies) and massive atoms that can vibrate inside of the crystal structure, allows the reduction of the lattice thermal conductivity. Based on this idea, new materials like skutterudites, clathrates, zintl phases were developed.[41,42] An improvement of *ZT* has been reported for these materials due to their low thermal conductivity, leading values up to 1.5.[43]

On the other hand, theoretical predictions suggest that low dimensional materials could improve *ZT,* by increasing *S* due to the quantum confinement effects, and by the reduction of lattice thermal conductivity because nanostructuring introduces large density of interfaces in which increases the phonon scattering.[44,45] Experimentally, Bulk nanostructured materials have already shown a successful decouple of the transport properties leading to enhanced *ZT*.[33,46–49]

In order to obtain nanostructured materials, we can follow two routes: the top-down and the bottom-up approach. In the first, the starting crystalline ingot is divided into small pieces to obtain fine particles with sizes down to several nanometers. Ball-milling is the most used technique[50], but other strategies like nanoscale precipitations also allow obtaining nanostructured materials.[51,52]

On the other hand, bottom-up approaches start with the production of the nanoparticles that are the constituent elements, to later assemble them into dense solids. Different techniques like cold press

(CP), hot press (HP) or spark plasma sintering (SPS)[53] can be used to consolidate the nanoparticles into dense nanocrystalline materials. Among bottom-up techniques, solution based approaches are low cost and also suitable to scale up. Specifically, the colloidal synthesis allows producing nanoparticles from 1 nm to 100 nm with a high control of size, shape, and composition[54–63]. At the nanoscale regime, the electronic, optical and magnetic properties depend on the size of the particles, this feature opens up a wide range of opportunities to tune NCs properties.[55,64–70] NCs can be used as building blocks of solid nanostructured materials and it is possible to use low cost solution processes like spin coating, dip coating or inkjet printing for the fabrication of different electronic and optoelectronic devices.[71]

The colloidal synthesis of NCs is based on the reaction of the appropriated molecular precursors in the presence of organic surfactants at relative low temperatures (from 150 ºC up to 300 ºC). Several stages can be identified in a colloidal synthesis route: i) homogeneous solution in which the precursors are transformed into an active atomic or molecular species (monomers), ii) nucleation into clusters, iii) further growth into NCs of the desired size and shape, iv) isolation and purification of the NCs.[66] Since, in this work we are interested in bulk nanostructured materials that consist in three dimensional nanograins, the NCs pass through an additional surface treatment, drying and consolidation into a pellet.

Nevertheless, the use of colloidal NCs presents several challenges. The principal is the presence of organic surfactant at the NCs surface that forms a highly insulating barrier between the NCs. This insulating barrier affects the electronic transport and need to be removed. In recent years big efforts have been addressed to replace long carbon ligands for small molecules, for instance, the molecular metal chalcogenide complex (MCC), or metal free inorganic ligands.[72,73]

On the other hand, several reports have pointed out the low electronical conductivity of the nanocrystalline materials. This is

because its low charge carrier mobility and because only a small quantity of charge carriers is available for conduction. In order to increase the carrier concentration it is necessary to be able to dope the NCs. Frequently, this is not an easy task, because the control of the doping level at the nanometer scale is difficult.[22,64,74]

Finally combining NCs in a fully dense solid is not straightforward. The use of techniques like HP or SPS helps to improve the density of the final pellet, but involves high temperatures and/or high electric fields, both of which increase the NCs size. Therefore it is necessary to optimize all the synthesis and the fabrication conditions of the nanostructured material to optimize their efficiency.

## 1.1 Thermoelectricity

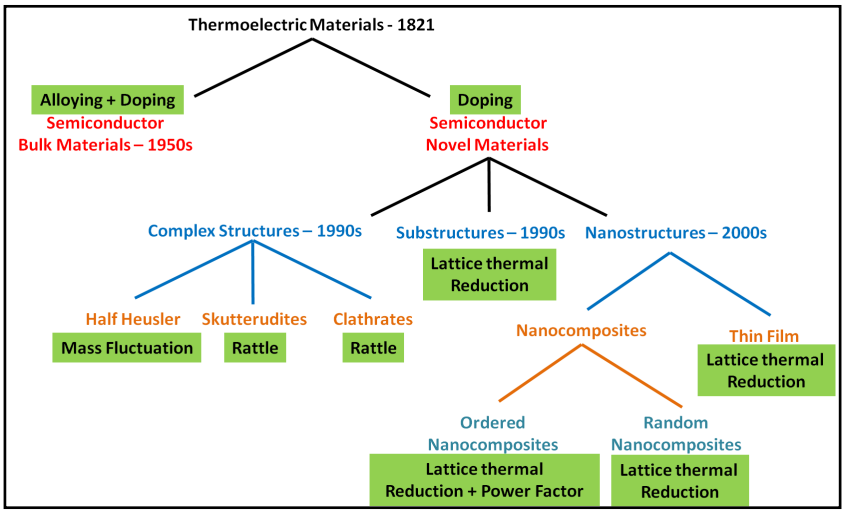


**Figure 1.2** Efforts for increasing ZT through the history.[45]

TE phenomena are associated with the simultaneous flow of electric current and heat in a system. Throughout the history, thermoelectricity has had different stages of progress (Figure 1.2). It started in the first half of the 19$^{th}$ century when TE effects, Seebeck,

Peltier and Thomson, were discovered and understood. In a second stage, between 1940 and 1960, the microscopic TE effects were studied and a large quantity of new TE materials was found. This was mainly due to the introduction of semiconductors as TE materials.[75] The values of the *ZT*, which determine the efficiency of the TE material, remained constant at around 1 for several decades. Starting in the 90's decade a renewed interest for thermoelectricity began. Since then and during the past two decades we had witnessed a huge progress in this field, associated with two main strategies: engineering new bulk PGEC materials[3,76,77] and nanostructuration.[78] These concepts inspired the scientific community and several reports of *ZT* values higher than 1 appeared. The higher figures of merit reported were for epitaxial multilayer structures based on $Sb_2Te_3/Bi_2Te_3$[79] and quantum dot superlattices based on PbTeSe dots in a PbTe matrix,[80] which exhibited *ZT* of 2.4 and 1.6 at room temperature, respectively. More recently, different groups showed that nano- and micro- structuration together with the optimal doping allowed to obtain *ZT* values up to 2.2 at 915 K for p-type PbTe;[33] 1.3 at 923 K for p-type PbSe;[47] 1.1 at 923 K for n-type PbS;[48] and 1.2-1.3 at 900 K for nanostructured PbSe-PbS.[81]

With values of *ZT* crossing the barrier of the unity and increasingly approaching to 3, the constant development of new techniques to produce materials and devices, and the new theoretical models, thermoelectricity has become a technology with a wide range of applications in waste energy recovery, refrigeration, and numerous applications.

In general, the thermoelectric effects: Seebeck, Peltier and Thomson, can be conveniently discussed with reference to the schematic circuit formed by two dissimilar materials or a thermocouple, as in the Figure 1.3.

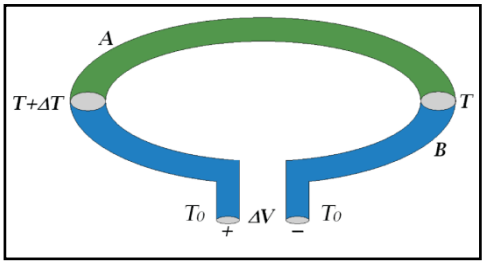


**Figure 1.3** Basic thermocouple circuit formed by two different materials *A* and *B*.

As discovered by **Thomas Seebeck** in 1821.[3,20,83] In a circuit formed by two different materials *A* and *B* in which their joins are at different temperature *T* and *T+ΔT*, an electromotive force is created. In open circuit conditions, it is possible to measure a voltage given by:

$$\Delta V = S_{AB}\Delta T \qquad (1.1)$$

Where $S_{AB}$ is defined as the relative Seebeck coefficient between the two materials.

Thirteen years later, in 1834, the French physicist **Jean Peltier** reported that there was an anomaly in the temperature (cooling or heating) of the junction between two different materials when an electric current passed through them.[3,20,83] When a current is applied in the circuit formed by the two dissimilar materials *A* and *B*, there is absorption/release of heat at the junctions, and the rate of the heat exchange at the junctions is:

$$Q = \Pi_{AB} I \qquad (1.2)$$

Where $\Pi_{AB}$ is the relative Peltier coefficient between the two materials.

Finally, **William Thomson** in 1851.[3] discovered a third TE effect, if there is a current and at the same time a temperature gradient in the circuit, there is a release or absorption of heat within each material that forms the circuit-This is the Thomson effect and the rate of heat

released or absorbed is proportional to the temperature gradient and to the current density, so that:

$$Q = \tau I \Delta T \qquad (1.3)$$

Where τ is the Thomson coefficient and has the same units as the Seebeck coefficient.

Thomson also derived the relations between the thermoelectric coefficients that are called Thomson equations:

$$\Pi = S_{AB} T \quad ; \quad \frac{\tau_{AB}}{T} = \frac{dS_{AB}}{dT} \qquad (1.4)$$

## 1.1.1 Thermoelectric effects

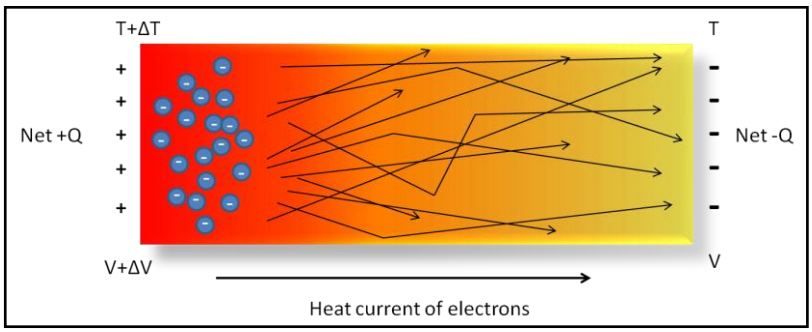


**Figure 1.4** Scheme of the electron diffusion due to a temperature gradient.

The thermoelectric phenomena can be intuitively understood by considering a simple model (Figure 1.4). If the material is in thermal equilibrium ($\Delta T = 0$), the probability that electrons diffuse in any direction is the same. Therefore the net flux of electrons is zero. However, if one side of the material is at higher temperature than the other, the electrons at the hot side will have more energy to move, therefore a net flux of charge will be established from the hot to the cold side. This process will continue until the flux of charge reaches a stationary state in which an accumulation of charge in each side is

present and hence a voltage is generated. The ratio between this voltage and the temperature difference is defined as the absolute Seebeck coefficient or thermopower *S* of the material:[82] $S=\Delta V/\Delta T$.

Usually, in a material where the majority charge carriers are electrons, if $\Delta T > 0$ then the voltage is negative and the Seebeck coefficient is also negative. Conversely, if the majority charge carriers are holes *S* is generally positive.

*S* is an absolute property of the material, but to measure it a second material (contact material) is required. Therefore, what is measured is the relative Seebeck coefficient between the two materials.

The Peltier effect comes from the fact that charge carriers can also transport heat or thermal energy when they flow. If the material is in thermal equilibrium, and a flux of electrons is imposed (i.e. by applying a voltage), there will be not only an electrical current, but also a net flow of heat. The Peltier effect can be observed when there is a current through a junction between two materials. This current produces either heating or cooling at the junction depending on its direction (equation 1.2)

The effect of producing a net flow of carriers and at the same time imposing a temperature gradient on the material results in either heating or cooling effect (Thomson effect). If the net flow of carriers goes from the hot to the cold end of the material, energy will be given by these electrons to the lattice, resulting in a heating effect. In contrast, of the carriers have to move from cold to hot end, they will require extra energy to be in equilibrium at the hot end. Therefore, cooling effect is produced. Thomson effect is a property of a given material and not of a combination of materials (equation 1.3)

## 1.2 Derivation of the transport properties

In order to understand the basic thermoelectric properties and the relationships between them, it is possible to follow two paths in the derivation of the thermoelectric properties, the microscopic and the macroscopic point of view. The first has to do with the development of the kinetic theory of electronic conduction (Drude, Lorentz) and uses semi-classical statistical mechanics, which describes microscopic processes. The second comes from the relationships developed by Onsager (1931),[84] in the framework of thermodynamics of irreversible processes.[85] The comparison between the two analysis provides a greater understanding not only of thermoelectric phenomena, but also generally of transport phenomena in materials.[86]

The transport properties of a material, the electrical conductivity $\sigma$, the thermal conductivity $\kappa$, the Seebeck coefficient $S$, the Hall coefficient $R_H$, the magnetoresistance coefficient $M$ and Nernst coefficient $Q$, can be studied by performing a statistical processing of the electron conduction with the carrier distribution function. This leads to the Boltzmann transport equation. From the general equations of transport, the macroscopic transport coefficients of the material can be obtained.[87–89] A brief description of the most important procedures is presented in the next section.

### 1.2.1 Boltzmann transport equation

The distribution function $f$ is used to analyze the transport properties of a crystalline material. Consider a crystal, in which the charge carriers are electrons, they form a system of particles whose behaviour is described by their distribution function, which depends on their energy and represents the probability that an energy state in equilibrium is occupied. $f_k$ $(r_t)$, describes the local concentration of electrons in the state k, in the spatial neighbourhood $r$. Under equilibrium conditions, the half-integer spin particles, such as

electrons, which obey the Pauli exclusion principle, satisfy the function of Fermi-Dirac distribution.[87]

$$f_k^0 = \frac{1}{\frac{\varepsilon-\xi}{e^{k_B T}}+1} = f^0(\varepsilon_k) \qquad (1.5)$$

Where $k_B$ is the Boltzmann constant, $T$ is the absolute temperature and $\xi$ is the Fermi energy or chemical potential, i.e., the necessary work to change the number of particles in the system. In general, the distribution function of the charge carriers can be affected by external fields, like electric and magnetic; the diffusion of the particles caused by temperature or concentration gradients; and the scattering from collisions between elements of the system. When the carriers in the crystal, are affected by some of these agents, the system will be described by a distribution function $f_k$, which is not in equilibrium. The Boltzmann transport equation postulate that in steady state,[87] the net rate of change of the distribution function must be zero, i.e.:

$$\left(\frac{\partial f}{\partial t}\right)_{field} + \left(\frac{\partial f}{\partial t}\right)_{diff} + \left(\frac{\partial f}{\partial t}\right)_{coll} = 0 \qquad (1.6)$$

Where each of the terms corresponds to changes in the distribution function resulting from the external fields, diffusion of carriers, and scattering by collisions, respectively. It is possible to obtain expressions for each one of the terms in the equation 1.6 and the resulting integral-differential equation is the Boltzmann transport equation in the steady state. Solving this equation can be very difficult, even for the stationary case, but can be considerably simplified by using the concept of relaxation time, which is the time it takes the system to return to equilibrium, after stopping the disruptive force. Therefore, it is possible to obtain an expression for the function distribution, and also for the density of electrical current and the thermal flow, that are given in terms of the distribution function.

$$\vec{J} = \int e v_k f_k dk \qquad (1.7)$$

$$\overrightarrow{J_Q} = \int f\{\varepsilon_k - \xi\} v_k dk \quad (1.8)$$

As a result, it is possible to write the general transport equations that define the transport coefficients, using the electrochemical potential μ:

$$\vec{J} = C_{11}\vec{\nabla}\mu + C_{12}\vec{\nabla}T \quad (1.9)$$

$$\overrightarrow{J_Q} = C_{21}\vec{\nabla}\mu + C_{22}\vec{\nabla}T \quad (1.10)$$

On the other hand, we can apply boundary conditions and obtain the transport equations in terms of known properties:

$$\vec{J} = \sigma\vec{E} + \gamma\vec{\nabla}T \quad (1.11)$$

$$\overrightarrow{J_Q} = J^2\rho\vec{u} - J\beta\vec{\nabla}T \quad (1.12)$$

Where $\sigma$, $\gamma$, $\rho$ and $\beta$ represent the electrical conductivity, electrothermal coefficient, electrical resistivity and Thomson coefficient respectively, and $\bar{u}$ is a unit vector in the direction of Joule heat release. So that the vector sum of $\bar{u}$ y $\nabla T$ gives the direction of absorption or release of heat.

### 1.2.2 Relation of the transport properties with non-equilibrium statistic

As was pointed out above, the thermoelectric effects are phenomena associated to a simultaneous electric and heat flow in a system. This type of phenomena can be studied in a very natural way with the modern theories of statistical thermodynamic irreversibility

The irreversible thermodynamics (or non-equilibrium statistical mechanics), deals with the physical processes rather than equilibrium states. Briefly, the theory that describes irreversible process uses the concepts of generalized forces that drive the process and the flows that are the system response to these forces.[84–86]

Table 1.1 describes some of the usual forces and flows, for the heat conduction, the diffusion of the particles, the electrical current and the chemical reactions in a general system.

**Table 1.1** Some examples of systems that can be modelled by Forces and Flows.

| | **Force $F_i$** | **Flow (Current) $J_i$** |
|---|---|---|
| **Heat Conduction** | $\nabla\frac{1}{T}$ | Energy Flow $J_i$ |
| **Diffusion** | $-\nabla\frac{\mu_i}{T}$ | Current of Diffusion $J_i$ |
| **Electrical current** | $-\nabla\frac{\phi}{T}=\frac{E}{T}$ | Current density of ions $I_i$ |
| **Chemical Reactions** | $\frac{A_i}{T}$ | Velocity of Reaction $v_i=\frac{1}{V}\frac{d\xi}{dt}$ |

Considering the case of a solid in which the charge carriers are the electrons, it is possible write equation for the variation of the local entropy H, as well as for the density of entropy, heat flow and number of electrons $J_H$, $J_Q$ and $J_N$.[90]

$$dH=\frac{1}{T}dU+\frac{\mu}{T}dN \;\Rightarrow\; J_H=\frac{1}{T}J_U+\frac{\mu}{T}J_N \qquad (1.13)$$

Where $U$ is the local energy, $\mu$ is the electrochemical potential and $J_E$, $J_U$ and $J_N$ are the current densities of entropy, energy and number of electrons.

Therefore the dynamic equations for the one-dimensional case are given by:[84,85]

$$J_{\mathrm{N}}=\gamma_{11}\frac{1}{T}\nabla\mu+\gamma_{12}\frac{1}{T^2}\nabla T \qquad (1.14)$$

$$J_Q=\gamma_{21}\frac{1}{T}\nabla\mu+\gamma_{22}\frac{1}{T^2}\nabla T \qquad (1.15)$$

Where $\gamma_{ij}$ are the kinetic coefficients and according to Onsager theorem $\gamma_{12}=\gamma_{21}$. The equations 1.14 and 1.15 form the basis for the

study of the heat and charge flows, when they flow parallel to the *x* axis in a system. In steady state without magnetic field, these three kinetic coefficients can be related with known magnitudes, using the boundary conditions:

$$J_{\mathrm{N}} = \left(-\frac{\sigma}{e^2}\right)\nabla\mu - \left(\frac{\sigma S}{e}\right)\nabla T \qquad (1.16)$$

$$J_{\mathrm{N}} = -\left(\frac{T\sigma S}{e}\right)\nabla\mu - \left(T\sigma S^2 + \kappa\right)\nabla T \qquad (1.17)$$

Where $\sigma$, $S$ and $\kappa$, represent the electrical conductivity, Seebeck coefficient and thermal conductivity. These equations describe the behaviour of any system in which there are simultaneous electrical and heat flows[86] and are equivalent to the equations 1.11 and 1.12 obtained with the semi-classical statistical mechanics.

This theory is a powerful tool to describe and study different kind of systems due to its generality. Additionally, this is a suitable theory to analyse systems that are not in thermodynamic equilibrium (majority of the systems in the nature) which are related to the transport process and with the rates of the chemical potential.

## 1.3 Thermoelectric devices

### 1.3.1 Application: thermoelectric generator

The conversion of energy (thermal in electrical and viceversa) constitutes the main applications: the solid state refrigeration and the electrical power generation from thermal sources.[20,91]

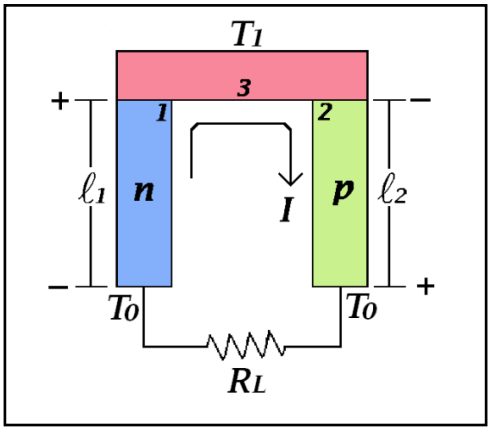


**Figure 1.5** Scheme of the thermoelectric generator.

The basic TE power generator (Figure 1.5) consists of two branches or elements, one p-type and the other n-type, joined by a third contact element, usually a metal. The ends of the two branches are connected to a load resistor $R_L$ and are maintained at a fixed temperature $T_0$, while the other two are kept at a temperature $T_1$, by means of a heat source. In this way, a temperature difference $\Delta T = (T_1 - T_0)$ is established. This temperature difference causes the charge carriers to diffuse from the hot junction ($T_1$) to the cold junction ($T_0$), across each of the arms of the device. As a result of the charge diffusing, there is a charge accumulation on each of the ends and therefore a voltage difference in each arm, which gives rise to a net current flow through the TE load resistor $R_L$.

#### 1.3.1.1 Calculation of efficiency

The efficiency of a single TE element is defined as the ratio of the useful electrical power delivered to the load resistance and the heat supplied by the source per second, $\dot{Q}_a$ .

$$\Psi = \frac{I^2 R_L}{\dot{Q}_a} \qquad (1.18)$$

The heat absorbed per second from the source, $\dot{Q}_a$, in steady state, is equal to the sum of the heat conduction rate $\dot{Q}_k$ in the TE element,

the Peltier heat $\dot{Q}_p$ (which develops due to the generated current) and the Joule heat $\dot{Q}_J$. It is assumed that half of the Joule heat generated returns to the hot junction and half to the cold junction. Hence, the heat balance equation is:

$$\dot{Q}_a = \dot{Q}_p + \dot{Q}_k - \frac{1}{2}\dot{Q}_j \qquad (1.19)$$

Where

$$\dot{Q}_p = \Pi I = ST_1 I$$

$$\dot{Q}_J = I^2 \mathrm{R}$$

$$\dot{Q}_k = \kappa(T_1 - T_0) = \kappa \Delta T$$

Where R is the total resistance of the TE elements, and κ is the total heat quantity driven by both arms per second and per degree of temperature.

And therefore:

$$\dot{Q}_a = ST_1 I - \frac{I^2}{2}\mathrm{R} + \kappa \Delta T \qquad (1.20)$$

On the other hand, the electric current in the circuit is given by:

$$I = \frac{V}{R+R_L} = \frac{S\Delta T}{\mathrm{R}+R_L} \qquad (1.21)$$

Replacing equations 1.20 and 1.21 into 1.18, we obtain:

$$\Psi = \frac{S^2(\Delta T^2)R_L/(R+R_L)^2}{\frac{S^2 T_1 \Delta T}{\mathrm{R}+R_L} + \kappa\, \Delta T - \frac{1}{2}S^2\frac{(\Delta T)^2 r}{(R+R_L)^2}} \qquad (1.22)$$

Making $m=R_L/R$ and simplifying:

$$\Psi = \frac{\Delta T}{T_1}\left[\frac{m/(m+1)}{1+\frac{\kappa R m+1}{S^2\ T_1} - \frac{1\Delta T\ \ 1}{2T_1 m+1}}\right] \qquad (1.23)$$

Defining $Z = \frac{S^2}{\kappa R}$ and maximizing $\Psi$ regarding to *m*, we obtain:

$$m_{opt} = \sqrt{1 + Z\bar{T}} \quad ; \quad \bar{T} = \frac{T_1 + T_0}{2} \qquad (1.24)$$

Substituting back into the equation (1.24), the efficiency of a single TE in terms of *Z* and $\Delta T$ can be written as:

$$\Psi = \frac{\Delta T}{T_1}\left[\frac{\sqrt{1+Z\bar{T}}-1}{\sqrt{1+Z\bar{T}}+T_1/T_2}\right] \qquad (1.25)$$

If $Z\bar{T} \to \infty$ therefore $\Psi_{max} = \frac{\Delta T}{T_1}$ that is the Carnot efficiency.

Z is known as a figure of merit of the TE material and is a direct function of the electrical and thermal transport properties. Because $\Psi$ depends directly on the figure of merit, high *Z* values causes an increase in the efficiency of the device, as seen in Figure 1.6.

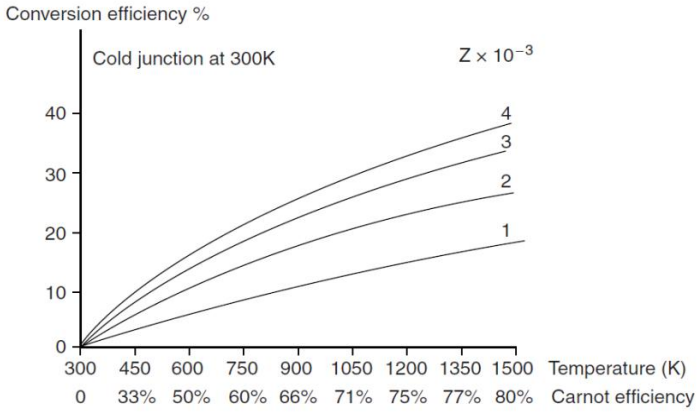


**Figure 1.6** Thermoelectric generator efficiency as a function of the temperature gradient, for different *Z* values. [3]

According to the definition of *Z*, the materials used to construct a thermoelectric device must have high Seebeck coefficients and electrical conductivities and low values of thermal conductivity. The big challenge in the search for thermoelectric materials is that these three properties are correlated each other and it is difficult to

decouple them. There are many studies focused on reducing the thermal conductivity and others focused on increasing the power factor ($PF = \sigma S^2$). High values for the PF are essential to improve the TE properties of a specific material.

$Z$ has units of [$K^{-1}$], therefore, it is better to work with a dimensionless quantity as $ZT$.

Practical devices usually are made of modules that contain several junctions n-p connected electrically in series and thermally in parallel. This allows increasing the voltage generated by the device as the effect of each couple can be added.

### 1.3.2 Application: thermoelectric refrigerator

Similarly to the generator, the basic thermoelectric cooler (Figure 1.7) consists of two thermocouples (n-type and p-type semiconductors) and a contact element, which must possess Seebeck coefficient, electrical resistivity and thermal resistivity negligible compared to the two semiconductors. The two thermoelectric elements are connected to a power source, which injects a current $I$ through the circuit.

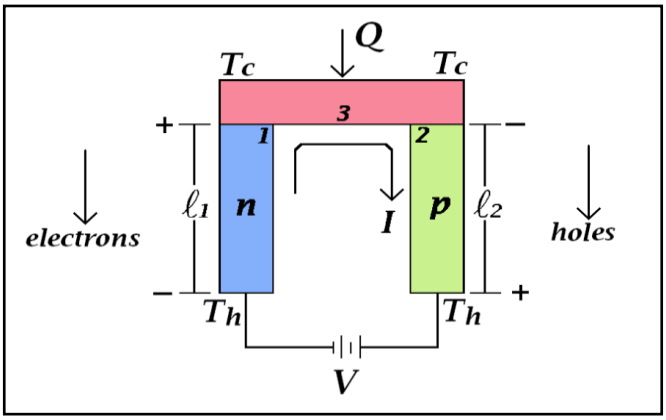


**Figure 1.7** Scheme of the thermoelectric refrigerator.

The charge flow through the circuit and the current is defined as positive in the direction positive charge flow (holes). A net flow of carriers in the same physical direction across the two arms exists, since the charge carriers transport thermal energy from the contact material towards the ends of the thermocouple. As a result, the junction with temperature $T_c$ absorbs heat (cooling) and the junction with temperature $T_h$ releases heat (heating).

#### 1.3.2.1 Calculation of efficiency

The coefficient of performance (COP), $\Phi$, of a cooling device is defined as the ratio between the net amount of heat absorbed per second, $\dot{Q}$, and the electric power supplied to the device $P$.

$$\Phi = \frac{\dot{Q}}{P} \qquad (1.26)$$

There is a cooling rate at cold junction, $\dot{Q}_p$ as a result of the Peltier effect, this cooling effect is counteracted by the Joule effect $\dot{Q}_j$ and also by heat conducted from the hot junction to the cold junction, due to thermal conduction, $\dot{Q}_k$. The temperature difference established by the carrier flow is $\Delta T = T_h - T_c$ and the average temperature between the hot and cold ends is $T_m = (T_h + T_c) / 2$. Therefore $T_c = T_m - \Delta T/2$.

The balance heat equation is given by:

$$\dot{Q} = \dot{Q}_p - \frac{1}{2}\dot{Q}_J - \dot{Q}_k \qquad (1.27)$$

Where,

$$\dot{Q}_p = \Pi I = S T_C I = S\left(T_m - \frac{\Delta T}{2}\right) I$$

$$\dot{Q}_J = \frac{1}{2} I^2 R$$

$$\dot{Q}_k = \kappa \Delta T$$

Therefore the heat balance equation is writing as:

$$\dot{Q} = S\left(T_m - \frac{\Delta T}{2}\right) I - \frac{1}{2} I^2 R + \kappa \Delta T \quad (1.28)$$

The power supplied to the device can be expressed as:

$$P = S\Delta T I + I^2 R \quad (1.29)$$

Replacing (1.28) and (1.29) in equation (1.26):

$$\Phi = \frac{S\left(T_m - \frac{\Delta T}{2}\right) I - \frac{1}{2} I^2 R + \kappa \Delta T}{S\Delta T I + I^2 R} \quad (1.30)$$

Defining $Z = \frac{S^2}{\kappa R}$ and maximizing regarding to *IR* ($\partial\Phi/\partial(IR)=0$):

$$(IR)_{opt} = \frac{S^2 \Delta T}{\sqrt{1+ZT_m}+1} \quad (1.31)$$

Replacing the value of $(IR)_{opt}$, gives the expression for the COP of the TE cooler:

$$\Phi = \frac{T_m\left(\sqrt{1+ZT_m}-1\right)}{\Delta T\sqrt{1+ZT_m}+1} - \frac{1}{2} \quad (1.32)$$

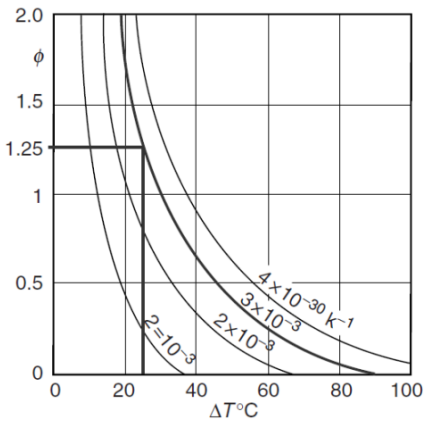


**Figure 1.8** Coefficient of performance of thermoelectric refrigerator as a function of the temperature gradient, for different Z values. [3]

The COP increases when increasing Z as shows Figure 1.8. Also, the COP of TE device is very high for low T gradients but very low at high temperatures.

When $Z \rightarrow \infty$ the COP approaches to the ideal heat or Carnot engine.

$$\Phi(Z \rightarrow \infty) = \frac{T_m}{\Delta T} - \frac{1}{2} = \frac{T_m - \Delta T/2}{\Delta T} = \frac{T_c}{T_h - T_c} \qquad (1.33)$$

In general the COP of a cooling device of a standard system, based on gas-compression technology, is 1.2 to 1.4, for a refrigerator working in a temperature range from 263 K to 323 K. This corresponds to TE devices with *ZT* between 3 and 4.

## 1.4 How to improve ZT

*ZT* strongly depends on the carrier concentration as shown in Figure 1.1.[35,42] The maximum values for *ZT* are reached when the carrier concentration corresponds to a strongly doped semiconductor with ~$10^{19}$ charge carriers.

In general, the research in TE materials can be divided on the reduction of the thermal conductivity[3,31,92] and the increases of the *PF*.[23,24,93–95]

A large progress has been made by reducing the thermal conductivity. One main approach in this direction consists in the use of alloy systems. In alloys thermal conductivity lower than each component can be obtained and this is called "alloy limit".[21] It is also common to use materials with atoms having a large mass difference or alternatively, the use of materials with complex crystal structures. The idea to search complex structures comes from the concept of the PGEC,[76] in where the complexity of the crystal structure would act as an effective phonon scattering tool, due to the presence of vacancies and rattlers atoms located in cages of some of

these structures. PGEC idea gave rise to a huge amount of research in different materials as: Skuterrudites,[96] Clathrates[43] and Zinth phases,[97] for which maximum *ZT* values reported, are between 1 and 1.5.[4,42,43]

On the other hand, the nanostructuration has become a successful strategy to increase *ZT*.[26,45,98–101] Nanostructures has allowed a dramatic reduction in thermal conductivity, even below the alloy limit.[28] The decrease in thermal conductivity is based on the effective phonon scattering at interfaces or grain boundaries. It is important to note that phonons with different wavelengths contribute to heat transport. The scattering of mid- to long wavelength phonons is efficient through the interfaces, while short wavelength phonons are more efficiently blocked through alloying.[99,100] This phonon blocking can be done without affecting significantly the carrier mobility, due to much shorter mean free path of electrons than phonons in the heavy doped semiconductors[53] Actually, interfaces in nanostructured materials can also act as energy filters[102] preferentially scattering the low energy charge carriers, which may lead to an increase of the Seebeck coefficient.[31]

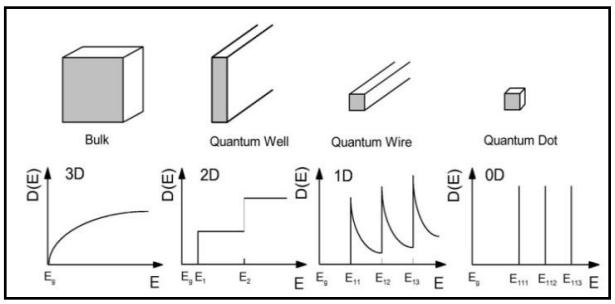


**Figure 1.9** Density of states as a function of the dimensionality for semiconductors.[78]

Theoretical reports indicate that quantum confinement could enhance the thermoelectric efficiency by decoupling the Seebeck coefficient and the electrical conductivity.[78,103] In quantum confined materials, the density of states has sharper changes as compared with the bulk (Figure 1.9). Since the Seebeck is related with the

derivative of the electronic density of states at the Fermi level (Mott Relation),[104] an increased Seebeck coefficient in quantum confinement nanomaterials is possibly expected. Pioneer reports on superlattices[79,80] inspired a huge amount of works in bulk nanostructured materials with record ZT values around 2.[33,47,48,81] However, the main cause to the TE efficiency improvement in nanostructured materials is the effective phonon blocking.

## 1.5 Synthesis of the nanomaterials

As nanostructuring can induce decoupling of the transport properties of the materials, it has become a key strategy to improve the TE performance, both by increasing the *PF* and by decreasing the $\kappa_l$.[31,51] Therefore, the aim of this section is to present different techniques to produce nanostructured materials.

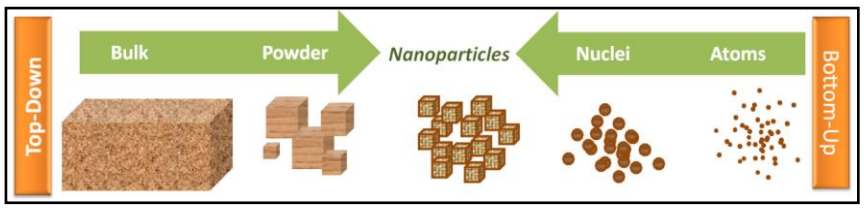


**Figure 1.10** Scheme Top-Down and Bottom-Up approaches.

In general, there are two main approaches to produce nanomaterials, the ***top-down*** and the ***bottom-up***[51,54,55] (Figure 1.10). In the former, the bulk material is broken into micro- or nano-sized particles usually by means of ball milling, spin melting or thermal cycling. Although this approach is the most frequently used and allows obtaining a wide range of nanostructured materials, it has some important drawbacks: i) it is not possible to control the size of the nanocrystalline domains and ii) the use of high temperatures and long processing times increase the energy spend and the cost of production.

On the other hand, the bottom–up approach consists in the production of the nanomaterials starting from atoms or nanoparticles. This approach includes high vacuum techniques, like molecular beam epitaxy (MBE) or chemical vapour deposition (CVD) to produce nanostructured films. A particularly interesting bottom-up approach is the use of nanoparticles as building blocks to produce nanostructured materials. To produce these nanoparticles, solution phase synthesis has become a very important tool. Examples of these methods are hydrothermal synthesis, sol-gel, electrochemical deposition, and ***Colloidal Synthesis***. The solution based synthesis offer a low cost alternative to produce nanostructured materials, because the low reaction temperatures and low processing times and the use of non-ultrapure precursors. Thanks to these advantages, the solution based synthesis has the potential to play an important role in the production of high efficiency TE nanostructured materials.[21,53,54]

## 1.5.1 Solution process: colloidal synthesis

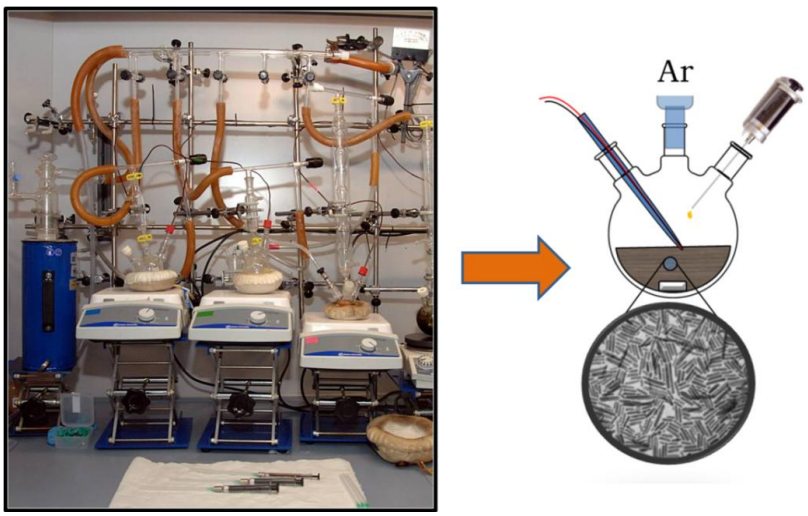


**Figure 1.11** Colloidal synthesis set up and scheme of the procedure to obtain the colloidal NCs.

As I discussed above, solution chemistry approaches to prepare nanomaterials are less costly than vacuum based techniques and have a large potential for scale-up. Especially synthetic routes like colloidal synthesis allow a precise control over size, shape and even composition of the NCs. It is possible to engineer NCs to use them as building blocks of thin film superlattices or bulk NCs solids. Additionally, colloidal NCs can be used in the production of electronic devices with inexpensive solution based-processes like spin coating, dip coating, spray deposition or inkjet printing, and they are compatible with inexpensive and flexible substrates.[55]

A typical synthesis to produce colloidal NCs (Figure 1.11) required three components: ***precursors***, ***organic surfactants*** and ***solvents***. In some cases the solvents also play the role of surfactants. This mixture is heated up to a reaction temperature in which the components are transformed into the active atomic/molecular species, also called monomers. Later, these monomers nucleate and growth controlled by the surfactants.[64]

The usual organic ligands used include long chain carboxylic and phosphonic acids (e.g., oleic acid and n-octadecylphosphonic acid), alkanethiols (e.g. dodecanethiol), alkyl phosphines, alkyl phosphines oxides (like trioctylphosphine TOP and trioctylphosphine oxide TOPO) and alkylamines (as hexadecylmine), among others. A common feature of the typically used surfactants is their polar head groups, functional parts capable of donating electron pairs. Therefore the surfactants can be defined as Lewis bases and the influence in controlling the growth of NCs is mainly addressed by their ability to form complexes with the free species in solution and by their ability to bind the atoms on the surface of the NCs.[64,66]

Although there is not a complete theoretical framework that explains the NCs formation mechanism, it is possible to understand the general features of the NCs formation, through the classical nucleation theory (CNT).[105–107] This theory only considers spherical nuclei NCs and in some cases is not successful in predicting nucleation rates. However, some groups that use computer

simulations have presented predictions of crystals nucleation rates without making use of any adjustable fit parameters.[107,108]

In general, the formation of the NCs involves two important stages: the ***nucleation*** and the ***growth.*** The precursors form a supersaturated solution of monomers that undergo a rapid nucleation of NCs seeds. Then the preformed nuclei grow by incorporating others monomers that remains in the solution.[67]

In order to obtain NCs with a narrow size distribution, a temporal separation between the nucleation and the growth stages is necessary. This can be done by the hot injection technique.[109] Here a rapid addition of the reagents to the reaction flask raises the precursor concentration above the nucleation threshold causing a short nucleation burst that partially relieves the supersaturation. In some cases it is possible to have the separation between the nucleation and the growth using a steady heating which is a more simple procedure.

According to the CNT,[106,109–111] monomers can combine to form small and unstable clusters. The change in free energy $\Delta G(n)$ for the formation of a spherical cluster with $n$ units and radius $r$, in a supersaturated solution, is given by:

$$\Delta G(n) = \frac{4}{3}\pi r^3(\Delta\mu) + 4\pi r^2(\gamma) \qquad (1.34)$$

Where $\Delta\mu(<0)$ is the decrease in free energy per unit volume due to the formation of the cluster (solid), and $\gamma(>0)$ is the surface free energy per unit of surface area (cost of creating a solid-liquid interface). Figure 1.12 shows the behaviour of the $\Delta G(n)$, for small radius. The free energy increases until a maximum value that corresponds to a critical radius $r_c = 2\gamma/|\Delta\mu|$ and the height of the nucleation barrier is $\Delta G_c = \frac{16\pi}{3}\gamma^3/(|\Delta\mu|)^2$. For clusters bigger than the critical size ($r_c$) the free energy decreases with the radius. Thus, the behaviour of the created cluster depends on its size, so they can either grow or redissolve in the solution.

The crystal nucleation rate can be expressed as $J = Ae^{(-\Delta G/k_B T)}$. Therefore, the CNT expression for the nucleation rate can be written as:

$$J = Ae^{\left[-\frac{16\pi}{3}\gamma^3/(|\Delta\mu|)^2\right]} \quad (1.35)$$

Where A is the kinetic factor. Since $\Delta\mu$ can be given in terms of the degree of supersaturation ($s$) and the temperature, this equation shows the three important parameters that guide the nucleation rate (the surface energy $\gamma$, the temperature and the ratio of concentration solution to the equilibrium saturation concentration $s$).

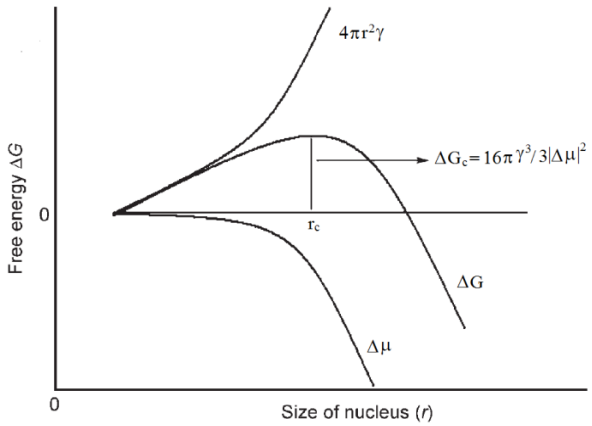


**Figure 1.12** Diagram of the free energy for the nucleation processes.[110]

In the presence of high concentration of free atomic species in the solution (early phases of growth), the smaller crystals grow faster than the bigger, because they are more reactive. In this case, the starting size distribution narrows with the time. This situation is called ***focusing regime.***[108] However, with the time passing, the concentration of free species in the solution decreases. So there are not enough monomers to supply the fast growth of the smaller particles and the growth rate of the bigger particles increases leading to a broaden size distribution, ***defocusing regime***. Finally when the

concentration of free species continues decreasing, the small NCs dissolve and feed the larger crystals. This is called the "Oswald Ripening" regime.

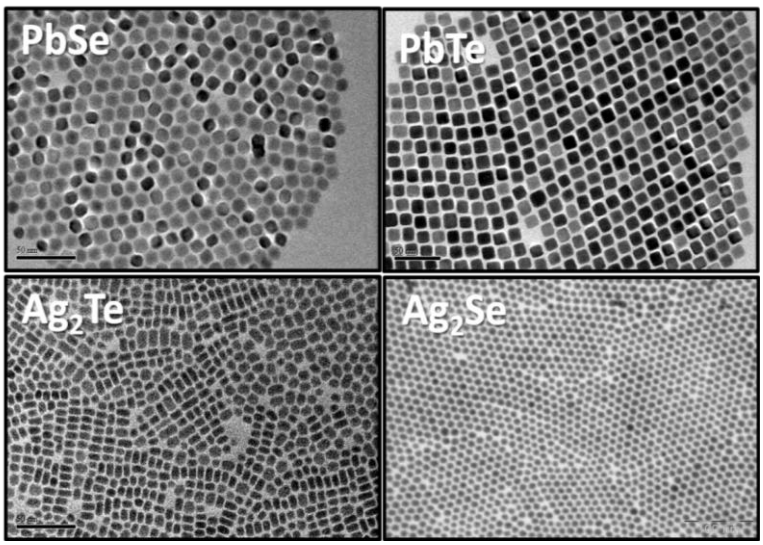


**Figure 1.13** NCs produced by means of colloidal synthesis during this thesis.

The last parts of the synthesis procedure consist in the isolation and purification of the NCs. The NCs are isolated from their growth solution by the introduction of another solvent that is miscible with the first solvent but have an unfavourable interaction with the organic ligand, called "nonsolvent". This nonsolvent reduces the barrier to aggregation and destabilizes the NCs dispersion. Centrifuging the resulting suspension allows the NCs to precipitate and be isolated. The resultant material consists in NCs with an organic capping layer that can be redispersed in a variety of solvents and with further redispersion-precipitation steps their purification is completed. Figure 1.13 shows some of the NCs produced by colloidal synthesis during this thesis.

#### 1.5.1.1 Size, Shape and morphology control

As it was mentioned above, the main advantage of the colloidal synthesis is the possibility to tune size and shape of the NCs. The narrow size distribution can be obtained with the control of the monomers concentration in the nucleation and growth stages, i.e., ***focusing regime.*** In general, it is important to maintain the temporal separation between the nucleation and growth stages. This means that the nucleation must occur in a short time.

To control the size, shape, and composition of the NCs, it is necessary to adjust the reaction parameters, such as the reaction time, temperature, concentration as well as to select the correct reagents and surfactants.[110,112–115] Tuning the reagents to surfactants concentration ratio provide a way to control de NCs size, because usually a high concentration of surfactants or stabilizers facilitates the formation of small NCs. The surfactants bonded to the NCs surface provide a dynamic organic shell that stabilizes the NCs in solution and mediates their growth.

There are different approaches to the shape control. In some of those the organic surfactants play a key role. The selective adhesion of surfactant molecules allows tuning the growth of different crystal facets and as a consequence it is possible to tailor the NCs shape from spherical to highly anisotropic shapes. It is also possible to use mixtures of organic ligands that provide this difference in the growth rates. As an example, depending on the length of the alkyl and the concentration of alkylphosphonic acid, CdSe NCs can be synthesized in different shapes as rods, arrows, or tetrapods.[65]

Another technique is the oriented attachment in which the nanoparticles attach to each other and fuse along the same crystal facets forming oriented chains, which allows obtaining nanowires or nanorods. This kind of anisotropic assembly has been reported in Ag,[116] CdTe,[117] and ZnO,[56] among others.

## 1.5.2 Nanocrystals macroscopic arrangement

In order to construct devices with the NCs as building blocks, it is necessary to assemble them at a macroscopic scale. The behaviour of the NCs arrays not only depends on the NCs individual properties but also on the interconnection between them, the packing density and the mutual orientation of the NCs.[64,118] NCs can be assembled into films or bulk nanostructured solids and they can be ordered or disordered structures.

Ordered NC films, also known as superlattices, are anisotropic materials with a three dimensional periodicity.[118,119] To obtain superlattices, several factors have to be considered like the monodispersity of the NCs (narrow size distribution), their solubility, the evaporation rate of the solvent, etc. The uniformity of periodic nanoparticle arrays (films, 3D crystals) is especially attractive for practical applications and for fundamental studies. In spite of this, their application in the construction of the actual electronic devices is still under optimization because they are difficult to be scaled up and reproduced. On the other hand, colloidal NCs assembled into a bulk nanostructured solid[120] with a short-range order among the NCs, have high reproducibility .
The production of new nanostructured materials like binary assemblies both ordered and disordered, obtained by a simple mixture of two different colloidal NCs, is an example of the versatility of the bottom-up approach. Figure 1.14 shows the schematic structures that can be obtained, a binary NCs superlattice and a bulk NCs assembly.

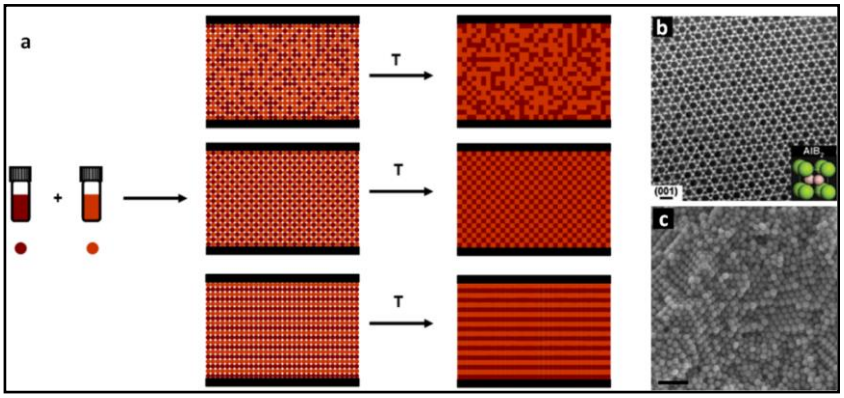


**Figure 1.14** (a) Scheme of binary assemblies from colloidal NCs (b) binary nanoparticle superlattices of 6.7 nm PbS and 3.0 nm Pd, scale bar of 10nm [118] and (c) Bulk NCs assembly of CuS NCs produced by the author, scale bar of 100nm.

### 1.5.3 Challenges of the use of colloidal NCs for thermoelectrics

Since the production of the NCs takes place in solution and in the presence of organic surfactant molecules, the NCs are covered by an isolating shell. The surface ligands become a significant challenge to use NCs in applications where the electronic transport is crucial, since the presence of the organic surface molecules creates highly insulating barriers which block the charge carriers.[72,121]

To control the charge carrier concentration is the second big challenge. The attempts to increase the carrier concentration in NCs have found some difficulties. The incorporation of atomic impurities or doping is challenging due to the small distance the atom need to diffuse to exit the NCs.[122] Other approaches has been used like expose the NCs to a specific atmosphere, e.g. potassium vapour.[123] Tuning the NCs stoichiometry is another powerful technique to dope them.[61]

On the other hand, in order for a material to be used in an actual TE device, it must be consolidated into a dense bulk pellet, which is a

challenge in the bottom-up processing of bulk nanostructure materials assembled from colloidal NCs. Low density materials usually have poor mechanical properties and are difficult to work with. Also the electrical properties can degrade by orders of magnitude due to the porosity.[124–126] When the material is not completely dense there is an additional charge scattering and disruption on the mean free path of the electron as it travels between grains.

Here I will employ a bottom-up approach using colloidal NCs as building blocks to produce nanostructured materials with enhanced TE properties. First, I will show how binary nanocomposites from $Ag_2Te$ and PbTe NCs present enhance thermoelectric properties as compared to the single $Ag_2Te$ nanostructured material. This shows the advantages of the solution processing to tune the structure of the nanocomposites. Then, I will investigate the ligand exchange process to improve the electrical transport in the NCs assemblies. I present a simple strategy to make an organic ligand displacement by metal salts which results in a drastic improvement of the figure of merit of the $Ag_2Te$ bulk nanostructured material. Afterwards, I will also study how to control charge carrier concentration by ligand exchange process that allows controlling NCs surface composition. Finally, I will study the methods to improve bulk nanostructured material density by using SPS technique to consolidate $Cu_2SnSe_3$ NCs obtained by a novel synthesis.

## 1.6 References

(1) BP Statistical Review of World Energy June 2013 http://www.bp.com/statisticalreview.

(2) European Commission Energy. Energy 2020 - A strategy for competitive, sustainable and secure energy http://ec.europa.eu/energy/strategies/2010/2020_en.htm.

(3) Rowe, D. M. *Thermoelectrics Handbook: Macro to Nano*; CRC Press INC, 2006.

(4) Sootsman, J. R.; Chung, D. Y.; Kanatzidis, M. G. New and Old Concepts in Thermoelectric Materials. *Angew. Chem. Int. Ed Engl.* **2009**, *48*, 8616–8639.

(5) Crabtree, G. W.; Lewis, N. S. Solar Energy Conversion. *Phys. Today* **2007**, *60*, 37–42.

(6) Rowley, J. C. Geothermal Energy Development. *Phys. Today* **2008**, *30*, 36–45.

(7) Tritt, T. M.; Böttner, H.; Chen, L. Thermoelectrics: Direct Solar Thermal Energy Conversion. *MRS Bull.* **2008**, *33*, 366–368.

(8) Reynolds, G. T. Energy Research for Physicists. *Phys. Today* **2008**, *29*, 34–41.

(9) Shakouri, A. Recent Developments in Semiconductor Thermoelectric Physics and Materials. *Annu. Rev. Mater. Res.* **2011**, *41*, 399–431.

(10) Vining, C. B. An Inconvenient Truth about Thermoelectrics. *Nat. Mater.* **2009**, *8*, 83–85.

(11) Goldsmid, H. J. *Thermoelectric Refrigeration*; Plenum Press, 1964.

(12) MacDonald, D. K. C. *Thermoelectricity: An Introduction to the Principles*; Dover Publications, 2006.

(13) Zebarjadi, M.; Esfarjani, K.; Dresselhaus, M. S.; Ren, Z. F.; Chen, G. Perspectives on Thermoelectrics: From Fundamentals to Device Applications. *Energy Environ. Sci.* **2012**, *5*, 5147.

(14) Staff, P. T. E. IPF 2011: Cars, Batteries, and Thermoelectrics. *Phys. Today* **2011**.

(15) DiSalvo, F. J. Thermoelectric Cooling and Power Generation. *Science* **1999**, *285*, 703–706.

(16) Tritt, T. M.; Subramanian, M. A. Thermoelectric Materials, Phenomena, and Applications: A Bird's Eye View. *MRS Bull.* **2006**, *31*, 188–198.

(17) Van Der Sluis, P. Improvements in Cooking Stoves. WO/2006/103613, October 6, 2006.

(18) Amatya, R.; Ram, R. J. Solar Thermoelectric Generator for Micropower Applications. *J. Electron. Mater.* **2010**, *39*, 1735–1740.

(19) Bell, L. E. Cooling, Heating, Generating Power, and Recovering Waste Heat with Thermoelectric Systems. *Science* **2008**, *321*, 1457–1461.

(20) Goldsmid, H. J. *Introduction to Thermoelectricity*; Springer: Heidelberg; New York, 2010.

(21) Szczech, J. R.; Higgins, J. M.; Jin, S. Enhancement of the Thermoelectric Properties in Nanoscale and Nanostructured Materials. *J. Mater. Chem.* **2011**, *21*, 4037–4055.

(22) Zebarjadi, M.; Joshi, G.; Zhu, G.; Yu, B.; Minnich, A.; Lan, Y.; Wang, X.; Dresselhaus, M.; Ren, Z.; Chen, G. Power Factor Enhancement by Modulation Doping in Bulk Nanocomposites. *Nano Lett* **2011**, *11*, 2225–2230.

(23) Zebarjadi, M.; Liao, B.; Esfarjani, K.; Dresselhaus, M.; Chen, G. Enhancing the Thermoelectric Power Factor by Using Invisible Dopants. *Adv. Mater.* **2013**, *25*, 1577–1582.

(24) Mingo, N. Thermoelectric Figure of Merit and Maximum Power Factor in III–V Semiconductor Nanowires. *Appl. Phys. Lett.* **2004**, *84*, 2652–2654.

(25) Tian, Z.; Lee, S.; Chen, G. Heat Transfer in Thermoelectric Materials and Devices. *J. Heat Transf.* **2013**, *135*, 061605–061605.

(26) Liu, W.; Yan, X.; Chen, G.; Ren, Z. Recent Advances in Thermoelectric Nanocomposites. *Nano Energy* **2012**, *1*, 42–56.

(27) Pei, Y.; Shi, X.; LaLonde, A.; Wang, H.; Chen, L.; Snyder, G. J. Convergence of Electronic Bands for High Performance Bulk Thermoelectrics. *Nature* **2011**, *473*, 66–69.

(28) Dresselhaus, M. S.; Chen, G.; Tang, M. Y.; Yang, R. G.; Lee, H.; Wang, D. Z.; Ren, Z. F.; Fleurial, J.-P.; Gogna, P. New Directions for Low-Dimensional Thermoelectric Materials. *Adv. Mater.* **2007**, *19*, 1043–1053.

(29) Ohta, H.; Kim, S.; Mune, Y.; Mizoguchi, T.; Nomura, K.; Ohta, S.; Nomura, T.; Nakanishi, Y.; Ikuhara, Y.; Hirano, M.; et al. Giant Thermoelectric Seebeck Coefficient of a Two-Dimensional Electron Gas in $SrTiO_3$. *Nat. Mater.* **2007**, *6*, 129–134.

(30) Liu, W.-S.; Zhao, L.-D.; Zhang, B.-P.; Zhang, H.-L.; Li, J.-F. Enhanced Thermoelectric Property Originating from Additional Carrier Pocket in Skutterudite Compounds. *Appl. Phys. Lett.* **2008**, *93*, 042109.

(31) Minnich, A. J.; Dresselhaus, M. S.; Ren, Z. F.; Chen, G. Bulk Nanostructured Thermoelectric Materials: Current Research and Future Prospects. *Energy Environ. Sci.* **2009**, *2*, 466.

(32) Bhandari, C. M.; Rowe, D. M. The Effect of Phonon-Grain Boundary Scattering, Doping and Alloying on the Lattice Thermal Conductivity of Lead Telluride. *J. Phys. Appl. Phys.* **1983**, *16*, L75.

(33) Biswas, K.; He, J.; Blum, I. D.; Wu, C.-I.; Hogan, T. P.; Seidman, D. N.; Dravid, V. P.; Kanatzidis, M. G. High-Performance Bulk Thermoelectrics with All-Scale Hierarchical Architectures. *Nature* **2012**, *489*, 414–418.

(34) Mahan, G. D.; Sofo, J. O. The Best Thermoelectric. *Proc. Natl. Acad. Sci.* **1996**, *93*, 7436–7439.

(35) Sofo, J. O.; Mahan, G. D. Optimum Band Gap of a Thermoelectric Material. *Phys. Rev. B* **1994**, *49*, 4565–4570.

(36) Fan, Z.; Wang, H.-Q.; Zheng, J.-C. Searching for the Best Thermoelectrics through the Optimization of Transport Distribution Function. *J. Appl. Phys.* **2011**, *109*, 073713.

(37) Mahan, G.; Sales, B.; Sharp, J. Thermoelectric Materials: New Approaches to an Old Problem. *Phys. Today* **2008**, *50*, 42–47.

(38) Wood, C. Materials for Thermoelectric Energy Conversion. *Rep. Prog. Phys.* **1988**, *51*, 459.

(39) Gao, M.-R.; Xu, Y.-F.; Jiang, J.; Yu, S.-H. Nanostructured Metal Chalcogenides: Synthesis, Modification, and Applications in Energy Conversion and Storage Devices. *Chem. Soc. Rev.* **2013**, *42*, 2986.

(40) Rowe, D. M. *CRC Handbook of Thermoelectrics*; CRC Press, 1995.

(41) Nolas, G. S.; Poon, J.; Kanatzidis, M. Recent Developments in Bulk Thermoelectric Materials. *MRS Bull.* **2006**, *31*, 199–205.

(42) Snyder, G. J.; Toberer, E. S. Complex Thermoelectric Materials. *Nat. Mater.* **2008**, *7*, 105–114.

(43) Kleinke, H. New Bulk Materials for Thermoelectric Power Generation: Clathrates and Complex Antimonides. *Chem. Mater.* **2010**, *22*, 604–611.

(44) Vineis, C. J.; Shakouri, A.; Majumdar, A.; Kanatzidis, M. G. Nanostructured Thermoelectrics: Big Efficiency Gains from Small Features. *Adv. Mater.* **2010**, *22*, 3970–3980.

(45) Alam, H.; Ramakrishna, S. A Review on the Enhancement of Figure of Merit from Bulk to Nano-Thermoelectric Materials. *Nano Energy* **2013**, *2*, 190–212.

(46) Poudel, B.; Hao, Q.; Ma, Y.; Lan, Y.; Minnich, A.; Yu, B.; Yan, X.; Wang, D.; Muto, A.; Vashaee, D.; et al. High-Thermoelectric Performance of Nanostructured Bismuth Antimony Telluride Bulk Alloys. *Science* **2008**, *320*, 634–638.

(47) Lee, Y.; Lo, S.-H.; Androulakis, J.; Wu, C.-I.; Zhao, L.-D.; Chung, D.-Y.; Hogan, T. P.; Dravid, V. P.; Kanatzidis, M. G. High-Performance Tellurium-Free Thermoelectrics: All-Scale Hierarchical Structuring of P-Type PbSe–MSe Systems (M = Ca, Sr, Ba). *J. Am. Chem. Soc.* **2013**.

(48) Zhao, L.-D.; Lo, S.-H.; He, J.; Li, H.; Biswas, K.; Androulakis, J.; Wu, C.-I.; Hogan, T. P.; Chung, D.-Y.; Dravid, V. P.; et al. High Performance Thermoelectrics from Earth-Abundant Materials: Enhanced Figure of Merit in PbS by Second Phase Nanostructures. *J. Am. Chem. Soc.* **2011**, *133*, 20476–20487.

(49) Martín-González, M.; Caballero-Calero, O.; Díaz-Chao, P. Nanoengineering Thermoelectrics for 21st Century: Energy

Harvesting and Other Trends in the Field. *Renew. Sustain. Energy Rev.* **2013**, *24*, 288–305.

(50) Cadavid, D.; Rodriguez, J. E. Thermoelectric Properties of Bi-Sb Samples Grown by Mechanical Alloy. *Phys. Status Solidi C* **2005**, *2*, 3677–3680.

(51) Lan, Y.; Minnich, A. J.; Chen, G.; Ren, Z. Enhancement of Thermoelectric Figure-of-Merit by a Bulk Nanostructuring Approach. *Adv. Funct. Mater.* **2010**, *20*, 357–376.

(52) Liu, W.-S.; Zhang, B.-P.; Li, J.-F.; Zhang, H.-L.; Zhao, L.-D. Enhanced Thermoelectric Properties in $CoSb_{3-x}Te_x$ Alloys Prepared by Mechanical Alloying and Spark Plasma Sintering. *J. Appl. Phys.* **2007**, *102*, 103717.

(53) Bux, S. K.; Fleurial, J.-P.; Kaner, R. B. Nanostructured Materials for Thermoelectric Applications. *Chem. Commun.* **2010**, *46*, 8311.

(54) Zhao, Y.; Dyck, J. S.; Burda, C. Toward High-Performance Nanostructured Thermoelectric Materials: The Progress of Bottom-up Solution Chemistry Approaches. *J. Mater. Chem.* **2011**, *21*, 17049.

(55) Alivisatos, A. P. Nanocrystals: Building Blocks for Modern Materials Design. *Endeavour* **1997**, *21*, 56–60.

(56) Pacholski, C.; Kornowski, A.; Weller, H. Self-Assembly of ZnO: From Nanodots to Nanorods. *Angew. Chem. Int. Ed.* **2002**, *41*, 1188–1191.

(57) Cadavid, D.; Ibáñez, M.; Gorsse, S.; López, A. M.; Cirera, A.; Morante, J. R.; Cabot, A. Bottom-up Processing of Thermoelectric Nanocomposites from Colloidal Nanocrystal Building Blocks: The Case of $Ag_2Te$–PbTe. *J. Nanoparticle Res.* **2012**, *14*, 1–10.

(58) Cadavid, D.; Ibáñez, M.; Shavel, A.; Durá, O. J.; Torre, M. A. L. de la; Cabot, A. Organic Ligand Displacement by Metal Salts to Enhance Nanoparticle Functionality: Thermoelectric Properties of $Ag_2Te$. *J. Mater. Chem. A* **2013**, *1*, 4864–4870.

(59) Ibáñez, M.; Cadavid, D.; Anselmi-Tamburini, U.; Zamani, R.; Gorsse, S.; Li, W.; López, A. M.; Morante, J. R.; Arbiol, J.; Cabot, A. Colloidal Synthesis and Thermoelectric Properties of Cu2SnSe3 Nanocrystals. *J. Mater. Chem. A* **2012**, *1*, 1421–1426.

(60) Ibáñez, M.; Zamani, R.; LaLonde, A.; Cadavid, D.; Li, W.; Shavel, A.; Arbiol, J.; Morante, J. R.; Gorsse, S.; Snyder, G. J.; et al. $Cu_2ZnGeSe_4$ Nanocrystals: Synthesis and Thermoelectric Properties. *J Am Chem Soc* **2012**, *134*, 4060–4063.

(61) Ibáñez, M.; Cadavid, D.; Zamani, R.; García-Castelló, N.; Izquierdo-Roca, V.; Li, W.; Fairbrother, A.; Prades, J. D.; Shavel, A.; Arbiol, J.; et al. Composition Control and Thermoelectric Properties of Quaternary Chalcogenide Nanocrystals: The Case of Stannite $Cu_2CdSnSe_4$. *Chem Mater* **2012**, *24*, 562–570.

(62) Ibáñez, M.; Zamani, R.; Gorsse, S.; Fan, J.; Ortega, S.; Cadavid, D.; Morante, J. R.; Arbiol, J.; Cabot, A. Core–Shell Nanoparticles As Building Blocks for the Bottom-Up Production of Functional Nanocomposites: PbTe–PbS Thermoelectric Properties. *ACS Nano* **2013**, *7*, 2573–2586.

(63) Shavel, A.; Cadavid, D.; Ibáñez, M.; Carrete, A.; Cabot, A. Continuous Production of $Cu_2ZnSnS_4$ Nanocrystals in a Flow Reactor. *J. Am. Chem. Soc.* **2012**, *134*, 1438–1441.

(64) Talapin, D. V.; Lee, J.-S.; Kovalenko, M. V.; Shevchenko, E. V. Prospects of Colloidal Nanocrystals for Electronic and Optoelectronic Applications. *Chem. Rev.* **2010**, *110*, 389–458.

(65) Manna, L.; Scher, E. C.; Alivisatos, A. P. Synthesis of Soluble and Processable Rod-, Arrow-, Teardrop-, and Tetrapod-

Shaped CdSe Nanocrystals. *J. Am. Chem. Soc.* **2000**, *122*, 12700–12706.

(66) Murray, C. B.; Kagan, C. R.; Bawendi, M. G. Synthesis and Characterization of Monodisperse Nanocrystals and Close-Packed Nanocrystal Assemblies. *Annu. Rev. Mater. Sci.* **2000**, *30*, 545–610.

(67) Yin, Y.; Alivisatos, A. P. Colloidal Nanocrystal Synthesis and the Organic–inorganic Interface. *Nature* **2004**, *437*, 664–670.

(68) Michalet, X.; Pinaud, F. F.; Bentolila, L. A.; Tsay, J. M.; Doose, S.; Li, J. J.; Sundaresan, G.; Wu, A. M.; Gambhir, S. S.; Weiss, S. Quantum Dots for Live Cells, in Vivo Imaging, and Diagnostics. *Science* **2005**, *307*, 538–544.

(69) Alivisatos, A. P. Semiconductor Clusters, Nanocrystals, and Quantum Dots. *Science* **1996**, *271*, 933–937.

(70) Alivisatos, A. P. Perspectives on the Physical Chemistry of Semiconductor Nanocrystals. *J. Phys. Chem.* **1996**, *100*, 13226–13239.

(71) Mitzi, D. B. Solution Processing of Chalcogenide Semiconductors via Dimensional Reduction. *Adv. Mater.* **2009**, *21*, 3141–3158.

(72) Kovalenko, M. V.; Scheele, M.; Talapin, D. V. Colloidal Nanocrystals with Molecular Metal Chalcogenide Surface Ligands. *Science* **2009**, *324*, 1417–1420.

(73) Kovalenko, M. V.; Spokoyny, B.; Lee, J.-S.; Scheele, M.; Weber, A.; Perera, S.; Landry, D.; Talapin, D. V. Semiconductor Nanocrystals Functionalized with Antimony Telluride Zintl Ions for Nanostructured Thermoelectrics. *J Am Chem Soc* **2010**, *132*, 6686–6695.

(74) Buonsanti, R.; Milliron, D. J. Chemistry of Doped Colloidal Nanocrystals. *Chem. Mater.* **2013**.

(75) Tritt, T. M. *Recent Trends in Thermoelectric Materials Research 3*; Acad. Press: San Diego, Calif., 2001.

(76) Slack, G. A. Design Concepts for Improved Thermoelectric Materials. In *MRS Online Proceedings Library*; 1997; Vol. 478, p. 47.

(77) Tritt, T. M. Thermoelectric Phenomena, Materials, and Applications. *Annu. Rev. Mater. Res.* **2011**, *41*, 433–448.

(78) Hicks, L. D.; Dresselhaus, M. S. Effect of Quantum-Well Structures on the Thermoelectric Figure of Merit. *Phys. Rev. B* **1993**, *47*, 12727–12731.

(79) Venkatasubramanian, R.; Siivola, E.; Colpitts, T.; O'Quinn, B. Thin-Film Thermoelectric Devices with High Room-Temperature Figures of Merit. *Nature* **2001**, *413*, 597–602.

(80) Harman, T. C.; Taylor, P. J.; Walsh, M. P.; LaForge, B. E. Quantum Dot Superlattice Thermoelectric Materials and Devices. *Science* **2002**, *297*, 2229–2232.

(81) Androulakis, J.; Todorov, I.; He, J.; Chung, D.-Y.; Dravid, V.; Kanatzidis, M. Thermoelectrics from Abundant Chemical Elements: High-Performance Nanostructured PbSe–PbS. *J. Am. Chem. Soc.* **2011**, *133*, 10920–10927.

(82) Lovell, M. C.; Avery, A. J.; Vernon, M. W. *Physical Properties of Materials*; Springer, 1976.

(83) Ioffe, A. F. *Semiconductor Thermoelements, and Thermoelectric Cooling*; Infosearch, ltd., 1957.

(84) Onsager, L. Reciprocal Relations in Irreversible Processes. I. *Phys. Rev.* **1931**, *37*, 405–426.

(85) Pathria, R. K.; Beale, P. D. *Statistical Mechanics*; Academic Press, 2011.

(86) Kondepudi, D. K.; Prigogine, I. *Modern Thermodynamics: From Heat Engines to Dissipative Structures*; John Wiley, 1998.

(87) Ziman, J. M. *Principles of the Theory of Solids*; Cambridge University Press, 1972.

(88) Ziman, J. M. *Electrons and Phonons: The Theory of Transport Phenomena in Solids*; Oxford University Press, 2001.

(89) Zhou, J.; Li, X.; Chen, G.; Yang, R. Semiclassical Model for Thermoelectric Transport in Nanocomposites. *Phys. Rev. B* **2010**, *82*, 115308.

(90) Goupil, C. Thermodynamics of the Thermoelectric Potential. *J. Appl. Phys.* **2009**, *106*, 104907.

(91) Nolas, G. S.; Sharp, J.; Goldsmid, J. *Thermoelectrics: Basic Principles and New Materials Developments*; Springer, 2001.

(92) Christensen, M.; Abrahamsen, A. B.; Christensen, N. B.; Juranyi, F.; Andersen, N. H.; Lefmann, K.; Andreasson, J.; Bahl, C. R. H.; Iversen, B. B. Avoided Crossing of Rattler Modes in Thermoelectric Materials. *Nat. Mater.* **2008**, *7*, 811–815.

(93) Vineis, C. J.; Harman, T. C.; Calawa, S. D.; Walsh, M. P.; Reeder, R. E.; Singh, R.; Shakouri, A. Carrier Concentration and Temperature Dependence of the Electronic Transport Properties of Epitaxial PbTe and PbTe/PbSe Nanodot Superlattices. *Phys. Rev. B* **2008**, *77*, 235202.

(94) Ikeda, H.; Salleh, F. Influence of Heavy Doping on Seebeck Coefficient in Silicon-on-Insulator. *Appl. Phys. Lett.* **2010**, *96*, 012106.

(95) Vashaee, D.; Shakouri, A. Improved Thermoelectric Power Factor in Metal-Based Superlattices. *Phys. Rev. Lett.* **2004**, *92*, 106103.

(96) Nolas, G. S.; Morelli, D. T.; Tritt, T. M. Skutterudites: A Phonon-Glass-Electron Crystal Approach to Advanced Thermoelectric Energy Conversion Applications. *Annu. Rev. Mater. Sci.* **1999**, *29*, 89–116.

(97) Toberer, E. S.; May, A. F.; Snyder, G. J. Zintl Chemistry for Designing High Efficiency Thermoelectric Materials. *Chem. Mater.* **2010**, *22*, 624–634.

(98) Nielsch, K.; Bachmann, J.; Kimling, J.; Böttner, H. Thermoelectric Nanostructures: From Physical Model Systems towards Nanograined Composites. *Adv. Energy Mater.* **2011**, *1*, 713–731.

(99) Vaqueiro, P.; Powell, A. V. Recent Developments in Nanostructured Materials for High-Performance Thermoelectrics. *J. Mater. Chem.* **2010**, *20*, 9577.

(100) Kanatzidis, M. G. Nanostructured Thermoelectrics: The New Paradigm? *Chem. Mater.* **2010**, *22*, 648–659.

(101) Gorsse, S.; Bellanger, P.; Brechet, Y.; Sellier, E.; Umarji, A.; Ail, U.; Decourt, R. Nanostructuration via Solid State Transformation as a Strategy for Improving the Thermoelectric Efficiency of PbTe Alloys. *Acta Mater.* **2011**, *59*, 7425–7437.

(102) Bahk, J.-H.; Bian, Z.; Shakouri, A. Electron Energy Filtering by a Nonplanar Potential to Enhance the Thermoelectric Power Factor in Bulk Materials. *Phys. Rev. B* **2013**, *87*, 075204.

(103) Vashaee, D.; Shakouri, A. Electronic and Thermoelectric Transport in Semiconductor and Metallic Superlattices. *J. Appl. Phys.* **2004**, *95*, 1233–1245.

(104) Mott, N. F.; Davis, E. A. *Electronic Processes in Non-Crystalline Materials*; Oxford University Press, 2012.

(105) LaMer, V. K.; Dinegar, R. H. Theory, Production and Mechanism of Formation of Monodispersed Hydrosols. *J. Am. Chem. Soc.* **1950**, *72*, 4847–4854.

(106) Burda, C.; Chen, X.; Narayanan, R.; El-Sayed, M. A. Chemistry and Properties of Nanocrystals of Different Shapes. *Chem. Rev.* **2005**, *105*, 1025–1102.

(107) Auer, S.; Frenkel, D. Prediction of Absolute Crystal-Nucleation Rate in Hard-Sphere Colloids. *Nature* **2001**, *409*, 1020–1023.

(108) Abe, S.; Čapek, R. K.; De Geyter, B.; Hens, Z. Tuning the Postfocused Size of Colloidal Nanocrystals by the Reaction Rate: From Theory to Application. *ACS Nano* **2012**, *6*, 42–53.

(109) De Mello Donegá, C.; Liljeroth, P.; Vanmaekelbergh, D. Physicochemical Evaluation of the Hot-Injection Method, a Synthesis Route for Monodisperse Nanocrystals. *Small* **2005**, *1*, 1152–1162.

(110) Kumar, S.; Nann, T. Shape Control of II-VI Semiconductor Nanomaterials. *Small Weinh. Bergstr. Ger.* **2006**, *2*, 316–329.

(111) Pellegrino, T.; Kudera, S.; Liedl, T.; Muñoz Javier, A.; Manna, L.; Parak, W. J. On the Development of Colloidal Nanoparticles towards Multifunctional Structures and Their Possible Use for Biological Applications. *Small Weinh. Bergstr. Ger.* **2005**, *1*, 48–63.

(112) Ibáñez, M.; Guardia, P.; Shavel, A.; Cadavid, D.; Arbiol, J.; Morante, J. R.; Cabot, A. Growth Kinetics of Asymmetric Bi2S3 Nanocrystals: Size Distribution Focusing in Nanorods. *J Phys Chem C* **2011**, *115*, 7947–7955.

(113) Li, W.; Shavel, A.; Guzman, R.; Rubio-Garcia, J.; Flox, C.; Fan, J.; Cadavid, D.; Ibáñez, M.; Arbiol, J.; Morante, J. R.; et al.

Morphology Evolution of $Cu_{2-x}S$ Nanoparticles: From Spheres to Dodecahedrons. *Chem. Commun.* **2011**, *47*, 10332–10334.

(114) Ibáñez, M.; Fan, J.; Li, W.; Cadavid, D.; Nafria, R.; Carrete, A.; Cabot, A. Means and Limits of Control of the Shell Parameters in Hollow Nanoparticles Obtained by the Kirkendall Effect. *Chem. Mater.* **2011**, *23*, 3095–3104.

(115) Ibáñez, M.; Zamani, R.; Li, W.; Cadavid, D.; Gorsse, S.; Katcho, N. A.; Shavel, A.; López, A. M.; Morante, J. R.; Arbiol, J.; et al. Crystallographic Control at the Nanoscale to Enhance Functionality: Polytypic $Cu_2GeSe_3$ Nanoparticles as Thermoelectric Materials. *Chem. Mater.* **2012**.

(116) Korgel, B. A.; Fitzmaurice, D. Self-Assembly of Silver Nanocrystals into Two-Dimensional Nanowire Arrays. *Adv. Mater.* **1998**, *10*, 661–665.

(117) Tang, Z.; Kotov, N. A.; Giersig, M. Spontaneous Organization of Single CdTe Nanoparticles into Luminescent Nanowires. *Science* **2002**, *297*, 237–240.

(118) Shevchenko, E. V.; Talapin, D. V.; Kotov, N. A.; O'Brien, S.; Murray, C. B. Structural Diversity in Binary Nanoparticle Superlattices. *Nature* **2006**, *439*, 55–59.

(119) Kang, Y.; Ye, X.; Chen, J.; Qi, L.; Diaz, R. E.; Doan-Nguyen, V.; Xing, G.; Kagan, C. R.; Li, J.; Gorte, R. J.; et al. Engineering Catalytic Contacts and Thermal Stability: Gold/Iron Oxide Binary Nanocrystal Superlattices for CO Oxidation. *J. Am. Chem. Soc.* **2013**.

(120) Komarneni, S. Feature Article. Nanocomposites. *J. Mater. Chem.* **1992**, *2*, 1219–1230.

(121) Nag, A.; Kovalenko, M. V.; Lee, J.-S.; Liu, W.; Spokoyny, B.; Talapin, D. V. Metal-Free Inorganic Ligands for Colloidal Nanocrystals: $S^{2-}$, $HS^-$, $Se^{2-}$, $HSe^-$, $Te^{2-}$, $HTe^-$, $TeS_3^{2-}$, $OH^-$, and

$NH_2^-$ as Surface Ligands. *J. Am. Chem. Soc.* **2011**, *133*, 10612–10620.

(122) Norris, D. J.; Efros, A. L.; Erwin, S. C. Doped Nanocrystals. *Science* **2008**, *319*, 1776–1779.

(123) Yu, D.; Wang, C.; Guyot-Sionnest, P. N-Type Conducting CdSe Nanocrystal Solids. *Science* **2003**, *300*, 1277–1280.

(124) Sumirat, I.; Ando, Y.; Shimamura, S. Theoretical Consideration of the Effect of Porosity on Thermal Conductivity of Porous Materials. *J. Porous Mater.* **2006**, *13*, 439–443.

(125) Crocker, A. J.; Rogers, L. M. Interpretation of the Hall Coefficient, Electrical Resistivity and Seebeck Coefficient of P-Type Lead Telluride. *Br. J. Appl. Phys.* **1967**, *18*, 563–573.

(126) Euler, F. Simple Geometric Model for the Effect of Porosity on Material Constants. *J. Appl. Phys.* **2004**, *28*, 1342–1345.

# Chapter 2 Methods and techniques

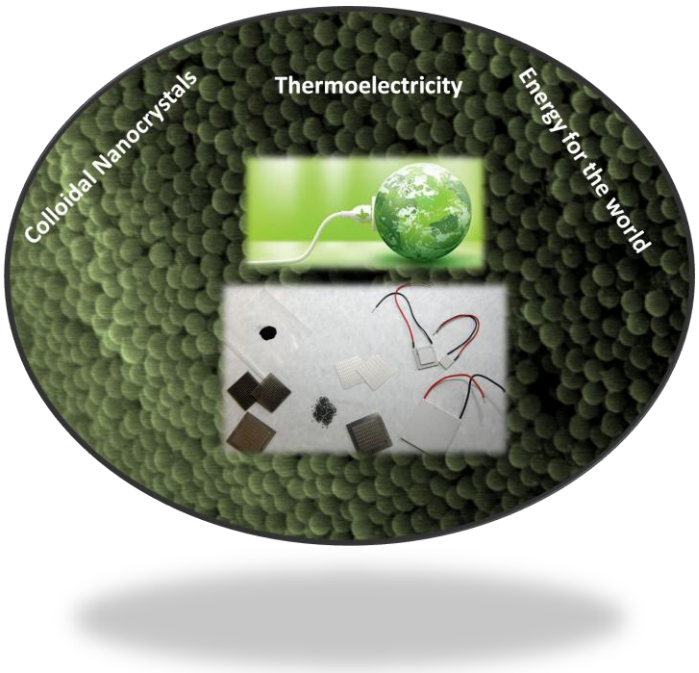


To produce nanocomposites using the bottom-up approach, colloidal NCs were prepared and further assembled into dense solids or bulk nanostructured materials. The resulting samples are then characterized structurally, chemically and morphologically and their transport properties were measured to evaluate their TE efficiency.

This chapter describes the production of the nanocomposites as well as the methods and systems used to study their transport properties.

## 2.1 Production of the bulk nanostructured material

The simplest process to obtain bulk nanostructured material from colloidal NCs, consist in drying by vacuum the solvent where the NCs are dispersed to obtain a powder. Then, this powder is subjected to heat treatment at temperatures between 300 ºC and 500 ºC. The heat treatment is carried out in an atmosphere free of oxygen, under argon or nitrogen flow. To characterize and to use the material in a TE device, it is necessary to consolidate the power into a dense solid. In general, the most common consolidation methods are: cold pressing, hot pressing and spark plasma sintering. In this thesis I used these three techniques.

### 2.1.1 Consolidation Techniques

#### 2.1.1.1 Cold pressing (CP)

**Figure 2.1** Hydraulic pressing machine employed for cold pressing consolidation.

The material in powder is placed into a die, usually made of stainless steel, under a hydrostatic pressure from 2 tons up to 5 tons (for a 10

mm die from to 0.2 GPa to 0.6 GPas) during certain time. Although this method is very simple, the relative densities that can be reached are low, usually from 60 % to 80 %. The CP is preceded or followed by a sintering of the nanomaterials using a heat treatment. In this thesis I used a simple hydraulic press as it is shown in the Figure 2.1. I used specifically a 10 mm die, between 2 and 3 tons and this pressure were maintained from 5 to 20 minutes.

#### 2.1.1.2 Hot pressing (HP)

**Figure 2.2** Custom-made hot-pressing machine used in this thesis.

In the HP technique the nanopowder is placed into a graphite die and a hydrostatic pressure from tens to hundreds of MPas is applied, while the sample is maintained at a relatively high temperature. Heating may be done by an induction oven to have high heating ramps. In such way, it is possible to achieve high temperatures in short times. The relative densities that can be reached by this method are higher than 90 %. In this thesis, I used a custom-made machine that consists in a hydraulic press coupled to an induction oven (Figure 2.2). The specific conditions I used were: 10 mm die, 40MPa and 350 ºC for 1 to 5 minutes.

#### 2.1.1.3 Spark plasma sintering (SPS)


**Figure 2.3** Commercial SPS machine.

The SPS technique (also known as field assisted sintering technique, FAST) consists in a pulsed DC current that pass through the graphite die while a hydrostatic pressure is applied. With this technique is also possible to achieve high temperatures in short times (minutes). The ON-OFF electrical field causes high-speed migration of ions and also discharges between particles of powder, among other phenomena, that together with the joule heating and the pressure, promote a effectively sintering.
In this thesis, I used custom-made spark plasma sintering (SPS) system. This equipment is composed by a graphite die, two plungers that are in direct contact with the specimen, a set of spacers, also made of graphite, and the electrodes. By applying a voltage difference between the electrodes, a current flows through the entire assembly providing it with the electrical power required for heating. The specific conditions I used were: heating rate of 200 ºC/min and about 90 MPa of pressure. The sample was held under these conditions for about 5 minutes.

## 2.2 Thermoelectric characterization

Once the nanostructured material is consolidated into dense solids or pellets, they are ready to be characterized. The three important properties that have to be measured for the TE characterization are Seebeck coefficient, electrical resistivity/conductivity and thermal conductivity. Having measured these properties it is possible to calculate the figure of merit of the material as it was described in the previous chapter. Among the many different experimental techniques to measure these properties[1–4], in this section I will explain the ones that I used during this thesis.

### 2.2.1 Seebeck coefficient

**Figure 2.4** Equipment to measure Seebeck coefficient and electrical conductivity.

As was discussed before, the Seebeck coefficient $S$ is one of the important parameters in the TE characterization. It also gives information about the type of charge carriers and the transport mechanism in the material[5].

The Seebeck coefficient was measured by using a Linseis - LSR 3 system (Figure 2.4). In this instrument the sample temperature is varied along the measurement range, and a temperature gradient across the sample ($\Delta T=T_B-T_A$) is generated at each temperature. This allows measuring the Seebeck voltage generated as a function of the

sample temperature. Figure 2.5 shows the circuit formed by the sample (*A*) and the material of the contacts (*B*). Using this setup, the relative Seebeck coefficient between these two materials $S_{AB}$ is measured. As the absolute Seebeck coefficient of the contact material $S_B$ is known, from the relationship between the voltage $\Delta V$ and the temperature gradient $\Delta T$, the absolute Seebeck coefficient of the sample $S_A$ can be obtained as:

$$S_{AB} = \frac{\Delta V}{\Delta T} \tag{2.1}$$

$$S_{AB} = S_A - S_B \;\Rightarrow\; S_A = S_{AB} + S_B \tag{2.2}$$

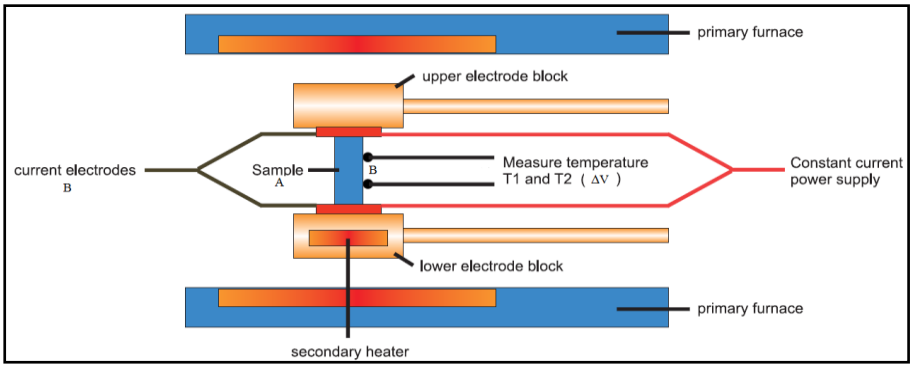


**Figure 2.5** Schematic diagram of the equipment used to measure Seebeck coefficient and electrical conductivity. The primary furnace controls the sample temperature and the secondary heater produce the temperature gradient across the sample. The material of both the current and the voltage electrodes is Alumel.

## 2.2.2 Electrical resistivity

Electrical resistivity and Seebeck coefficient were measured simultaneously using the Linseis - LSR 3 system under helium atmosphere.

The electrical resistivity was measured by means of a standard four probe technique in the temperature range from 300 K to 750 K. Here a constant current $I$ is applied to the sample and the voltage generated across the sample is measured by two electrodes, as can

be seen in Figure 2.6. By using the electrical resistance and the shape and size of the sample is possible to obtain its electrical resistivity[2].

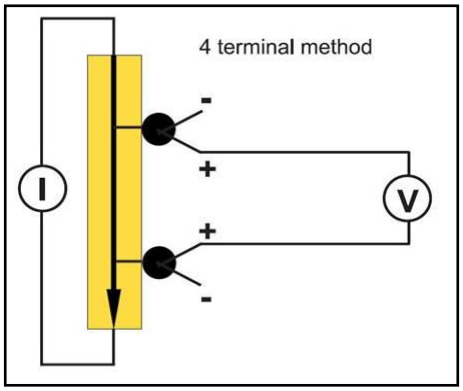


**Figure 2.6** Four points electrical resistivity measurement scheme.

### 2.2.3 Thermal conductivity

**Figure 2.7** Laser Flash system to measure thermal diffusivity.

The techniques to measure thermal conductivity can be divided in two categories, the steady state methods and the transient methods[6]. In the first category the sample is subjected to a static heat flow, and the thermal conductivity can be obtained by the Fourier Law.[7] On

the other hand, in the transient methods the temperature distribution through the sample varies in time and the differential equation of the heat flux need to be solved to obtain the thermal conductivity.[3,7] In this thesis I used the laser flash method that is a transient method.

In the Laser flash system, a face of the sample is radiated with a pulse (≤ 1 ms) of laser light and an infrared detector registers the temperature rise on the opposite face. The thermal diffusivity is a measure of the speed at which a body can change its temperature. In practice the thermal diffusivity of the sample is obtained by plotting the increase in temperature recorded by the detector as a function of time.[8] Then the thermal conductivity is calculated as $\kappa = DC_pd$, where $D$ is the thermal diffusivity, $C_p$ is the heat capacity, and d is the density. $C_p$ can be measured or calculated by using the mass density and the Dulong-Petit approximation. In this thesis I used two types of laser flash machines: Linseis LFA 1000 (Figure 2.7) and the Netzsch LFA-457 Microflash.

## 2.3 Structural and chemical characterization

During this thesis different structural, morphological and chemical techniques were used to characterize the NCs and the bulk nanostructured materials prepared. Here I provide a brief description of them:

The crystallographic phase of the samples was determined by using X-ray power diffraction (XRD). XRD were carried out on a Bruker AXS D8 ADVANCE X-ray diffractometer with Cu Kα1 radiation (λ = 1.5406 Å). To perform XRD experiments on a heated sample, an Anton Paar XRK900 temperature chamber and a TCU750 controller integrated with the Bruker control software were used.

Size and shape of the NCs were examined by transmission electron microscopy (TEM) using a JEOL 2100 operating at 200 keV and ZEISS LIBRA 120, operating at 120 keV accelerating voltage.

Morphology of the bulk nanostructured material were study by means of scanning electron microscopy (SEM) using a ZEISS Auriga SEM.

To study the chemical composition of the NCs, I used inductively coupled plasma/optical emission spectroscopy (ICP/OES) and energy dispersive X-ray spectroscopy (EDX). The EDX detector was coupled to the SEM and the ICP/OES were carried out in a Perkin Elmer Optima 3200 RL system.

The surface chemical composition of the NCs were determined by means of Fourier-transform infrared (FTIR), nuclear magnetic resonance (NMR) and X-ray photoelectron spectroscopy (XPS). FTIR spectra were acquired using an Alpha Bruker FTIR spectrometer with a platinum attenuated total reflectance (ATR) single reflection module. FTIR data were typically averaged over 64 scans. The NMR spectra ($^{1}$H-NMR, $^{13}$C-NMR, $^{31}$P-NMR) were acquired using a Varian Mercury Plus 400 MHz at 25 ºC using deuterated chloroform ($CDCl_3$) and dimethyl sulfoxide (DMSO) as a solvents. XPS spectra were used to analysis the surface of the NCs obtained by using a SPECS SAGE ESCA System employing Mg Kα as the X-ray source.

Thermal gravimetric analyses (TGA) were done to study the behaviour of the NCs under the heat treatments. The TGA was carried out by using Perkin-Elmer TGA 4000 equipment in the temperature range from 30 $^{o}$C to 500 $^{o}$C under nitrogen flow.

## 2.4 References

(1) Rowe, D. M. *CRC Handbook of Thermoelectrics*; CRC Press, 1995.

(2) Runyan, W. R. *Semiconductor Measurements and Instrumentation*; McGraw Hill Professional, 1998.

(3) Gaskell. *An Introduction to Transport Phenomena in Materials Engineering*; Momentum Press, 2012.

(4) Rowe, D. M. *Materials, Preparation, and Characterization in Thermoelectrics*; CRC Press, 2012.

(5) Martin, J. Protocols for the High Temperature Measurement of the Seebeck Coefficient in Thermoelectric Materials. *Meas. Sci. Technol.* **2013**, *24*, 085601.

(6) Parrott, J. E.; Stuckes, A. D. *Thermal Conductivity of Solids*; Pion, 1975.

(7) Tritt, T. M. *Thermal Conductivity: Theory, Properties, and Applications*; Springer, 2004.

(8) Corbin, S. F.; Turriff, D. M. Thermal Diffusivity by The Laser Flash Technique. In *Characterization of Materials*; John Wiley & Sons, Inc., 2002.

# Chapter 3 Bottom-up processing of thermoelectric nanocomposites $Ag_2Te$-PbTe

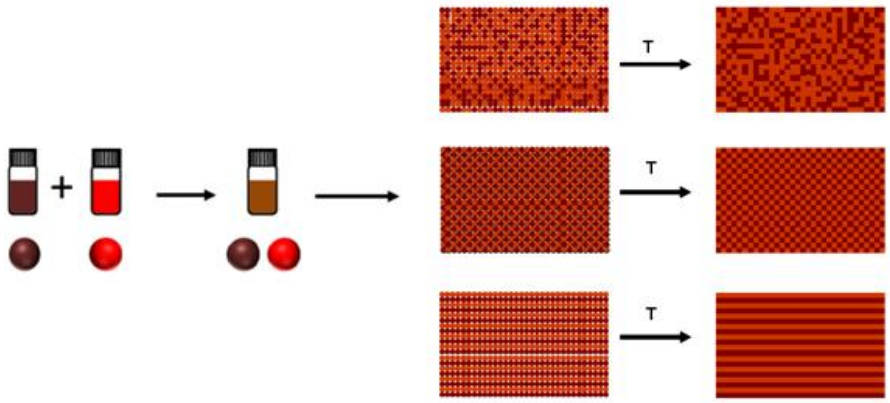


## 3.1 Introduction

Today's main strategy to engineer highly efficient TE materials is to reduce thermal conductivity by introducing phonon scattering centers at different length scales.[1,2] Alloys of heavy elements and complex solid solutions including 1D phonon scattering centers or 2D layered structures trigger phonon scattering at the atomic length scale.[3–6] On the other hand, nanomaterials, having large interface

densities introduced by the reduction to the nanoscale of their crystal domains, can efficiently scatter phonons at the 1-100 nm scale. [7–11] A particularly interesting class of nanostructured materials is that of nanocomposites containing crystal domains with different phases and/or compositions. In nanocomposites, interfaces between dissimilar materials may boost phonon scattering due to mismatches in the acoustic impedances. [12] Heterointerfaces may even allow reducing the electronic contribution to the thermal conductivity. [13–15] Moreover, nanocomposites offer a mechanism to improve electrical conductivity through removing ionized impurities from avenues of charge carrier transport. [16,17] An additional potential advantage of nanocomposites is the possibility to decouple the Seebeck coefficient from electrical conductivity. [18–20] In this regard, the increase of the electronic density of states near the Fermi level in quantum confined nanostructures has been predicted to enhance the Seebeck coefficient. [9,21] Additionally, energy filtering at NCs interfaces may further enhance the thermopower of nanostructured material by selectively scattering low energy charge carriers. [22–25]

The ball-milling of crystalline ingots into fine powders and the posterior bulk reconstruction by hot-pressing is the most usual and general technique to obtain bulk nanocrystalline materials. [26] However, such top-down industrial approach is time and energy consuming and no control on the size and shape of the nanoparticles is possible. The formation of nanoscale precipitates or organized superstructures by phase segregation in metastable solid solutions is a more elegant method to produce nanocomposites. [27–30] Nevertheless, this procedure is limited to specific compositions and lacks of a high degree of control over the size and shape of the nanoinclusions.

Solution-synthesis routes are particularly well suited for the bottom-up production of nanocomposites [31–33] with a high degree of control over the size, shape and composition of the crystal nanodomains. [34–37] Nanocomposites can be easily obtained by simply mixing solutions of different nanoparticles. Blending NCs while dispersed in solution allows an intimate intermixing of the different

components. After removal of organics, NCs can be consolidated into macroscopic nanocomposites by techniques such as spark-plasma-sintering and cold or hot pressing. Even though the complete removal of surfactants is still a difficulty, important progress has been achieved also in this area.[33,38] On the other hand, self-purification allows the use of relatively low purity precursors, which is economically advantageous. However, it hampers the potential for NCs doping.[39–41] This drawback can be overcome using ternary or quaternary compounds, which offer multiple possibilities for valence balance control.[42,43] Another possibility to control carrier concentration in nanocomposites obtained by bottom-up approaches is to cleverly select the combination of materials and their correct proportions.[44,45]

An especially appealing thermoelectric nanomaterial is the one obtained from the combination of lead and silver tellurides.[46–49] The control of the carrier concentration and the formation of nanocrystalline inclusions in these nanocomposites have allowed reaching *ZT* values up to 1.6.[47]

In this chapter I explore the potential of solution-processing techniques to obtain binary bulk nanocomposites with superior TE properties in the system Ag-Pb-Te. Binary $Ag_2Te$-PbTe bulk nanocomposites were produced by blending in solution PbTe and $Ag_2Te$ NCs in different proportions. The TE properties of the formed nanocomposites were analyzed in the temperature range from 300 K to 700 K.[50]

## 3.2 Experimental details

### 3.2.1 Materials

Triocthiyphosphine (TOP, 97 %) and silver chloride (99.9 %) were purchased from Strem. Tellurium pieces (99.999 %), lead acetate trihydrate (99.999 %), 1-octadecene (ODE, 90 %), oleylamine (OLA

tech. 70 %) and oleic acid (OA, tech. 90 %) were purchased from Aldrich. Analytical grade ethanol, hexane and toluene were purchase from Panreac. All chemicals were used without further purifications. Stock solution of TOP-Te (1 M) and TOP-Ag (1 M) were prepared dissolving 12.76 g of tellurium pieces and 14.33 g of silver chloride in 100 ml of TOP, respectively. The solutions described above were prepared and stored inside an Ar-filled glovebox.

All nanocrystal preparations were carried out using standard airless techniques: a vacuum/dry Ar Schlenk line was used for the synthesis and an Ar-filled glovebox for storing and handling air- and moisture-sensitive chemicals.

### 3.2.2 Preparation of PbTe nanocrystals

For the preparation of PbTe nanocrystals, was used a modified approach of that used by Urban et al.[51] In a typical procedure, lead acetate tryhidrate (0.5670 g, 1.5 mM) and oleic acid (1.5 ml, 4.75 mM) were dissolved in 10 ml ODE. This mixture was degassed at 70 ºC and 150 °C for 0.5 h to form lead oleate complex and remove water and acetic acid. The solution was flushed with Ar and the temperature was raised up to 180 ºC. Afterwards, 2 ml of 1 M TOP:Te were rapidly injected. The reaction mixture was maintained in the range 160 ºC – 180 ºC for 3 minutes and then quickly cooled down to room temperature using a water bath. After cooling, the nanoparticles were precipitated by adding hexane/ethanol (3:1) followed by centrifugation. This procedure was repeated twice. The precipitated nanoparticles were transferred to an Ar-filled glovebox, where they were stored until future use.

### 3.2.3 Preparation of $Ag_2Te$ nanocrystals

$Ag_2Te$ nanocrystals were produced using a modified version of the method developed by Ko et al.[45] In a typical procedure, 10 ml of OLA were added to a three neck flask and heated up to 100 ºC under vacuum for 1 hour to remove low boiling point impurities and water.

Afterwards, the reaction flask was flushed with Ar and temperature was raised up to 160 ºC. A mixture of 5 ml of Ag/TOP stock solution and 2.5 ml of Te/TOP was quickly injected. After injection, the reaction temperature was maintained between 130 ºC and 160 ºC for 3 minutes. Then the reaction solution was cooled using a cold water bath. $Ag_2Te$ nanocrystals were precipitated and redispersed using ethanol and toluene twice. Finally the nanocrystals were dispersed in toluene and stored in the glovebox.

### 3.2.4 Nanocomposite preparation

PbTe and $Ag_2Te$ nanoparticles dispersed in toluene were blended at various molar fractions, 25/75, 50/50 and 75/25. After several additional precipitation and redispersion cycles, the resultant blends were dried under Ar atmosphere. The blends were annealed at 500 ºC during 2 hours in Ar flow. Finally, the resulting materials were pressed under a load of 5 tons at room temperature into pellets of 13 mm diameter and 1mm thickness.

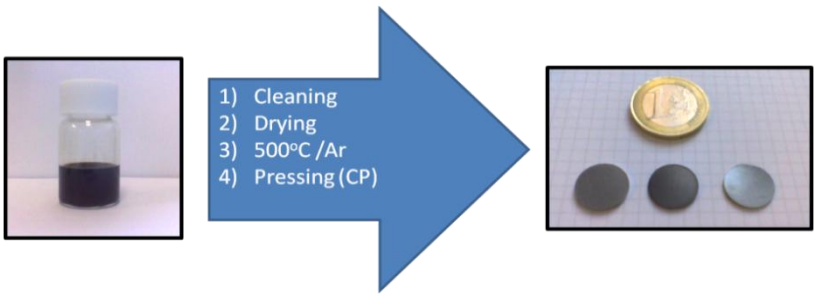


**Figure 3.1** Nanocomposites production.

## 3.3 Results and discussion

Figure 3.2 shows representative TEM micrographs of the PbTe and $Ag_2Te$ nanoparticles used as building blocks to produce the

$(Ag_2Te)_x(PbTe)_{1-x}$ (x = 0.25, 0.50, 0.75) nanocomposites. Insets display the histograms of their size distribution. PbTe nanoparticles had cubic morphologies and a face centered cubic crystal phase (JCPDS 38-1435). Their average size, taken as the diagonal of one of their faces was 19 nm and their size distribution had 5 % dispersion. $Ag_2Te$ nanoparticles had disk-like morphology and a monoclinic crystal phase at ambient temperature (JCPDS 34-0142). Their average diameter was 10 nm and their size dispersion was close to 10 %. PbTe and $Ag_2Te$ nanoparticles were not intentionally doped by extrinsic impurities.

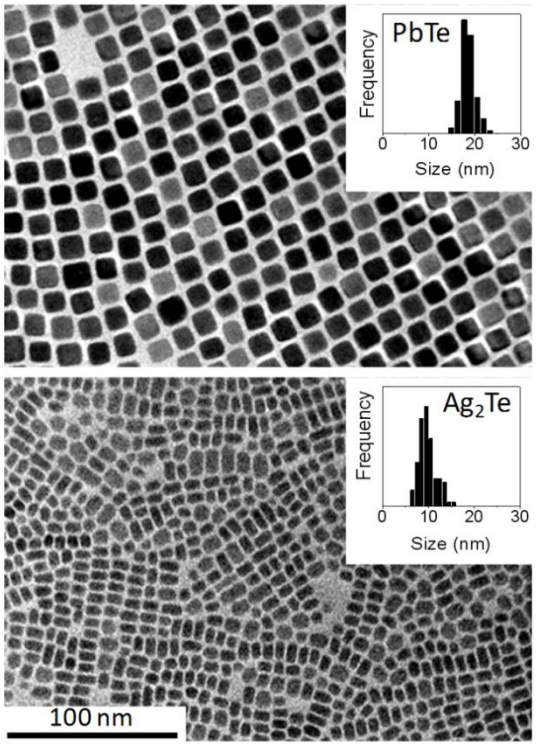


**Figure 3.2** Representative TEM micrographs of the PbTe (top) and Ag2Te (bottom) nanoparticles used to produce the nanocomposites. Insets display the histograms of the particle size distributions.

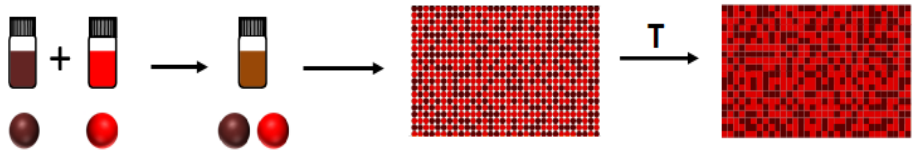


**Figure 3.3** Scheme of the procedure used to produce binary nanocomposites from solution-processed nanocrystals.

Figure 3.3 shows a scheme of the procedure used to produce the binary nanocomposites from solutions containing the PbTe and $Ag_2Te$ colloidal building blocks. While short range ordering of the nanocrystals at submicron scales may exist, at the macroscopic level the different phases must be considered as randomly distributed. The nanoparticle mixture was prepared while having the particles well dispersed in toluene to ensure a homogeneous blending of the two phases at the nanometer scale. Three different compositions were prepared, having the following mass fractions: $(Ag_2Te)_{0.75}(PbTe)_{0.25}$, $(Ag_2Te)_{0.50}(PbTe)_{0.50}$ and $(Ag_2Te)_{0.25}(PbTe)_{0.75}$. Once mixed, the nanoparticle blends were thoroughly purified by multiple precipitation and redispersion steps. Final nanoparticles were not soluble anymore, probing the high degree of surfactant removal from their surfaces. The purified nanoparticle blends were annealed at 500 ºC during 2 h in an argon flow atmosphere. The concentration of residual carbon in the final materials was less than 2 %, as determined by elemental analysis. The annealed nanocomposite powders were cold-pressed into 13 mm pellets by applying 380 MPa pressure with a hydraulic press. At the same time, pure $Ag_2Te$ and PbTe pellets were prepared following the same protocol and the exact same nanocrystals used to obtain the blends. The density of the different pellets obtained were all around 80 % of the theoretical value. Figure 3.4 shows a SEM image of the $(Ag_2Te)_{0.75}(PbTe)_{0.25}$ nanopowders obtained after annealing. Elemental mappings obtained by SEM-EDX characterization of the nanocomposite's chemical

composition showed the spatial distribution of the two phases to be highly homogeneous

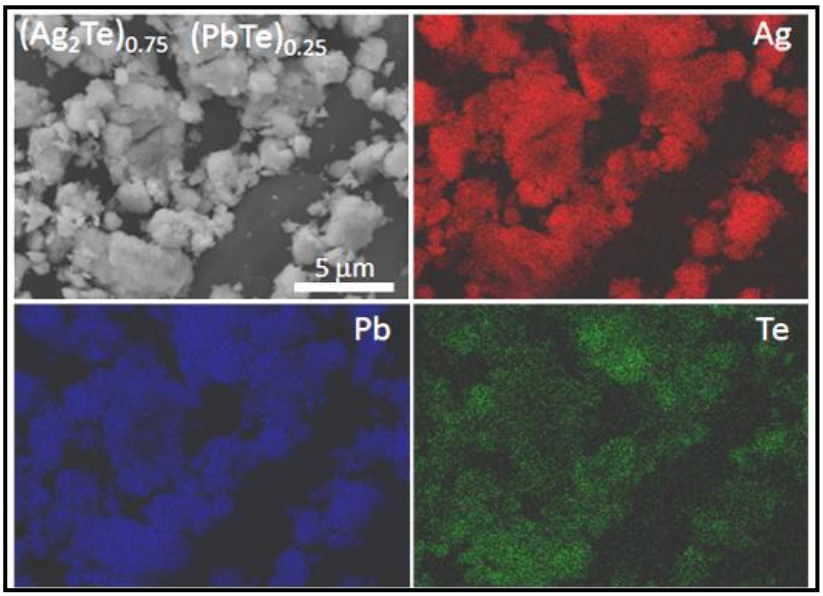


**Figure 3.4** SEM image and EDX elemental maps of the annealed (Ag2Te) 0.75 (PbTe) 0.25 nanocomposites.

Figure 3.5 shows the XRD patterns of the annealed nanomaterials. The XRD patterns of the nanocomposites resembled the combination of the XRD patterns obtained from the pure materials. No evidences of alloying between the two phases could be obtained from this analysis. At the same time, no secondary phases were detected. The fitting of the XRD patterns allowed detecting a growth of the crystallographic domains with the thermal treatment. From the Scherer equation, the crystal domain size of both phases in the annealed material was estimated to be approximately 40 nm.

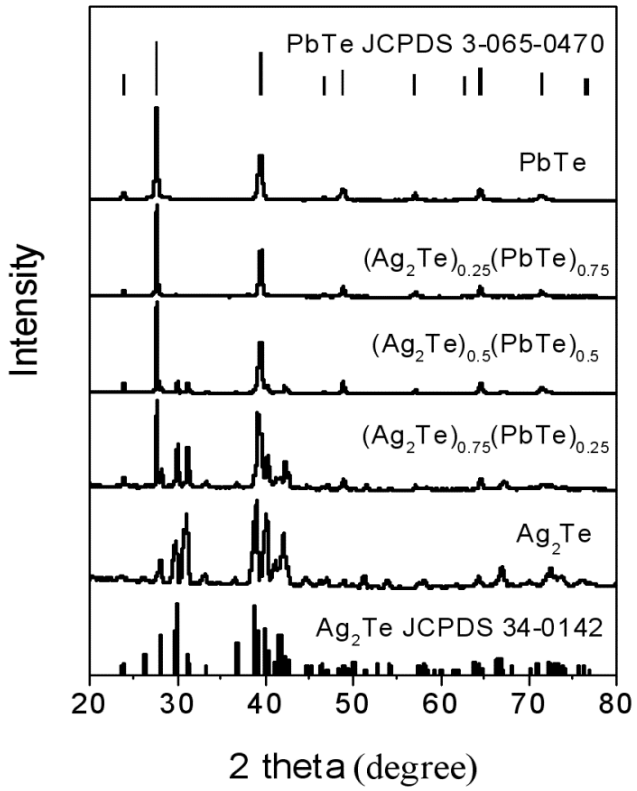


**Figure 3.5** XRD patterns of the annealed nanocomposites. The Ag2Te (JCPDS 34-0142) and PbTe (JCPDS 38-1435) patterns have been included as a reference.

The electrical conductivity and Seebeck coefficient of the nanocomposites were characterized in the temperature range from 300 K to 700 K. Figure 3.6a-b display the temperature dependence of the electrical conductivity and Seebeck coefficient for the three $(Ag_2Te)_x(PbTe)_{1-x}$ (x=0.25, 0.50, 0.75) nanocomposites and the pure PbTe and $Ag_2Te$ nanomaterials.

One first clearly noticeable feature in Figure 3.6a is the non-monotonic evolution of the pure $Ag_2Te$ electrical conductivity with temperature. For this material, a decrease of electrical conductivity of over an order of magnitude was systematically obtained in the

temperature range between 400 K and 450 K. This is associated to the well-known phase transition from the low temperature monoclinic α-$Ag_2Te$ to the high-temperature cubic β-$Ag_2Te$. The low temperature α-$Ag_2Te$ phase is a very narrow band-gap semiconductor (Eg = 0.025 eV), which in bulk displays high electron mobility and a low lattice thermal conductivity.[52–60] A slight decrease of electrical conductivity with temperature and a negative Seebeck coefficient in the range 300-400 K were obtained for this material. These results are consistent with previous reports showing the low temperature α-$Ag_2Te$ to be a degenerate semiconductor displaying n-type conductivity.[61] Our experimental results showed the phase transformation for this material to be accompanied by a transition from n-type to p-type conductivity. The high temperature β-$Ag_2Te$ bulk nanomaterial displayed a positive Seebeck coefficient and its electrical conductivity increased with temperature in all the range measured. In intrinsic β-$Ag_2Te$, the much lower effective masses for electrons than holes usually translate into an n-type conductivity[53]. However, the conductivity type of this material is known to be highly dependent on composition. In this regards, stoichiometric and Ag-rich samples show n-type conductivity, while Te-rich $Ag_2Te$ displays p-type conductivity.[62,63] Aside from composition variations, the p-type conductivity obtained here could be explained by a possible surface oxidation of the small colloidal nanocrystals during their processing into pellets. From the lineal dependence of $ln\ \sigma T^{3/2}$ with the inverse of temperature in the high temperature range, activation energy for electrical conductivity of 0.18 eV was calculated. This activation energy could be associated with the thermal generation of electron-hole pairs through a 0.36 eV band gap. The flattening of the Seebeck coefficient evolution with the temperature supports the hypothesis of an intrinsic semiconductor character at this high temperature region. However, the obtained band gap is considerably higher than the 0.20-0.28 eV measured previously for this material.[64] From the maximum of the Seebeck coefficient obtained for this material and using the equation $E_g=2eS_{max}T_{max}$,[65] a 0.2 eV band gap was calculated. This value is consistent with previously published band gap estimates. Thus, the calculated activation energy for electrical conductivity should be at

least in part associated with mobility energy barriers at the grain boundaries, which are probably associated to the presence of an oxide layer at the nanoparticles surface.[45,66]

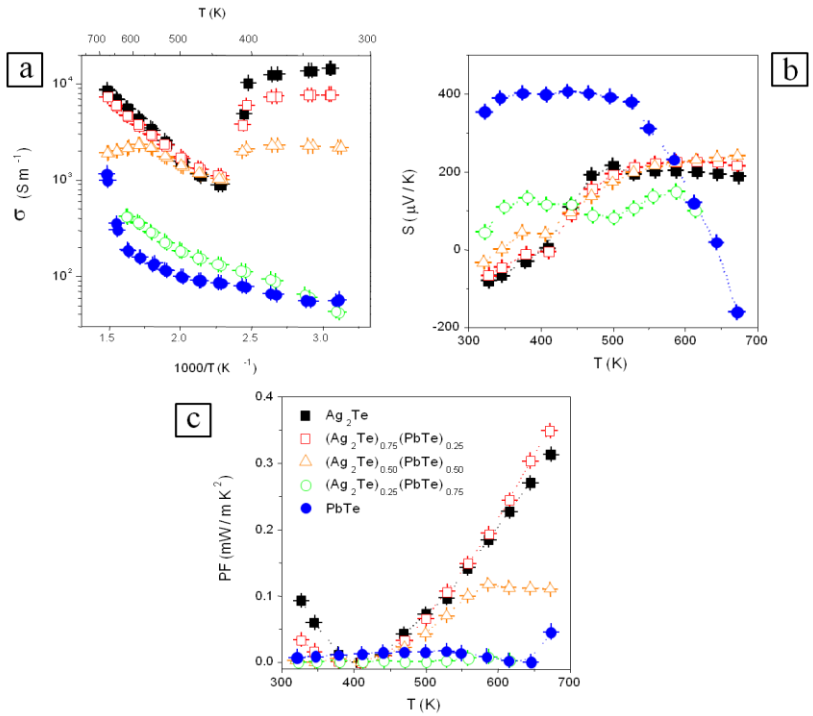


**Figure 3.6** (a) Temperature dependence of the electrical conductivity, (b) Seebeck coefficient and (c) power factor obtained from the produced nanomaterials: $Ag_2Te$ (■); $(Ag_2Te)_{0.75}(PbTe)_{0.25}$ (□); $(Ag2Te)_{0.5}(PbTe)_{0.5}$ (△); $(Ag2Te)_{0.25}(PbTe)_{0.75}$ (○); PbTe (●)

Pure PbTe pellets displayed p-type electrical conductivity in most of the temperature range measured. The p-type character of the PbTe nanocrystalline pellet had its origin on a thin oxide layer at the nanoparticles surface,[67–70] the presence of electrically active lattice defects associated with deviations from stoichiometry or on the broken bonds at the grain boundaries.[71–78] Slight increase of electrical conductivity with temperature in the low temperature range and the constant Seebeck coefficient obtained pointed towards the full ionization of acceptor levels at temperatures above 350 K.

From the maximum of the Seebeck coefficient, a 0.30 eV band gap was calculated. This value correlated well with the optical band gap previously measured for this material[79]. A sign inversion in the carrier type, from p to n, was clearly observed at approximately 650 K. This conduction type inversion was accompanied by a strong increase of electrical conductivity above 600 K. This was probably associated with the thermal activation of electron-hole pairs through the semiconductor band gap. The higher mobilities for electrons than holes in this material would compensate the higher holes concentration and trigger the conduction type inversion.

In the low temperature range, the blending of $Ag_2Te$ with PbTe nanocrystals resulted in nanocomposites with electrical conductivities lower than that of $Ag_2Te$. This electrical conductivity decrease was associated with a reduction of the charge carrier mobility with the blending, or with a reduction of the charge carrier density with the reduction of the relative $Ag_2Te$ content. A partial compensation of the majority carriers of each material may also contribute to the lower electrical conductivities observed. Below the $Ag_2Te$ phase transition temperature, a shift of the Seebeck coefficient towards positive values was also obtained when increasing the PbTe ratio in the blend.

In the full temperature range, the temperature dependences of the electrical conductivities and Seebeck coefficients obtained with the $(Ag_2Te)_{0.75}(PbTe)_{0.25}$ and $(Ag_2Te)_{0.5}(PbTe)_{0.5}$ nanocomposites clearly resembled that of pure $Ag_2Te$. In these two nanocomposites, a step change in the conductivity and the Seebeck coefficient was also observed at around 420 K. This was associated with the monoclinic to cubic phase transition taking place within the $Ag_2Te$ crystallographic domains. Like in the case of pure $Ag_2Te$, in the low temperature range, nanocomposites showed n-type conductivity with a minor temperature dependence of the conductivity. On the other hand, above 450 K, nanocomposites displayed p-type character and a clear increase of electrical conductivity with temperature. In both nanocomposites, a similar activation energy for conductivity as that obtained for pure $Ag_2Te$ material could be observed. However, in

the 50 % blend, a clear influence of PbTe was also obtained above 600 K, where a decrease of electrical conductivity was obtained. This was most probably related with the recombination of the n-type carriers created within the PbTe nanocrystals with the majority holes within the $Ag_2Te$. This decrease of electrical conductivity resulted in a limitation of this material's power factor above 600 K, as shown in Fig. 5.

The temperature dependence of the electrical conductivity measured from the $(Ag_2Te)_{0.25}(PbTe)_{0.75}$ nanocomposite resembled that of the pure PbTe nanomaterial. It showed a monotone increase with the temperature. Different lineal regions were observed when plotting the logarithm of conductance against reciprocal temperature, revealing the existence of multiple energy activated barriers and thus the contribution of multiple acceptor and donor states to charge transport.

Nanocomposites were characterized by temperature dependences of the electrical conductivity and Seebeck coefficient that clearly resembled those of the pure materials. This fact pointed towards the coexistence of the two phases within the nanocomposite, which was consistent with the results obtained from the XRD characterization of the materials. The alloying of the two materials would be expected to result in a modification of the semiconductor band gap and thus into different dependences of the thermoelectric properties with temperature.[48]

The best power factors were finally obtained from the pure $Ag_2Te$ nanomaterial and the $(Ag_2Te)_{0.75}(PbTe)_{0.25}$ nanocomposites. For these two materials, the thermal conductivity was also measured (Figure 3.7). A clear decrease of the thermal conductivity with the low temperature monoclinic $\alpha$-$Ag_2Te$ to the high-temperature cubic $\beta$-$Ag_2Te$ phase transition was noticed at around 400 K. The already very low thermal conductivities obtained for the pure $Ag_2Te$ nanomaterial hinder a further decrease of thermal conductivity with the blending of the two different phases. Only in the high temperature range, the nanocomposite displayed lower thermal

conductivities than the pure material. The low thermal conductivities obtained for both samples in all the temperature range measured are related to the very high density of interfaces and the relatively low density of the pellets measured. Higher pellet densities would have associated both a higher thermal conductivity and a higher electrical conductivity. This effect was estimated to account for up to a 40 % variation of both thermal and electric conductivity of the theoretical value to be expected for an absolutely dense sample.[38]

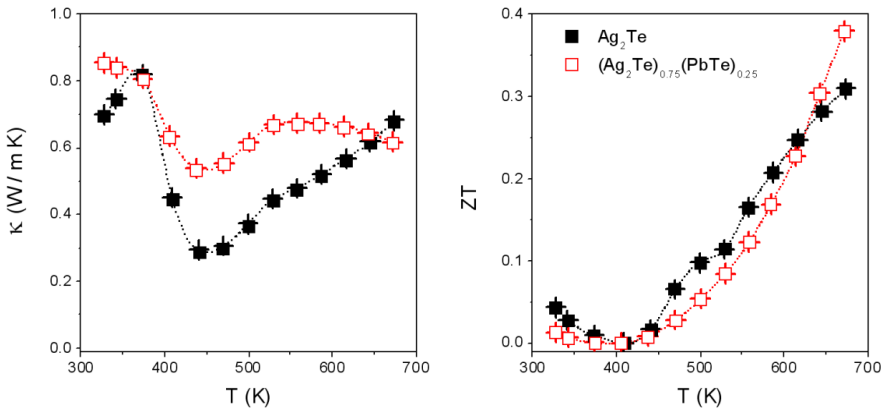


**Figure 3.7** Temperature dependence of the thermal conductivity (left) and thermoelectric figure of merit (right) obtained from the $(Ag2Te)_{0.75}(PbTe)_{0.25}$ nanocomposite (□) and the Ag2Te nanomaterial (■).

The thermoelectric figure of merit reached up to 0.38 for the $(Ag_2Te)_{0.75}(PbTe)_{0.25}$ nanocomposite at 670 K (Figure 3.7). This represents a 25 % increase over pure $Ag_2Te$ and it is an excellent ZT value taking into account that no extrinsic doping was intentionally introduced in these materials. The production of nanocomposites with much higher thermoelectric figures of merit (ZT>1.5) by bottom-up approaches based on solution processed nanocrystals will necessarily require the control of the carrier concentration of each compound through doping.

## 3.4 Conclusion

$(Ag_2Te)_x(PbTe)_{1-x}$ nanocomposites with controlled composition were obtained by means of a very facile bottom-up approach consisting in the solution blending of colloidal NCs. The temperature dependence of the electrical conductivity and Seebeck coefficient of the obtained materials could be described from the combination of the properties of the two constituent materials. Undoped $(Ag_2Te)_{0.75}(PbTe)_{0.25}$ nanocomposites displayed best power factors among the different nanocomposites tested and reached ZT values up to 0.38 at 670 K.

## 3.5 References

(1) Zebarjadi, M.; Esfarjani, K.; Dresselhaus, M. S.; Ren, Z. F.; Chen, G. Perspectives on Thermoelectrics: From Fundamentals to Device Applications. *Energy Environ. Sci.* **2012**, *5*, 5147.

(2) Vineis, C. J.; Shakouri, A.; Majumdar, A.; Kanatzidis, M. G. Nanostructured Thermoelectrics: Big Efficiency Gains from Small Features. *Adv. Mater.* **2010**, *22*, 3970–3980.

(3) Dresselhaus, M. S.; Chen, G.; Tang, M. Y.; Yang, R. G.; Lee, H.; Wang, D. Z.; Ren, Z. F.; Fleurial, J.-P.; Gogna, P. New Directions for Low-Dimensional Thermoelectric Materials. *Adv. Mater.* **2007**, *19*, 1043–1053.

(4) Gascoin, F.; Ottensmann, S.; Stark, D.; Haïle, S. M.; Snyder, G. J. Zintl Phases as Thermoelectric Materials: Tuned Transport Properties of the Compounds $Ca_xYb_{1-x}Zn_2Sb_2$. *Adv. Funct. Mater.* **2005**, *15*, 1860–1864.

(5) Feldman, J.; Singh, D.; Mazin, I.; Mandrus, D.; Sales, B. Lattice Dynamics and Reduced Thermal Conductivity of Filled Skutterudites. *Phys. Rev. B* **2000**, *61*, R9209–R9212.

(6) Snyder, G. J.; Toberer, E. S. Complex Thermoelectric Materials. *Nat. Mater.* **2008**, *7*, 105–114.

(7) Vaqueiro, P.; Powell, A. V. Recent Developments in Nanostructured Materials for High-Performance Thermoelectrics. *J. Mater. Chem.* **2010**, *20*, 9577.

(8) Bux, S. K.; Fleurial, J.-P.; Kaner, R. B. Nanostructured Materials for Thermoelectric Applications. *Chem. Commun.* **2010**, *46*, 8311.

(9) Szczech, J. R.; Higgins, J. M.; Jin, S. Enhancement of the Thermoelectric Properties in Nanoscale and Nanostructured Materials. *J. Mater. Chem.* **2011**, *21*, 4037–4055.

(10) Medlin, D. L.; Snyder, G. J. Interfaces in Bulk Thermoelectric Materials: A Review for Current Opinion in Colloid and Interface Science. *Curr. Opin. Colloid Interface Sci.* **2009**, *14*, 226–235.

(11) Poudel, B.; Hao, Q.; Ma, Y.; Lan, Y.; Minnich, A.; Yu, B.; Yan, X.; Wang, D.; Muto, A.; Vashaee, D.; et al. High-Thermoelectric Performance of Nanostructured Bismuth Antimony Telluride Bulk Alloys. *Science* **2008**, *320*, 634–638.

(12) Cahill, D. G.; Ford, W. K.; Goodson, K. E.; Mahan, G. D.; Majumdar, A.; Maris, H. J.; Merlin, R.; Phillpot, S. R. Nanoscale Thermal Transport. *J. Appl. Phys.* **2003**, *93*, 793–818.

(13) Bian, Z.; Zebarjadi, M.; Singh, R.; Ezzahri, Y.; Shakouri, A.; Zeng, G.; Bahk, J.-H.; Bowers, J. E.; Zide, J. M. O.; Gossard, A. C. Cross-Plane Seebeck Coefficient and Lorenz Number in Superlattices. *Phys. Rev. B* **2007**, *76*, 205311.

(14) Minnich, A. J.; Dresselhaus, M. S.; Ren, Z. F.; Chen, G. Bulk Nanostructured Thermoelectric Materials: Current Research and Future Prospects. *Energy Environ. Sci.* **2009**, *2*, 466.

(15) Humphrey, T. E.; Linke, H. Reversible Thermoelectric Nanomaterials. *Phys. Rev. Lett.* **2005**, *94*, 096601.

(16) Dingle, R.; Störmer, H. L.; Gossard, A. C.; Wiegmann, W. Electron Mobilities in Modulation doped Semiconductor Heterojunction Superlattices. *Appl. Phys. Lett.* **1978**, *33*, 665–667.

(17) Zebarjadi, M.; Joshi, G.; Zhu, G.; Yu, B.; Minnich, A.; Lan, Y.; Wang, X.; Dresselhaus, M.; Ren, Z.; Chen, G. Power Factor Enhancement by Modulation Doping in Bulk Nanocomposites. *Nano Lett* **2011**, *11*, 2225–2230.

(18) Hicks, L. D.; Dresselhaus, M. S. Effect of Quantum-Well Structures on the Thermoelectric Figure of Merit. *Phys. Rev. B* **1993**, *47*, 12727–12731.

(19) Vashaee, D.; Shakouri, A. Improved Thermoelectric Power Factor in Metal-Based Superlattices. *Phys. Rev. Lett.* **2004**, *92*, 106103.

(20) Sootsman, J. R.; Kong, H.; Uher, C.; D'Angelo, J. J.; Wu, C.-I.; Hogan, T. P.; Caillat, T.; Kanatzidis, M. G. Large Enhancements in the Thermoelectric Power Factor of Bulk PbTe at High Temperature by Synergistic Nanostructuring. *Angew. Chem.* **2008**, *120*, 8746–8750.

(21) Cornett, J. E.; Rabin, O. Thermoelectric Figure of Merit Calculations for Semiconducting Nanowires. *Appl. Phys. Lett.* **2011**, *98*, 182104–182104–3.

(22) Heremans, J. P.; Thrush, C. M.; Morelli, D. T. Thermopower Enhancement in Lead Telluride Nanostructures. *Phys. Rev. B* **2004**, *70*, 115334.

(23) Martin, J.; Wang, L.; Chen, L.; Nolas, G. S. Enhanced Seebeck Coefficient through Energy-Barrier Scattering in PbTe Nanocomposites. *Phys. Rev. B* **2009**, *79*, 115311.

(24) Popescu, A.; Woods, L. M.; Martin, J.; Nolas, G. S. Model of Transport Properties of Thermoelectric Nanocomposite Materials. *Phys. Rev. B* **2009**, *79*, 205302.

(25) Faleev, S. V.; Léonard, F. Theory of Enhancement of Thermoelectric Properties of Materials with Nanoinclusions. *Phys. Rev. B* **2008**, *77*, 214304.

(26) Lan, Y.; Minnich, A. J.; Chen, G.; Ren, Z. Enhancement of Thermoelectric Figure-of-Merit by a Bulk Nanostructuring Approach. *Adv. Funct. Mater.* **2010**, *20*, 357–376.

(27) Hsu, K. F.; Loo, S.; Guo, F.; Chen, W.; Dyck, J. S.; Uher, C.; Hogan, T.; Polychroniadis, E. K.; Kanatzidis, M. G. Cubic $AgPb_mSbTe_{2+m}$: Bulk Thermoelectric Materials with High Figure of Merit. *Science* **2004**, *303*, 818–821.

(28) Quarez, E.; Hsu, K.-F.; Pcionek, R.; Frangis, N.; Polychroniadis, E. K.; Kanatzidis, M. G. Nanostructuring, Compositional Fluctuations, and Atomic Ordering in the Thermoelectric Materials $AgPb_mSbTe_{2+m}$. The Myth of Solid Solutions. *J. Am. Chem. Soc.* **2005**, *127*, 9177–9190.

(29) Gorsse, S.; Bauer Pereira, P.; Decourt, R.; Sellier, E. Microstructure Engineering Design for Thermoelectric Materials: An Approach to Minimize Thermal Diffusivity. *Chem Mater* **2009**, *22*, 988–993.

(30) Gorsse, S.; Bellanger, P.; Brechet, Y.; Sellier, E.; Umarji, A.; Ail, U.; Decourt, R. Nanostructuration via Solid State Transformation as a Strategy for Improving the Thermoelectric Efficiency of PbTe Alloys. *Acta Mater.* **2011**, *59*, 7425–7437.

(31) Zhao, Y.; Dyck, J. S.; Burda, C. Toward High-Performance Nanostructured Thermoelectric Materials: The Progress of Bottom-up Solution Chemistry Approaches. *J. Mater. Chem.* **2011**, *21*, 17049.

(32) Prasher, R. Ultralow Thermal Conductivity of a Packed Bed of Crystalline Nanoparticles: A Theoretical Study. *Phys. Rev. B* **2006**, *74*, 165413.

(33) Kovalenko, M. V.; Spokoyny, B.; Lee, J.-S.; Scheele, M.; Weber, A.; Perera, S.; Landry, D.; Talapin, D. V. Semiconductor Nanocrystals Functionalized with Antimony Telluride Zintl Ions for Nanostructured Thermoelectrics. *J Am Chem Soc* **2010**, *132*, 6686–6695.

(34) Ibáñez, M.; Guardia, P.; Shavel, A.; Cadavid, D.; Arbiol, J.; Morante, J. R.; Cabot, A. Growth Kinetics of Asymmetric $Bi_2S_3$

Nanocrystals: Size Distribution Focusing in Nanorods. *J Phys Chem C* **2011**, *115*, 7947–7955.

(35) Li, W.; Shavel, A.; Guzman, R.; Rubio-Garcia, J.; Flox, C.; Fan, J.; Cadavid, D.; Ibáñez, M.; Arbiol, J.; Morante, J. R.; et al. Morphology Evolution of $Cu_{2-x}S$ Nanoparticles: From Spheres to Dodecahedrons. *Chem. Commun.* **2011**, *47*, 10332–10334.

(36) Cadavid, D.; Ibáñez, M.; Shavel, A.; Durá, O. J.; Torre, M. A. L. de la; Cabot, A. Organic Ligand Displacement by Metal Salts to Enhance Nanoparticle Functionality: Thermoelectric Properties of $Ag_2Te$. *J. Mater. Chem. A* **2013**, *1*, 4864–4870.

(37) Ibáñez, M.; Cadavid, D.; Anselmi-Tamburini, U.; Zamani, R.; Gorsse, S.; Li, W.; López, A. M.; Morante, J. R.; Arbiol, J.; Cabot, A. Colloidal Synthesis and Thermoelectric Properties of $Cu_2SnSe_3$ Nanocrystals. *J. Mater. Chem. A* **2012**, *1*, 1421–1426.

(38) Scheele, M.; Oeschler, N.; Veremchuk, I.; Reinsberg, K.-G.; Kreuziger, A.-M.; Kornowski, A.; Broekaert, J.; Klinke, C.; Weller, H. ZT Enhancement in Solution-Grown $Sb_{(2-x)}Bi_xTe_3$ Nanoplatelets. *ACS Nano* **2010**, *4*, 4283–4291.

(39) Dalpian, G. M.; Chelikowsky, J. R. Self-Purification in Semiconductor Nanocrystals. *Phys. Rev. Lett.* **2006**, *96*, 226802.

(40) Norris, D. J.; Efros, A. L.; Erwin, S. C. Doped Nanocrystals. *Science* **2008**, *319*, 1776–1779.

(41) Erwin, S. C.; Zu, L.; Haftel, M. I.; Efros, A. L.; Kennedy, T. A.; Norris, D. J. Doping Semiconductor Nanocrystals. *Nature* **2005**, *436*, 91–94.

(42) Ibáñez, M.; Cadavid, D.; Zamani, R.; García-Castelló, N.; Izquierdo-Roca, V.; Li, W.; Fairbrother, A.; Prades, J. D.; Shavel, A.; Arbiol, J.; et al. Composition Control and Thermoelectric Properties of Quaternary Chalcogenide Nanocrystals: The Case of Stannite $Cu_2CdSnSe_4$. *Chem Mater* **2012**, *24*, 562–570.

(43) Ibáñez, M.; Zamani, R.; LaLonde, A.; Cadavid, D.; Li, W.; Shavel, A.; Arbiol, J.; Morante, J. R.; Gorsse, S.; Snyder, G. J.; et al. $Cu_2ZnGeSe_4$ Nanocrystals: Synthesis and Thermoelectric Properties. *J Am Chem Soc* **2012**, *134*, 4060–4063.

(44) Urban, J. J.; Talapin, D. V.; Shevchenko, E. V.; Kagan, C. R.; Murray, C. B. Synergism in Binary Nanocrystal Superlattices Leads to Enhanced P-Type Conductivity in Self-Assembled PbTe/$Ag_2Te$ Thin Films. *Nat. Mater.* **2007**, *6*, 115–121.

(45) Ko, D.-K.; Urban, J. J.; Murray, C. B. Carrier Distribution and Dynamics of Nanocrystal Solids Doped with Artificial Atoms. *Nano Lett* **2010**, *10*, 1842–1847.

(46) Lensch-Falk, J. L.; Sugar, J. D.; Hekmaty, M. A.; Medlin, D. L. Morphological Evolution of $Ag_2Te$ Precipitates in Thermoelectric PbTe. *J. Alloys Compd.* **2010**, *504*, 37–44.

(47) Pei, Y.; Heinz, N. A.; Snyder, G. J. Alloying to Increase the Band Gap for Improving Thermoelectric Properties of $Ag_2Te$. *J. Mater. Chem.* **2011**, *21*, 18256.

(48) Pei, Y.; Lensch-Falk, J.; Toberer, E. S.; Medlin, D. L.; Snyder, G. J. High Thermoelectric Performance in PbTe Due to Large Nanoscale $Ag_2Te$ Precipitates and La Doping. *Adv. Funct. Mater.* **2011**, *21*, 241–249.

(49) Paul, B.; V, A. K.; Banerji, P. Embedded Ag-Rich Nanodots in PbTe: Enhancement of Thermoelectric Properties through Energy Filtering of the Carriers. *J. Appl. Phys.* **2010**, *108*, 064322.

(50) Cadavid, D.; Ibáñez, M.; Gorsse, S.; López, A. M.; Cirera, A.; Morante, J. R.; Cabot, A. Bottom-up Processing of Thermoelectric Nanocomposites from Colloidal Nanocrystal Building Blocks: The Case of $Ag_2Te$–PbTe. *J. Nanoparticle Res.* **2012**, *14*, 1–10.

(51) Urban, J. J.; Talapin, D. V.; Shevchenko, E. V.; Murray, C. B. Self-Assembly of PbTe Quantum Dots into Nanocrystal Superlattices and Glassy Films. *J. Am. Chem. Soc.* **2006**, *128*, 3248–3255.

(52) Sakuma, T.; Saitoh, S. Structure of α-$Ag_2Te$. *J. Phys. Soc. Jpn.* **1985**, *54*, 3647–3648.

(53) Fujikane, M.; Kurosaki, K.; Muta, H.; Yamanaka, S. Electrical Properties of α- and β-Ag2Te. *J. Alloys Compd.* **2005**, *387*, 297–299.

(54) Fujikane, M.; Kurosaki, K.; Muta, H.; Yamanaka, S. Thermoelectric Properties of α- and β-$Ag_2Te$. *J. Alloys Compd.* **2005**, *393*, 299–301.

(55) Taylor, P. F.; Wood, C. Thermoelectric Properties of $Ag_2Te$. *J. Appl. Phys.* **1961**, *32*, 1–3.

(56) Capps, J.; Drymiotis, F.; Lindsey, S.; Tritt, T. M. Significant Enhancement of the Dimensionless Thermoelectric Figure of Merit of the Binary $Ag_2Te$. *Philos. Mag. Lett.* **2010**, *90*, 677–681.

(57) Dalven, R. Fundamental Optical Absorption in β-Silver Telluride. *Phys. Rev. Lett.* **1966**, *16*, 311–312.

(58) Dalven, R.; Gill, R. Electrical Properties of β-$Ag_2Te$ and β-$Ag_2Se$ from 4.2°K to 300°K. *J. Appl. Phys.* **1967**, *38*, 753–756.

(59) Schneider, J.; Schulz, H. X-Ray Powder Diffraction of $Ag_2Te$ at Temperatures up to 1123 K. *Z. Für Krist.* **1993**, *203*, 1–15.

(60) Wood, C.; Harrap, V.; Kane, W. M. Degeneracy in $Ag_2Te$. *Phys. Rev.* **1961**, *121*, 978–982.

(61) Das, V. D.; Karunakaran, D. Thermoelectric Studies on Semiconducting $Ag_2Te$ Thin Films: Temperature and Dimensional Effects. *Phys. Rev. B* **1984**, *30*, 2036–2041.

(62) Capps, J.; Ma, B.; Drye, T.; Nucklos, C.; Lindsey, S.; Rhodes, D.; Zhang, Q.; Modic, K.; Cawthorne, S.; Drymiotis, F. The Effect of Ag Concentration on the Structural, Electrical and Thermal Transport Behavior of Pb:Te:Ag:Se Mixtures and Improvement of Thermoelectric Performance via Cu Doping. *J. Alloys Compd.* **2011**, *509*, 1544–1549.

(63) Max-Planck-Gesellschaft zur Förderung der Wissenschaften. *Gmelin Handbuch Der Anorganischen Chemie*; 8. völlig neu bearbeitete Aufl.; Springer-Verlag: Berlin, 1924.

(64) Van Dong, N.; Tung, P. N. Transport Properties of Silver Telluride in the Solid and Liquid States. *Phys. Status Solidi B* **1968**, *30*, 557–567.

(65) Goldsmid, H.; Sharp, J. Estimation of the Thermal Band Gap of a Semiconductor from Seebeck Measurements. *J. Electron. Mater.* **1999**, *28*, 869–872.

(66) Scheele, M.; Oeschler, N.; Veremchuk, I.; Peters, S.-O.; Littig, A.; Kornowski, A.; Klinke, C.; Weller, H. Thermoelectric Properties of Lead Chalcogenide Core–Shell Nanostructures. *ACS Nano* **2011**, *5*, 8541–8551.

(67) B. Paul; P. Banerji. Enhancement in Thermoelectric Power in Lead Telluride Nanocomposite: Role of Oxygen Vis-À-Vis Nanostruct. *J. Nano- Electron. Phys.* **2011**, *3*, 691–697.

(68) Rogacheva, E. I.; Krivulkin, I. M.; Nashchekina, O. N.; Sipatov, A. Y.; Volobuev, V. V.; Dresselhaus, M. S. Effect of Oxidation on the Thermoelectric Properties of PbTe and PbS Epitaxial Films. *Appl. Phys. Lett.* **2001**, *78*, 1661–1663.

(69) Schenk, M.; Berger, H.; Klimakow, A.; Mühlberg, M.; Wienecke, M. Nonstoichiometry and Point Defects in PbTe. *Cryst. Res. Technol.* **1988**, *23*, 77–84.

(70) Wang, R. Y.; Feser, J. P.; Lee, J.-S.; Talapin, D. V.; Segalman, R.; Majumdar, A. Enhanced Thermopower in PbSe Nanocrystal Quantum Dot Superlattices. *Nano Lett* **2008**, *8*, 2283–2288.

(71) Borisova, L. D. Thermoelectric Properties of Impurity Doped PbTe. *Phys. Status Solidi A* **1979**, *53*, K19–K22.

(72) Breschi, R.; Camanzi, A.; Fano, V. Defects in PbTe Single Crystals. *J. Cryst. Growth* **1982**, *58*, 399–408.

(73) Crocker, A. J.; Rogers, L. M. Interpretation of the Hall Coefficient, Electrical Resistivity and Seebeck Coefficient of P-Type Lead Telluride. *Br. J. Appl. Phys.* **1967**, *18*, 563–573.

(74) Martin, J.; Nolas, G. S.; Zhang, W.; Chen, L.; State Key Laboratory of High Performance Ceramics and Superfine Microstructures, S. I. of C. Pbte Nanocomposites Synthesized from Pbte Nanocrystals. *Appl. Phys. Lett.* **2007**, *90*.

(75) Allgaier, R. S. Valence Bands in Lead Telluride. *J. Appl. Phys.* **1961**, *32*, 2185–2189.

(76) Grekov, Y.; Shlyakhov, T.; Semikolenova, N. Inversion of the Conduction Type of Epitaxial Films of PbSnTe Solid Solutions under the Influence of Laser Irradiation at Subthreshold Power. *Semiconductors* **1997**, *31*, 844–846.

(77) Scanlon, W. W. Precipitation of Te and Pb in PbTe Crystals. *Phys. Rev.* **1962**, *126*, 509–513.

(78) Dashevsky, Z.; Kreizman, R.; Dariel, M. P. Physical Properties and Inversion of Conductivity Type in Nanocrystalline PbTe Films. *J. Appl. Phys.* **2005**, *98*, 094309–094309–5.

(79) Zemel, J. N.; Jensen, J. D.; Schoolar, R. B. Electrical and Optical Properties of Epitaxial Films of PbS, PbSe, PbTe, and SnTe. *Phys. Rev.* **1965**, *140*, A330–A342.

# Chapter 4 Organic ligand displacement by metal salts to enhance nanoparticle functionality: Thermoelectric properties of $Ag_2Te$

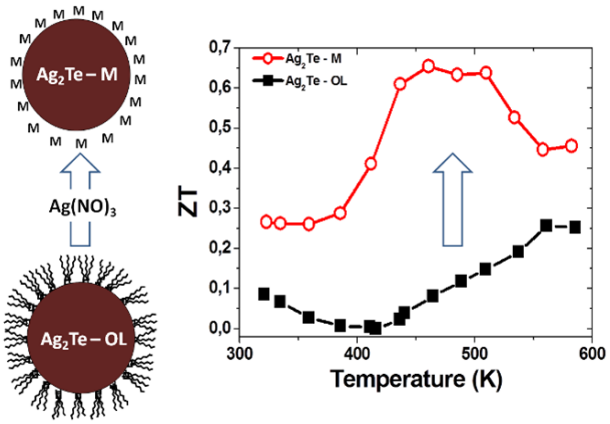


## 4.1 Introduction

Colloidal NCs are excellent building blocks to produce functional materials with properties engineered at the nanometer scale. Their

wide fundamental and technological interest have driven the development of tools and processes to control their composition, size, shape and crystal structure with an outstanding precision[1–5]. Most current synthetic routes to produce high quality NCs make use of organic surfactants. These organic molecules limit the NC growth, direct its morphology and provide it with stability in an organic media. While some organic ligands have demonstrated really efficient in these tasks, the surface barrier for charge transfer/transport that they introduce is an important downside. Most organic ligands used in colloidal synthesis routes are electrical insulators. Such electrically insulating barriers at the NC surface strongly limit its performance in a variety of applications where charge carrier transfer and transport through NCs or between the NCs and the liquid/gas/solid medium play a fundamental role: e.g. lighting, photovoltaics, TE, catalysis.[6–9]

Serious efforts have been made to exchange large organic ligands by shorter organic groups or inorganic ligands at the NC surface. While in some cases the exact specie left at the NC surface is not known, some compounds were certainly useful in various particular applications: e.g. pyridine,[10] molecular metal chalcogenides complexes (MCC) stabilized by hydrazine,[11–15] nitrosonium,[16] diazonium[16] and trialkyl oxonium tetrafluoroborates;[17] tetrafluoroborate acids ($HBF_4$, $HPF_6$),[18] ammonium thiocianate ($NH_4SCN$);[19,20] sulphides like $Na_2S$, $NH_4S$, and $K_2S$,[18,21,22] halide anions such as $Cl^-$, $Br^-$ and $I^-$.[23–25] However, some of these compounds require the manipulation of highly toxic chemicals (e.g. hydrazine); others can introduce large concentrations of foreign impurities, which may strongly modify the material properties (e.g. halide anions); some may even modify the chemical composition of the NC or NC-based material (e.g. $Na_2S$, $NH_4S$, and $K_2S$ used with non-sulphide NCs).

We present a scalable and general procedure to displace organic ligands by means of a matched metal salt solution. We use $Ag_2Te$ nanoparticles as the model material and thermoelectricity as the paradigmatic application to exemplify the detailed processes. $Ag_2Te$

is a technologically important material, displaying a high ionic conductivity at room temperature.[26] The low temperature α-$Ag_2Te$ phase is a very narrow band-gap semiconductor (Eg = 0.025 eV), with a low electron effective mass, high electron mobility and a low lattice thermal conductivity.[27–34] $Ag_2Te$ also shows excellent TE properties, both in bulk and nanocrystalline form.[35,36]

Thermoelectricity is a particularly interesting application for advanced functional nanomaterials. TE energy conversion has an enormous potential for economic and social impact.[37–39] However, current TE devices lack of high enough efficiency to compete in most potential markets. TE efficiency can be improved by controlling material composition at the nanometer scale. To date, most thermoelectric materials with high thermoelectric figures of merit ($Z=\sigma S^2/\kappa$) are nanostructured. The confinement of the lattice dimensions to the nanometer scale allows improving the thermoelectric efficiency by promoting phonon scattering at crystal interfaces and reducing in such a way the thermal conductivity (κ) of the materials.[40,41] Furthermore, the selective scattering of the low energy charge carriers at crystal interfaces provides a path towards higher Seebeck coefficients *S*.[42,43] In this scenario, the bottom-up assembly of colloidal nanoparticles is emerging as a suitable approach to produce efficient thermoelectric materials.[44–49]

In this chapter, we detail a procedure to displace organic ligands from NCs surfaces based on the use of a metal salt solution. Considering $Ag_2Te$ as the model material and $Ag^+$ as the matched metal ion, we demonstrate the effectiveness of this process to improve the thermoelectric figure of merit of $Ag_2Te$ nanomaterials obtained from the bottom up assembly of colloidal $Ag_2Te$ NC building blocks[50].

## 4.2 Experimental details

### 4.2.1 Materials

Tri-n-octylphosphine (TOP, 97 %) and silver chloride (99.9 %) were purchased from Strem, tellurium pieces (99.999 %), silver nitrate (99.8 %), 1-octadecene (ODE, 90 %), oleylamine (OLA, tech. 70 %), and formamide (FA, ≥99.5 %) were purchased from Aldrich. Analytical grade ethanol, chloroform and toluene were purchased from Panreac. All chemicals were used without further purifications. Stock solution of tri-n-octylphosphine telluride (TOPTe 1 M) and Ag-TOP (1 M) were prepared dissolving 12.76 g of tellurium and 14.33 g of silver chloride in 100 ml of TOP. These solutions were prepared and stored inside an argon-filled glovebox. All NC preparations were carried out using standard airless technique: a vacuum/dry-argon Schlenk line was used for the synthesis and an argon-filled glovebox for storing and handling air- and moisture-sensitive chemicals.

### 4.2.2 Preparation of $Ag_2Te$ nanocrystals

In a typical procedure, 10 ml of OLA were added to a three neck flask and maintained at 100 ºC under vacuum for 1 h to remove low boiling point impurities and water. Afterwards, the reaction flask was flushed with Ar and temperature was raised up to 160 ºC. At this temperature, a mixture of 5 ml of Ag-TOP and 2.5 ml of TOPTe stock solutions was quickly injected. After injection, the reaction temperature was maintained between 130 ºC and 160 ºC for 3 minutes. Then the reaction solution was cooled using a water bath. $Ag_2Te$ NCs were precipitated and redispersed using ethanol and toluene twice. Finally, the NCs were dispersed in toluene and stored in the glovebox.

### 4.2.3 Organic ligand displacement by metal salts

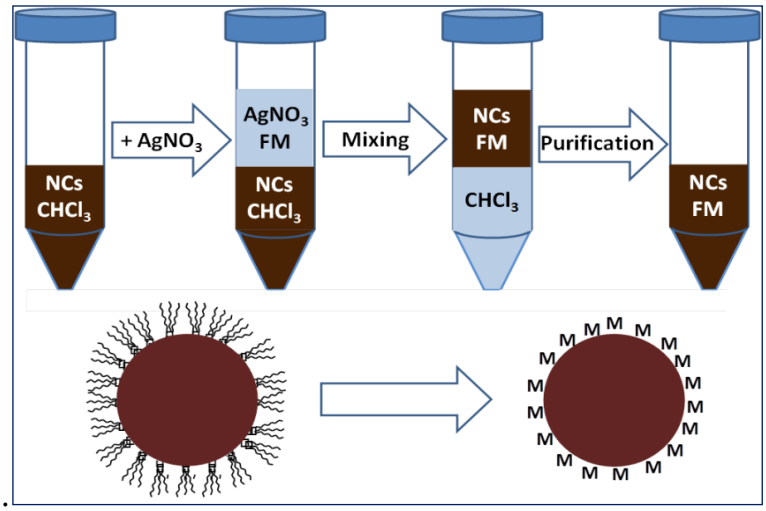


**Figure 4.1** Schematized view of the displacement of TOP molecules from the surface of $Ag_2Te$ nanocrystals. A silver nitrate solution in formamide (FM) is added to the colloidal nanocrystals dispersed in chloroform. Mixing the two immiscible phases, the organic ligands are displaced from the NC surface, rendering them soluble in FM.

PbTe and $Ag_2Te$ nanoparticles dispersed in toluene were blended at various molar fractions, 25/75, 50/50 and 75/25. After several additional precipitation and redispersion cycles, the resultant blends were dried under Ar atmosphere. The blends were annealed at 500 ºC during 2 hours in Ar flow. Finally, the resulting materials were pressed under a load of 5 tons at room temperature into pellets of 13 mm diameter and 1mm thickness. **Figure 4.1** shows the scheme of the procedure.

### 4.2.4 Preparation of bulk nanostructured material

To produce $Ag_2Te$ bulk nanostructured materials, NCs were dried using an Ar flow. The obtained nanopowder was annealed at 350 ºC for 1 h and afterward compacted at 250 ºC into disk-shaped pellets

of 10 mm of diameter and 1 mm of thickness under 90 MPa of pressure. Custom-made hot-press (HP) equipment, with an induction heater coupled to a hydraulic press, was used for pellet preparation. The system was operated under Ar using a graphite die. Pellets with relative densities over 90 % were produced.

## 4.3 Results and discussion

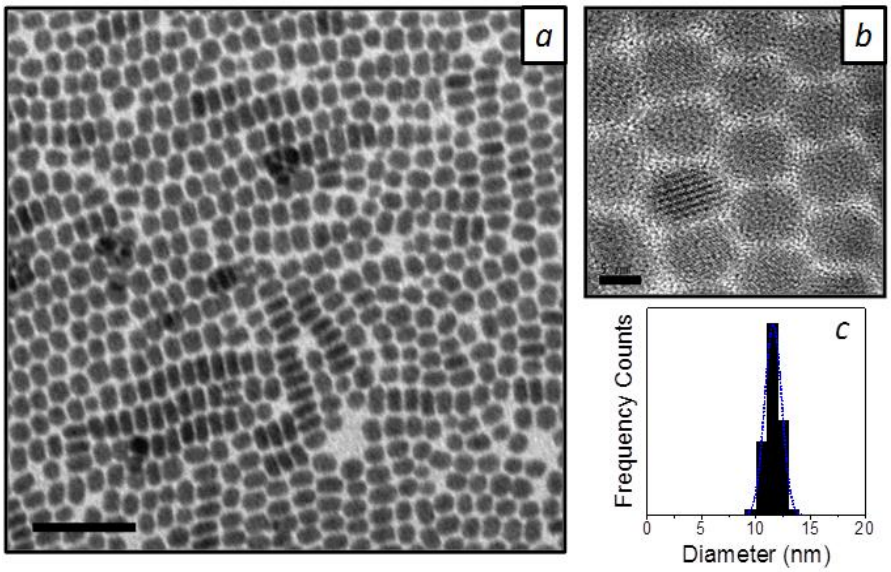


**Figure 4.2** TEM (*a*) and HRTEM (*b*) micrographs of $Ag_2Te$ nanoparticles. Scale bars correspond to 100 and 5 nm for the TEM and HRTEM micrographs, respectively. (c) Histogram with the diameter distribution for the displayed $Ag_2Te$ nanoparticles.

$Ag_2Te$ nanoparticles were prepared by reacting TOPTe and Ag-TOP in OLA. Figure 4.2 show representative TEM and HRTEM micrographs of $Ag_2Te$ NCs obtained by the procedure detailed above. Highly monodisperse NCs with a disk-like shape and size dispersion below 10 % were systematically obtained. Figure 1c displays the histogram with the diameter distribution of the $Ag_2Te$

nanoparticles characterized here. From this histogram an average nanoparticle diameter of 11 ± 1 nm was calculated.

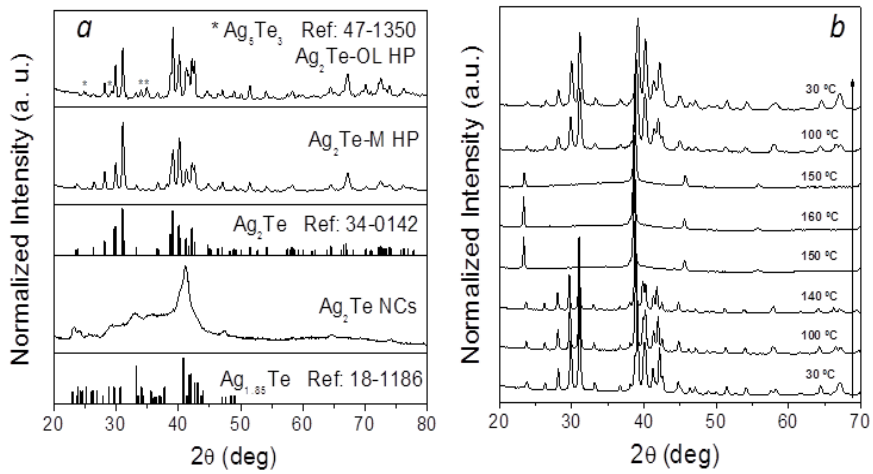


**Figure 4.3** (a) Room temperature XRD patterns of the $Ag_2Te$ NCs and of the $Ag_2Te$ nanomaterial ($Ag_2Te$ HP) obtained after annealing the NCs at 350 ºC and pressing them at 250 ºC under 90 MPa. (b) Evolution of the XRD pattern of $Ag_2Te$ NCs at different temperatures, from 30 ºC to 160 ºC. XRD patterns were measured at 30ºC, 100ºC, 140ºC, 150ºC, and 160ºC while increasing temperature and at 150ºC, 100ºC and 30ºC while decreasing temperature.

Figure 4.3 displays the XRD pattern of the $Ag_2Te$ NCs prepared. Although broad XRD peaks were obtained due to the small size of the crystallographic domains, the XRD pattern was matched with the hexagonal $Ag_{1.85}Te$ phase (JCPDS 18-1186).

From the synthesis procedure described above, $Ag_2Te$ NCs with a surface layer of TOP molecules were obtained.[51] Such electrically insulating layer strongly limits the $Ag_2Te$ NCs use in applications requiring a charge exchange between NCs or between the NC and the medium. To exploit the NCs technological potential, the organic layer needs to be removed. When choosing the chemical procedure used to eliminate the organic ligands from the $Ag_2Te$ NC surface, the following drawbacks need to be considered: i) the use of S-based compounds, such as $NH_4S$, results in the sulfidation of the

nanoparticles during its annealing at moderate temperatures (≥350 ºC); ii) the use of MCCs involves the manipulation of concentrated hydrazine, which is a highly toxic compound and is not commercial available in Europe.

Here, we used a solution of $AgNO_3$ in FA to displace the organic ligands from the $Ag_2Te$ surface and render the NCs stable in a polar media. While different metal salts were successfully tested, to match the cation with the NC composition $AgNO_3$ was selected. We speculate that after organic ligand displacement particles are stabilized by silver ions, but we cannot exclude nitrate to play a role. After organic ligand displacement, NCs were stable in solution during relatively short periods of time, but long enough to allow their purification and their bottom-up assembly or deposition to produce organic-free bulk nanocrystalline materials or thin films.

We used FTIR and NMR spectroscopies to characterize the efficiency of the organic ligand displacement. Figure 4.4a shows the ATR-FTIR spectra of dried $Ag_2Te$ NCs before ($Ag_2Te$ with organic ligands, $Ag_2Te$-OL), and after the organic ligand displacement with the metal salt ($Ag_2Te$-M). The $Ag_2Te$-OL spectrum showed the characteristic features of TOP molecules: C-H vibration modes have a strong band in the high-frequency region (2800-3000 $cm^{-1}$) and various peaks in the lower frequency region, between 700 $cm^{-1}$ and 1500 $cm^{-1}$.[18] These features completely disappeared from the $Ag_2Te$-M spectrum.

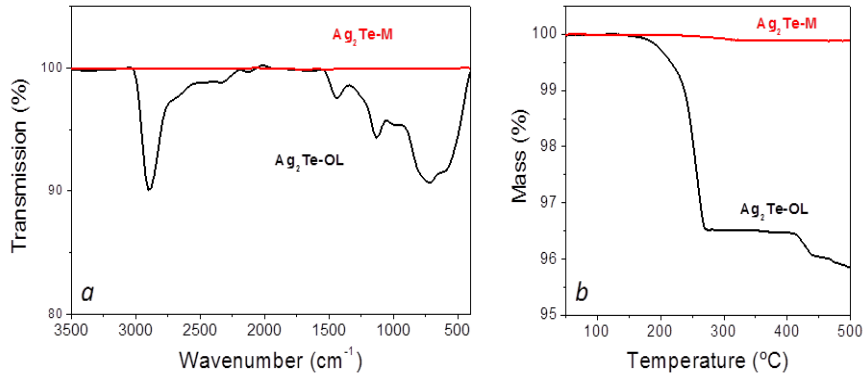


**Figure 4.4** (a) ATR-FTIR spectra and (b) TGA from $Ag_2Te$-OL and $Ag_2Te$-M nanocrystals

Figure 4.5 displays the $^{1}$H-NMR, $^{13}$C-NMR and $^{31}$P-NMR spectra of the $Ag_2Te$-OL and $Ag_2Te$-M NCs. In both, $^{1}$H-NMR and $^{13}$C-NMR spectra of $Ag_2Te$-OL NCs, bands corresponding to the $CH_3(CH_2)_7$ chains from TOP were easily identified. For the $Ag_2Te$-M NCs, the TOP fingerprints disappeared and only the peaks associated to the solvent DMSO and some residual FA and water, were visible. In a similar way, the $^{31}$P-NMR spectrum of $Ag_2Te$-OL clearly showed the peak corresponding to TOP, but this was not visible in the $Ag_2Te$-M spectrum. These results probed the complete removal of TOP from the $Ag_2Te$ surface.

Thoroughly purified and dried NCs were also characterized by TGA. Figure 4.4b displays the mass loss as a function of the material temperature for $Ag_2Te$-OL and $Ag_2Te$-M NCs. TGA showed a relative mass decrease of a 4 % for the $Ag_2Te$-OL NCs. This can be associated to the decomposition or evaporation of the surface organic molecules. In contrast, the $Ag_2Te$-M NCs showed almost no mass variation when increasing temperature up to 500 ºC. This represents a further evidence of the organic-free surfaces characterizing the $Ag_2Te$-M NCs. The percentage of carbon remaining after annealing the $Ag_2Te$ NCs was measured by elemental analysis. About 2% of carbon was obtained from the analysis of the annealed $Ag_2Te$-OL. On the other hand, the carbon

percentage obtained for $Ag_2Te$-M NCs was on the limit of our system resolution: < 0.1 %. In the same way, no nitrogen was detected, what points towards Ag ions instead of $NO_3$ as stabilizing agent.

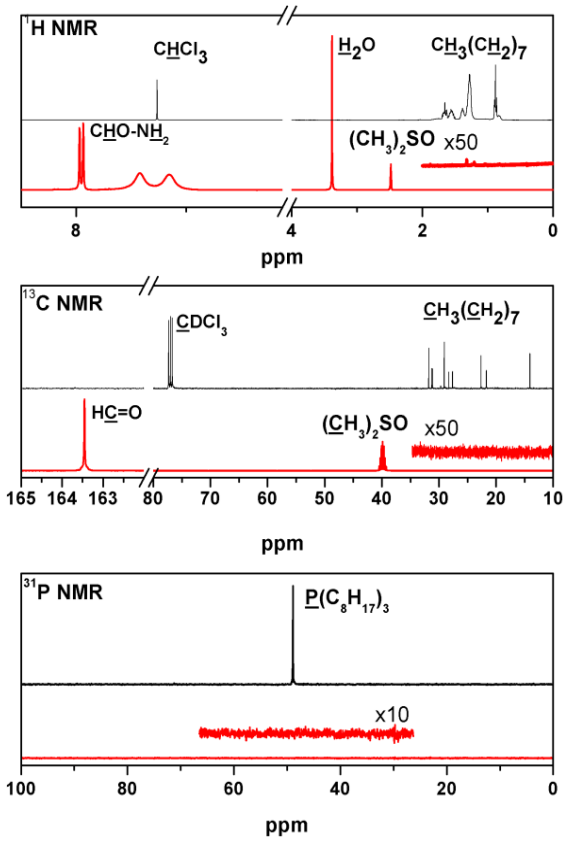


**Figure 4.5** $^1$H-NMR, $^{13}$C-NMR and $^{31}$P-NMR spectra of the $Ag_2Te$-OL (top black spectra) and $Ag_2Te$-M NCs (bottom red spectra).

To validate the potential of the described procedure to prepare nanomaterials with enhanced performances, we characterized the thermoelectric properties of $Ag_2Te$ nanomaterials obtained from the bottom-up assembly of $Ag_2Te$ NCs. We produced and processed approximately 2 g of colloidal $Ag_2Te$ NCs. The organic ligands were

displaced from 1 g of NCs using $AgNO_3$ ($Ag_2Te$-M). The other 1 g was left untreated ($Ag_2Te$-OL). Both samples were thoroughly purified, dried and annealed. The obtained $Ag_2Te$ nanopowders were consolidated into dense disk-shaped pellets with 10 mm of diameter and 1 mm thickness. HP conditions (250 ºC for 1 min) were carefully adjusted to maximize the pellet density, but minimizing at the same time the crystal domain growth. The relative densities of the samples obtained in these conditions were around 92 %. Figure 4.6 displays a representative SEM image of the $Ag_2Te$ nanomaterials obtained. During annealing and hot press processes, the $Ag_2Te$ crystal domains underwent a factor 5 growth: from 11 nm to approximately 50 nm, as calculated from the XRD pattern using Scherrer equation. No clear differences were obtained in this respect between $Ag_2Te$-M and $Ag_2Te$-OL nanomaterials. Figure 4.3a displays the XRD pattern of the $Ag_2Te$ nanomaterial obtained after HP. The patterns obtained for both samples, $Ag_2Te$-M and $Ag_2Te$-OL, matched with the α-$Ag_2Te$ monoclinic phase (mP12, Hessite, JCPDS 34-0142). However, the XRD-pattern of the $Ag_2Te$-OL nanomaterials (Figure 2a) also displayed the presence of weak peaks associated to the Ag-poor $Ag_5Te_3$ hexagonal phase (JCPDS 47-1350). In the $Ag_2Te$-M samples, the transformation of the initial Ag-poor $Ag_{1.85}Te$ phase into the stoichiometric α-$Ag_2Te$ crystal structure is understood by the excess of Ag introduced during ligand displacement. The phase transition of the untreated $Ag_{1.85}Te$ nanoparticles into α-$Ag_2Te$ was accompanied by the formation of a small amount of a secondary Ag-poor phase.

We speculate the $Ag_2Te$-M samples to be slightly Ag-rich due to the excess of Ag introduced during ligand displacement, and the $Ag_2Te$-OL samples to be slightly Ag poor, as the initially formed NCs. We characterized the surface composition of the $Ag_2Te$ nanomaterials by means of XPS. From the XPS spectra, a slight excess of Ag in the $Ag_2Te$-M nanomaterial was observed. This excess also points towards the presence of Ag ions at the NC surface after the organic ligand displacement.

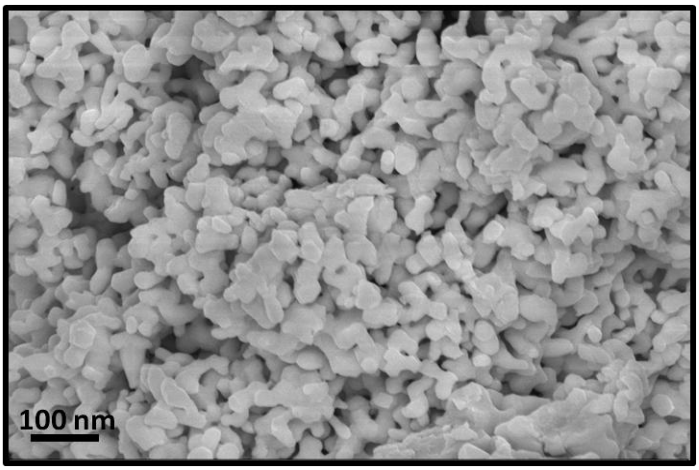


**Figure 4.6** SEM micrograph of the $Ag_2Te$-M nanomaterial obtained after pressing the $Ag_2Te$-M NCs using a hot press.

Figure 4.7 displays the electrical conductivity (σ), Seebeck coefficient (S), thermal conductivity (κ) and dimensionless thermoelectric figure of merit (ZT) of $Ag_2Te$-M and $Ag_2Te$-OL nanomaterials.

Significantly higher electrical conductivities were systematically measured for $Ag_2Te$-M when compared to $Ag_2Te$-OL. As displayed in figure 6a, above one order of magnitude enhancements were obtained when displacing the organic ligands from the NC surface before assembly. We associate this large increase of electrical conductivity to the absence of residual carbon at the NCs surface. A slight silver excess in the $Ag_2Te$-M nanomaterials may also contribute increasing the charge carrier density. Besides, a marked decrease of electrical conductivity was observed for both samples in the temperature range between 400 K and 450 K. $Ag_2Te$ undergoes a phase transformation at around 420 K from the low-temperature monoclinic α-$Ag_2Te$ to a high-temperature cubic β-$Ag_2Te$ (F23, JCPDS 01-076-0137). Figure 2b shows the evolution of the $Ag_2Te$ XRD pattern with temperature. A relatively sharp and reversible phase transition was clearly visible from this evolution. The electrical conductivity decrease was also associated to this phase transition. At temperatures above the phase transition the electrical

conductivity of the $Ag_2Te$-M slightly decreased, which is consistent with the complete ionization of the shallow donor states introduced by the excess of silver. On the other hand, the $Ag_2Te$-OL materials displayed an increase of electrical conductivity with temperature, which we associate to an increase of the charge carrier concentration by the ionization of Ag vacancies acting as deep acceptor levels[31,52].

The temperature evolution of the Seebeck coefficient (Figure 4.3b) also displayed a jump at around 420 K, which we associate to the $Ag_2Te$ phase transition. For $Ag_2Te$-OL, the phase transition was accompanied by a change from n-type to p-type conductivity, as noticed by the sign inversion of the Seebeck coefficient, from negative to positive values. In contrast, in $Ag_2Te$-M the Seebeck coefficient was negative in all the temperature range. $Ag_2Te$ electrical conductivity strongly depends on composition. While Ag-rich samples generally show n-type conductivity, Ag-poor $Ag_2Te$ has p-type conductivity. [31] This is consistent with the excess and shortage of Ag in $Ag_2Te$-M and $Ag_2Te$-OL nanomaterials, respectively.

$Ag_2Te$-M nanomaterials displayed higher thermal conductivities than $Ag_2Te$-OL samples. The lower thermal conductivities obtained from $Ag_2Te$-OL could be also associated to the presence of carbon at the $Ag_2Te$-OL interfaces. Carbon layers may enhance phonon scattering efficiency due to acoustic impedance mismatch. The thermal conductivity of both nanomaterials also underwent a strong variation with the crystallographic phase transition at around 400 K. Exceptionally low thermal conductivities, 0.3 W $m^{-1}K^{-1}$, were obtained at around this temperature. These very low thermal conductivities were associated to the combination of a high structural disorder at around the phase transition temperature and the high density of crystal interfaces characterizing nanomaterials. Both, structural disorder and crystal interfaces effectively blocked phonon propagation, thus reducing thermal conductivity. At temperatures above the phase transition a slight increase of thermal conductivity associated to the re-ordering of the silver and tellurium ions into the high temperature β-$Ag_2Te$ was obtained. At even higher

temperatures, the electronic contribution would explain the further increase of thermal conductivity.

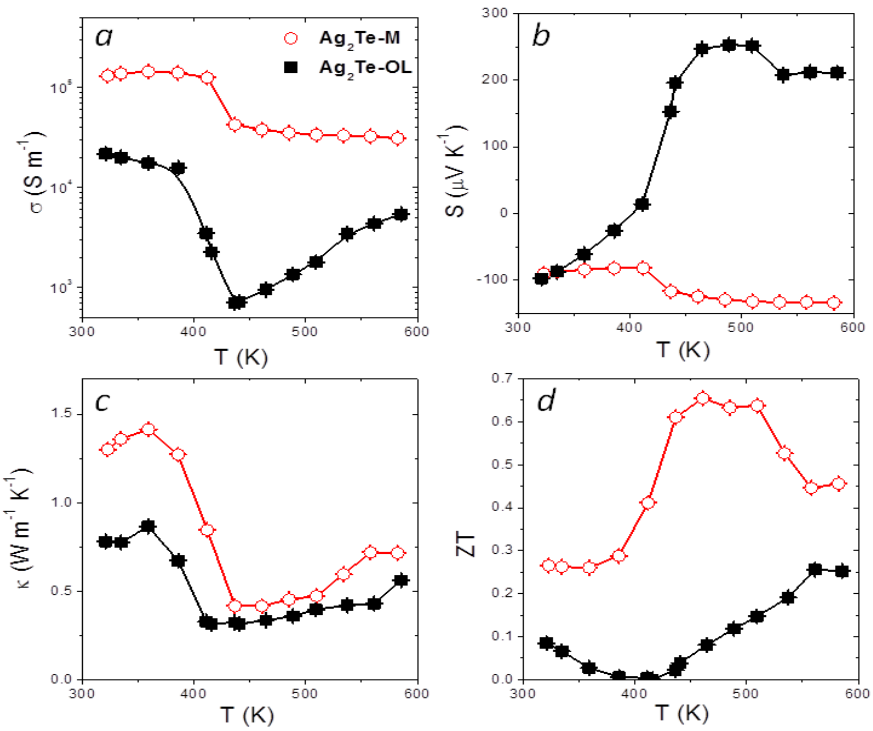


**Figure 4.7** Electrical conductivity (σ), Seebeck coefficient (S), thermal conductivity (κ) and thermoelectric figure of merit (ZT) of $Ag_2Te$-OL (■) and $Ag_2Te$-M (○) nanomaterials

Figure 4.7d displays the dimensionless TE figure of merit for both $Ag_2Te$ nanomaterials: $Ag_2Te$-M and $Ag_2Te$-OL. $Ag_2Te$-M samples were characterized by much larger figures of merit than $Ag_2Te$-OL. A factor 6 enhancement of the TE figure of merit was reached in the middle temperature range where $Ag_2Te$-M had its maximum ZT. This improvement was mainly related to the much higher electrical conductivities of $Ag_2Te$-M compared to $Ag_2Te$-OL. TE figures of merit up to ZT = 0.66 at 450 K were obtained for the $Ag_2Te$-M nanomaterial. This value is slightly higher than best results previously obtained for pure $Ag_2Te$.[35] This improvement is related

to the lower thermal conductivities of the nanomaterials produced here, which result from their reduced crystal domains.

## 4.4 Conclusion

We presented a simple, general and scalable strategy to remove electrically insulating organic ligands from the surface of colloidal nanocrystals. The process uses a metal salt solution and renders the NCs soluble in polar solvents during enough time to purify and assemble/deposit them into technologically useful macroscopic nanomaterials. The potential of the detailed approach was demonstrated by producing thermoelectric $Ag_2Te$ nanomaterials with up to a 6-fold enhancement of their TE figure of merit. The procedure reported here can be used to improve the performance of NCs-based materials and devices in a wide range of applications

## 4.5 References

(1) Yin, Y.; Alivisatos, A. P. Colloidal Nanocrystal Synthesis and the Organic–inorganic Interface. *Nature* **2004**, *437*, 664–670.

(2) Ibáñez, M.; Guardia, P.; Shavel, A.; Cadavid, D.; Arbiol, J.; Morante, J. R.; Cabot, A. Growth Kinetics of Asymmetric $Bi_2S_3$ Nanocrystals: Size Distribution Focusing in Nanorods. *J Phys Chem C* **2011**, *115*, 7947–7955.

(3) Li, W.; Shavel, A.; Guzman, R.; Rubio-Garcia, J.; Flox, C.; Fan, J.; Cadavid, D.; Ibáñez, M.; Arbiol, J.; Morante, J. R.; et al. Morphology Evolution of $Cu_{2-x}S$ Nanoparticles: From Spheres to Dodecahedrons. *Chem. Commun.* **2011**, *47*, 10332–10334.

(4) Ibáñez, M.; Fan, J.; Li, W.; Cadavid, D.; Nafria, R.; Carrete, A.; Cabot, A. Means and Limits of Control of the Shell Parameters in Hollow Nanoparticles Obtained by the Kirkendall Effect. *Chem. Mater.* **2011**, *23*, 3095–3104.

(5) Ibáñez, M.; Zamani, R.; Li, W.; Shavel, A.; Arbiol, J.; Morante, J. R.; Cabot, A. Extending the Nanocrystal Synthesis Control to Quaternary Compositions. *Cryst. Growth Des.* **2012**, *12*, 1085–1090.

(6) Talapin, D. V.; Lee, J.-S.; Kovalenko, M. V.; Shevchenko, E. V. Prospects of Colloidal Nanocrystals for Electronic and Optoelectronic Applications. *Chem. Rev.* **2010**, *110*, 389–458.

(7) Sargent, E. H. Colloidal Quantum Dot Solar Cells. *Nat. Photonics* **2012**, *6*, 133–135.

(8) Ibáñez, M.; Cadavid, D.; Zamani, R.; García-Castelló, N.; Izquierdo-Roca, V.; Li, W.; Fairbrother, A.; Prades, J. D.; Shavel, A.; Arbiol, J.; et al. Composition Control and Thermoelectric

Properties of Quaternary Chalcogenide Nanocrystals: The Case of Stannite $Cu_2CdSnSe_4$. *Chem Mater* **2012**, *24*, 562–570.

(9) Herranz, T.; Deng, X.; Cabot, A.; Guo, J.; Salmeron, M. Influence of the Cobalt Particle Size in the CO Hydrogenation Reaction Studied by In Situ X-Ray Absorption Spectroscopy. *J. Phys. Chem. B* **2009**, *113*, 10721–10727.

(10) Huynh, W. U.; Dittmer, J. J.; Alivisatos, A. P. Hybrid Nanorod-Polymer Solar Cells. *Science* **2002**, *295*, 2425–2427.

(11) Kovalenko, M. V.; Scheele, M.; Talapin, D. V. Colloidal Nanocrystals with Molecular Metal Chalcogenide Surface Ligands. *Science* **2009**, *324*, 1417–1420.

(12) Kovalenko, M. V.; Bodnarchuk, M. I.; Zaumseil, J.; Lee, J.-S.; Talapin, D. V. Expanding the Chemical Versatility of Colloidal Nanocrystals Capped with Molecular Metal Chalcogenide Ligands. *J. Am. Chem. Soc.* **2010**, *132*, 10085–10092.

(13) Kovalenko, M. V.; Spokoyny, B.; Lee, J.-S.; Scheele, M.; Weber, A.; Perera, S.; Landry, D.; Talapin, D. V. Semiconductor Nanocrystals Functionalized with Antimony Telluride Zintl Ions for Nanostructured Thermoelectrics. *J Am Chem Soc* **2010**, *132*, 6686–6695.

(14) Kovalenko, M. V.; Bodnarchuk, M. I.; Talapin, D. V. Nanocrystal Superlattices with Thermally Degradable Hybrid Inorganic−Organic Capping Ligands. *J. Am. Chem. Soc.* **2010**, *132*, 15124–15126.

(15) Lee, J.-S.; Kovalenko, M. V.; Huang, J.; Chung, D. S.; Talapin, D. V. Band-like Transport, High Electron Mobility and High Photoconductivity in All-Inorganic Nanocrystal Arrays. *Nat. Nanotechnol.* **2011**, *6*, 348–352.

(16) Dong, A.; Ye, X.; Chen, J.; Kang, Y.; Gordon, T.; Kikkawa, J. M.; Murray, C. B. A Generalized Ligand-Exchange Strategy

Enabling Sequential Surface Functionalization of Colloidal Nanocrystals. *J. Am. Chem. Soc.* **2011**, *133*, 998–1006.

(17) Rosen, E. L.; Buonsanti, R.; Llordes, A.; Sawvel, A. M.; Milliron, D. J.; Helms, B. A. Exceptionally Mild Reactive Stripping of Native Ligands from Nanocrystal Surfaces by Using Meerwein's Salt. *Angew. Chem. Int. Ed.* **2012**, *51*, 684–689.

(18) Nag, A.; Kovalenko, M. V.; Lee, J.-S.; Liu, W.; Spokoyny, B.; Talapin, D. V. Metal-Free Inorganic Ligands for Colloidal Nanocrystals: $S^{2-}$, $HS^{-}$, $Se^{2-}$, $HSe^{-}$, $Te^{2-}$, $HTe^{-}$, $TeS_3^{2-}$, $OH^{-}$, and $NH_2^{-}$ as Surface Ligands. *J. Am. Chem. Soc.* **2011**, *133*, 10612–10620.

(19) Fafarman, A. T.; Koh, W.; Diroll, B. T.; Kim, D. K.; Ko, D.-K.; Oh, S. J.; Ye, X.; Doan-Nguyen, V.; Crump, M. R.; Reifsnyder, D. C.; et al. Thiocyanate-Capped Nanocrystal Colloids: Vibrational Reporter of Surface Chemistry and Solution-Based Route to Enhanced Coupling in Nanocrystal Solids. *J. Am. Chem. Soc.* **2011**, *133*, 15753–15761.

(20) Koh, W.; Saudari, S. R.; Fafarman, A. T.; Kagan, C. R.; Murray, C. B. Thiocyanate-Capped PbS Nanocubes: Ambipolar Transport Enables Quantum Dot Based Circuits on a Flexible Substrate. *Nano Lett.* **2011**, *11*, 4764–4767.

(21) Zhang, H.; Hu, B.; Sun, L.; Hovden, R.; Wise, F. W.; Muller, D. A.; Robinson, R. D. Surfactant Ligand Removal and Rational Fabrication of Inorganically Connected Quantum Dots. *Nano Lett.* **2011**, *11*, 5356–5361.

(22) Nag, A.; Chung, D. S.; Dolzhnikov, D. S.; Dimitrijevic, N. M.; Chattopadhyay, S.; Shibata, T.; Talapin, D. V. Effect of Metal Ions on Photoluminescence, Charge Transport, Magnetic and Catalytic Properties of All-Inorganic Colloidal Nanocrystals and Nanocrystal Solids. *J. Am. Chem. Soc.* **2012**, *134*, 13604–13615.

(23) Tang, J.; Kemp, K. W.; Hoogland, S.; Jeong, K. S.; Liu, H.; Levina, L.; Furukawa, M.; Wang, X.; Debnath, R.; Cha, D.; et al. Colloidal-Quantum-Dot Photovoltaics Using Atomic-Ligand Passivation. *Nat. Mater.* **2011**, *10*, 765–771.

(24) Zhitomirsky, D.; Furukawa, M.; Tang, J.; Stadler, P.; Hoogland, S.; Voznyy, O.; Liu, H.; Sargent, E. H. N-Type Colloidal-Quantum-Dot Solids for Photovoltaics. *Adv. Mater.* **2012**, *24*, 6181–6185.

(25) Ning, Z.; Ren, Y.; Hoogland, S.; Voznyy, O.; Levina, L.; Stadler, P.; Lan, X.; Zhitomirsky, D.; Sargent, E. H. All-Inorganic Colloidal Quantum Dot Photovoltaics Employing Solution-Phase Halide Passivation. *Adv. Mater.* **2012**, *24*, 6295–6299.

(26) Harpeness, R.; Palchik, O.; Gedanken, A.; Palchik, V.; Amiel, S.; Slifkin, M. A.; Weiss, A. M. Preparation and Characterization of $Ag_2E$ (E = Se, Te) Using the Sonochemically Assisted Polyol Method. *Chem. Mater.* **2002**, *14*, 2094–2102.

(27) Sakuma, T.; Saitoh, S. Structure of α-$Ag_2Te$. *J. Phys. Soc. Jpn.* **1985**, *54*, 3647–3648.

(28) Taylor, P. F.; Wood, C. Thermoelectric Properties of $Ag_2Te$. *J. Appl. Phys.* **1961**, *32*, 1–3.

(29) Wood, C.; Harrap, V.; Kane, W. M. Degeneracy in $Ag_2Te$. *Phys. Rev.* **1961**, *121*, 978–982.

(30) Dalven, R. Fundamental Optical Absorption in B-Silver Telluride. *Phys. Rev. Lett.* **1966**, *16*, 311–312.

(31) Dalven, R.; Gill, R. Electrical Properties of β-$Ag_2Te$ and β-$Ag_2Se$ from 4.2°K to 300°K. *J. Appl. Phys.* **1967**, *38*, 753–756.

(32) Fujikane, M.; Kurosaki, K.; Muta, H.; Yamanaka, S. Electrical Properties of α- and β-$Ag_2Te$. *J. Alloys Compd.* **2005**, *387*, 297–299.

(33) Fujikane, M.; Kurosaki, K.; Muta, H.; Yamanaka, S. Thermoelectric Properties of α- and β-$Ag_2Te$. *J. Alloys Compd.* **2005**, *393*, 299–301.

(34) Schneider, J.; Schulz, H. X-Ray Powder Diffraction of $Ag_2Te$ at Temperatures up to 1123 K. *Z. Für Krist.* **1993**, *203*, 1–15.

(35) Capps, J.; Drymiotis, F.; Lindsey, S.; Tritt, T. M. Significant Enhancement of the Dimensionless Thermoelectric Figure of Merit of the Binary $Ag_2Te$. *Philos. Mag. Lett.* **2010**, *90*, 677–681.

(36) Xiao, C.; Xu, J.; Li, K.; Feng, J.; Yang, J.; Xie, Y. Superionic Phase Transition in Silver Chalcogenide Nanocrystals Realizing Optimized Thermoelectric Performance. *J. Am. Chem. Soc.* **2012**, *134*, 4287–4293.

(37) Bux, S. K.; Fleurial, J.-P.; Kaner, R. B. Nanostructured Materials for Thermoelectric Applications. *Chem. Commun.* **2010**, *46*, 8311.

(38) Vaqueiro, P.; Powell, A. V. Recent Developments in Nanostructured Materials for High-Performance Thermoelectrics. *J. Mater. Chem.* **2010**, *20*, 9577.

(39) Shakouri, A. Recent Developments in Semiconductor Thermoelectric Physics and Materials. *Annu. Rev. Mater. Res.* **2011**, *41*, 399–431.

(40) Rowe, D. M. *Thermoelectrics Handbook: Macro to Nano*; CRC Press INC, 2006.

(41) Nielsch, K.; Bachmann, J.; Kimling, J.; Böttner, H. Thermoelectric Nanostructures: From Physical Model Systems towards Nanograined Composites. *Adv. Energy Mater.* **2011**, *1*, 713–731.

(42) Kanatzidis, M. G. Nanostructured Thermoelectrics: The New Paradigm? *Chem. Mater.* **2010**, *22*, 648–659.

(43) Zebarjadi, M.; Esfarjani, K.; Dresselhaus, M. S.; Ren, Z. F.; Chen, G. Perspectives on Thermoelectrics: From Fundamentals to Device Applications. *Energy Environ. Sci.* **2012**, *5*, 5147.

(44) Vineis, C. J.; Shakouri, A.; Majumdar, A.; Kanatzidis, M. G. Nanostructured Thermoelectrics: Big Efficiency Gains from Small Features. *Adv. Mater.* **2010**, *22*, 3970–3980.

(45) Ibáñez, M.; Zamani, R.; LaLonde, A.; Cadavid, D.; Li, W.; Shavel, A.; Arbiol, J.; Morante, J. R.; Gorsse, S.; Snyder, G. J.; et al. $Cu_2ZnGeSe_4$ Nanocrystals: Synthesis and Thermoelectric Properties. *J Am Chem Soc* **2012**, *134*, 4060–4063.

(46) Zhao, Y.; Dyck, J. S.; Burda, C. Toward High-Performance Nanostructured Thermoelectric Materials: The Progress of Bottom-up Solution Chemistry Approaches. *J. Mater. Chem.* **2011**, *21*, 17049.

(47) Ibáñez, M.; Cadavid, D.; Tamburini, U. A.; Zamani, R.; Gorsse, S.; Li, W.; Shavel, A.; López, A. M.; Morante, J. R.; Arbiol, J.; et al. Colloidal Synthesis and Thermoelectric Properties of $Cu_2SnSe_3$ Nanocrystals. *J. Mater. Chem. A* **2012**.

(48) Ibáñez, M.; Zamani, R.; Li, W.; Cadavid, D.; Gorsse, S.; Katcho, N. A.; Shavel, A.; López, A. M.; Morante, J. R.; Arbiol, J.; et al. Crystallographic Control at the Nanoscale to Enhance Functionality: Polytypic $Cu_2GeSe_3$ Nanoparticles as Thermoelectric Materials. *Chem. Mater.* **2012**.

(49) Cadavid, D.; Ibáñez, M.; Gorsse, S.; López, A. M.; Cirera, A.; Morante, J. R.; Cabot, A. Bottom-up Processing of Thermoelectric Nanocomposites from Colloidal Nanocrystal Building Blocks: The Case of $Ag_2Te$–PbTe. *J. Nanoparticle Res.* **2012**, *14*, 1–10.

(50) Cadavid, D.; Ibáñez, M.; Shavel, A.; Durá, O. J.; Torre, M. A. L. de la; Cabot, A. Organic Ligand Displacement by Metal Salts

to Enhance Nanoparticle Functionality: Thermoelectric Properties of Ag2Te. *J. Mater. Chem. A* **2013**, *1*, 4864–4870.

(51) Ko, D.-K.; Urban, J. J.; Murray, C. B. Carrier Distribution and Dynamics of Nanocrystal Solids Doped with Artificial Atoms. *Nano Lett* **2010**, *10*, 1842–1847.

(52) Capps, J.; Ma, B.; Drye, T.; Nucklos, C.; Lindsey, S.; Rhodes, D.; Zhang, Q.; Modic, K.; Cawthorne, S.; Drymiotis, F. The Effect of Ag Concentration on the Structural, Electrical and Thermal Transport Behavior of Pb:Te:Ag:Se Mixtures and Improvement of Thermoelectric Performance via Cu Doping. *J. Alloys Compd.* **2011**, *509*, 1544–1549.

# Chapter 5 Surface ligand influence on PbSe thermoelectric properties

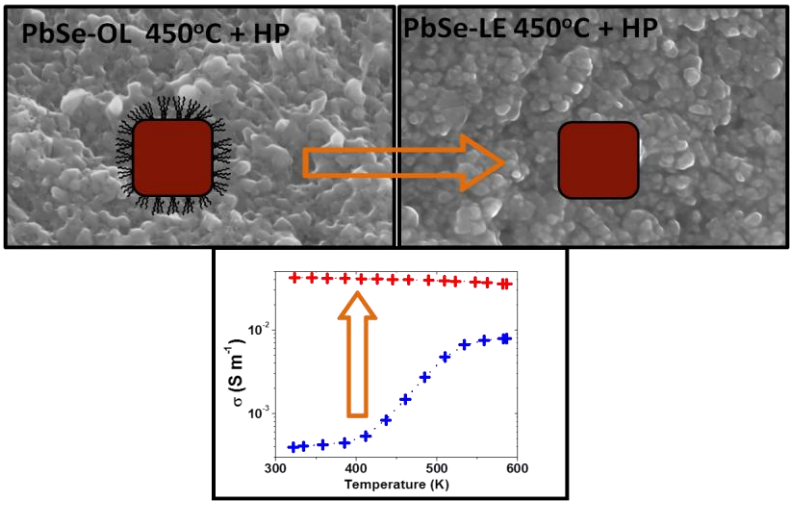


## 5.1 Introduction

The use of colloidal nanocrystals (NCs), with controlled size, shape, crystallographic phase and composition, as building blocks to

produce bulk nanomaterials provides a wide range of tunable parameters to engineer nanomaterials with precisely controlled functional properties.[1,2] Moreover, solution processing methods not only provide the means to produce metamaterials by design, but also allows their production in a cost-effective manner. Therefore recently, there has been a great effort to develop efficient solution processed electronic and optoelectronic devices.

However, as was discussed in the last chapter, one first main issue that strongly limits the performance of bottom-up assembled nanostructured materials in fields such as electronics, optoelectronics, catalysis, and thermoelectricity are the electrically insulating organic molecules used during NCs synthesis. The organic ligands (OL) introduced to control NCs growth usually contain long hydrocarbon chains that block charge transport, injection and extraction between NCs and between the NCs and the media. Since, the charge transportation is dominated by the interparticle media, several compounds have been proposed to displaced or replaced such OL: pyridine,[3] metal chalcogenides complexes (MCC) stabilized by hydrazine,[4–8] nitrosonium, diazonium[9] and trialkyl oxonium tetrafluoroborates;[10] tetrafluoroborate acids ($HBF_4$, $HPF_6$),[11] ammonium thiocianate ($NH_4SCN$),[12,13] sulphides such as $Na_2S$, $NH_4S$, and $K_2S$,[11,14,15] or halide anions like $Cl^-$, $Br^-$ and $I^-$.[16–18] In spite of these different possibilities, the obtaining of bare NCs remains challenging due to different aspects as the toxicity of the ligands that have been used in the organic ligand removal/exchange, e.g. hydrazine, and their composition and reactivity, which may modify the properties of the final nanomaterial, among others.

A second main challenge is the adjustment of the charge carrier concentration in bulk nanomaterials obtained from the bottom-up assembly of colloidal NCs. The main limitation is the difficult introduction of controlled small amounts of external elements within the NCs lattice. Multi-valence ternary and quaternary NCs offer a simple solution to tune charge carrier concentration by controlling the ratio of the different elements.[19–24] Even in this case, the control

of the composition at the required precision level is not as trivial as to mix the proper amounts of precursors, since nucleation and growth kinetics play a key role in controlling the final NCs composition. Furthermore, even in nominally stoichiometric and pure semiconducting nanomaterials, large charge carrier concentrations may exist. They provide from uncontrolled surface donor and acceptor states, which make the charge carrier concentration strongly dependent on the surface composition. Notice in this regard that 10 nm NCs contain on the order of $10^{20} – 10^{21}$ $cm^{-3}$ not fully coordinated surface atoms, thus $10^{20} – 10^{21}$ $cm^{-3}$ potential donor or acceptor states. Therefore the control of the surface composition is crucial to tune the charge carrier concentration of the bulk nanomaterial. Thus, ligand exchange processes are a potentially interesting strategy to control the charge carrier concentration. Such strategy has been scarcely explored in part due to the critical need for reliable models able to extract consistent conclusions from charge transport measurements in nanocrystalline materials.

Lead chalcogenides have demonstrated superior thermoelectric properties and specially PbSe has attract attention recently due to the higher abundance of Se in comparison with Te[25,26], also high ZT values have been reported recently for PbSe bulk materials (ZT ~ 1.3 for PbSe:Al at 850 K, ~1.2 for $Pb_{1-x}Na_xSe$ at 850 K )[27,28] and theoretical predictions of heavy doped PbSe have shown that ZT values around 2 (at 1000 K) are possible,[29] provide motivation to continue study this system.

We present here a simple procedure to displace the surface OL from PbSe NCs, using a sodium salt, to produce PbSe bulk nanomaterials. We demonstrate the influence of the ligand exchange procedure on the transport properties of the nanomaterial, reporting an enhanced of the electrical conductivity, as well as an increasing in the carrier concentration at room temperature which leads a doped nanomaterial. We further support our conclusions on a charge transport model used to fit the obtained Seebeck and electrical conductivity data and to discern between the influence of the NCs surface barriers and the introduced doping.

## 5.2 Experimental details

### 5.2.1 Materials

Selenium pieces (99.999 %), lead (II) oxide (99.9%) and lead acetate trihydrate (99.999 %), 1-octadecene (ODE, technical grade 90 %), oleic acid (OA, technical grade 90 %), lead nitrate (99.0 %), Sodium amide (95 %), anhydrous methanol, anhydrous chloroform and formamide (FA, ≥99.5 %) were purchased from Aldrich. Triocthiylphosphine (OL, 97 %) were purchased from Strem. Analytical grade ethanol, hexane and chloroform were purchase from Panreac. All chemicals were used without further purification. Stock solution of OL-Se (1 M) was prepared dissolving 7.89 g of selenium pieces in 100 ml of OL. All nanocrystal preparations were carried out using standard airless techniques: a vacuum/dry Ar Schlenk line was used for the synthesis and an Ar-filled glovebox for storing and handling air- and moisture-sensitive chemicals.

### 5.2.2 PbSe nanoparticles

A modified approach of that used by Murphy et al.[30] was used to synthesize PbSe NCs. In a typical procedure, 4 mmol (0.89 g) of lead oxide was dissolved in ODE (11.8 g) along with OA (3.1 g). The mixture was heated up to 100 $^{o}$C under vacuum for 1.5 H. Afterwards, the solution was flushed with Ar and temperature was raised up to 190 $^{o}$C. At this temperature, 6 ml of OL-Se stock solution was quickly injected. After injection, the reaction temperature was maintained between 170 $^{o}$C and 180 $^{o}$C for 4 minutes. Then the reaction solution was cooled using a water bath. PbSe NCs were precipitated and redispersed using ethanol and hexane several times. Finally, the NCs were dispersed in chloroform and stored in the glovebox.

### 5.2.3 Organic ligand displacement

PbSe NCs (250 mg) were dispersed in 10 ml of chloroform and mixed at room temperature with 10 ml of $NaNH_2$ solution (0.01 M) in methanol. The solution was shacked to displace the OL attached to the NCs surface during 1-2 minute approximately. Afterward, the NCs were precipitated by centrifugation. NCs were thoroughly purified using chloroform/methanol to remove the remaining organic species. Finally, PbSe NCs were precipitated and dried under vacuum or redispersed in polar solvents like FA, DMF or ethanol for further analysis. To avoid the oxidation of the chalcogenide NCs, the OL replacement was conducted inside the glove-box, under Ar atmosphere.

### 5.2.4 PbSe bulk nanomaterial

To produce PbSe bulk nanostructured materials, NCs were dried under vacuum, annealed at 450 $^{o}$C for 1 h and compacted at 350 $^{o}$C for 2 minutes into disk-shaped pellets of 10 mm of diameter and 1 mm of thickness under 4 MPa of pressure. A custom-made hot-press (HP) equipment[31], with an induction heater coupled to a hydraulic press, was used for pellet preparation. The system was operated under Ar using a graphite die. Pellets with relative densities over 90 % were produced.

## 5.3 Results

### 5.3.1 PbSe OL

Cubic PbSe NC building blocks were synthesized by reacting PbO dissolved in ODE and OA with TOP-Se at 180 ºC for 4 minutes (Figure 5.1). We will refer to these initial NCs as PbSe-OL. They

had an average size of 16 ± 2 nm with a ~10 % size dispersion as shown in the size distribution histogram displayed as an inset in figure 1. Their crystallographic phase was identified as face centered cubic (JCPDS 1-78-1903) from the XRD pattern (Figure 5.2).

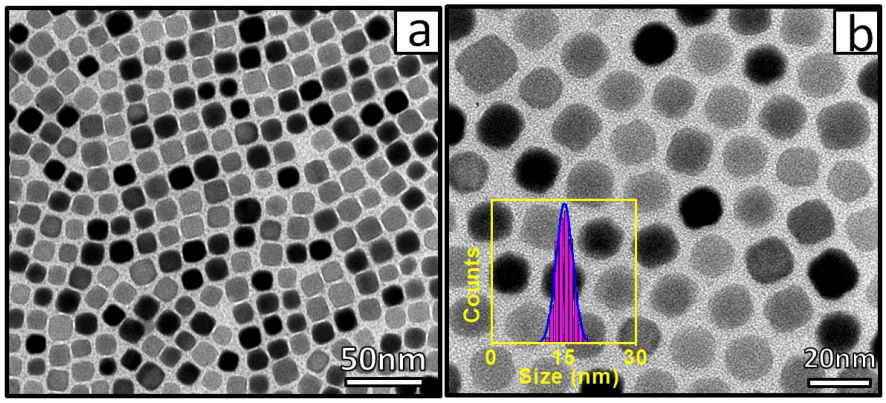


**Figure 5.1** TEM micrographs of the 16±2 nm cubic PbSe NCs used as building blocks to produce bulk nanocrystalline PbSe. Inset shows a histogram of the particle size distribution

Significant amount of OL, used to control the PbSe NCs growth in solution, remained attached to the PbSe surface even after multiple purification steps. The amount of OL in the final PbSe NCs was ~6 % of the total mass as measured by NMR and TGA analysis (Figure 5.3).

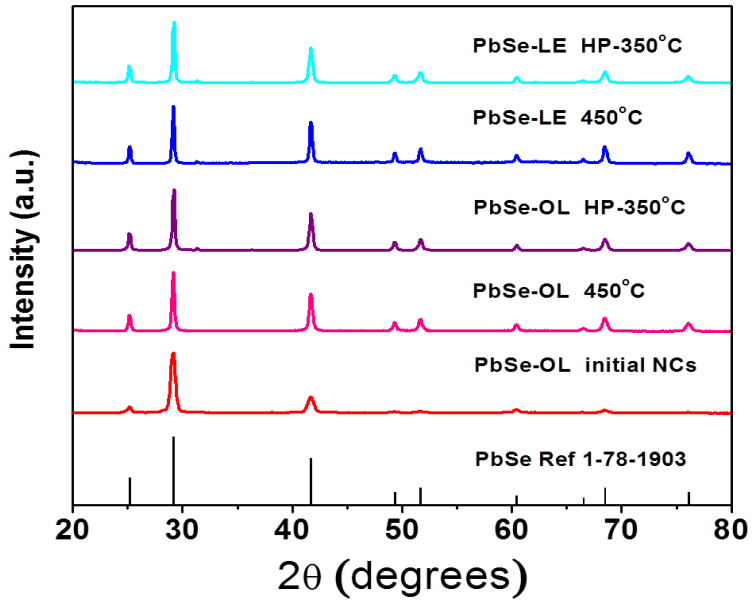


**Figure 5.2** XRD patterns of PbSe initial nanocrystals (PbSe-OL), the nanocomposites after OL replacement (PbSe-LE) and heat treatment, and the final samples after densification with HP

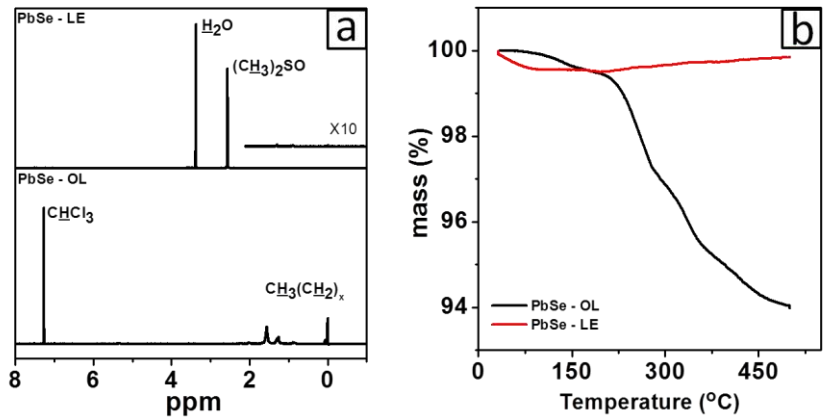


**Figure 5.3** (a) $^{1}$H NMR spectra and (b) TGA profile of PbSe NCs before and after OL replacement.

To produce bulk nanostructured PbSe, ~1 g of PbSe-OL NCs were thoroughly cleaned, dried and annealed at 450 $^{o}$C for 1h in an argon atmosphere. The annealed material was afterwards compacted at 350 $^{o}$C under 40 MPa of pressure using a hot press. The final pellet obtained from PbSe-OL NCS, and thus we will name also PbSe-OL, had relative densities close to 90 %. Figure 5.4 shows representative SEM micrographs of the initial PbSe-OL NCs, the PbSe-OL powder after the heat treatment at 450 $^{o}$C and the PbSe-OL pellet after hot press at 350 $^{o}$C.

During the thermal treatment at 450 ºC, the average crystal domain size increased from the initial 16 ± 2 nm to ~ 20 nm as determined from the fitting of the XRD pattern. An additional growth of the crystal domains was obtained during the hot press, from ~ 20 nm to ~ 25 nm. After the two heat treatments, the PbSe cubic crystallographic phase was preserved, but small peaks corresponding to PbO appeared. This is consistent with a slight reduction of the Se content, Pb/Se~1.10 observed from ICP chemical analysis after hot-press. The annealing treatment in an inert atmosphere also entailed the decomposition of the organics initially present at the NCs surface, mainly TOP. However, relatively large amounts of carbon were left behind after the OL decomposition. Elemental analysis allowed us to quantify the amount of carbon left within the nanocrystalline material at about 2 %.

Figure 5.5a-b display the electrical conductivity ($\sigma$) and Seebeck coefficient (S) obtained from the nanocrystalline PbSe-OL pellet in the temperature range from 300 K to 600 K. The temperature evolution of the electrical conductivity of PbSe-OL displayed a step increase in the temperature range from 420 to 520 K, which denoted the thermal activation of a large concentration of charge carriers.

This step change in the electrical conductivity was accompanied by a parallel step variation and a sign inversion of the Seebeck coefficient, from positive to negative values, which points towards the thermal activation of negative charge carriers. The Seebeck coefficient of the PbSe-OL pellet monotonously decreased with

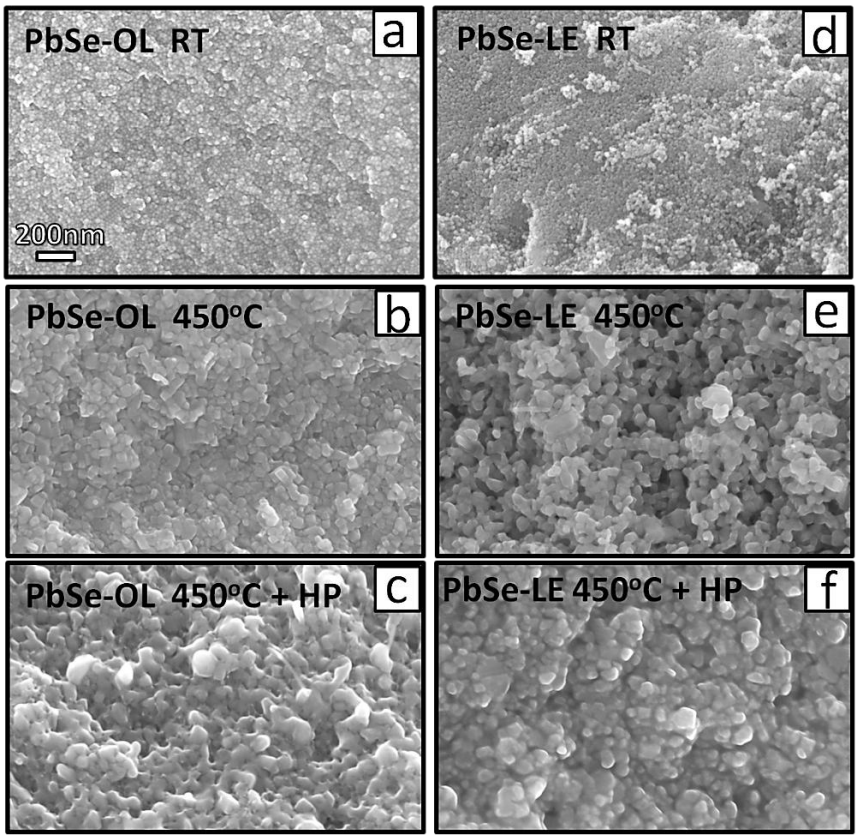


**Figure 5.4** (a) SEM micrographs of the initial PbSe-OL NCs at room temperature. (b) PbSe-OL NCs after heat treatment at 450°C with an average size of 20±2 nm and (c) PbSe-OL NCs after hot-press at 350 °C for 2 min, with an average size of 25±2 nm. (d) PbSe NCs after OL replacement at room temperature. (e) PbSe-LE NCs after heat treatment at 450 °C with an average size of 30±4 nm and (f) PbSe-LE NCs after hot-press at 350 °C for 2 min, with an average size of 35±4 nm.

temperature, changing sign at around 400 K, and reaching values below -200 μV/K at 600 K.

The electrical conductivity of the PbSe-OL pellet was relatively low, in the range $10^2$-$10^3$ S $m^{-1}$. This low electrical conductivities strongly reduced the overall power factor of the material and makes such bottom-up processed nanocrystalline materials useless for

practical applications. We associate these low electrical conductivities to the large concentration of interfaces in the nanocrystalline material, which limit the charge carrier mobility. The carbon present from the TOP decomposition at may further enhance charge carrier scattering. At the same time, note that no doping was intentionally introduced in these materials to increase the electrical conductivity. In this regard, Na and Ag are two main p-type dopants and Sb, Bi or Al n-type dopants in PbSe and PbTe. However, our efforts to introduce these elements during the colloidal synthesis have been so far unsuccessful.

We decided to test $NaNH_2$ as a ligand exchange agent to kill two birds with one stone; to get rid of the OL before decomposition, which may help to increase the charge carrier mobility, and to introduce controlled amounts of Na, which would allow us to tune the charge carrier concentration.

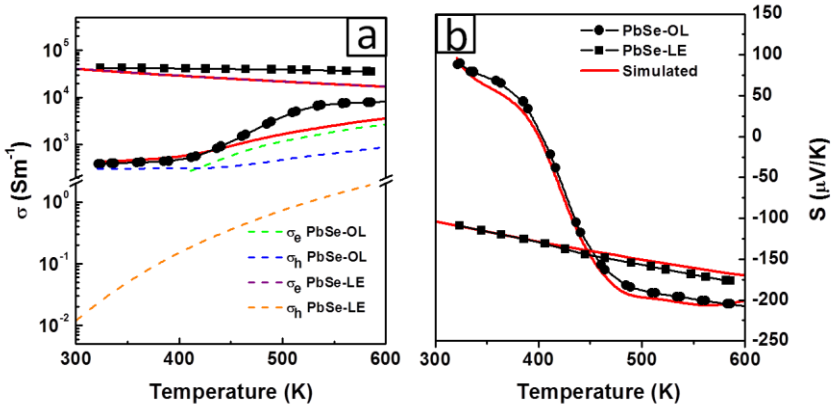


**Figure 5.5** (a) Electrical conductivity and (b) Seebeck coefficient as a function of temperature for the PbSe-OL NCs (black circles) and PbSe-LE NCs (black squares) and the calculated values from the model describe below (red continuous line). For the PbSe-OL is also shown the contribution of phonon and electron conductivity (dashed lines).

### 5.3.2 PbSe-LE

$NaNH_2$ was used to displace TOP from the PbSe-OL NCs surface by means of the procedure detailed in the experimental section. Briefly, PbSe-OL NCs dispersed in chloroform were mixed with a $NaNH_2$ solution in methanol. The resulting mixture was vigorously shaken at room temperature for few minutes. Through this very simple process, TOP was displaced from the PbSe-OL NCs surface and charge stabilized PbSe NCs, which we name PbSe-LE, moved from the chloroform to the methanol phase. PbSe- LE NCs preserved their shape and size and were relatively soluble in polar solvents like FA, DMF or alcohols for a limited amount of time. PbSe- LE NCs were washed with chloroform to remove the remaining organic species and they were finally precipitated and dried under vacuum to obtain a nanocrystaline powder. All this process was carried out inside and Ar-filled glove-box to avoid the NC surface oxidation.

$^1$H-NMR spectroscopy allowed us to follow the OL replacement procedure (Figure 5.3). $^1$H-NMR spectrum of PbSe-OL NCs in chloroform displayed the characteristic $CH_3(CH_2)_7$ bands from TOP. Such TOP fingerprint vanished from the 1H-NMR spectrum of PbSe- LE NCs in DMSO, where only the peaks associated to the DMSO and residual water were observed. While a previous work identified $NH_2^-$ as the surface ligand remaining at the surface of CdSe NCs,[11] we did not find the $NH_2^-$ fingerprints in the PbSe- LE 1H-NMR spectrum. Nevertheless, this does not rule out this ligand as the one replacing TOP on the NCs surface and rendering them soluble in polar media. While the ligand exchange procedure was carried out in a glove-box, for NMR characterization the powder was exposed to air, which may have modified the NCs surface, especially taking into account the high reactivity of the amide group.

The thermogravimetric profile of purified and dried PbSe-LE NCs showed a 0.5 % relative mass loss at relatively low temperatures, 20-105 $^o$C, which may be associated to the decomposition of $NH_2$ or the evaporation of residual DMSO. Above 100 $^o$C, within our TGA system, the PbSe-LE mass slightly increased due to a slight

oxidation of the material with residual amounts of oxygen in the used nitrogen atmosphere (Figure 5.3b). Elemental analysis of the final PbSe-LE nanocrystalline powder showed residual carbon to be within the limit of detection of our system, ~0.1 %. Further EDX and ICP analysis of PbSe-LE showed no evidence of the presence of Na in the PbSe-LE nanopowder obtained from drying the PbSe- LE NCs in vacuum.

Bulk nanostructured PbSe- LE with relative densities above 90 % were obtained by pressing at 350 ºC ~1 g of PbSe- LE NCs pre-annealed at 450 $^{o}$C for 1h in an argon atmosphere. Figure 5.4 shows representative SEM micrographs of the PbSe- LE NCs before and after the heat treatment at 450 $^{o}$C and the hot press at 350 $^{o}$C. During the thermal treatment, the average size of the PbSe- LE crystal domains increased from the initial 16 ± 2 nm to ~ 30 nm and they further grew during the hot press, up to ~ 35 nm.

Notice that the removal of TOP and therefore of the residual carbon left after its decomposition, resulted in larger NC growth rates during the annealing. Thus it is evident that the presence of the OL blocked the atomic diffusion and reorganization to form larger crystal domains.

Like in the case of PbSe-OL, for PbSe- LE the Se content was slightly reduced with the thermal treatments, being the final Pb/Se ration ~1.10, as obtained by ICP analysis.

The OL removal helped to increase the materials electrical conductivity. Overall, significantly higher electrical conductivities were obtained from PbSe- LE ($4x10^{4}$ $Sm^{-1}$), than for PbSe-OL ($4x10^{2}$ - $8x10^{3}$ $Sm^{-1}$). The electrical conductivity of PbSe- LE slightly decreased with temperature as it corresponds to a degenerated semiconductor. On the other hand, negative Seebeck coefficients were measured for the entire temperature range tested and its absolute value increased monotonically with temperature from 100 to 180 μV/K.

Room temperature measurements of the Hall charge carrier concentration and mobility confirmed the different sign of the majority charge carriers for PbSe-OL and PbSe- LE. However, the same order of magnitude, $10^{19}$, was obtained for the charge carrier concentration in the two nanocrystalline materials: $n_h = 1.0x10^{19}$ $cm^{-3}$ for PbSe-OL and $n_e = 3.7x10^{19}$ $cm^{-3}$ for PbSe- LE. This very large and similar charge carrier concentration translated in relatively low charge carrier mobilities for PbSe-OL, $\mu_h$~2.5 $cm^2 V^{-1} s^{-1}$ and slightly larger for PbSe- LE, $\mu_e$ ~ 71 $cm^2 V^{-1} s^{-1}$. The high charge carrier concentrations obtained for PbSe-OL, with no intentional external doping, as well as its p-type character at room temperature were associated to the presence of surface acceptor states having their origin in uncoordinated or oxidized Se atoms. On the other hand, $NaNH_2$ acted as a reducing agent, introducing donor states in the NC surfaces. XPS analysis confirmed the presence of a larger concentration of more electronegative Pb atoms at the PbSe-OL surface when compared with that of the PbSe-LE.

OLs not only block the crystal domain growth and the charge carrier transport, but also the phonon propagation. Figure 5.6a displays the temperature evolution of the thermal conductivity ($\kappa$) in the temperature range 300-600 K, for both, PbSe-OL and PbSe- LE. In both materials, the thermal conductivity monotonously decreases with temperature. PbSe-OL was characterized by 2-3 fold lower thermal conductivities than PbSe- LE. These lower thermal conductivities are related to several factors: i) the residual carbon present in the nanocrystalline PbSe-OL may introduce additional phonon scattering; ii) the larger interface density of PbSe-OL associated with its smaller crystal domains also drives towards reducing thermal conductivity; iii) the more continuous crystal surface in PbSe-f will scatter phonons less effectively.

The thermoelectric figure of merit Figure 5.6b, $ZT=TS^2\sigma/\kappa$, increased with temperature for both materials, reaching values up to 0.5 and 0.6 for PbSe-OL and PbSe- LE, respectively. These values are significantly higher than those obtained for undoped bulk PbSe

and are comparable with those obtained from bulk PbSe doped with Ag or Na at 600 K.[28,32]

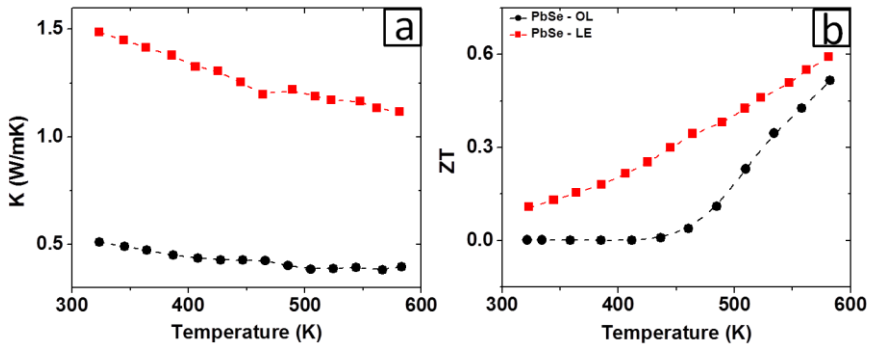


**Figure 5.6** (a) Thermal conductivity and (b) figure of merit ZT as a function of temperature for nanocrystalline PbSe-OL and PbSe-LE.

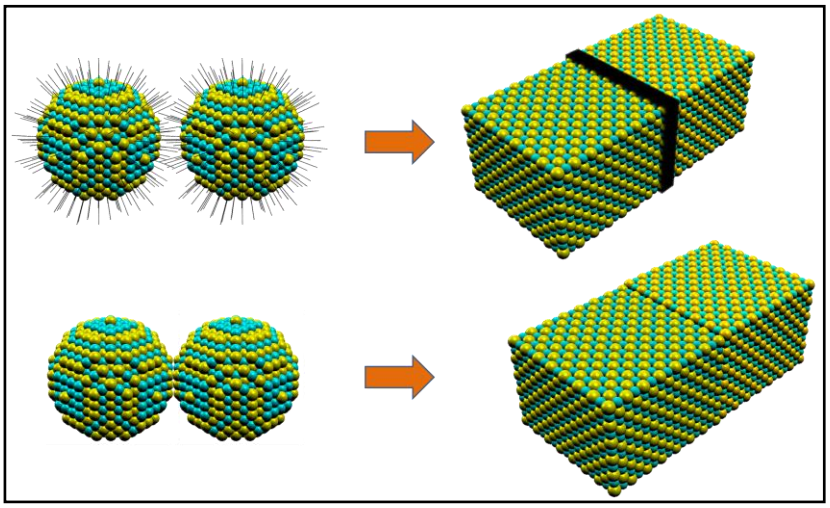

**Figure 5.7** Schemes of the NCs differences with and without OL.

## 5.4 Discussion

### 5.4.1 Charge transport model

Because of its high density, interfaces have a great impact over the electronic transport of nanocrystalline materials, both because grain-boundary potential barrier scattering is one of the main parameters controlling charge carriers mobility,[33] and because interfaces accumulate large densities of acceptor or donor states.[34]

To further expose the role of crystal barriers and the different charge carrier types, we developed a model using the standard Boltzmann transport equation[35] with the relaxation time approximation (RTA). In the RTA, the different transport coefficients, i.e., electrical conductivity and Seebeck coefficient at zero electric field can be obtained. The model considers electrical carriers in two bands with the Kane model. Assuming that the scattering events are independent with each other, the Mathiessen's sum rule can be used

$$\frac{1}{\tau_{tot}^{i}} = \frac{1}{\tau_a} + \frac{1}{\tau_o} + \frac{1}{\tau_{po}} + \frac{1}{\tau_b}, \qquad (5.1)$$

where $\tau_{tot}^{i}$ is the total relaxation time, and the $\tau_a$, $\tau_o$, $\tau_{po}$ are the acoustic phonons, the optical phonons, the polar optical phonons, and the barrier scattering relaxation times, respectively. Here, i=(e,h) represents the electrons (e) and holes (h). The expressions for the different scattering mechanism within the Kane model were presented in previous works for different authors.[36-38]

In narrow bang-gap semiconductors the dependence of the energy on crystal momentum deviates from the quadratic dependence. The effective mass reflects this non-parabolic trend being energy dependent. In the Kane model[39] the energy dispersion is given by

$$\varepsilon_{\vec{k}}(1+\frac{\varepsilon_{\vec{k}}}{E_g})=\frac{\hbar^2}{2}(\frac{2k_t^2}{m_t}+\frac{k_l^2}{m_l}), \quad (5.2)$$

Where $E_g$ is the band gap, $\hbar$ is the Plank constant, $m_l$ and $m_t$ are the longitudinal and transversal effective mass, respectively. The temperature dependence of the band gap $E_g(T)$ has been included assuming a linear dependence[40,41] and the density of states and electron/hole velocity were assumed to be similar to that reported before.[40,42,43] Therefore, the total conductivity and the Seebeck coefficient can be expressed as:

$$\sigma=\sigma_n+\sigma_p, \quad (5.3)$$

$$S=\frac{\sigma_n S_n+\sigma_p S_p}{\sigma}, \quad (5.4)$$

Where $\sigma_i$ and $S_i$ is given by

$$\sigma_i=e^2\int_0^\infty d\varepsilon(-\frac{\partial f_i}{\partial\varepsilon})\sum_i(\varepsilon,T) \quad (5.5)$$

$$S_i=\frac{e}{T\sigma_i}\int_0^\infty d\varepsilon(-\frac{\partial f_i}{\partial\varepsilon})\sum_i(\varepsilon,T)(\varepsilon-\mu)^2 \quad (5.6)$$

$$\sum_i=\frac{2}{3}\gamma_i\frac{(2m_i)^{1/2}}{\pi^2\hbar^3}\left[\varepsilon(1+\frac{\varepsilon}{E_g})^{3/2}(1+\frac{2\varepsilon}{E_g})^{-1}\right]\tau_i(\varepsilon,T) \quad (5.7)$$

Where $\gamma_i$ is the degeneracy of the conduction and valence band (i = e, h), $\mu$ is the position of the chemical potential, $\tau_i$ is the total scattering rate, e is the carrier charge and $m_i$ is the effective mass for each band defined by $m_i=(m_l m_t^2)^{1/3}$. $f_i$ is the equilibrium Fermi

distribution function at temperature $T$ and chemical potential $\mu$. The temperature dependence of the transport coefficients (σ and S, in this case) has its origin in the temperature dependence of the parameters described above, it was also included the effective mass temperature dependence.

The concentration of carriers, electrons and holes, for the Kane model is given by

$$n, p = \frac{\sqrt{2}}{\pi^2 \hbar^3} \gamma m^{3/2} \int_0^\infty d\varepsilon \frac{\left[\varepsilon(1 + \frac{\varepsilon}{E_g})\right]^{1/2} (1 + \frac{2\varepsilon}{E_g})}{\exp\left(\frac{\varepsilon - \mu}{k_B T}\right) + 1} \quad (5.8)$$

Here $k_B$ is the Boltzmann constant. The position of the chemical potential is obtained solving numerically the neutrality equation, taking into account the acceptor/donor doping concentration ($N_a$ and $N_d$)

$$n = p + N_d^+ \text{ for n-type} \quad (5.9)$$

$$p = n + N_a^- \text{ for p-type} \quad (5.10)$$

The chemical potential is temperature dependent and also depends on the doping concentration.For thermoelectric bulk materials, the most relevant scattering mechanisms are the acoustic and optical phonons and polar optical phonons. However, for nanostructured materials an additional scattering mechanism from the grain interfaces has to be included. As proposed by other authors,[43] [44] the grain interfaces in the material are modelled as a rectangular potential barrier. The carriers transmit through the potential barrier of the interfaces one by one with transmission probability P and the scattering time is

$$\tau_b(\varepsilon) = \frac{1}{v}\frac{P(\varepsilon)L}{1-P(\varepsilon)}, \qquad (5.11)$$

where

$$P(\varepsilon) = \begin{cases} \left[1 + \dfrac{E_b \sinh^2\left[\sqrt{\dfrac{2mE_b w^2}{\hbar^2}(1-\dfrac{\varepsilon}{E_b})}\right]}{4\varepsilon(1-\dfrac{\varepsilon}{E_b})}\right]^{-1} ; \varepsilon < E_b \\ \left[1 + \dfrac{E_b \sin^2\left[\sqrt{\dfrac{2mE_b w^2}{\hbar^2}(\dfrac{\varepsilon}{E_b}-1)}\right]}{4\varepsilon(\dfrac{\varepsilon}{E_b}-1)}\right]^{-1} ; \varepsilon > E_b \end{cases} . \qquad (5.12)$$

The probability term takes into account the barrier height $E_b$ and the barrier width $w$. $L$ is the grain mean size and $v$ is the average velocity of the carriers defined by

$$v = \sqrt{\frac{2\varepsilon(1+\varepsilon/E_g)}{m(1+2\varepsilon/E_g)^2}} \qquad (5.13)$$

.

Regarding the scattering times, the used parameters are summarized Table 5.1. The temperature dependence of the band gap $E_g$ can be approximately given by

$$E_g(T) = 0.16 + (0.51x10^{-3})T, \qquad (5.14)$$

this dependence has been fitted from the linear part of the data presented by M. Baleva et al.[41]

**Table 5.1** Parameters used to calculate the different relaxation times for both PbSe-OL and PbSe-$NH_2^-$ nanocrystalline samples. The values used for the acoustic deformation potential $E_{ac}$ and the optical deformation potential $E_{oc}$ have a strong dependence with the concentration and nature of the doping of the sample and are in the range measured by A. Popescu, et al.[45] and Zhou et al.[46]

| Parameter | Value |
|---|---|
| $\varepsilon_0$ | 204 [38] |
| $\varepsilon_\infty$ | 25 [38] |
| $C_l$ | 0.15E11 [40] $N/m^2$ |
| $\hbar\omega_0$ | 16.7 [38] $meV$ |
| $a$ | 6.12 [39] $\text{Å}$ |
| $\rho$ | 8270 [38] $Kg/m^3$ |
| $E_{ac}$ | 15 $eV$ |
| $E_{oc}$ | 15 $eV$ |
| $K_a = K_o$ for n-type | 1.0 |
| $K_a = K_o$ for p-type | 1.5 |

The electrical conductivity and the Seebeck coefficient were calculated using the previous two band model in the temperature range from 300 K to 600 K (solid line Figure 5.5a-b). Specifically we adjusted the effective masses and the parameters that describe the interface scattering while the parameters associated to the other scattering processes remains without changes. This means that the

variations in the internal structure are considered within the effective mass and the effect of the OL displacement that affect the surface of the NCs change the interface scattering parameters.

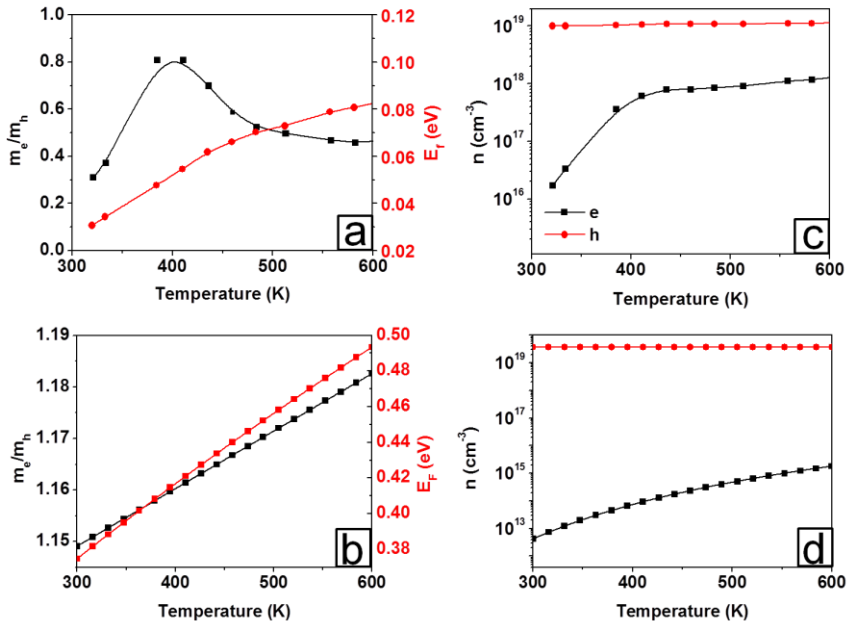


**Figure 5.7** (a-b) Electron/hole effective masses ratio (black square) as a function of the temperature, and evolution of the Fermi level position (red circles) for the nanocrystalline PbSe-OL and PbSe-LE. Note the slightly degenerate (~$3K_BT$) behavior of the sample. (b-c) Evolution of the carrier concentration as a function of the temperature for the nanocrystalline PbSe-OL and PbSe-LE. In PbSe-OL the holes concentration remains constant, while the electron concentration increases with the temperature. We have used $\gamma_e$=4 and $\gamma_h$=3.

For PbSe-OL ($n_h$ = *1.0x10$^{19}$ cm$^{-3}$*), as it was pointed out before the electrical conductivity increases with the temperature with a step form, and this is accompany for the inversion of sign in the Seebeck coefficient, therefore the two band model is suitable to simulate this change in the majority charge carriers due to the energy activation process. The first analysis has been done adjusting the interface scattering parameters, and after this preliminary adjust, the effective electron and hole masses have been fitted to reproduce the experimental data for each temperature point. Since, in this case, the

two carriers play an important role, we considerer two different energy barriers. $E_{be} = 0.01\ eV$ and $E_{bh} = 0.45\ eV$ for electrons and holes, respectively, and $w = 1.1\ nm$, $L = 26\ nm$. The difference in the barrier height for each carrier comes from the difference conduction/valence band offset between the NCs and the surrounding material. The Figure 5.7b shows the charge carrier concentration estimated for the temperature range from *300 K* to *600 K*.

It is possible to separate the electrical conductivity in three different regions, from *300 K* to *425 K*, *425 K* to *525 K* and *525 K* to *600 K*. Figure 5.7a shows the calculated ratio between the effective masses of the charge carriers and the evolution of the Fermi energy as a function of temperature. In the low temperature region, this doping concentration shows a slightly degenerate semiconductor (Figure 5.7c), the unusual slightly increase in σ, can be explained by the increases in the electron concentration, additionally its contribution to σ is in the same order as the hole contribution. However, the holes concentration is several order of magnitudes larger than the electron concentration, therefore a major hole contribution to the electrical conductivity should be expected. This means that holes scattering processes diminish its conductivity. We include different electron/hole barrier height, being $E_{bh} >> E_{be}$. Also, the effective masses of the carriers affect their conductivity. In the intermediate temperature region, the conductivity highly increases, due to the increases of the electron concentration, as well as its contribution to σ. Since the electron barrier height is lower than the holes barrier the electron conductivity becomes the dominant term of the total σ. The holes concentration remains constant but the changes in the holes effective mass leads a increases in the holes conductivity with the temperature. Finally in the high temperature region, the pure electron conductivity dominates and the electrical conductivity slightly increases.

The PbSe-LE nanocrystalline sample ($n_e$ = $3.7x10^{19}\ cm^{-3}$) shows a degenerated semiconductor behavior, and in this case the electronic

transport is dominated only by the electrons as the majority charge carriers. From experimental data the effectives masses fitted are $me/m0 = 0.2 + 2 \times 10^{-5} T$ with degeneracy $\gamma_e = 3$ for electron, $mh/m0 = 0.148$ and $\gamma_e = 3$ for holes. To describe the interface scattering we use a potential barrier $E_b = 0.15\ eV$, the barrier width of $w = 1\ nm$ and the grain size $L = 35\ nm$ (value extracted from the XRD analysis). The theoretical model overestimates the scattering effects resulting in smaller values for electrical conductivity. However, for the Seebeck coefficient the simulated values matches well with the experimental values.

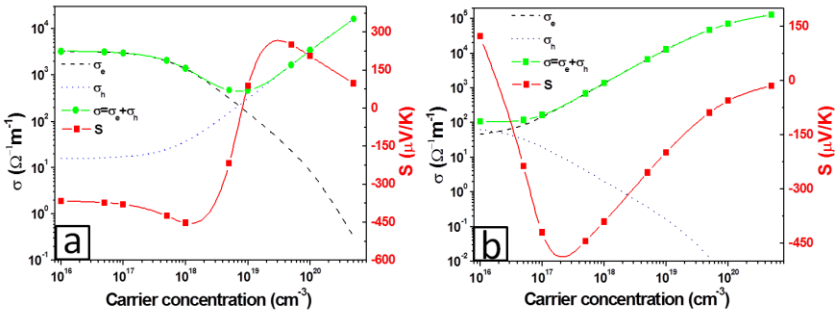


**Figure 5.8** (a) Evolution of the electron/hole conductivity, the total conductivity and (b) the Seebeck coefficient for nanocrystalline PbSe-OL and PbSe-LE, as a function of the carrier concentration at T=321K. The effective mass used were previously fitted.

The carrier concentration and the position of the chemical potential can be obtained solving Equation 5.9, where we assume that all the impurities are ionized. The electron concentration remains constant $n = N_d$ (where $N_d$ is the doping concentration) while the hole concentration is negligible. The chemical potential follows a lineal trend well described by $\mu = 3.95x10^{-4}T + 0.258$, measured from the top of the valence band. PbSe-LE is a highly degenerate semiconductor since the chemical potential is always inside the conduction band. The conductivity of this sample decreases because the electron concentration is constant and the scattering times decrease with the temperature.

As a comparison, for metals or degenerate semiconductors (parabolic band and energy-independent scattering approximation) the Seebeck coefficient is given by[47]

$$S = \frac{8\pi^2 k_B^2}{3eh^2} mT\left(\frac{\pi}{3n}\right)^{2/3}. \quad (5.15)$$

Where *m* is the effective mass of the carriers and *n* is the doping concentration. Note that the previous equation cannot be compared directly with the model, equation 5.4, because it does not consider parabolic bands. However, equation 5.15 gives a first approximation of the majority carrier's effective mass. Furthermore, from the experimental Seebeck coefficient and equation 5.15, it is possible to obtain the electron effective mass, in this case, *m/m0 = 0.427 ± 0.003*. This value falls within the range employed in the simulations (*0.428-0.441*) $m_0$.

The calculated electrical conductivity and the Seebeck coefficient as a function of the carrier concentration for the PbSe-OL (Figure 5.8a) and PbSe-LE (Figure 5.8b) pointing out the importance in the tuning of the carrier concentration in order to obtain higher power factor ($PF=\sigma S^2$) and consequently highly efficiency thermoelectric materials.

## 5.5 Conclusion

In summary, we were able to obtain nanocrystalline PbSe materials from bottom-up approach, and tune their carrier concentration by using a simple procedure of organic ligand replacement, which means that OL replacement can be used as a doping strategy to improve transport properties of the nanocrystals. With the OL replacement, the electrical conductivity of the nanocrystalline material increases more than one order of magnitude, and the result

figure of merit at 600 K is 0.6 for the PbSe-LE, showing the potential of the bottom-up approach combined with a simple procedure of OL replacement to improve the electronic behaviour of the nanostructured materials. Additionally we were able to analyses the effect of the scattering from the energy barrier at the surfaces of the grains to the electronic transport.

## 5.6 References

(1) Cadavid, D.; Ibáñez, M.; Gorsse, S.; López, A. M.; Cirera, A.; Morante, J. R.; Cabot, A. Bottom-up Processing of Thermoelectric Nanocomposites from Colloidal Nanocrystal Building Blocks: The Case of Ag2Te–PbTe. *J. Nanoparticle Res.* **2012**, *14*, 1–10.

(2) Ibáñez, M.; Zamani, R.; Gorsse, S.; Fan, J.; Ortega, S.; Cadavid, D.; Morante, J. R.; Arbiol, J.; Cabot, A. Core–Shell Nanoparticles As Building Blocks for the Bottom-Up Production of Functional Nanocomposites: PbTe–PbS Thermoelectric Properties. *ACS Nano* **2013**, *7*, 2573–2586.

(3) Huynh, W. U.; Dittmer, J. J.; Alivisatos, A. P. Hybrid Nanorod-Polymer Solar Cells. *Science* **2002**, *295*, 2425–2427.

(4) Kovalenko, M. V.; Scheele, M.; Talapin, D. V. Colloidal Nanocrystals with Molecular Metal Chalcogenide Surface Ligands. *Science* **2009**, *324*, 1417–1420.

(5) Kovalenko, M. V.; Bodnarchuk, M. I.; Zaumseil, J.; Lee, J.-S.; Talapin, D. V. Expanding the Chemical Versatility of Colloidal Nanocrystals Capped with Molecular Metal Chalcogenide Ligands. *J. Am. Chem. Soc.* **2010**, *132*, 10085–10092.

(6) Kovalenko, M. V.; Spokoyny, B.; Lee, J.-S.; Scheele, M.; Weber, A.; Perera, S.; Landry, D.; Talapin, D. V. Semiconductor Nanocrystals Functionalized with Antimony Telluride Zintl Ions for Nanostructured Thermoelectrics. *J Am Chem Soc* **2010**, *132*, 6686–6695.

(7) Kovalenko, M. V.; Bodnarchuk, M. I.; Talapin, D. V. Nanocrystal Superlattices with Thermally Degradable Hybrid Inorganic−Organic Capping Ligands. *J. Am. Chem. Soc.* **2010**, *132*, 15124–15126.

(8) Lee, J.-S.; Kovalenko, M. V.; Huang, J.; Chung, D. S.; Talapin, D. V. Band-like Transport, High Electron Mobility and High Photoconductivity in All-Inorganic Nanocrystal Arrays. *Nat. Nanotechnol.* **2011**, *6*, 348–352.

(9) Dong, A.; Ye, X.; Chen, J.; Kang, Y.; Gordon, T.; Kikkawa, J. M.; Murray, C. B. A Generalized Ligand-Exchange Strategy Enabling Sequential Surface Functionalization of Colloidal Nanocrystals. *J. Am. Chem. Soc.* **2011**, *133*, 998–1006.

(10) Rosen, E. L.; Buonsanti, R.; Llordes, A.; Sawvel, A. M.; Milliron, D. J.; Helms, B. A. Exceptionally Mild Reactive Stripping of Native Ligands from Nanocrystal Surfaces by Using Meerwein's Salt. *Angew. Chem. Int. Ed.* **2012**, *51*, 684–689.

(11) Nag, A.; Kovalenko, M. V.; Lee, J.-S.; Liu, W.; Spokoyny, B.; Talapin, D. V. Metal-Free Inorganic Ligands for Colloidal Nanocrystals: S2–, HS–, Se2–, HSe–, Te2–, HTe–, TeS32–, OH–, and NH2– as Surface Ligands. *J. Am. Chem. Soc.* **2011**, *133*, 10612–10620.

(12) Fafarman, A. T.; Koh, W.; Diroll, B. T.; Kim, D. K.; Ko, D.-K.; Oh, S. J.; Ye, X.; Doan-Nguyen, V.; Crump, M. R.; Reifsnyder, D. C.; et al. Thiocyanate-Capped Nanocrystal Colloids: Vibrational Reporter of Surface Chemistry and Solution-Based Route to Enhanced Coupling in Nanocrystal Solids. *J. Am. Chem. Soc.* **2011**, *133*, 15753–15761.

(13) Koh, W.; Saudari, S. R.; Fafarman, A. T.; Kagan, C. R.; Murray, C. B. Thiocyanate-Capped PbS Nanocubes: Ambipolar Transport Enables Quantum Dot Based Circuits on a Flexible Substrate. *Nano Lett.* **2011**, *11*, 4764–4767.

(14) Zhang, H.; Hu, B.; Sun, L.; Hovden, R.; Wise, F. W.; Muller, D. A.; Robinson, R. D. Surfactant Ligand Removal and Rational Fabrication of Inorganically Connected Quantum Dots. *Nano Lett.* **2011**, *11*, 5356–5361.

(15) Nag, A.; Chung, D. S.; Dolzhnikov, D. S.; Dimitrijevic, N. M.; Chattopadhyay, S.; Shibata, T.; Talapin, D. V. Effect of Metal Ions on Photoluminescence, Charge Transport, Magnetic and Catalytic Properties of All-Inorganic Colloidal Nanocrystals and Nanocrystal Solids. *J. Am. Chem. Soc.* **2012**, *134*, 13604–13615.

(16) Tang, J.; Kemp, K. W.; Hoogland, S.; Jeong, K. S.; Liu, H.; Levina, L.; Furukawa, M.; Wang, X.; Debnath, R.; Cha, D.; et al. Colloidal-Quantum-Dot Photovoltaics Using Atomic-Ligand Passivation. *Nat. Mater.* **2011**, *10*, 765–771.

(17) Zhitomirsky, D.; Furukawa, M.; Tang, J.; Stadler, P.; Hoogland, S.; Voznyy, O.; Liu, H.; Sargent, E. H. N-Type Colloidal-Quantum-Dot Solids for Photovoltaics. *Adv. Mater.* **2012**, *24*, 6181–6185.

(18) Ning, Z.; Ren, Y.; Hoogland, S.; Voznyy, O.; Levina, L.; Stadler, P.; Lan, X.; Zhitomirsky, D.; Sargent, E. H. All-Inorganic Colloidal Quantum Dot Photovoltaics Employing Solution-Phase Halide Passivation. *Adv. Mater.* **2012**, *24*, 6295–6299.

(19) Ibáñez, M.; Cadavid, D.; Zamani, R.; García-Castelló, N.; Izquierdo-Roca, V.; Li, W.; Fairbrother, A.; Prades, J. D.; Shavel, A.; Arbiol, J.; et al. Composition Control and Thermoelectric Properties of Quaternary Chalcogenide Nanocrystals: The Case of Stannite Cu2CdSnSe4. *Chem Mater* **2012**, *24*, 562–570.

(20) Ibáñez, M.; Zamani, R.; LaLonde, A.; Cadavid, D.; Li, W.; Shavel, A.; Arbiol, J.; Morante, J. R.; Gorsse, S.; Snyder, G. J.; et al. Cu2ZnGeSe4 Nanocrystals: Synthesis and Thermoelectric Properties. *J Am Chem Soc* **2012**, *134*, 4060–4063.

(21) Ibáñez, M.; Zamani, R.; Li, W.; Shavel, A.; Arbiol, J.; Morante, J. R.; Cabot, A. Extending the Nanocrystal Synthesis Control to Quaternary Compositions. *Cryst. Growth Des.* **2012**, *12*, 1085–1090.

(22) Shavel, A.; Cadavid, D.; Ibáñez, M.; Carrete, A.; Cabot, A. Continuous Production of Cu2ZnSnS4 Nanocrystals in a Flow Reactor. *J. Am. Chem. Soc.* **2012**, *134*, 1438–1441.

(23) Ibáñez, M.; Zamani, R.; Li, W.; Cadavid, D.; Gorsse, S.; Katcho, N. A.; Shavel, A.; López, A. M.; Morante, J. R.; Arbiol, J.; et al. Crystallographic Control at the Nanoscale to Enhance Functionality: Polytypic Cu2GeSe3 Nanoparticles as Thermoelectric Materials. *Chem. Mater.* **2012**.

(24) Ibáñez, M.; Cadavid, D.; Tamburini, U. A.; Zamani, R.; Gorsse, S.; Li, W.; Shavel, A.; López, A. M.; Morante, J. R.; Arbiol, J.; et al. Colloidal Synthesis and Thermoelectric Properties of Cu2SnSe3 Nanocrystals. *J. Mater. Chem. A* **2012**.

(25) Lee, Y.; Lo, S.-H.; Androulakis, J.; Wu, C.-I.; Zhao, L.-D.; Chung, D.-Y.; Hogan, T. P.; Dravid, V. P.; Kanatzidis, M. G. High-Performance Tellurium-Free Thermoelectrics: All-Scale Hierarchical Structuring of P-Type PbSe–MSe Systems (M = Ca, Sr, Ba). *J. Am. Chem. Soc.* **2013**.

(26) Androulakis, J.; Todorov, I.; He, J.; Chung, D.-Y.; Dravid, V.; Kanatzidis, M. Thermoelectrics from Abundant Chemical Elements: High-Performance Nanostructured PbSe–PbS. *J. Am. Chem. Soc.* **2011**, *133*, 10920–10927.

(27) Zhang, Q.; Wang, H.; Liu, W.; Wang, H.; Yu, B.; Zhang, Q.; Tian, Z.; Ni, G.; Lee, S.; Esfarjani, K.; et al. Enhancement of Thermoelectric Figure-of-Merit by Resonant States of Aluminium Doping in Lead Selenide. *Energy Environ. Sci.* **2012**, *5*, 5246–5251.

(28) Wang, H.; Pei, Y.; LaLonde, A. D.; Snyder, G. J. Heavily Doped P-Type PbSe with High Thermoelectric Performance: An Alternative for PbTe. *Adv. Mater.* **2011**, *23*, 1366–1370.

(29) Parker, D.; Singh, D. J. High-Temperature Thermoelectric Performance of Heavily Doped PbSe. *Phys. Rev. B* **2010**, *82*, 035204.

(30) Murphy, J. E.; Beard, M. C.; Norman, A. G.; Ahrenkiel, S. P.; Johnson, J. C.; Yu, P.; Mićić, O. I.; Ellingson, R. J.; Nozik, A. J. PbTe Colloidal Nanocrystals: Synthesis, Characterization, and Multiple Exciton Generation. *J. Am. Chem. Soc.* **2006**, *128*, 3241–3247.

(31) LaLonde, A. D.; Ikeda, T.; Snyder, G. J. Rapid Consolidation of Powdered Materials by Induction Hot Pressing. *Rev. Sci. Instrum.* **2011**, *82*, 025104–025104–4.

(32) Wang, S.; Zheng, G.; Luo, T.; She, X.; Li, H.; Tang, X. Exploring the Doping Effects of Ag in P-Type PbSe Compounds with Enhanced Thermoelectric Performance. *J. Phys. Appl. Phys.* **2011**, *44*, 475304.

(33) Martin, J.; Wang, L.; Chen, L.; Nolas, G. S. Enhanced Seebeck Coefficient through Energy-Barrier Scattering in PbTe Nanocomposites. *Phys. Rev. B* **2009**, *79*, 115311.

(34) Mentzel, T. S.; Porter, V. J.; Geyer, S.; MacLean, K.; Bawendi, M. G.; Kastner, M. A. Charge Transport in PbSe Nanocrystal Arrays. *Phys. Rev. B* **2008**, *77*, 075316.

(35) Ziman, J. M. *Principles of the Theory of Solids*; University Press: Cambridge [Eng.], 1972.

(36) Ravich, Y. I.; Efimova, B. A.; Tamarchenko, V. I. Semiconducting Lead Chalcogenides. *Plenum N. Y.* **1970**.

(37) D.M. Freik; L.I. Nykyruy; V.M. Shperun. Scattering Mechanisms of Electrons in Monocrystalline PbTe, PbSe and PbS. *Semicond. Phys. Quantum Electron. Optoelectron. 5*, 362–367.

(38) Ravich, Y. I.; Efimova, B. A.; Tamarchenko, V. I. Scattering of Current Carriers and Transport Phenomena in Lead Chalcogenides. *Phys. Status Solidi B* **1971**, *43*, 11–33.

(39) Harris, J. J.; Ridley, B. K. Room Temperature Transport Properties of P-Type PbTe. *J. Phys. Chem. Solids* **1972**, *33*, 1455–1464.

(40) Ahmad, S.; Mahanti, S. D. Energy and Temperature Dependence of Relaxation Time and Wiedemann-Franz Law on PbTe. *Phys. Rev. B* **2010**, *81*, 165203.

(41) Baleva, M.; Georgiev, T.; Lashkarev, G. On the Temperature Dependence of the Energy Gap in PbSe and PbTe. *J. Phys. Condens. Matter* **1990**, *2*, 2935.

(42) Vineis, C. J.; Harman, T. C.; Calawa, S. D.; Walsh, M. P.; Reeder, R. E.; Singh, R.; Shakouri, A. Carrier Concentration and Temperature Dependence of the Electronic Transport Properties of Epitaxial PbTe and PbTe/PbSe Nanodot Superlattices. *Phys. Rev. B* **2008**, *77*, 235202.

(43) Zhou, J.; Li, X.; Chen, G.; Yang, R. Semiclassical Model for Thermoelectric Transport in Nanocomposites. *Phys. Rev. B* **2010**, *82*, 115308.

(44) Popescu, A.; Woods, L. M.; Martin, J.; Nolas, G. S. Model of Transport Properties of Thermoelectric Nanocomposite Materials. *Phys. Rev. B* **2009**, *79*, 205302.

(45) Popescu, A.; Datta, A.; Nolas, G. S.; Woods, L. M. Thermoelectric Properties of Bi-Doped PbTe Composites. *J. Appl. Phys.* **2011**, *109*, 103709.

(46) Zhou, J.; Yang, R. Quantum and Classical Thermoelectric Transport in Quantum Dot Nanocomposites. *J. Appl. Phys.* **2011**, *110*, 084317.

(47) Cutler, M.; Leavy, J. F.; Fitzpatrick, R. L. Electronic Transport in Semimetallic Cerium Sulfide. *Phys. Rev.* **1964**, *133*, A1143–A1152.

# Chapter 6 Colloidal Synthesis and Thermoelectric Properties of $Cu_2SnSe_3$ Nanocrystals

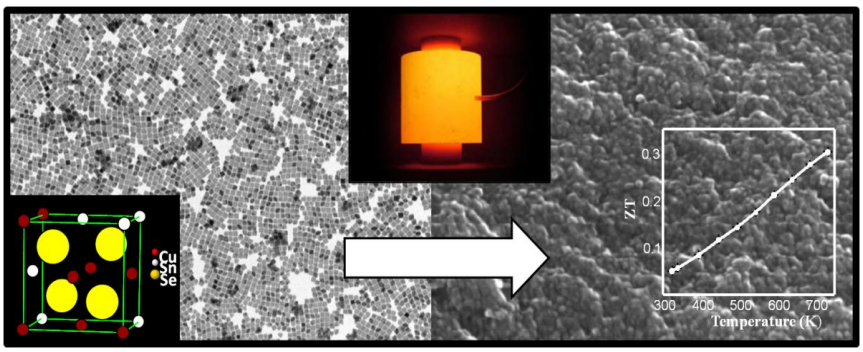


## 6.1 Introduction

The numerous possibilities for chemical substitutions and structural modifications in ternary diamond-like chalcogenides allow significant range in engineering their fundamental chemical and physical properties. Such ample chemical and structural freedom

permits the use of ternary chalcogenides in multiple applications. Ternary diamond-like semiconductors of the family $I_2$-IV-$VI_3$ (I = Cu, Ag; IV = Ge, Sn; VI = S, Se, Te) find applications in the fields of photovoltaics,[1] Li-ion batteries,[2,3] thermoelectrics[4,5], and in acousto-optic devices.[6]

In particular, $Cu_2SnSe_3$ (CTSe) is a p-type semiconductor with a direct band gap of 0.84 eV and a high optical absorption coefficient $>10^4$ $cm^{-1}$.[7–9] CTSe monocrystals are characterized by a hole mobility of 870 $cm^2V^{-1}s^{-1}$[10], and a hole effective mass of 1.2 $m_e$.[9] CTSe has been reported to crystallize in a cubic sphalerite-like phase (space group F-43m) or in the monoclinic structure, space group Cc, with a sphalerite superstructure.[9,11–13]

CTSe is an interesting candidate for acousto-optic applications in the IR region because of its low melting temperature (690 $^oC$), relative low energy band gap, high mean atomic weight and high refractive indices.[9] It has been also extensively studied as an important ternary phase in the processing of $Cu_2ZnSnSe_4$, which is a potential low-cost solar cell absorber.[14,15]

Furthermore, like other copper-based ternary and quaternary selenides,[4,16–23] CTSe shows excellent TE properties. In CTSe the Cu-Se bond network stabilizes the structure and forms an electrically conductive framework. While Cu-Se bonds play the dominant role in controlling hole transport, Sn orbitals do not contribute much to the p-type carrier transport but allow tuning electrical conductivity by their partial substitution by a group III element.[16] At the same time, ionic substitutions create atomic mass fluctuations that promote phonon scattering and help reducing the thermal conductivities of ternary chalcogenides.[4,16,24] These properties have allowed the production of bulk CTSe with figures of merit up to 1.14 at 850 K and 0.41 at 716 K when doped with In or Mn atoms.[16,25]

Thermal conductivities can be further reduced by confining the material crystal domains to the nanoscale.[26–33] The ball-milling of crystalline ingots into small pieces and they posterior

reconsolidation into bulk nanocrystalline materials by hot-pressing or spark plasma sintering is currently the most used approach in this direction.[34] Nevertheless, in the very last years, the bottom-up production of nanocrystalline materials from solution-processed nanoparticles is becoming a serious alternative to produce efficient thermoelectric nanomaterials.[22,23,29]

In this scenario, while a high degree of control on the solution-processing of binary chalcogenide NCs exists,[35,36] the synthesis of ternary and quaternary nanocrystals with sufficient control over their physical, structural and chemical properties still represents an important challenge.[37] Furthermore, while the literature on the production, characterization and application of CTSe thin films[38–40] and nanocrystals[41–44] is minimal, there is still no report on the characterization of the thermoelectric properties of nanocrystalline CTSe.

In this chapter, a new colloidal synthesis route to prepare CTSe NCs with high control over their size and shape is presented. The high yield of the reported procedure allowed its scaling-up to the production of grams of colloidal CTSe nanocrystals. These nanocrystals were used for the production of CTSe nanostructured materials by spark plasma sintering in order to improve their TE efficiency, therefore the TE properties of these nanocrystalline materials are discussed[45].

## 6.2 Experimental details

### 6.2.1 Materials

Copper (I) chloride (reagent grade, 97%), 1-octadecene (ODE, 90%), oleic acid (OA, tech. 90%), selenium shots (99.999%) and hexadecylamine (HDA, tech. 90%) were purchased from Aldrich. Tin (IV) chloride pentahydrate (98%) was purchased from Across. Selenium (IV) oxide (99.8%) and tri-*n*-octylphosphine (TOP, 97%)

were purchased from Strem. n-octadecylphosphonic acid was purchased from PCI Synthesis. Chloroform, isopropanol and ethanol were of analytical grade and obtained from various sources. All chemicals were used as received without further purification.

All syntheses were carried out using standard airless techniques: a vacuum/dry argon gas Schlenk line was used for the syntheses and an argon glove-box for storing and handling air and moisture-sensitive chemicals.

### 6.2.2 Synthesis of $Cu_2SnSe_3$ nanocrystals

Copper (I) chloride (50 mg, 0.5 mmol), tin (IV) chloride pentahydrate (88 mg, 0.25 mmol), hexadecylamine (1230 mg, 5 mM), n-octadecylphosphonic acid (33 mg, 0.1 mmol) were dissolved in 10 ml ODE. The solution was heated under argon flow to 200 °C and maintained at this temperature during 1 h to remove low-boiling point impurities. Separately, the Se precursor solutions were prepared. While the ODE:Se solution (4 mL, 3 mM), was obtained by dissolving selenium (IV) oxide in ODE at 180 °C , the TOPSe (0,9 mL, 2,21 mM) was done by dissolving Se shots in TOP at room temperature. Afterwards, the mixture containing the metal salts was heated to the reaction temperature (285 °C). Then selenium solution was rapidly injected through a septum into the reaction flask. Following the injection, the temperature dropped to around 260 °C and then it slowly recovered to 285 °C. The solution was kept at a temperature between 260 ºC and 285 °C for 5 min and then quickly cooled down. The formation of CTSe nanocrystals could be qualitatively followed by the color change of the mixture from an initial light yellow to green and eventually to the black color of the solution containing the CTSe nanocrystals. 3 mL of oleic acid were added to the mixture during the cooling at ~70 °C to replace the weakly bonded HDA. The crude solution was mixed with 10 ml of chloroform and sonicated at 50 °C for 5 minutes. The CTSe nanoparticles were isolated by centrifugation at 4000 rpm during 5 minutes. The black precipitate was redispersed in chloroform (~20

ml) and sonicated again at 50 °C for 5 minutes. Then the product was additionally precipitated by adding isopropanol (~10 ml) and centrifuging. Finally, the nanocrystals were re-dispersed in chloroform (~5 ml) and stored for their posterior use.

The same synthesis procedure was scaled up for the production of grams of nanoparticles. In the scaled-up procedure, 8 times larger amounts of all precursor, surfactant and solvent were used.

### 6.2.3 Spark plasma sintering (SPS)

For TE characterization, CTSe NCs were carefully washed and dried out from solution under an argon atmosphere. Afterward, the obtained CTSe nanopowder was heated to 500 °C for 2 hours under an Ar flow inside a tube furnace. The annealed material was compacted into pellets (15 mm diameter; 2 mm thickness) using a home-made spark plasma sintering (SPS) system. The set up of the equipment was based in a graphite die, two plungers that were in direct contact with the specimen, a set of spacers, and the bottom and up electrodes. The die, the plungers and spacers were made of conductive graphite. The electrical power was supplied by applying a voltage difference between the electrodes, so that the current intensity flowed through the entire assembly. The die was loaded in the equipment and the temperature was increased with a heating rate of 200 ºC/min. Once the sample reached the designated temperature the pressure was rapidly increased up to 92 MPa. The sample was held under these conditions for 5 minutes and then the pressure was quickly released and the power was turned off**.**

## 6.3 Results and discussion

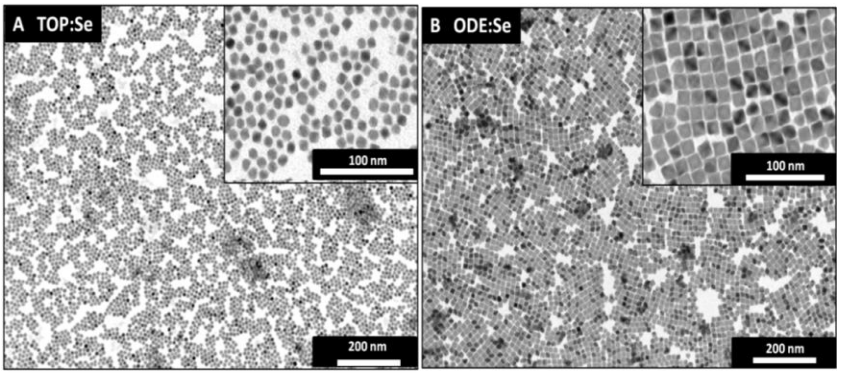


**Figure 6.1** (a) TEM micrographs of $Cu_2SnSe_3$ nanoparticles obtained using TOP:Se and (b) ODE:Se as the Se source

Figure 6.1 shows representative TEM micrographs of the CTSe nanoparticles obtained by the procedure detailed above using either TOPSe (Figure 6.1a) or ODE:Se (Figure 6.1b) as the Se source. The introduction of Se in coordination with TOP resulted in nanoparticles with relatively good size distribution and polyhedral geometry. However, the presence of TOP in the final solution limited the chemical stability of the produced nanoparticles, which slowly re-dissolved. On the other hand, the introduction of Se in ODE not only resulted in nanoparticles with both excellent size and shape distributions, but at the same time, the final nanoparticles remained stable in solution for long periods of time. Moreover, the synthesis procedure yield was significantly improved with the use of ODE:Se instead of TOPSe. Therefore, ODE:Se was the Se source used to prepare the CTSe nanoparticles for the following thermoelectric characterization.

Figure 6.2 shows a HRTEM micrograph and the corresponding indexed power spectrum of a CTSe nanoparticle. HRTEM characterization of the nanocrystals showed them to be highly crystalline and to have a cubic structure (S.G.: F4-3m).[46] The calculated cell parameters and the indexation of the power spectrum

frequencies were in good agreement with a cubic cell composed by [$Cu_2SnSe_3$] tetrahedrons with Cu and Sn atoms randomly occupying the same positions in an occupancy ratio corresponding to $Cu_{0.667} - Sn_{0.333}$.

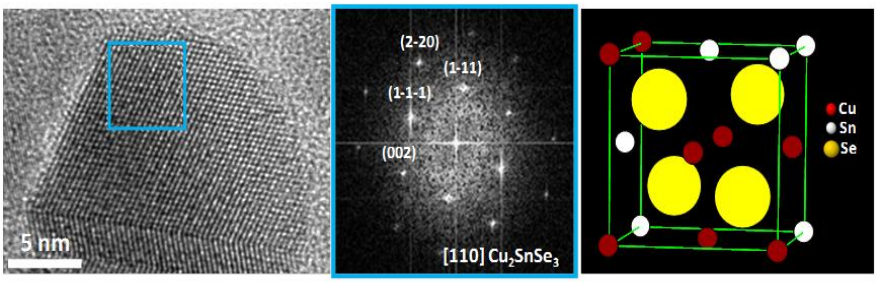


**Figure 6.2** HRTEM and indexed power spectrum of a $Cu_2SnSe_3$ nanoparticle. A scheme of the cubic $Cu_2SnSe_3$ crystal structure with space group F4-3m is also shown

XRD analysis of the obtained CTSe nanoparticles confirmed their cubic structure. Figure 6.3 shows the XRD pattern of CTSe nanoparticles with 12 nm crystal domain sizes. No secondary phase was detected from the XRD characterization of the materials produced. The chemical composition of the nanocrystals obtained was very close to the required stoichiometry as determined from EDX and ICP analysis. At the same time, single particle analysis of the nanocrystals composition showed the three elements to be present in all nanoparticles and the composition to be highly homogeneous from particle to particle across the whole sample.

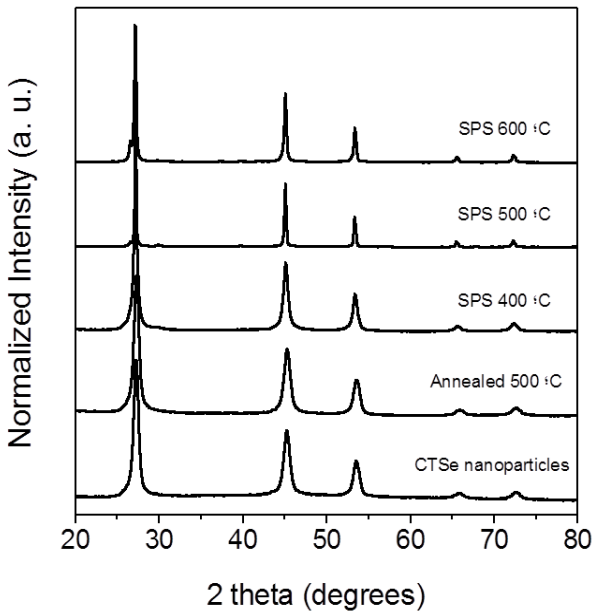


**Figure 6.3** XRD patterns of $Cu_2SnSe_3$ nanoparticles, before and after an annealing treatment at 500 $^oC$ and after spark plasma sintering at 400 $^oC$, 500 $^oC$ and 600 $^oC$

For TE characterization, the synthesis procedure was up-scaled for the production of nanoparticles at the gram scale. Right after synthesis, the nanoparticles were thoroughly washed by means of multiple precipitation and redispersion steps. The final dried powder was not soluble anymore in organic solvents, what probed the large extend of removal of the surface ligands used to control the nanoparticle size, shape and solubility during synthesis. The final nanopowder was annealed at 500 $^oC$ in an argon atmosphere to remove any remaining organic ligand or synthesis/washing byproduct. The annealing process did not appreciably modify the composition or crystal domain size, as observed from the XRD patterns (Figure 6.3). The annealed nanopowder was then consolidated into nanocrystalline pellets by means of spark plasma sintering. For this process, a homemade system was used. Sintering temperatures in the range from 400 $^oC$ to 600 $^oC$ and different times and pressures were carefully tested to optimize the pellet density

while preventing the crystal domain growth and the modification of the material composition. All sintering processes were performed under vacuum. Particles from the exact same batch, having an average crystal domain size of 12 nm and the stoichiometric composition were used for all the optimization tests. Finally, the sintering time was set to 5 min and the uniaxial sintering pressure to 92 MPa. In these conditions, sintering temperatures of 400 $^{o}$C, 500 $^{o}$C and 600 $^{o}$C resulted in an increase of the crystal domain size from the original 12 nm to 15 nm, 25 nm and 30 nm, respectively. These values were calculated from the fitting of the XRD patterns through the use of the Scherrer's equation. The highest processing temperatures resulted in a slight loss of Sn and the formation of CuSe as a secondary phase, as concluded from the XRD characterization of the material. Figure 6.4 shows SEM micrographs of the final nanocrystalline pellets produced by spark plasma sintering at different processing temperatures.

For TE characterization, two pellets 15 mm in diameter and 2 mm thick were produced using the optimized spark plasma sintering conditions (92 MPa, 400 $^{o}$C, 5 min). In these conditions, the relative density of the obtained pellets was approximately 90 %.

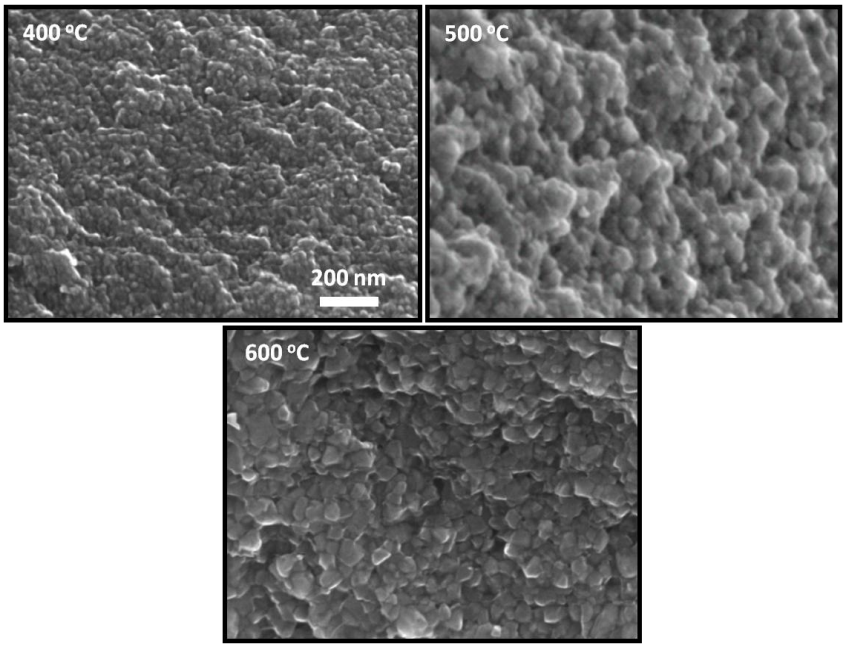


**Figure 6.4** SEM micrographs of the nanocrystalline $Cu_2SnSe_3$ pellets obtained by spark plasma sintering at 400 °C, 500 °C and 600 °C (from left to right).

The TE properties of the nanocrystalline CTSe were measured in the temperature range from 300 K to 720 K. Figure 5 shows the electrical conductivity, Seebeck coefficient, thermal conductivity and TE figure of merit of the nanocrystalline CTSe pellets produced. Electrical conductivities up to 8450 S $m^{-1}$ were obtained from nanocrystalline CTSe. These relatively high values prove the large extend of removal of the surface ligands used in the solution-processing of the material. These values were just a 30 % lower than those obtained from bulk CTSe produced by the reaction of the constituent elements at high temperatures and during long periods of time. These 30 % lower electrical conductivities are explained in part by the scattering of charge carriers at the high density of grain boundaries and structural defects. On the other hand, the relatively lower pellet densities obtained by the bottom-up assembly of the nanocrystals most probably also played an important role in the electrical conductivity decrease. An estimation of the electrical

conductivity that would be measured from a 100 % dense sample can be obtained using a Maxwell-Eucken expression.[29,47,48]

$$\sigma_{100} = \sigma_P \frac{1+\beta P}{1-P} \quad (6.1)$$

Where $\sigma_{100}$ is the electrical conductivity in the 100 % dense medium, P is the degree of porosity in the range between 0 and 1, and b is an empirical parameter related to the pore geometry, which we fixed to 2.0.[48] This equation yields electrical conductivities up to 11200 S $m^{-1}$. The remaining 10 % reduction of electrical conductivity when compared to bulk CTSe must be associated to charge carrier scattering at crystal interfaces.

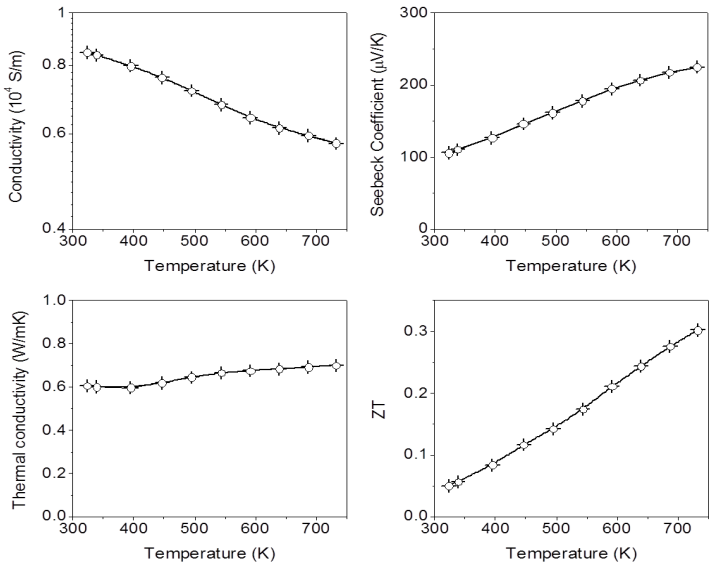


**Figure 6.5** Temperature dependence of the electrical conductivity, Seebeck coefficient, thermal conductivity and thermoelectric figure of merit of a representative nanocrystalline $Cu_2SnSe_3$ pellet obtained by the spark plasma sintering at 400 $^oC$ of solution-processed $Cu_2SnSe_3$ nanocrystals.

The electrical conductivity of the CTSe nanocrystalline pellets decreased with the temperature in the whole range tested. This metallic-like character was probably associated to the thermal

activation of an acceptor level at temperatures below 300 K. Above this temperature, the combination of the empty impurity band and the decrease of the hole mobility with temperature due to the enhancement of acoustic phonon scattering would explain the observed metallic-like behavior. The same evolution of the electrical conductivity with temperature has been previously observed in bulk crystalline materials, what discards a major role of interfaces in this characteristic behaviour.[16,25]

The positive Seebeck coefficients measured from nanocrystalline CTSe demonstrated the p-type character of the obtained materials. While a relatively large range of values has been reported, the Seebeck coefficients measured here from nanocrystalline CTSe were slightly lower than the best values obtained previously for pure CTSe bulk materials.[4,16,25]

On the other hand, the thermal conductivities of nanocrystalline CTSe measured in this work were significantly lower than those previously reported for bulk CTSe. Even correcting for the slightly larger porosity of the materials here characterized, the thermal conductivity of the nanocrystalline materials was between a factor 2 and 4 lower than those obtained previously. This strong decrease of thermal conductivity must be associated to phonon scattering at the very high density of interfaces present in nanocrystalline CTSe.

These characteristics finally resulted in thermoelectric figure of merit up to 0.3 at 730 K. This value is very close to the best figure of merit reported for undoped CTSe and it might be notably improved with the introduction of controlled amounts of dopants. When comparing with current solid state methods, it should be kept in mind that while the bottom-up processing of nanocrystalline CTSe from colloidal CTSe nanocrystals allowed obtaining thermoelectric materials with relatively high figures of merit, it also represents an important advantage in terms of processing time and energy consumption. Moreover, the high versatility of the processes here reported should allow a rapid and facile screening of the materials

composition and structural properties to further optimize the material figure of merit.

## 6.4 Conclusion

A new colloidal synthetic route for the production of CTSe nanoparticles was detailed. The use of ODE:Se instead of TOPSe as the Se source was demonstrated to result in stable nanoparticles with unprecedented size and shape distributions and very high production yields. The reported procedure was up-scaled to the production of grams of CTSe colloidal nanocrystals. The potential of these nanoparticles for the bottom-up production of nanocrystalline materials by means of spark plasma sintering was further demonstrated. The obtained nanocrystalline CTSe was characterized by figures of merit comparable to those obtained from bulk materials, but using considerably less time-consuming and energy-intensive processes. The introduction of doping elements in the CTSe structure is expected to allow a further improvement of the TE figures of merit here reported.

## 6.5 References

(1) Fernandes, P. A.; Salomé, P. M. P.; Cunha, A. F. da. A Study of Ternary $Cu_2SnS_3$ and $Cu_3SnS_4$ Thin Films Prepared by Sulfurizing Stacked Metal Precursors. *J. Phys. Appl. Phys.* **2010**, *43*, 215403.

(2) Qu, B.; Li, H.; Zhang, M.; Mei, L.; Chen, L.; Wang, Y.; Li, Q.; Wang, T. Ternary $Cu_2SnS_3$ Cabbage-like Nanostructures: Large-Scale Synthesis and Their Application in Li-Ion Batteries with Superior Reversible Capacity. *Nanoscale* **2011**, *3*, 4389–4393.

(3) Qu, B.; Zhang, M.; Lei, D.; Zeng, Y.; Chen, Y.; Chen, L.; Li, Q.; Wang, Y.; Wang, T. Facile Solvothermal Synthesis of Mesoporous $Cu_2SnS_3$ Spheres and Their Application in Lithium-Ion Batteries. *Nanoscale* **2011**, *3*, 3646–3651.

(4) Skoug, E. J.; Cain, J. D.; Morelli, D. T. Thermoelectric Properties of the $Cu_2SnSe_3$–$Cu_2GeSe_3$ Solid Solution. *J. Alloys Compd.* **2010**, *506*, 18–21.

(5) Ibáñez, M.; Zamani, R.; Li, W.; Cadavid, D.; Gorsse, S.; Katcho, N. A.; Shavel, A.; López, A. M.; Morante, J. R.; Arbiol, J.; et al. Crystallographic Control at the Nanoscale to Enhance Functionality: Polytypic $Cu_2GeSe_3$ Nanoparticles as Thermoelectric Materials. *Chem. Mater.* **2012**.

(6) Samanta, L. K. On Some Properties of $I_2$-IV-$VI_3$ Compounds. *Phys. Status Solidi A* **1987**, *100*, K93–K97.

(7) Zhai, Y.-T.; Chen, S.; Yang, J.-H.; Xiang, H.-J.; Gong, X.-G.; Walsh, A.; Kang, J.; Wei, S.-H. Structural Diversity and Electronic Properties of $Cu_2SnX_3$ (X=S, Se): A First-Principles Investigation. *Phys. Rev. B* **2011**, *84*, 075213.

(8) Chandra, G. H.; Kumar, O. L.; Rao, R. P.; Uthanna, S. Influence of Substrate and Selenization Temperatures on the Growth of $Cu_2SnSe_3$ Films. *J. Mater. Sci.* **2011**, *46*, 6952–6959.

(9) Marcano, G.; Rincón, C.; Chalbaud, L. M. de; Bracho, D. B.; Pérez, G. S. Crystal Growth and Structure, Electrical, and Optical Characterization of the Semiconductor $Cu_2SnSe_3$. *J. Appl. Phys.* **2001**, *90*, 1847–1853.

(10) Berger, L. I. *Ternary Diamond-Like Semiconductors*; 1 edition.; Springer, 1995.

(11) Delgado, G. E.; Mora, A. J.; Marcano, G.; Rincón, C. Crystal Structure Refinement of the Semiconducting Compound $Cu_2SnSe_3$ from X-Ray Powder Diffraction Data. *Mater. Res. Bull.* **2003**, *38*, 1949–1955.

(12) Gulay, L. D.; Daszkiewicz, M.; Ostapyuk, T. A.; Klymovych, O. S.; Zmiy, O. F. Monoclinic $Cu_2Se_3Sn$. *Acta Crystallogr. Sect. C* **2010**, *66*, i58–i60.

(13) Marcano, G.; de Chalbaud, L. .; Rincón, C.; Sánchez Pérez, G. Crystal Growth and Structure of the Semiconductor $Cu_2SnSe_3$. *Mater. Lett.* **2002**, *53*, 151–154.

(14) Shavel, A.; Arbiol, J.; Cabot, A. Synthesis of Quaternary Chalcogenide Nanocrystals: Stannite $Cu_2Zn_xSn_ySe_{1+x+2y}$. *J. Am. Chem. Soc.* **2010**, *132*, 4514–4515.

(15) Shavel, A.; Cadavid, D.; Ibáñez, M.; Carrete, A.; Cabot, A. Continuous Production of $Cu_2ZnSnS_4$ Nanocrystals in a Flow Reactor. *J. Am. Chem. Soc.* **2012**, *134*, 1438–1441.

(16) Shi, X.; Xi, L.; Fan, J.; Zhang, W.; Chen, L. Cu−Se Bond Network and Thermoelectric Compounds with Complex Diamondlike Structure. *Chem. Mater.* **2010**, *22*, 6029–6031.

(17) Liu, M.-L.; Huang, F.-Q.; Chen, L.-D.; Chen, I.-W. A Wide-Band-Gap P-Type Thermoelectric Material Based on Quaternary Chalcogenides of $Cu_2ZnSnQ_4$(Q=S,Se). *Appl. Phys. Lett.* **2009**, *94*, 202103.

(18) Sevik, C.; Çağın, T. Assessment of Thermoelectric Performance of $Cu_2ZnSnX_4$, X=S, Se, and Te. *Appl. Phys. Lett.* **2009**, *95*, 112105.

(19) Schorr, S. Structural Aspects of Adamantine like Multinary Chalcogenides. *Thin Solid Films* **2007**, *515*, 5985–5991.

(20) Cho, J. Y.; Shi, X.; Salvador, J. R.; Meisner, G. P.; Yang, J.; Wang, H.; Wereszczak, A. A.; Zhou, X.; Uher, C. Thermoelectric Properties and Investigations of Low Thermal Conductivity in Ga-Doped $Cu_2GeSe_3$. *Phys. Rev. B* **2011**, *84*, 085207.

(21) Cho, J. Y.; Shi, X.; Salvador, J. R.; Yang, J.; Wang, H. Thermoelectric Properties of Ternary Diamondlike Semiconductors $Cu_2Ge_{1+x}Se_3$. *J. Appl. Phys.* **2010**, *108*, 073713.

(22) Ibáñez, M.; Cadavid, D.; Zamani, R.; García-Castelló, N.; Izquierdo-Roca, V.; Li, W.; Fairbrother, A.; Prades, J. D.; Shavel, A.; Arbiol, J.; et al. Composition Control and Thermoelectric Properties of Quaternary Chalcogenide Nanocrystals: The Case of Stannite $Cu_2CdSnSe_4$. *Chem Mater* **2012**, *24*, 562–570.

(23) Ibáñez, M.; Zamani, R.; LaLonde, A.; Cadavid, D.; Li, W.; Shavel, A.; Arbiol, J.; Morante, J. R.; Gorsse, S.; Snyder, G. J.; et al. $Cu_2ZnGeSe_4$ Nanocrystals: Synthesis and Thermoelectric Properties. *J Am Chem Soc* **2012**, *134*, 4060–4063.

(24) Irie, T. Lattice Thermal Conductivity of Disordered Alloys of Ternary Compound Semiconductors $Cu_2$(Sn, Ge)(Se, S)$_3$ (Ag, Pb, Sb)$Te_2$, and (Ag, Sn, Sb)$Te_2$. *Jpn. J. Appl. Phys.* **1966**, *5*, 854–859.

(25) Sun, H.; Morelli, D. T. Thermoelectric Properties of $Co_{1-x}Rh_XSi_{0.98}B_{0.02}$ Alloys. *J. Electron. Mater.* **2012**, *41*, 1125–1129.

(26) Zebarjadi, M.; Esfarjani, K.; Dresselhaus, M. S.; Ren, Z. F.; Chen, G. Perspectives on Thermoelectrics: From Fundamentals to Device Applications. *Energy Environ. Sci.* **2012**, *5*, 5147.

(27) Vineis, C. J.; Shakouri, A.; Majumdar, A.; Kanatzidis, M. G. Nanostructured Thermoelectrics: Big Efficiency Gains from Small Features. *Adv. Mater.* **2010**, *22*, 3970–3980.

(28) Szczech, J. R.; Higgins, J. M.; Jin, S. Enhancement of the Thermoelectric Properties in Nanoscale and Nanostructured Materials. *J. Mater. Chem.* **2011**, *21*, 4037–4055.

(29) Scheele, M.; Oeschler, N.; Veremchuk, I.; Reinsberg, K.-G.; Kreuziger, A.-M.; Kornowski, A.; Broekaert, J.; Klinke, C.; Weller, H. ZT Enhancement in Solution-Grown $Sb_{(2-x)}Bi_xTe_3$ Nanoplatelets. *ACS Nano* **2010**, *4*, 4283–4291.

(30) Gorsse, S.; Bauer Pereira, P.; Decourt, R.; Sellier, E. Microstructure Engineering Design for Thermoelectric Materials: An Approach to Minimize Thermal Diffusivity. *Chem Mater* **2009**, *22*, 988–993.

(31) Gorsse, S.; Bellanger, P.; Brechet, Y.; Sellier, E.; Umarji, A.; Ail, U.; Decourt, R. Nanostructuration via Solid State Transformation as a Strategy for Improving the Thermoelectric Efficiency of PbTe Alloys. *Acta Mater.* **2011**, *59*, 7425–7437.

(32) Cadavid, D.; Ibáñez, M.; Gorsse, S.; López, A. M.; Cirera, A.; Morante, J. R.; Cabot, A. Bottom-up Processing of Thermoelectric Nanocomposites from Colloidal Nanocrystal Building Blocks: The Case of $Ag_2Te$–PbTe. *J. Nanoparticle Res.* **2012**, *14*, 1–10.

(33) Cadavid, D.; Ibáñez, M.; Shavel, A.; Durá, O. J.; Torre, M. A. L. de la; Cabot, A. Organic Ligand Displacement by Metal Salts to Enhance Nanoparticle Functionality: Thermoelectric Properties of $Ag_2Te$. *J. Mater. Chem. A* **2013**, *1*, 4864–4870.

(34) Lan, Y.; Minnich, A. J.; Chen, G.; Ren, Z. Enhancement of Thermoelectric Figure-of-Merit by a Bulk Nanostructuring Approach. *Adv. Funct. Mater.* **2010**, *20*, 357–376.

(35) Ibáñez, M.; Guardia, P.; Shavel, A.; Cadavid, D.; Arbiol, J.; Morante, J. R.; Cabot, A. Correction to Growth Kinetics of Asymmetric $Bi_2S_3$ Nanocrystals: Size Distribution Focusing in Nanorods. *J. Phys. Chem. C* **2011**, *115*, 11888–11888.

(36) Li, W.; Shavel, A.; Guzman, R.; Rubio-Garcia, J.; Flox, C.; Fan, J.; Cadavid, D.; Ibáñez, M.; Arbiol, J.; Morante, J. R.; et al. Morphology Evolution of $Cu_{2-x}S$ Nanoparticles: From Spheres to Dodecahedrons. *Chem. Commun.* **2011**, *47*, 10332–10334.

(37) Ibáñez, M.; Zamani, R.; Li, W.; Shavel, A.; Arbiol, J.; Morante, J. R.; Cabot, A. Extending the Nanocrystal Synthesis Control to Quaternary Compositions. *Cryst. Growth Des.* **2012**, *12*, 1085–1090.

(38) Babu, G. S.; Kumar, Y. B. K.; Reddy, Y. B. K.; Raja, V. S. Growth and Characterization of $Cu_2SnSe_3$ Thin Films. *Mater. Chem. Phys.* **2006**, *96*, 442–446.

(39) Kuo, D.-H.; Haung, W.-D.; Huang, Y.-S.; Wu, J.-D.; Lin, Y.-J. Single-Step Sputtered $Cu_2SnSe_3$ Films Using the Targets Composed of $Cu_2Se$ and $SnSe_2$. *Thin Solid Films* **2010**, *518*, 7218–7221.

(40) Kuo, D.-H.; Haung, W.-D.; Huang, Y.-S.; Wu, J.-D.; Lin, Y.-J. Effect of Post-Deposition Annealing on the Performance of D.C. Sputtered $Cu_2SnSe_3$ Thin Films. *Surf. Coat. Technol.* **2010**, *205, Supplement 1*, S196–S200.

(41) Chen, X.; Wang, X.; An, C.; Liu, J.; Qian, Y. Preparation and Characterization of Ternary Cu–Sn–E (E=S, Se) Semiconductor Nanocrystallites via a Solvothermal Element Reaction Route. *J. Cryst. Growth* **2003**, *256*, 368–376.

(42) Li, B.; Xie, Y.; Huang, J.; Qian, Y. Solvothermal Synthesis to $Cu_2SnSe_4$ Nanocrystals at Low Temperature. *Solid State Ion.* **1999**, *126*, 359–362.

(43) Jeong, J.; Chung, H.; Ju, Y. C.; Moon, J.; Roh, J.; Yoon, S.; Do, Y. R.; Kim, W. Colloidal Synthesis of $Cu_2SnSe_3$ Nanocrystals. *Mater. Lett.* **2010**, *64*, 2043–2045.

(44) Norako, M. E.; Greaney, M. J.; Brutchey, R. L. Synthesis and Characterization of Wurtzite-Phase Copper Tin Selenide Nanocrystals. *J. Am. Chem. Soc.* **2012**, *134*, 23–26.

(45) Ibáñez, M.; Cadavid, D.; Anselmi-Tamburini, U.; Zamani, R.; Gorsse, S.; Li, W.; López, A. M.; Morante, J. R.; Arbiol, J.; Cabot, A. Colloidal Synthesis and Thermoelectric Properties of $Cu_2SnSe_3$ Nanocrystals. *J. Mater. Chem. A* **2012**, *1*, 1421–1426.

(46) Sharma, B. B.; Ayyar, R.; Singh, H. Stability of the Tetrahedral Phase in the AI2BIVCVI3 Group of Compounds. *Phys. Status Solidi A* **1977**, *40*, 691–696.

(47) Yang, L.; Wu, J. S.; Zhang, L. T. Synthesis of Filled Skutterudite Compound $La_{0.75}Fe_3CoSb_{12}$ by Spark Plasma Sintering and Effect of Porosity on Thermoelectric Properties. *J. Alloys Compd.* **2004**, *364*, 83–88.

(48) Adachi, J.; Kurosaki, K.; Uno, M.; Yamanaka, S. Effect of Porosity on Thermal and Electrical Properties of Polycrystalline Bulk ZrN Prepared by Spark Plasma Sintering. *J. Alloys Compd.* **2007**, *432*, 7–10.

# Conclusions

In this thesis, I detailed the progress I did towards the production and characterization of high efficiency nanostructured TE materials. I showed the advantages of the bottom-up approach, as an alternative to conventional methods of production of efficient TE materials:

$(Ag_2Te)_x(PbTe)_{1-x}$ nanocomposites with controlled composition were obtained by means of a facile bottom-up approach consisting in the solution blending of colloidal NCs. The temperature dependence of the electrical conductivity and Seebeck coefficient of the obtained materials could be described from the combination of the properties of the two constituent materials. Undoped $(Ag_2Te)_{0.75}(PbTe)_{0.25}$ nanocomposites displayed best power factors among the different nanocomposites tested and reached *ZT* values up to 0.38 at 670 K, these are values comparables to the bulk counterparts.

I developed a simple, general and scalable strategy to remove electrically insulating organic ligands from the surface of colloidal nanocrystals. The process uses a metal salt solution and renders the NCs soluble in polar solvents during enough time to purify and assemble/deposit them into technologically useful macroscopic nanomaterials. The potential of the detailed approach was

demonstrated by producing thermoelectric $Ag_2Te$ nanomaterials with up to a 6-fold enhancement of their TE figure of merit compared to the nanomaterials obtained with no ligand replacement. The procedure reported here can be used to improve the performance of NCs-based materials and devices in a wide range of applications.

I was able to obtain nanocrystalline PbSe materials from bottom-up approach at gram scale, and understand the effect of the LE in this material. With the OL replacement, the electrical conductivity of the nanocrystalline material increase more than one order of magnitude, and the resulting figure of merit at 600 K was 0.6. This shows the potential of the bottom-up approach combined with a simple procedure of OL replacement to improve the electronic behaviour of the nanostructured materials. Additionally we were able to analysed the effect of scattering to the electronic transport

Also I detailed a new colloidal synthetic route to produce of CTSe nanoparticles. The use of ODE:Se instead of TOPSe as the Se source was demonstrated to result in stable nanoparticles with unprecedented size and shape distributions and very high production yields. The reported procedure was up-scaled to the production of grams of CTSe colloidal NCs. The potential of these NCs for the bottom-up production of nanocrystalline materials by means of spark plasma sintering was further demonstrated. The obtained nanocrystalline CTSe was characterized by figures of merit comparable to those obtained from bulk materials, but using considerably less time-consuming and energy-intensive processes.

# Future work

In this thesis, I have shown different paths to improve the TE efficiency of bulk nanostructured materials produced from the bottom-up assembly of colloidal NCs. However, still many factors can be improved to obtain TE materials with higher efficiency.

Binary nanocomposites showed potential to increase the TE efficiency by means of increased phonon blocking and providing a mean to increase carrier concentration. However, more sophisticated routes to produce these nanocomposites such as the use of core-shell NCs instead of just blend the NCs, could enhance the homogeneity of the binary NCs distribution while keeping the heterogeneous phase distribution at the nanoscale.

Ligand exchange procedures effectively improve the electronic transport properties of nanostructured materials produced from colloidal NCs. Nevertheless, this very recent technique needs to be better understood. In depth theoretical and experimental studies regarding the NCs surface chemistry and the interaction between the NCs and the ligands would help to better design ligand exchange approaches to enhance electronic properties of the nanomaterials.

Another important factor for controlling the TE efficiency of nanostructured materials is the charge carrier concentration. To control the charge carrier concentration, different strategies of NCs doping can be implemented. In spite of the extensive work done in this field, NCs doping still remains as a challenge. Further efforts needs to be done to solve the dopant incorporation problems as well as to develop tools for characterizing the impurities.

Solution-based approaches have shown its versatility to produce different kind of NCs for TE applications. Another important challenge is to develop other materials beyond the chalcogenides that can be used for TE applications, especially around room temperature, where only a few TE materials are available. In the same direction, one more important challenge is the use of nontoxic and abundant materials that can be readily implemented in actual consumer devices.

Although great progress has been achieved by bottom-up approaches, higher efficiencies and lower costs of fabrication are required. Still this is a young research area where there is room for new and disruptive developments that can push forward the TE field.

# CURRICULUM VITAE

## PERSONAL INFORMATION


Name **Doris Yaneth Cadavid Rodríguez**
Birth Date /place 5th November, 1981
Bogotá D.C. – Colombia

Current position PhD Student
Functional Nanomaterials group
Catalonia Institute for Research Energy (IREC)
Jardins de les Dones de Negre 1, 2ª Pl
Sant Adrià de Besòs, 08930
Barcelona, Spain
Phone: +34 693 688 146
E-mail: doris.cadavid.rodriguez@gmail.com,


## DEGREES - ACADEMIC QUALIFICATIONS

2010-Present **Doctor of Philosophy-Physics**.
University of Barcelona
Thesis: **Towards High Performance Nanostructured Thermoelectric Materials: A Bottom-Up Approach.**
Supervisor: Prof. Dr. Andreu Cabot.

| | |
|---|---|
| 2005-2008 | **Master of Science-Physics**.<br>National University of Colombia<br>Thesis: **Production and study of thermoelectric properties of $Zn_4Sb_3$ polycrystalline compounds.**<br>Supervisor: Prof. Dr. Julio Evelio Rodríguez.<br>Overall average: 4.8 (0-5) |
| 1999-2005 | **Physics**<br>National University of Colombia<br>Thesis: **Production and characterization of Bi-Sb thermoelectric compounds.**<br>Supervisor: Prof. Dr. Julio Evelio Rodríguez.<br>Overall average: 3.9 (0-5) |

## RESEARCH INTERESTS

I am interested in the production and characterization of semiconductor materials with potential properties for production of different electronic devices. My research so far has been focused in the engineering, production and characterization of semiconductor nanomaterials for energy applications, specifically high efficiency thermoelectric materials. I have gained expertise on the synthesis of a variety of semiconductor nanomaterials, such as chalcogenides and ternary/quaternary compounds by using solution processing approaches. A relevant task of my research is the characterization of the materials to retrieve their morphological, optical and transport properties. Thanks to this, I became an expert of electron microscopes, electronic transport characterization equipments and systems and XRD, FTIR and UV-Vis spectroscopy equipments, among others.

## PROFESSIONAL EXPERIENCE

| | |
|---|---|
| June - Sept 2013 | Visiting Researcher<br>Novel Materials Laboratory<br>University of South Florida<br>Group Leader: Prof. Dr. George Nolas |
| May 2011 | Visiting Researcher<br>Chemical-Physics Department<br>University of Pavia<br>Group Leader: Prof. Dr. Umberto Anselmi-Tamburini |
| 2011-2013 | Laboratory Technician<br>Advanced Materials for Energy Area<br>Catalonia Institute for Energy Research-IREC |
| 2008-2010 | Assistant Researcher<br>Departamento de Materiales Metálicos y Nanostructurados<br>Centro Atómico Bariloche |
| 2007-2008 | Lecturer<br>Engineering school<br>Piloto University of Colombia<br>Courses: Mechanics, electricity and magnetism, waves, thermodynamics |
| 2006 - 2007 | Teaching fellow<br>Department of Physics<br>National University of Colombia<br>Courses: Mechanics, Electricity and magnetism, waves, thermodynamics. |
| 2004-2005 | Teaching assistant<br>Department of Physics-Faculty of sciences<br>National University of Colombia |

# SCIENTIFIC PRODUCTION

## *Publications*

Title: Thermoelectric properties of bottom-up assembled $Bi_2S_{3-x}Te_x$ nanocomposites
Author(s): Doris Cadavid, María Ibáñez, Umberto Anselmi-Tamburini, Oscar Juan Durá, M.A. López de la Torre, and Andreu Cabot.
Citation: *Int. J. Nanotechnol* 2014, Accepted

Title: Organic ligand displacement by metal salts to enhance nanoparticle functionality: Thermoelectric properties of $Ag_2Te$
Author(s): Doris Cadavid, María Ibáñez, Alexey Shavel, Oscar Juan Durá, M.A. López de la Torre, and Andreu Cabot.
Citation: *J. Mater. Chem. A*, 2013,1, 4864-4870

Title: Bottom-up processing of thermoelectric nanocomposites from colloidal nanocrystal building blocks: the case of $Ag_2Te$–PbTe
Author(s): Doris Cadavid, María Ibáñez, Stéphane Gorsse, Antonio M. López, Albert Cirera, Joan Ramon Morante, and Andreu Cabot.
Citation: *J. Nanopart. Res.*, 2012, 14, 1328

Title: Colloidal synthesis and thermoelectric properties of $Cu_2SnSe_3$ nanocrystals
Author(s): María Ibáñez, Doris Cadavid, Umberto Anselmi-Tamburini, Reza Zamani, Stéphane Gorsse, Wenhua Li, Antonio M. López, Joan Ramon Morante, Jordi Arbiol, and Andreu Cabot.
Citation: *J. Mater. Chem. A, 2013, 1, 1421-1426*

Title: CuTe Nanocrystals: Shape and size control, plasmonic properties, and use as SERS probes and photothermal agents
Author(s): Wenhua Li, Reza Zamani, Pilar Rivera Gil, Beatriz Pelaz, María Ibáñez, Doris Cadavid, Alexey Shavel, Ramon A. Alvarez-Puebla, Wolfgang J. Parak, Jordi Arbiol, and Andreu Cabot.
Citation: *J. Am. Chem. Soc., 2013, 135 (19), 7098-7101*

Title: Metal ions to control the morphology of semiconductor nanoparticles: Copper Selenide Nanocubes
Author(s): Wenhua Li, Reza Zamani, María Ibáñez, Doris Cadavid, Alexey Shavel, J R Morante, Jordi Arbiol, and Andreu Cabot.
Citation: *J. Am. Chem. Soc., 2013, 135 (12), 4664-4667*

Title: Core–Shell Nanoparticles As Building Blocks for the Bottom-Up Production of Functional Nanocomposites: PbTe–PbS Thermoelectric Properties
Author(s): María Ibáñez, Reza Zamani, Stéphane Gorsse, Jiandong Fan, Silvia Ortega, Doris Cadavid, Joan Ramon Morante, Jordi Arbiol, and Andreu Cabot.
Citation: *ACS Nano, 2013, 7 (3), 2573-2586*

Title: Continuous Production of $Cu_2ZnSnS_4$ Nanocrystals in a Flow Reactor
Author(s): Alexey Shavel, Doris Cadavid, María Ibáñez, Alex Carrete, and Andreu Cabot.
Citation: *J. Am. Chem. Soc., 2012, 134 (3), 1438-1441*

Title: Crystallographic control at the nanoscale to enhance functionality: polytypic $Cu_2GeSe_3$ nanoparticles as thermoelectric materials
Author(s): María Ibáñez, Reza Zamani, Wenhua Li, Doris Cadavid, Stéphane Gorsse, N.A. Katcho, Alexey Shavel, A. M. López, Joan Ramon Morante, Jordi Arbiol, and Andreu Cabot.
Citation: *Chem. Mater., 2012, 24 (23), 4615-4622*

Title: Composition Control and Thermoelectric Properties of Quaternary Chalcogenide Nanocrystals: The Case of Stannite $Cu_2CdSnSe_4$
Author(s): María Ibáñez, Doris Cadavid, Reza Zamani, Nuria García-Castelló, Victor Izquierdo-Roca, Wenhua Li, Andrew Fairbrother, Joan Daniel Prades, Alexey Shavel, Jordi Arbiol, Alejandro Pérez-Rodriguez, Joan Ramon Morante, and Andreu Cabot.
Citation: *Chem. Mater., 2012, 24 (3), 562-570*

Title: $Cu_2ZnGeSe_4$ Nanocrystals: Synthesis and Thermoelectric Properties
Author(s): María Ibáñez, Reza Zamani, Aaron LaLonde, Doris Cadavid, Wenhua Li, Alexey Shavel, Jordi Arbiol, Joan Ramon Morante, Stéphane Gorsse, G. Jeffrey Snyder, and Andreu Cabot.
Citation: *J. Am. Chem. Soc., 2012, 134 (9), 4060-4063*

Title: Growth Kinetics of Asymmetric $Bi_2S_3$ Nanocrystals: Size Distribution Focusing in Nanorods
Author(s): María Ibáñez, Pablo Guardia, Alexey Shavel, Doris Cadavid, Jordi Arbiol, Joan Ramon Morante, and Andreu Cabot.
Citation: *J. Phys Chem. C., 2011, 115 (16), 7947-7955*

Title: Morphology evolution of $Cu_{2-x}S$ nanoparticles : from spheres to dodecahedrons
Author(s): Wenhua Li, Alexey Shavel, Roger Guzman, Javier Rubio- Garcia, Cristina Flox, Jiandong Fan, Doris Cadavid, María Ibáñez, Jordi Arbiol, Joan Ramon Morante, and Andreu Cabot.
Citation: *Chem. Commun., 2011, 47, 10332-10334*

Title: Means and Limits of Control of the Shell Parameters in Hollow Nanoparticles Obtained by the Kirkendall Effect
Author(s): María Ibáñez, Jiandong Fan, Wenhua Li, Doris Cadavid, Raquel Nafria, Alex Carrete, and Andreu Cabot.
Citation: *Chem. Mater., 2011, 23 (12), 3095-3104*

Title: Thermoelectric properties of polycrystalline $Zn_4Sb_3$ samples prepared by solid-state reaction method
Author(s): D. Cadavid, J.E. Rodríguez
Citation: *Physica B: Condensed Matter, Volume 403, Issues 21-22, November 2008,* 3976-3979

Title: Thermoelectric figure of merit of LSCoO–Mn perovskites
Author(s): J.E. Rodríguez, D. Cadavid, and L.C. Moreno
Citation: *Microelectronics Journal, Volume 39, Issue 11, November 2008, Pages 1236-1238*

Title: Thermoelectric power factor of LaSCoO compounds
Author(s): L.C. Moreno, D. Cadavid, J.E. Rodríguez
Citation: *Microelectronics Journal, Volume 39, Issues 3-4, March-April 2008,* 548-550

Title: Thermoelectric properties of Bi-Sb samples grown by mechanical alloy.
Author(s): D. Cadavid, J.E. Rodríguez
Citation: *Physica Status Solidi (C), Volume 2 (10), 2005, 3677-3680*

Title: Propiedades termoeléctricas de muestras policristalinas de $La_{1.9}\ Sr_{0.1}\ CuO_{4+d}$
Author(s): D. Cadavid, J.E. Rodríguez, A.P. Pardo
Citation: *Revista Colombiana de Física, V. 39, No. 1, p.1463, 2007.*

Title: Conductividad térmica de muestras policristalinas de $La_{1.9}\ Sr_{0.1}\ CuO_{4+d}$ deficientes en oxígeno
Author(s): D. Cadavid, L.E. Villamil, J.E. Rodríguez
Citation: *Revista Colombiana de Física, V. 39, No. 2, p.391, 2007.*

Title: Thermal Conductivity of Ag and Au Doped YBCO samples
Author(s): J.E. Rodríguez, D. Cadavid, A. Mariño
Citation: *Revista Colombiana de Física, V. 38, No. 3, p.293, 2006.*

Title: Thermoelectric power factor of Ag doped YBCO samples
Author(s): J.E. Rodríguez, D. Cadavid, A. Mariño
Citation: *Revista Colombiana de Física, V. 38, No. 4, p.1050, 2006.*

Title: Seebeck Coefficient of Bi-Sb Samples Grown by Mechanical Alloy
Author(s): J.E. Rodríguez, D. Cadavid
Citation: IEEE Proceedings of the XXIV INTERNATIONAL CONFERENCE ON THERMOELECTRICS, Pages 399-401, 2005

# *Conferences presentations*

**E- MRS 2013 Spring Meeting**
Oral presentation: *"Thermoelectric Properties of Solution-Processed Chalcogenide-Nanocomposites"*
Strasbourg, France
$27^{th}$ – $31^{th}$ May, 2013

**The $31^{st}$ International & $10^{th}$ European conference on Thermoelectrics**
Oral presentation:*" Solution-processed nanostructures to enhance the thermoelectric properties of chalcogenide-based nanocomposites"*
Aalborg, Denmark
$9^{th}$ – $12^{th}$ July, 2012

**The $31^{st}$ International & $10^{th}$ European conference on Thermoelectrics**
Oral presentation: "Bottom-up processing of thermoelectric nanocomposites"
Aalborg, Denmark
$9^{th}$ – $12^{th}$ July, 2012

**$9^{th}$ European conference on Thermoelectrics**
Oral presentation:*" Thermoelectric Properties of Solution-Processed Chalcogenide Nanocomposites"*
Thessaloniki, Greece
$28^{th}$ – $30^{th}$ September, 2011

**93 reunión Nacional de Física Argentina**
Poster: Síntesis y caracterización de nanoestructuras de $TiO_2$.
Buenos Aires, Argentina.
September 15 - 19, 2008.

**VIII Encuentro CNEA "Superficies y Materiales Nanoestructurados"**
Poster: Síntesis y caracterización de nanotubos de $TiO_2$.
Centro Atómico Bariloche, San Carlos de Bariloche, Argentina.
May 15 - 17, 2008.

**XIII Latin American Congress on Surface Science and its Applications – CLACSA**
Poster: Thermoelectric figure of merit of LSCoO-Mn perovskites
Santa Marta, Colombia.
December 3 - 7, 2007.

**Congreso Nacional de Física 2007**
Oral Presentation: Propiedades de transporte en muestras policristalinas de $Zn_4Sb_3$.
University of Tolima, Ibague, Colombia.
October 22-26, 2007

**VI International Conference on Low Dimensional Structures and Devices**
Poster 1: Thermoelectric power factor of polycrystalline LSCoO compounds.
Poster 2: Power Factor of Zn4Sb3 Compounds Prepared by Mechanical Alloy and Solid State Reaction.
San Andrés, Colombia.
April 15 - 20, 2007.

**VII Escuela nacional de Física de la materia condensada 2006**
Poster 1: Propiedades termoeléctricas de muestras policristalinas de $La_{1.9}\ Sr_{0.1}\ CuO_{4+d}$
Poster 2: Conductividad térmica de muestras policristalinas de $La_{1.9}\ Sr_{0.1}\ CuO_{4+d}$ deficientes en oxígeno
University Pedagogy and Technology of Colombia, Tunja, Colombia.
October 23-27, 2006.

**Congreso Nacional de Física 2005**
Poster: Propiedades termoeléctricas de muestras de Bi-Sb producidas por reacción de estado sólido
University of Atlantico, Barranquilla, Colombia.
October 24-28, 2005

**XXIV INTERNATIONAL CONFERENCE ON THERMOELECTRICS**
Oral presentation: Seebeck Coefficient of Bi-Sb Samples Grown by Mechanical Alloy
University of Clemson, Clemson, SC, USA
2005

**XVII SIMPOSIO LATINOAMERICANO DE FÍSICA DEL ESTADO SÓLIDO,**
Poster: Thermoelectric properties of Bi-Sb samples grown by mechanical alloy.
La Habana, Cuba
2004

## ACADEMIC EVENTS

**International Spring School on Field Assisted Sintering Technique (FAST)**
Materials Science Department of the Technische Universität Darmstadt
$20^{th}$ – $25^{th}$March, 2011

**EELS microscopy and electronic crystallography course**
University of Barcelona, Spain
November 10-12, 2010

**Latin-American workshop/School about Condensed Matter**
**"**Applications of Raman Scattering and Synchrotron Radiation to the Study of Solid State Matter".
*Experimental Techniques: introduction of solid state, X-ray diffraction, infrared, Raman ,X- ray absorption (EXAFS y XANES), magnetic dichroism, fluorescence, high pressure (DAC)*
Universidad del Nordeste, provincia de Corrientes (Argentina)
June 11-22, 2007

**V Regional school of crystallography and (X-ray) Diffraction (techniques). 2004.**
Instituto de Materiales y Reactivos Universidad de la Habana (Cuba)
December 1-4, 2004

# AWARDS

**Grant: Laboratory Technician –for Intitut de Recerca en Energia de Catalunya**
Programa de Tecnicos de Apoyo-Ministerio de Ciencia e Innovación España
Granted on: December 17, 2010
Duration: 3 Years

# Annex

J Nanopart Res (2012) 14:1328
DOI 10.1007/s11051-012-1328-0

RESEARCH PAPER

# Bottom-up processing of thermoelectric nanocomposites from colloidal nanocrystal building blocks: the case of $Ag_2Te$–PbTe

**Doris Cadavid · Maria Ibáñez · Stéphane Gorsse · Antonio M. López · Albert Cirera · Joan Ramon Morante · Andreu Cabot**

Received: 2 September 2012 / Accepted: 16 November 2012 / Published online: 28 November 2012


**Abstract** Nanocomposites are highly promising materials to enhance the efficiency of current thermoelectric devices. A straightforward and at the same time highly versatile and controllable approach to produce nanocomposites is the assembly of solution-processed nanocrystal building blocks. The convenience of this bottom-up approach to produce nanocomposites with homogeneous phase distributions and adjustable composition is demonstrated here by blending $Ag_2Te$ and PbTe colloidal nanocrystals to form $Ag_2Te$–PbTe bulk nanocomposites. The thermoelectric properties of these nanocomposites are analyzed in the temperature range from 300 to 700 K. The evolution of their electrical conductivity and Seebeck coefficient is discussed in terms of the blend composition and the characteristics of the constituent materials.

D. Cadavid · J. R. Morante · A. Cabot (✉)
Catalonia Institute for Energy Research, IREC,
08930 Sant Adrià del Besos (Barcelona), Spain
e-mail: acabot@irec.cat

M. Ibáñez · A. Cirera · J. R. Morante · A. Cabot
Departament d'Electrònica, Universitat de Barcelona,
08028 Barcelona, Spain

S. Gorsse
CNRS, Université de Bordeaux, ICMCB, 87 avenue du
Docteur Albert Schweitzer, 33608 Pessac Cedex, France

A. M. López
Departament d'Enginyeria Electrónica, Universitat
Politècnica de Catalunya, EPSEVG, Av.Victor Balaguer
s/n, 08800 Barcelona, Spain

**Keywords** Nanocomposites · Colloidal nanoparticles · $Ag_2Te$ · PbTe · Thermoelectric · Energy · Bottom-up

## Introduction

Today's main strategy to engineer highly efficient thermoelectric materials is to reduce thermal conductivity by introducing phonon scattering centers at different length scales (Zebarjadi et al. 2012; Vineis et al. 2010). Alloys of heavy elements and complex solid solutions including 1D phonon scattering centers or 2D layered structures trigger phonon scattering at the atomic length scale (Dresselhaus et al. 2007; Gascoin et al. 2005; Feldman et al. 2000; Snyder and Toberer 2008). On the other hand, nanomaterials, having large interface densities introduced by the reduction of their crystal domains to the nanoscale, can efficiently scatter phonons at the 1–100 nm scale (Vaqueiro and Powell 2010; Bux et al. 2010; Szczech et al. 2011; Medlin and Snyder 2009; Poudel et al. 2008). A particularly interesting class of nanostructured materials is that of nanocomposites containing crystal domains with different phases and/or compositions. In nanocomposites, interfaces between dissimilar materials boost phonon scattering due to acoustic impedance mismatches (Cahill et al. 2003). Heterointerfaces may even allow reducing the electronic contribution to the thermal conductivity (Bian et al. 2007; Minnich et al. 2009; Humphrey and Linke

2005). Moreover, nanocomposites offer a mechanism to improve electrical conductivity through removing ionized impurities from avenues of charge carrier transport (Dingle et al. 1978; Zebarjadi et al. 2011). An additional potential advantage of nanocomposites is the possibility to decouple the Seebeck coefficient from electrical conductivity (Hicks and Dresselhaus 1993; Vashaee and Shakouri 2004; Sootsman et al. 2008). In this regard, the increase of the electronic density of states near the Fermi level in quantum confined nanostructures has been predicted to enhance the Seebeck coefficient (Szczech et al. 2011; Cornett and Rabin 2011). Additionally, energy filtering at nanocrystal interfaces may further enhance the thermopower of nanostructured material by selectively scattering low energy charge carriers (Heremans et al. 2004; Martin et al. 2009; Popescu et al. 2009; Faleev and Léonard 2008).

The ball-milling of crystalline ingots into fine powders and the posterior bulk reconstruction by hot-pressing is the most usual and general technique to obtain bulk nanocrystalline materials (Lan et al. 2010). However, such top–down industrial approach is time and energy consuming and no control on the size and shape of the nanoparticles is possible. The formation of nanoscale precipitates or organized superstructures by phase segregation in metastable solid solutions is a more elegant method to produce nanocomposites (Hsu et al. 2004; Quarez et al. 2005; Gorsse et al. 2010, 2011). Nevertheless, this procedure is limited to specific compositions and lacks of a high degree of control over the size and shape of the nanoinclusions.

Solution-synthesis routes are particularly well suited to provide nanoparticles for the bottom-up production of nanocomposites (Zhao et al. 2011; Scheele et al. 2009, 2010; Prasher 2006; Kovalenko et al. 2010; Ibáñez et al. 2013a, b) with a high degree of control over the size, shape, and composition of the crystal nanodomains (Ibáñez et al. 2011; Li et al. 2011). Nanocomposites can be easily obtained by simply mixing solutions containing different nanoparticles. Blending nanocrystals while dispersed in solution allows an intimate intermixing of the different components. After removal of organics, nanocrystals can be consolidated into macroscopic nanocomposites by techniques such as spark-plasma-sintering and cold- or hot-pressing. Even though the complete removal of surfactants is still a difficulty, important progress has also been achieved in this area (Scheele et al. 2010; Kovalenko et al. 2010). On the other hand, self-purification allows the use of relatively low purity precursors, which is economically advantageous. However, it hampers the potential for nanocrystal doping (Dalpian and Chelikowsky 2006; Norris et al. 2008; Erwin et al. 2005). This drawback can be overcome by adjusting the composition in ternary or quaternary compounds (Ibáñez et al. 2012a, b, c). Another possibility to control carrier concentration in nanocomposites obtained by bottom-up approaches is to cleverly select the combination of materials and their correct proportions (Urban et al. 2007; Ko et al. 2010).

An especially appealing thermoelectric nanomaterial is the one obtained from the combination of lead and silver tellurides (Lensch-Falk et al. 2010; Pei et al. 2011a, b; Paul et al. 2010). The control of the carrier concentration and the formation of nanocrystalline inclusions in these nanocomposites have allowed reaching ZT values up to 1.6 (Pei et al. 2011a, b).

The present work explores the potential of solution-processing techniques to obtain binary bulk nanocomposites with superior thermoelectric properties in the system Ag-Pb-Te. Binary $Ag_2Te$–PbTe bulk nanocomposites were produced by blending in solution PbTe and $Ag_2Te$ nanocrystals in different proportions. The thermoelectric properties of the formed nanocomposites were analyzed in the temperature range from 300 to 700 K.

## Experimental details

### Materials

Tri-n-octylphosphine (TOP, 97 %) and silver chloride (99.9 %) were purchased from Strem. Tellurium pieces (99.999 %), lead acetate trihydrate (99.999 %), 1-octadecene (ODE, 90 %), oleylamine (OLA tech. 70 %), and oleic acid (OA, tech. 90 %) were purchased from Aldrich. Analytical grade ethanol, hexane, and toluene were purchased from Panreac. All chemicals were used without further purifications. Stock solutions of TOP-Te (1 M) and TOP-Ag (1 M) were prepared by dissolving 12.76 g of tellurium pieces and 14.33 g of silver chloride in 100 ml of TOP, respectively. These solutions were prepared and stored inside an Ar-filled glovebox.

All nanocrystal preparations were carried out using standard airless techniques: a vacuum/dry Ar Schlenk line was used for the synthesis and an Ar-filled

glovebox for storing and handling air- and moisture-sensitive chemicals.

### Preparation of PbTe nanocrystals

A modified approach of that used by Urban et al. (2006) was used for the preparation of PbTe nanocrystals. In a typical procedure, lead acetate tryhidrate (0.5670 g, 1.5 mM) and OA (1.5 ml, 4.75 mM) were dissolved in 10 ml ODE. This mixture was degassed at 70 and 150 °C for 0.5 h to form lead oleate complex and remove water and acetic acid. The solution was flushed with Ar and the temperature was raised up to 180 °C. Afterward, 2 ml of 1 M TOP-Te were rapidly injected. The reaction mixture was maintained in the temperature range 160–180 °C for 3 min and then quickly cooled down to room temperature using a water bath. After cooling, the nanoparticles were precipitated by adding a hexane/ethanol (3:1) combination followed by centrifugation. This procedure was repeated twice. The precipitated nanoparticles were transferred to an Ar-filled glovebox, where they were stored until future use.

### Preparation of $Ag_2Te$ nanocrystals

$Ag_2Te$ nanocrystals were produced using a modified version of the method developed by Ko et al. (2010). In a typical procedure, 10 ml of OLA were added to a three-neck flask and heated up to 100 °C under vacuum for 1 h to remove low boiling point impurities and water. Afterward, the reaction flask was flushed with Ar and temperature was raised up to 160 °C. A mixture of 5 ml of TOP-Ag stock solution and 2.5 ml of TOP-Ag was quickly injected. After injection, the reaction temperature was maintained between 130 and 160 °C for 3 min. Then the reaction solution was cooled using a cold water bath. $Ag_2Te$ nanocrystals were precipitated and redispersed using ethanol and toluene twice. Finally, the nanocrystals were dispersed in toluene and stored in the glovebox.

### Nanocomposite preparation

PbTe and $Ag_2Te$ nanoparticles dispersed in toluene were blended at various molar fractions, 25/75, 50/50, and 75/25. After several additional precipitation and redispersion cycles, the resultant blends were dried under Ar atmosphere. The blends were annealed at 500 °C during 2 h in Ar flow. Finally, the resulting materials were pressed under a load of 5 tons at room temperature. This way, dense pellets with 13 mm diameter and 1 mm thickness were obtained.

### Structural and chemical characterization

Powder X-ray diffraction (XRD) analysis were carried out on a Bruker AXS D8 ADVANCE X-ray diffractometer with Cu Kα1 radiation ($\lambda = 1.5406$ Å). Size and shape of the nanoparticles were examined by transmission electron microscopy (TEM) using a JEOL 2100 operating at 200 keV accelerating voltage. Scanning electron microscopy (SEM) was performed using a ZEISS Auriga SEM with an energy-dispersive X-ray spectroscopy (EDX) detector to study composition. X-ray photoelectron spectroscopy (XPS) spectra were obtained using a *SPECS SAGE ESCA* System employing Mg Kα ($E = 1{,}253.6$ eV) with a supplied power of 203 W as the X-ray source.

### Thermoelectric characterization

Seebeck coefficient and electrical resistivity were measured simultaneously using a Linseis—LSR 3 system under helium atmosphere. The Seebeck coefficient was obtained using a static DC method. The electrical resistivity was measured by means of a standard four probe technique in the temperature range from 300 to 700 K. Thermal conductivity measurements were obtained from flash diffusivity measurements (Netzsch LFA-457 Microflash) using the mass density and the Dulong-Petit approximation to determine the specific heat capacity. The thermal conductivity was calculated as $\kappa = DC_p d$, where $D$ is the thermal diffusivity, $C_p$ is the heat capacity, and $d$ is the density.

## Results and discussion

Figure 1 shows representative TEM micrographs of the PbTe and $Ag_2Te$ nanoparticles used as building blocks to produce the $(Ag_2Te)_x(PbTe)_{1-x}$ ($x = 0.25$, 0.50, 0.75) nanocomposites. Insets display the histograms of their size distribution. PbTe nanoparticles had cubic morphologies and a face-centered cubic crystal phase (JCPDS 38-1435). Their average size, taken as the diagonal of one of their faces was 19 nm

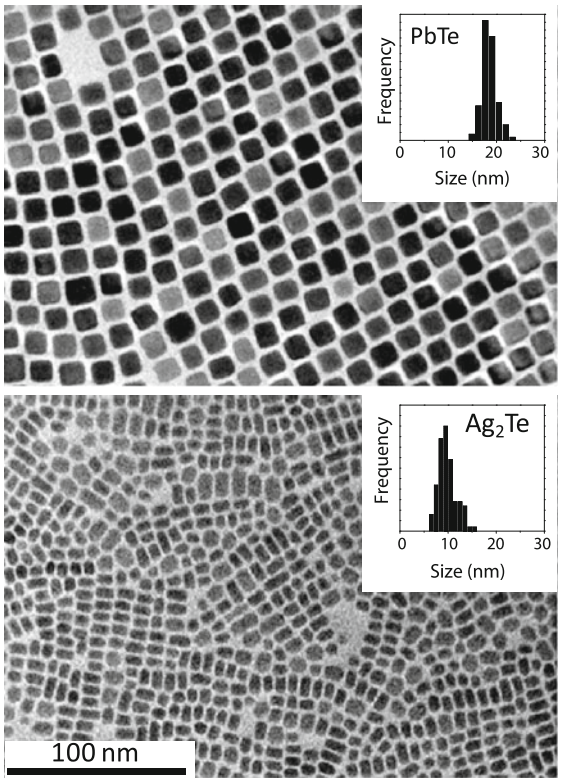


**Fig. 1** Representative TEM micrographs of the PbTe (*top*) and $Ag_2Te$ (*bottom*) nanoparticles used to produce the nanocomposites. *Insets* display the histograms of the particle size distributions

and their size distribution had 5 % dispersion. $Ag_2Te$ nanoparticles had disk-like morphology and a monoclinic crystal phase at ambient temperature (JCPDS 34-0142). Their average diameter was 10 nm and their size dispersion was close to 10 %. PbTe and $Ag_2Te$ nanoparticles were not intentionally doped by extrinsic impurities.

Figure 2 shows a scheme of the procedure used to produce the binary nanocomposites from solutions containing the PbTe and $Ag_2Te$ colloidal building blocks. While short range ordering of the nanocrystals at submicron scales may exist, at the macroscopic level the different phases must be considered as randomly distributed. The nanoparticle mixture was prepared while having the nanocrystals well dispersed in toluene to ensure a homogeneous blending of the two components at the nanometer scale. Three different compositions were prepared, having the following molar fractions: $(Ag_2Te)_{0.75}(PbTe)_{0.25}$, $(Ag_2Te)_{0.50}(PbTe)_{0.50}$, and $(Ag_2Te)_{0.25}(PbTe)_{0.75}$. Once mixed, the nanoparticle blends were thoroughly purified by multiple precipitation and redispersion steps. Final nanoparticles were not soluble, probing the high degree of surfactant removal from their surfaces. The purified nanoparticle blends were annealed at 500 °C during 2 h in an argon flow atmosphere. The concentration of residual carbon in the final materials was less than 2 %, as determined by elemental analysis. The annealed nanocomposite powders were cold-pressed into 13 mm pellets by applying 380 MPa pressure with a hydraulic press. At the same time, pure $Ag_2Te$ and PbTe pellets were prepared following the same protocol and using the exact same nanocrystals used to obtain the blends. The relative density of the produced pellets was around 80 %. Figure 3 shows a SEM image of the $(Ag_2Te)_{0.75}(PbTe)_{0.25}$ nanopowders obtained after annealing. Elemental mappings obtained by SEM-EDX characterization of the nanocomposites showed the spatial distribution of the two phases to be highly homogeneous (Fig. 3).

Figure 4 shows the XRD patterns of the annealed nanomaterials. The XRD patterns of the nanocomposites resembled the combination of the XRD patterns obtained from the pure materials. No evidences of alloying between the two phases could be obtained from this analysis. At the same time, no secondary phases were detected. The fitting of the XRD patterns allowed estimating the growth of the crystallographic domains with the thermal treatment. From the Scherer equation, the crystal domain size of both phases in the annealed material was calculated to be approximately 40 nm.

XPS analysis of the materials revealed an increase of the oxygen concentration at the nanoparticle surface with the annealing treatment. Typically, XPS analysis of the nanoparticle before annealing (but exposed to air for several hours) showed a 7 % concentration of oxygen. This value increased up to a 30 % with the annealing process. Therefore, we estimate oxidation to extend 1–2 nm from the particle surface, forming an amorphous oxide shell.

The electrical conductivity and Seebeck coefficient of the nanocomposites were characterized in the temperature range from 300 to 700 K. Figure 5(left) and (center) display the temperature dependence of the electrical conductivity and Seebeck coefficient for the three $(Ag_2Te)_x(PbTe)_{1-x}$ ($x = 0.25, 0.50, 0.75$) nanocomposites and for the pure PbTe and $Ag_2Te$ nanomaterials.

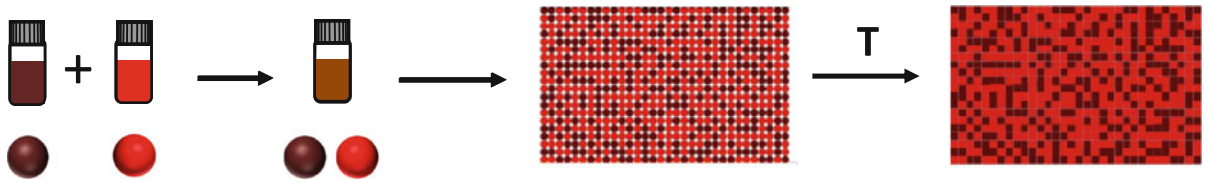


**Fig. 2** Scheme of the procedure used to produce binary nanocomposites from solution-processed nanocrystals

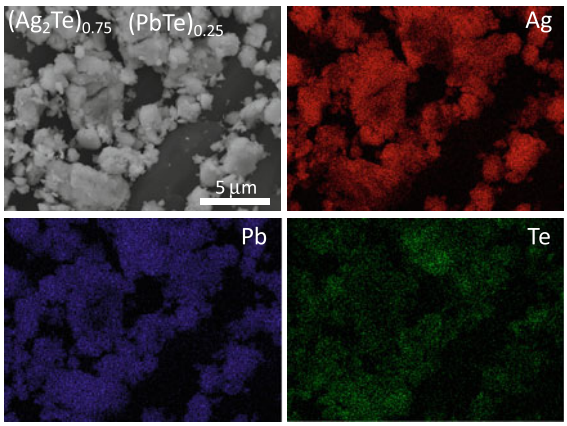


**Fig. 3** SEM image and EDX elemental maps of the annealed $(Ag_2Te)_{0.75}$ $(PbTe)_{0.25}$ nanocomposite powder

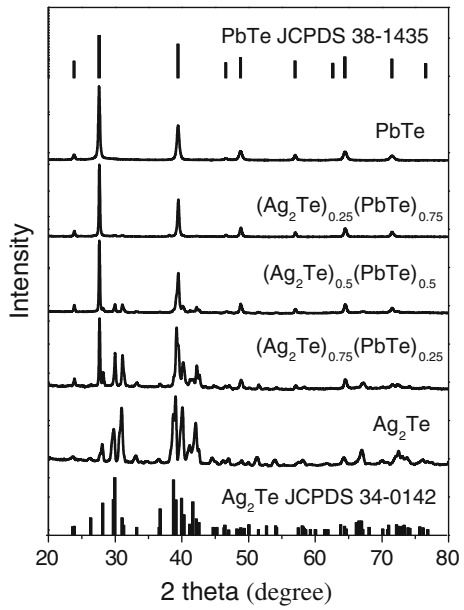


**Fig. 4** XRD patterns of the annealed nanocomposites. $Ag_2Te$ (JCPDS 34-0142) and PbTe (JCPDS 38-1435) patterns have been included as a reference

One first clearly noticeable feature in Fig. 5(left) is the non-monotonic evolution of the pure $Ag_2Te$ electrical conductivity with temperature. For this material, a decrease of electrical conductivity of over an order of magnitude was systematically obtained in the temperature range between 400 and 450 K. This is associated to the well-known phase transition from the low-temperature monoclinic α-$Ag_2Te$ to the high-temperature cubic β-$Ag_2Te$.[1] The low-temperature α-$Ag_2Te$ phase is a very narrow band-gap semiconductor ($E_g = 0.025$ eV), which in bulk displays high electron mobility and a low lattice thermal conductivity (Sakuma and Saitoh 1985; Fujikane et al. 2005a, b; Taylor and Wood 1961; Capps et al. 2010; Dalven and Gill 1966; Wood et al. 1961; Schneider and Schulz 1993; Dalven and Gill 1967). A slight decrease of electrical conductivity with temperature and a negative Seebeck coefficient in the range 300–400 K were measured for this material. These results are consistent with previous reports showing the low-temperature α-$Ag_2Te$ to be a degenerate semiconductor displaying n-type conductivity (Das and Karunakaran 1984). Our experimental results showed the phase transformation for this material to be accompanied by a transition from n-type to p-type conductivity. The high-temperature β-$Ag_2Te$ bulk nanomaterial displayed a positive Seebeck coefficient and its electrical conductivity increased with temperature in all the range measured. In intrinsic β-$Ag_2Te$, the much lower effective masses for electrons than holes usually translate into an n-type conductivity (Fujikane et al. 2005a, b). However, the conductivity type of this material is known to be highly dependent on composition. In this regards, stoichiometric and Ag-rich samples show n-type conductivity, while Te-rich $Ag_2Te$ displays p-type conductivity (Capps et al. 2011; Max-Planck-Gesellschaft 1973). Aside from composition variations, the p-type conductivity obtained here could be explained by a possible surface oxidation of the small colloidal nanocrystals during their processing into pellets. From

[1] Notice that there is some controversy in the nomenclature of the different $Ag_2Te$ phases. We use $\alpha$ to denote the low-temperature $Ag_2Te$ phase and $\beta$ for the high-temperature one.

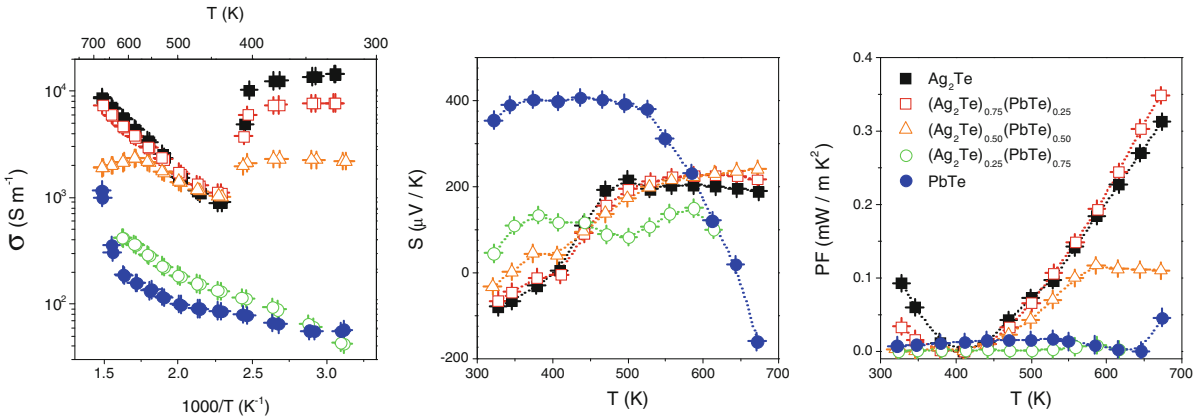


**Fig. 5** Temperature dependence of the electrical conductivity (*left*), Seebeck coefficient (*center*), and power factor (*right*) obtained from the produced nanomaterials: $Ag_2Te$ (*filled square*); $(Ag_2Te)_{0.75}(PbTe)_{0.25}$ (*open square*); $(Ag_2Te)_{0.5}(PbTe)_{0.5}$ (*open triangle*); $(Ag_2Te)_{0.25}(PbTe)_{0.75}$ (*open circle*); PbTe (*filled circle*)

the lineal dependence of ln $\sigma T^{-3/2}$ with the inverse of temperature in the high-temperature range, an activation energy for electrical conductivity of 0.18 eV was calculated. This activation energy could be associated with the thermal generation of electron-hole pairs through a 0.36 eV band gap. The flattening of the Seebeck coefficient evolution with the temperature supports the hypothesis of an intrinsic semiconductor character at this high-temperature region. However, the obtained band gap is considerably higher than the 0.20–0.28 eV measured previously for this material (Van Dong and Tung 1968). From the maximum of the Seebeck coefficient obtained for this material and using the equation $E_g = 2eS_{max}T_{max}$ (Goldsmid and Sharp 1999), a 0.2 eV band gap was calculated. This value is consistent with previously published band gap estimates. Thus, the calculated activation energy for electrical conductivity should be at least in part associated with mobility energy barriers at the grain boundaries, which probably results from the presence of an oxide layer at the nanoparticles surface (Ko et al. 2010; Scheele et al. 2011).

Pure PbTe pellets displayed p-type electrical conductivity in most of the temperature range measured. The p-type character of the PbTe nanocrystalline pellet had its origin on a thin oxide layer at the nanoparticles surface (Paul and Banerji 2011; Rogacheva et al. 2001; Schenk et al. 1988; Wang et al. 2008), on the presence of electrically active lattice defects associated with deviations from stoichiometry or on the broken bonds at the grain boundaries (Borisova 1979; Breschi et al. 1982; Crocker and Rogers 1967; Martin et al. 2007; Allgaier 1961; Grekov et al. 1997; Scanlon 1962; Dashevsky et al. 2005). The slight increase of electrical conductivity with temperature in the low temperature range and the constant Seebeck coefficient obtained pointed toward the full ionization of acceptor levels at temperatures above 350 K. From the maximum of the Seebeck coefficient, a 0.30 eV band gap was calculated. This value correlated well with the optical band gap previously measured for this material (Zemel et al. 1965). A sign inversion in the carrier type, from p to n, was clearly observed at approximately 650 K. This was probably associated with the thermal activation of electron-hole pairs through the semiconductor band gap. The higher mobilities for electrons than holes in this material would compensate the higher hole concentration and trigger the conduction type inversion. The conduction type inversion was accompanied by a strong increase of electrical conductivity above 600 K, most probably associated to the overcome of the energy barriers at the grain boundaries.

In the low-temperature range, the blending of $Ag_2Te$ with PbTe nanocrystals resulted in nanocomposites with electrical conductivities lower than that of $Ag_2Te$. This electrical conductivity decrease was associated with a reduction of the charge carrier mobility with the blending, or with a reduction of the charge carrier density with the reduction of the relative $Ag_2Te$ content. A partial compensation of the majority carriers of each material may also contribute to the lower electrical conductivities observed. Below the $Ag_2Te$ phase transition temperature, a shift of the

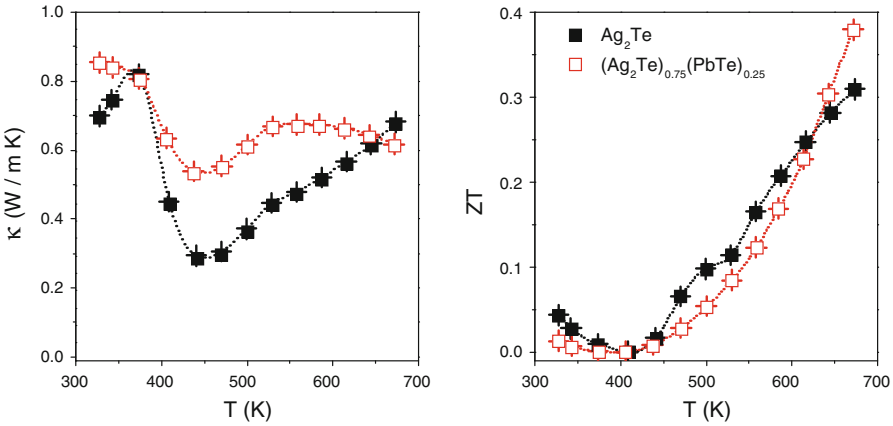


**Fig. 6** Temperature dependence of the thermal conductivity (*left*) and thermoelectric figure of merit (*right*) obtained from the $(Ag_2Te)_{0.75}(PbTe)_{0.25}$ nanocomposite (*open square*) and the $Ag_2Te$ nanomaterial (*filled square*)

Seebeck coefficient toward positive values was also obtained when increasing the PbTe ratio in the blend.

In the full temperature range, the temperature dependences of the electrical conductivities and Seebeck coefficients obtained with the $(Ag_2Te)_{0.75}(PbTe)_{0.25}$ and $(Ag_2Te)_{0.5}(PbTe)_{0.5}$ nanocomposites clearly resembled that of pure $Ag_2Te$. In these two nanocomposites, a step change in the conductivity and the Seebeck coefficient was also observed at around 420 K. This was associated with the monoclinic to cubic phase transition taking place within the $Ag_2Te$ crystallographic domains. Like in the case of pure $Ag_2Te$, in the low temperature range, nanocomposites showed n-type conductivity with a minor temperature dependence of the conductivity. On the other hand, above 450 K, nanocomposites displayed p-type character and a clear increase of electrical conductivity with temperature. In both nanocomposites, an activation energy for conductivity similar to that obtained for pure $Ag_2Te$ material could be observed. However, in the 50 % blend, a clear influence of PbTe was obtained above 600 K, where a decrease of electrical conductivity was obtained. This was most probably related with the recombination of the n-type carriers created within the PbTe nanocrystals with the majoritary holes within the $Ag_2Te$. This decrease of electrical conductivity resulted in a limitation of this material's power factor above 600 K, as shown in Fig. 5.

The temperature dependence of the electrical conductivity measured from the $(Ag_2Te)_{0.25}(PbTe)_{0.75}$ nanocomposite resembled that of the pure PbTe nanomaterial. It showed a monotone increase with the temperature. Different lineal regions were observed when plotting the logarithm of conductance against reciprocal temperature, revealing the existence of multiple energy activated barriers and thus the contribution of multiple acceptor and donor states to charge transport.

Nanocomposites were characterized by temperature dependences of the electrical conductivity and Seebeck coefficient that clearly resembled those of the pure materials. This fact pointed toward the coexistence of the two phases within the nanocomposite, which was consistent with the results obtained from the XRD characterization of the materials. The alloying of the two materials would be expected to result in a modification of the semiconductor band gap and thus into different dependences of the thermoelectric properties with temperature (Pei et al. 2011a, b).

The best power factors were finally obtained from the pure $Ag_2Te$ nanomaterial and the $(Ag_2Te)_{0.75}(PbTe)_{0.25}$ nanocomposites. For these two materials, the thermal conductivity was also measured (Fig. 6). A clear decrease of the thermal conductivity with the low temperature monoclinic $\alpha$-$Ag_2Te$ to the high-temperature cubic $\beta$-$Ag_2Te$ phase transition was noticed at around 400 K. The already very low thermal conductivities obtained for the pure $Ag_2Te$ nanomaterial hinder a further decrease of thermal conductivity with the blending of the two different phases. Only in the high-temperature range, the nanocomposite displayed lower thermal conductivities than the pure material. The low thermal conductivities obtained for both samples in all the temperature range measured are related to the very high density of interfaces and the relatively low density of the pellets measured. Higher pellet densities would have associated both a higher thermal conductivity and a higher electrical conductivity. This effect was estimated to

account for up to a 40 % variation of both thermal and electric conductivity of the theoretical value to be expected for sample with 100 % relative density (Scheele et al. 2010).

The thermoelectric figure of merit reached up to 0.38 for the $(Ag_2Te)_{0.75}(PbTe)_{0.25}$ nanocomposite at 670 K (Fig. 6). This represents a 25 % increase over pure $Ag_2Te$ and it is an excellent ZT value taking into account that no extrinsic doping was intentionally introduced in these materials. The production of nanocomposites with much higher thermoelectric figures of merit ($ZT > 1.5$) by bottom-up approaches based on solution-processed nanocrystals will necessarily require the control of the carrier concentration of each compound through doping.

## Conclusion

$(Ag_2Te)_x(PbTe)_{1-x}$ nanocomposites with controlled composition were obtained by means of a very facile bottom-up approach consisting in the solution blending of colloidal nanocrystals. The temperature dependence of the electrical conductivity and Seebeck coefficient of the obtained materials could be described from the combination of the properties of the two constituent materials. Undoped $(Ag_2Te)_{0.75}(PbTe)_{0.25}$ nanocomposites displayed the best power factors among the different nanocomposites tested and reached ZT values up to 0.38 at 670 K.

**Acknowledgments** The research was supported by the European Regional Development Funds and the Spanish MICINN Projects MAT2008-05779, MAT2008-03400-E/MAT, MAT2010-15138, MAT2010-21510, CSD2009-00050, and ENE2008-03277-E/CON. M.I. is grateful to the Spanish MICINN for her PhD grant. A. Cirera acknowledges support from ICREA Academia program. A. Cabot is grateful to the Spanish MICINN for financial support through the Ramón y Cajal program.

## References

Allgaier RS (1961) Valence bands in lead telluride. J Appl Phys 32:2185–2189

Bian Z, Zebarjadi M, Singh R et al (2007) Cross-plane Seebeck coefficient and Lorenz number in superlattices. Phys Rev B 76:205311

Borisova LD (1979) Thermoelectric properties of impurity doped PbTe. Physica Status Solidi (a) 53:K19–K22

Breschi R, Camanzi A, Fano V (1982) Defects in PbTe single crystals. J Cryst Growth 58:399–408

Bux SK, Fleurial J-P, Kaner RB (2010) Nanostructures materials for thermoelectric applications. Chem Comm 46:8311–8324

Cahill DG, Ford WK, Goodson KE et al (2003) Nanoscale thermal transport. J Appl Phys 93:793–818

Capps J, Drymiotis F, Lindsey S, Tritt TM (2010) Significant enhanced of the dimensionless thermoelectric figure of merit binary $Ag_2Te$. Phyl Mag Lett 90:677–681

Capps J, Ma B, Drye T et al (2011) The effect of Ag concentration on the structural, electrical and thermal transport behavior of Pb:Te:Ag:Se mixtures and improvement of thermoelectric performance via Cu doping. J Alloy Compd 509:1544–1549

Cornett JE, Rabin O (2011) Thermoelectric figure of merit calculations for semiconducting nanowires. Appl Phys Lett 98:182104–182104–3

Crocker AJ, Rogers LM (1967) Interpretation of the Hall coefficient, electrical resistivity and Seebeck coefficient of p-type lead telluride. Br J Appl Phys 18:563–573

Dalpian GM, Chelikowsky JR (2006) Self-purification in semiconductor nanocrystals. Phys Rev Lett 96:226802

Dalven R, Gill R (1966) Energy gap in β-$Ag_2Te$. Phys Rev 143:666–670

Dalven R, Gill R (1967) Electrical properties of β-$Ag_2Te$ and β-$Ag_2Se$ from 4.2° to 300°K. J Appl Phys 38:753–756

Das VD, Karunakaran D (1984) Thermoelectric studies on semiconducting $Ag_2Te$ thin films: temperature and dimensional effects. Phys Rev B 30:2036–2041

Dashevsky Z, Kreizman R, Dariel MP (2005) Physical properties and inversion of conductivity type in nanocrystalline PbTe films. J Appl Phys 98:094309–094309–5

Dingle R, Störmer HL, Gossard AC, Wiegmann W (1978) Electron mobilities in modulation-doped semiconductor heterojunction superlattices. Appl Phys Lett 33:665–667

Dresselhaus MS, Chen G, Tang MY et al (2007) New directions for low-dimensional thermoelectric materials. Adv Mater 19:1043–1053

Erwin SC, Zu L, Haftel MI et al (2005) Doping semiconductor nanocrystals. Nature 436:91–94

Faleev SV, Léonard F (2008) Theory of enhancement of thermoelectric properties of materials with nanoinclusions. Phys Rev B 77:214304

Feldman JL, Singh DJ, Mazin II, Mandrus D, Sales BC (2000) Lattice dynamics and reduced thermal conductivity of filled skutterudites. Phys Rev B 61:R9209–R9212

Fujikane M, Kurosaki K, Muta H, Yamanaka S (2005a) Thermoelectric properties of α- and β-$Ag_2Te$. J Alloy Compd 393:299–301

Fujikane M, Kurosaki K, Muta H, Yamanaka S (2005b) Electrical properties of α- and β-$Ag_2Te$. J Alloy Compd 387: 297–299

Gascoin F, Ottensmann S, Stark D, Haile SM, Snyder GJ (2005) Zintl phases as thermoelectric materials: tuned transport properties of the compounds $Ca_xYb_{1-x}Zn_2Sb_2$. Adv Funct Mater 15:1860–1864

Goldsmid H, Sharp J (1999) Estimation of the thermal band gap of a semiconductor from seebeck measurements. J Electron Mater 28:869–872

Gorsse S, Bauer Pereira P, Decourt R, Sellier E (2010) Microstructure engineering design for thermoelectric materials: an approach to minimize thermal diffusivity. Chem Mater 22:988–993

Gorsse S, Bellanger P, Brechet Y, Sellier E, Umarji A, Ail U, Decourt R (2011) Nanostructuration via solid state transformation as a strategy for improving the thermoelectric efficiency of PbTe alloys. Acta Mater 59:7425–7437

Grekov Y, Shlyakhov T, Semikolenova N (1997) Inversion of the conduction type of epitaxial films of PbSnTe solid solutions under the influence of laser irradiation at subthreshold power. Semiconductors 31:844–846

Heremans JP, Thrush CM, Morelli DT (2004) Thermopower enhancement in lead telluride nanostructures. Phys Rev B 70:115334

Hicks LD, Dresselhaus MS (1993) Effect of quantum-well structures on the thermoelectric figure of merit. Phys Rev B 47:12727–12731

Hsu KF, Loo S, Guo F et al (2004) Cubic AgPbmSbTe2+m: bulk thermoelectric materials with high figure of merit. Science 303:818–821

Humphrey TE, Linke H (2005) Reversible thermoelectric nanomaterials. Phys Rev Lett 94:096601

Ibáñez M, Guardia P, Shavel A et al (2011) Growth kinetics of asymmetric Bi2S3 nanocrystals: size distribution focusing in nanorods. J Phys Chem C 115:7947–7955

Ibáñez M, Cadavid D, Zamani R et al (2012a) Composition control and thermoelectric properties of quaternary chalcogenide nanocrystals: the case of stannite Cu2CdSnSe4. Chem Mater 24:562–570

Ibáñez M, Zamani R, LaLonde A et al (2012b) Cu2ZnGeSe4 nanocrystals: synthesis and thermoelectric properties. J Am Chem Soc 134:4060–4063

Ibáñez M, Zamani R, Li W, Shavel A, Arbiol J, Morante JR, Cabot A (2012c) Extending the nanocrystal synthesis control to quaternary compositions. Cryst Growth Des 12:1085–1090

Ibáñez M, Zamani R, Li W et al (2013a) Chem Mater. doi: 10.1021/cm303252q

Ibáñez M, Cadavid D, Anselmi-Tamburini U et al (2013b) J Mater Chem A. doi:10.1039/c2ta00419d

Ko D-K, Urban JJ, Murray CB (2010) Carrier distribution and dynamics of nanocrystal solids doped with artificial atoms. Nano Lett 10:1842–1847

Kovalenko MV, Spokoyny B, Lee J-S et al (2010) Semiconductor nanocrystals functionalized with antimony telluride zintl ions for nanostructured thermoelectrics. J Am Chem Soc 132:6686–6695

Lan Y, Minnich AJ, Chen G, Ren Z (2010) Enhancement of thermoelectric figure-of-merit by a bulk nanostructuring approach. Adv Funct Mater 20:357–376

Lensch-Falk JL, Sugar JD, Hekmaty MA, Medlin DL (2010) Morphological evolution of $Ag_2Te$ precipitates in thermoelectric PbTe. J Alloy Compd 504:37–44

Li W, Shavel A, Guzman R et al (2011) Morphology evolution of Cu2 − xS nanoparticles: from spheres to dodecahedrons. Chem Commun 47:10332

Martin J, Nolas GS, Zhang W, Chen L (2007) PbTe nanocomposites synthesized from PbTe nanocrystals. Appl Phys Lett 90:222112

Martin J, Wang L, Chen L, Nolas GS (2009) Enhanced Seebeck coefficient through energy-barrier scattering in PbTe nanocomposites. Phys Rev B 79:115311

Max-Planck-Gesellschaft zur Förderung der Wissenschaften (1973) Gmelin Handbuch der anorganischen Chemie, 8. völlig neu bearbeitete Aufl. Springer, Berlin

Medlin DL, Snyder GJ (2009) Interfaces in bulk thermoelectric materials: a review for current opinion in colloid and interface science. Curr Opin Colloid Interface Sci 14:226–235

Minnich AJ, Dresselhaus MS, Ren ZF, Chen G (2009) Bulk nanostructured thermoelectric materials: current research and future prospects. Energy Environ Sci 2:466–479

Norris DJ, Efros AL, Erwin SC (2008) Doped nanocrystals. Science 319:1776–1779

Paul B, Banerji PJ (2011) Enhancement in thermoelectric power in lead telluride nanocomposite: role of oxygen vis-à-vis nanostruct. Nano Electron Phys 3:691–697

Paul B, Kumar VA, Banerji P (2010) Embedded Ag-rich nanodots in PbTe: enhancement of thermoelectric properties through energy filtering of the carriers. J Appl Phys 108:064322

Pei Y, Heinz NA, Snyder GJ (2011a) Alloying to increase the band gap for improving thermoelectric properties of $Ag_2Te$. J Mater Chem 21:18256

Pei Y, Lensch-Falk J, Toberer ES, Medlin DL, Snyder GJ (2011b) High thermoelectric performance in PbTe due to large nanoscale $Ag_2Te$ precipitates and La doping. Adv Funct Mater 21:241–249

Popescu A, Woods LM, Martin J, Nolas GS (2009) Model of transport properties of thermoelectric nanocomposite materials. Phys Rev B 79:205302

Poudel B, Hao Q, Ma Y et al (2008) High-thermoelectric performance of nanostructured bismuth antimony telluride bulk alloys. Science 320:634–638

Prasher R (2006) Ultralow thermal conductivity of a packed bed of crystalline nanoparticles: a theoretical study. Phys Rev B 74:165413

Quarez E, Hsu K-F, Pcionek R, Frangis N, Polychroniadis EK, Kanatzidis MG (2005) Nanostructuring compositional fluctuations and atomic ordering in the thermoelectric materials $AgPb_mSbTe_{2+m}$ the myth of solid solutions. J Am Chem Soc 127:9177–9190

Rogacheva EI, Krivulkin IM, Nashchekina ON, Sipatov AYu, Volobuev VV, Dresselhaus MS (2001) Effect of oxidation on the thermoelectric properties of PbTe and PbS epitaxial films. Appl Phys Lett 78:1661–1663

Sakuma T, Saitoh S (1985) Structure of α-$Ag_2Te$. J Phys Soc Jpn 54:3647–3648

Scanlon W (1962) Precipitation of Te and Pb in PbTe crystals. Phys Rev 126:509–513

Scheele M, Oeschler N, Meier K, Kornowski A, Klinke C, Weller H (2009) Synthesis and thermoelectric characterization of $Bi_2Te_3$ nanoparticles. Adv Funct Mater 19:3476–3483

Scheele M, Oeschler N, Veremchuk I, Reinsberg K-G, Kreuziger A-M, Kornowski A, Broekaert J, Klinke C, Weller H (2010) ZT enhancement in solution-grown $Sb_{(2-x)}Bi_xTe_3$ nanoplates. ACS Nano 4:4283–4291

Scheele M, Oeschler N, Veremchuk I et al (2011) Thermoelectric properties of lead chalcogenide core–shell nanostructures. ACS Nano 5:8541–8551

Schenk M, Berger H, Klimakow A, Mühlberg M, Wienecke M (1988) Nonstoichiometry and point defects in PbTe. Cryst Res Technol 23:77–84

Schneider J, Schulz H (1993) X-ray powder diffraction of $Ag_2Te$ at temperatures up to 1123 K. Z Kristallogr 203: 1–15

Snyder GJ, Toberer ES (2008) Complex thermoelectric materials. Nat Mater 7:105–114

Sootsman JR, Kong H, Uher C et al (2008) Large enhancements in the thermoelectric power factor of bulk PbTe at high temperature by synergistic nanostructuring. Angew Chem 120:8746–8750

Szczech JR, Higgins JM, Jin S (2011) Enhancement of the thermoelectric properties in nanoscale and nanostructured materials. J Mater Chem 21:4037–4055

Taylor PF, Wood C (1961) Thermoelectric properties of $Ag_2Te$. J Appl Phys 32:1–3

Urban JJ, Talapin DV, Shevchenko EV, Murray CB (2006) Self-assembly of PbTe quantum dots into nanocrystal superlattices and glassy films. J Am Chem Soc 128:3248–3255

Urban JJ, Talapin DV, Shevchenko EV et al (2007) Synergism in binary nanocrystal superlattices leads to enhanced p-type conductivity in self-assembled PbTe/$Ag_2Te$ thin films. Nat Mater 6:115–121

Van Dong N, Tung PN (1968) Transport properties of silver telluride in the solid and liquid states. Physica status solidi (b) 30:557–567

Vaqueiro P, Powell AV (2010) Recent developments in nanostructured materials for high-performance thermoelectrics. J Mater Chem 20:9577

Vashaee D, Shakouri A (2004) Improved thermoelectric power factor in metal-based superlattices. Phys Rev Lett 92: 106103

Vineis CJ, Shakouri A, Majumdar A, Kanatzidis MG (2010) Nanostructured thermoelectrics: big efficiency gains from small features. Adv Mater 22:3970–3980

Wang RY, Feser JP, Lee J-S et al (2008) Enhanced thermopower in PbSe nanocrystal quantum dot superlattices. Nano Lett 8:2283–2288

Wood C, Harrap V, Kane WM (1961) Degeneracy in $Ag_2Te$. Phys Rev 121:978–982

Zebarjadi M, Joshi G, Zhu G et al (2011) Power factor enhancement by modulation doping in bulk nanocomposites. Nano Lett 11:2225–2230

Zebarjadi M, Esfarjani K, Dresselhaus MS et al (2012) Perspectives on thermoelectrics: from fundamentals to device applications. Energy Environ Sci 5:5147

Zemel JN, Jensen JD, Schoolar RB (1965) Electrical and optical properties of epitaxial films of PbS, PbSe, PbTe, and SnTe. Phys Rev 140:A330–A342

Zhao Y, Dyck JS, Burda C (2011) Toward high-performance nanostructured thermoelectric materials: the progress of bottom-up solution chemistry approaches. J Mater Chem 21:17049

Journal of Materials Chemistry A

RSC Publishing

PAPER

View Article Online
View Journal | View Issue



Cite this: J. Mater. Chem. A, 2013, 1, 4864

# Organic ligand displacement by metal salts to enhance nanoparticle functionality: thermoelectric properties of $Ag_2Te$

Doris Cadavid,[a] Maria Ibáñez,[b] Alexey Shavel,[a] Oscar Juan Durá,[c] M. A. López de la Torre[c] and Andreu Cabot*[ab]

Received 11th December 2012
Accepted 13th February 2013

DOI: 10.1039/c3ta01455j

www.rsc.org/MaterialsA

The presence of organic ligands on the surface of colloidal nanoparticles strongly limits their performance in technological applications where charge carrier transfer/transport plays an important role. We use metal salts, matched with the nanoparticle composition, to eliminate the surface organic ligands without introducing extrinsic impurities in the final nanomaterial. The potential of the simple, general and scalable processes presented here is demonstrated by characterizing the thermoelectric properties of nanostructured $Ag_2Te$ produced by the bottom up assembly of $Ag_2Te$ nanocrystals. A 6-fold increase of the thermoelectric figure of merit of $Ag_2Te$ was obtained when organic ligands were displaced by $AgNO_3$. The same procedure can enhance the performance of nanocrystals and nanocrystal-based devices in a broad range of applications, from photovoltaics and thermoelectrics to catalysis.

## Introduction

Colloidal nanocrystals (NCs) are excellent building blocks to produce functional materials with properties engineered at the nanometer scale. Their wide fundamental and technological interest has driven the development of tools and processes to control their composition, size, shape and crystal structure with outstanding precision.[1–5] Most current synthetic routes to produce high quality NCs make use of organic surfactants. These organic molecules limit the NC growth, direct its morphology and provide it with stability in an organic medium. While some organic ligands have been demonstrated to be really efficient in these tasks, the surface barrier for charge transfer/transport that they introduce is an important downside. Most organic ligands used in colloidal synthesis routes are electrical insulators. Such electrically insulating barriers at the NC surface strongly limit its performance in a variety of applications where charge carrier transfer and transport through NCs or between the NC and the liquid/gas/solid medium play a fundamental role: *e.g.* lighting, photovoltaics, thermoelectrics, and catalysis.[6–9]

Serious efforts have been made to displace large organic ligands by shorter organic groups or inorganic ligands at the NC surface. While in some cases the exact species left at the NC surface is not known, some compounds were certainly useful in various particular applications: *e.g.* pyridine,[10] molecular metal chalcogenide complexes (MCC) stabilized by hydrazine,[11–15] nitrosonium,[16] diazonium[16] and trialkyl oxonium tetrafluoroborates;[17] tetrafluoroborate acids ($HBF_4$, $HPF_6$);[18] ammonium thiocyanate ($NH_4SCN$);[19,20] sulphides like $Na_2S$, $[NH_4]_2S$, and $K_2S$;[18,21,22] and halide anions such as $Cl^-$, $Br^-$ and $I^-$.[23–25]

However, some of these compounds require the manipulation of highly toxic chemicals (*e.g.* hydrazine); others can introduce large concentrations of foreign impurities, which may strongly modify the material properties (*e.g.* halide anions); some may even modify the chemical composition of the NC or NC-based material (*e.g.* $Na_2S$, $[NH_4]_2S$, and $K_2S$ used with non-sulphide NCs).

We present a scalable and general procedure to displace organic ligands by means of a matched metal salt solution. We use $Ag_2Te$ nanoparticles as the model material and thermoelectricity as the paradigmatic application to exemplify the detailed processes. $Ag_2Te$ is a technologically important material, displaying a high ionic conductivity at room temperature.[26] The low temperature $\alpha$-$Ag_2Te$ phase is a very narrow band-gap semiconductor ($E_g = 0.025$ eV), with a low electron effective mass, high electron mobility and a low lattice thermal conductivity.[27–34] $Ag_2Te$ also shows excellent thermoelectric properties, both in bulk and nanocrystalline form.[35,36]

Thermoelectricity is a particularly interesting application for advanced functional nanomaterials. Thermoelectric energy conversion has an enormous potential for economical and social impact.[37–39] However, current thermoelectric devices lack high enough efficiency to compete in most potential markets.

[a]Catalonia Institute for Energy Research-IREC, C. Jardins de les Dones de Negre 1, 08930 Sant Adrià del Besos, Barcelona, Spain. E-mail: acabot@irec.cat; Fax: +34 933 563 802; Tel: +34 933 562 615

[b]Departament d'Electrónica, Universitat de Barcelona, C. Marti i Franqués 1, 08028 Barcelona, Spain

[c]Departamento de Física Aplicada, Universidad de Castilla-La Mancha, Avd. Camilo José Cela, Edificio Politécnico, ETSII, 13071 Ciudad Real, Spain

Thermoelectric efficiency can be improved by controlling material composition at the nanometer scale. To date, most thermoelectric materials with high thermoelectric figures of merit ($Z = \sigma S^2/\kappa$) are nanostructured. The confinement of the lattice dimensions to the nanometer scale allows improving the thermoelectric efficiency by promoting phonon scattering at crystal interfaces and reducing in such a way the thermal conductivity ($\kappa$) of the materials.[40,41] Furthermore, the selective scattering of the low energy charge carriers at crystal interfaces provides a path towards higher Seebeck coefficients ($S$).[42,43] In this scenario, the bottom-up assembly of colloidal nanoparticles is emerging as a suitable approach to produce efficient thermoelectric materials.[44–49]

In this work, we detail a procedure to displace organic ligands from NC surfaces based on the use of a metal salt solution. Considering $Ag_2Te$ as the model material and $Ag^+$ as the matched metal ion, we demonstrate the effectiveness of this process to improve the thermoelectric figure of merit of $Ag_2Te$ nanomaterials obtained from the bottom up assembly of colloidal $Ag_2Te$ NC building blocks.

## Experimental

### Materials

Tri-*n*-octylphosphine (TOP, 97%) and silver chloride (99.9%) were purchased from Strem, and tellurium pieces (99.999%), silver nitrate (99.8%), 1-octadecene (ODE, 90%), oleylamine (OLA, tech. 70%), and formamide (FA, ≥99.5%) were purchased from Aldrich. Analytical grade ethanol, chloroform and toluene were purchased from Panreac. All chemicals were used without further purification. Stock solutions of tri-*n*-octylphosphine telluride (TOPTe) (1 M) and Ag–TOP (1 M) were prepared by dissolving 12.76 g of tellurium and 14.33 g of silver chloride in 100 ml of TOP. These solutions were prepared and stored inside an argon-filled glovebox. All NC preparations were carried out using standard air-excluding techniques: a vacuum/dry-argon Schlenk line was used for the synthesis and an argon-filled glovebox for storing and handling air- and moisture-sensitive chemicals.

### Preparation of $Ag_2Te$ nanocrystals

In a typical procedure, 10 ml of OLA were added to a three neck flask and kept at 100 °C under vacuum for 1 h to remove low boiling point impurities and water. Afterwards, the reaction flask was flushed with Ar and temperature was raised up to 160 °C. At this temperature, a mixture of 5 ml of Ag–TOP and 2.5 ml of TOPTe stock solutions was quickly injected. After injection, the reaction temperature was maintained between 130 °C and 160 °C for 3 minutes. Then the reaction solution was cooled using a water bath. $Ag_2Te$ NCs were precipitated and redispersed using ethanol and toluene twice. Finally, the NCs were dispersed in toluene and stored in the glovebox.

### Organic ligand displacement by metal salts

$Ag_2Te$ colloidal NCs (200 mg) were dispersed in 10 ml of chloroform. This was mixed at room temperature with 5 ml of a $AgNO_3$ solution (0.01 M) in FA. The two immiscible phases were shaken for 2 minutes. During this time, $Ag_2Te$ NCs were transferred from the chloroform to the FA phase. Afterward, the FA phase was separated using a pipette. NCs in the FA phase were thoroughly purified using chloroform to remove the remaining organic species. Finally, $Ag_2Te$ NCs were precipitated with acetonitrile and redispersed in FA or acetone. Scheme 1 shows a cartoon of the process.

### Preparation of bulk nanostructured material

To produce $Ag_2Te$ bulk nanostructured materials, NCs were dried using an Ar flow. The obtained nanopowder was annealed at 350 °C for 1 h and afterward compacted at 250 °C into disk-shaped pellets of 10 mm diameter and 1 mm thickness under 90 MPa of pressure. A custom-made hot-press (HP) instrument, with an induction heater coupled to a hydraulic press, was used for pellet preparation. The system was operated under Ar using a graphite die. Pellets with relative densities over 90% were produced.

### Structural and optical characterization

X-ray power diffraction (XRD) analyses were carried out on a Bruker AXS D8 ADVANCE X-ray diffractometer with Cu K$\alpha$1 radiation ($\lambda$ = 1.5406 Å). To perform XRD experiments on a heated sample, an Anton Paar XRK900 temperature chamber and a TCU750 controller integrated with the Bruker control software were used.

The size and shape of the nanoparticles were examined by transmission electron microscope (TEM) using a JEOL 2100 TEM operating at 200 keV. Scanning electron microscopy (SEM) was performed using a ZEISS Auriga SEM with an energy dispersive X-ray spectroscopy (EDX) detector to study composition. Fourier-transform infrared (FTIR) spectra were acquired using an Alpha Bruker FTIR spectrometer with the platinum attenuated total reflectance (ATR) single reflection module. FTIR data were typically averaged over 64 scans. Nuclear magnetic resonance (NMR) spectra ($^1$H-NMR, $^{13}$C-NMR, $^{31}$P-NMR) were acquired using a Varian Mercury Plus 400 MHz at 25 °C using deuterated chloroform ($CDCl_3$) and dimethyl sulfoxide (DMSO) solvents. Thermal gravimetric analyses (TGA)

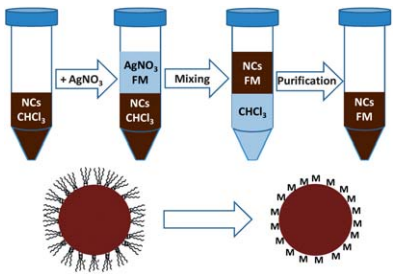


**Scheme 1** Schematized view of the displacement of TOP molecules from the surface of $Ag_2Te$ nanocrystals. A silver nitrate solution in formamide (FM) is added to the colloidal nanocrystals dispersed in chloroform. On mixing the two immiscible phases, the organic ligands are displaced from the NC surface, rendering them soluble in FM.

were done using Perkin-Elmer TGA 4000 equipment. The dried $Ag_2Te$ nanopowders were heated up to 500 °C under a nitrogen flow and with a heating ramp of 5 °C $min^{-1}$. X-ray photoelectron spectroscopy (XPS) spectra were obtained using a SPECS SAGE ESCA System employing Mg K$\alpha$ as the X-ray source.

### Thermoelectric characterization

Seebeck coefficients and electrical conductivities were measured simultaneously under a helium atmosphere in a Linseis – LSR 3 system. The Seebeck coefficient was obtained using a static DC method. The electrical conductivity was measured using a standard four probe technique. Thermal conductivity values were obtained from flash diffusivity measurements (Linseis LFA 1000) using the mass density and the Dulong–Petit approximation to determine the specific heat capacity. The thermal conductivity was calculated as $\kappa = DC_pd$, where $D$ is the thermal diffusivity, $C_p$ is the heat capacity, and $d$ is the measured density.

## Results and discussion

$Ag_2Te$ nanoparticles were prepared by reacting TOPTe and Ag–TOP in OLA. Fig. 1a and b show representative TEM and HRTEM micrographs of $Ag_2Te$ NCs obtained by the procedure detailed above. Highly monodisperse NCs with a disk-like shape and size dispersion below 10% were systematically obtained. Fig. 1c displays the histogram with the diameter distribution of the $Ag_2Te$ nanoparticles characterized here. From this histogram an average nanoparticle diameter of 11 ± 1 nm was calculated.

Fig. 2a displays the XRD pattern of the $Ag_2Te$ NCs prepared. Although broad XRD peaks were obtained due to the small size of the crystallographic domains, the XRD pattern was matched with the hexagonal $Ag_{1.85}Te$ phase (JCPDS 18-1186).

From the synthesis procedure described above, $Ag_2Te$ NCs with a surface layer of TOP molecules were obtained.[50] Such electrically insulating layer strongly limits the use of $Ag_2Te$ NCs in applications requiring a charge exchange between NCs or between the NC and the medium. To exploit the technological potential of NCs, the organic layer needs to be removed. When choosing the chemical procedure used to eliminate the organic ligands from the $Ag_2Te$ NC surface, the following drawbacks need to be considered: (i) the use of S-based compounds, such as $[NH_4]_2S$, results in sulfidation of the nanoparticles during their annealing at moderate temperatures (≥350 °C); (ii) the use of MCCs involves the manipulation of concentrated hydrazine, which is a highly toxic compound and is not commercially available in Europe.

Here, we used a solution of $AgNO_3$ in FA to displace the organic ligands from the $Ag_2Te$ surface and render the NCs stable in a polar medium. While different metal salts were successfully tested, to match the cation with the NC composition $AgNO_3$ was selected. We speculate that after organic ligand displacement, particles are stabilized by silver ions, but we cannot exclude the role of nitrate. After organic ligand displacement, NCs were stable in solution for relatively short periods of time, but long enough to allow their purification and their bottom-up assembly or deposition to produce organic-free bulk nanocrystalline materials or thin films.

We used FTIR and NMR spectroscopy to characterize the efficiency of the organic ligand displacement. Fig. 3a shows the ATR-FTIR spectra of dried $Ag_2Te$ NCs before ($Ag_2Te$ with organic ligands, $Ag_2Te$–OL) and after the organic ligand displacement with the metal salt ($Ag_2Te$–M). The $Ag_2Te$–OL spectrum showed the characteristic features of TOP molecules: C–H vibration

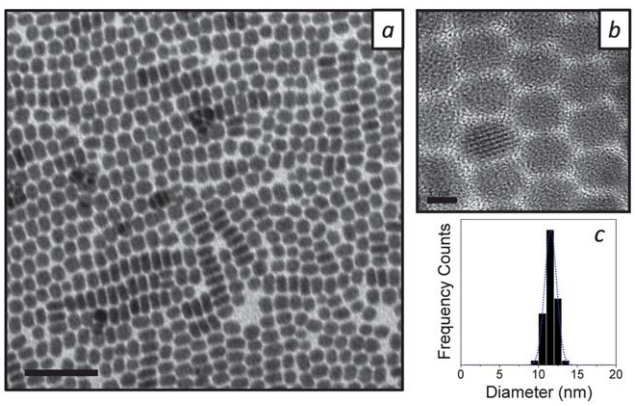


**Fig. 1** TEM (a) and HRTEM (b) micrographs of $Ag_2Te$ nanoparticles. Scale bars correspond to 100 and 5 nm for the TEM and HRTEM micrographs, respectively. (c) Histogram with the diameter distribution of the displayed $Ag_2Te$ nanoparticles.

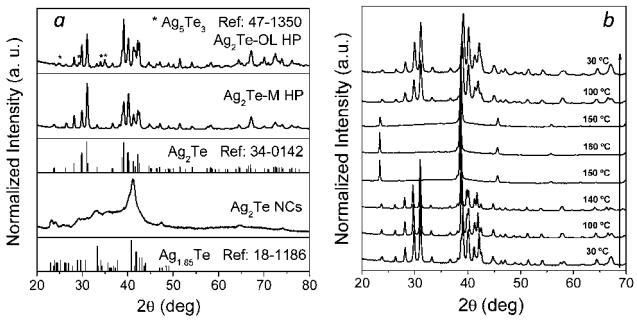


**Fig. 2** (a) Room temperature XRD patterns of the $Ag_2Te$ nanocrystals ($Ag_2Te$ NCs) and of the $Ag_2Te$ nanomaterial ($Ag_2Te$ HP) obtained after annealing the nanoparticles at 350 °C and pressing them at 250 °C under 90 MPa. (b) Evolution of the XRD pattern of $Ag_2Te$ nanocrystals at different temperatures, from 30 °C to 160 °C. XRD patterns were measured at 30 °C, 100 °C, 140 °C, 150 °C, and 160 °C while increasing temperature and at 150 °C, 100 °C and 30 °C while decreasing temperature.

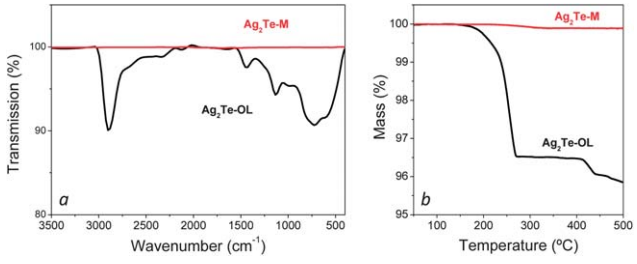


**Fig. 3** ATR-FTIR spectra (a) and TGA (b) of $Ag_2Te$–OL and $Ag_2Te$–M nanocrystals.

modes have a strong band in the high-frequency region (2800–3000 $cm^{-1}$) and various peaks in the lower frequency region, between 700 $cm^{-1}$ and 1500 $cm^{-1}$.[18] These features completely disappeared from the $Ag_2Te$–M spectrum.

Fig. 4 displays the $^1$H-NMR, $^{13}$C-NMR and $^{31}$P-NMR spectra of the $Ag_2Te$–OL and $Ag_2Te$–M NCs. In both $^1$H-NMR and $^{13}$C-NMR spectra of $Ag_2Te$–OL NCs, bands corresponding to the $CH_3(CH_2)_7$ chains from TOP were easily identified. For the $Ag_2Te$–M NCs, the TOP fingerprints disappeared and only the peaks associated with the solvent DMSO and some residual FA and water were visible. In a similar way, the $^{31}$P-NMR spectrum of $Ag_2Te$–OL clearly showed the peak corresponding to TOP, but this was not visible in the $Ag_2Te$–M spectrum. These results prove the complete removal of TOP from the $Ag_2Te$ surface.

Thoroughly purified and dried NCs were also characterized by TGA. Fig. 3b displays the mass loss as a function of material temperature for $Ag_2Te$–OL and $Ag_2Te$–M NCs. TGA showed a relative mass decrease of 4% for the $Ag_2Te$–OL NCs. This can be associated with the decomposition or evaporation of the surface organic molecules. In contrast, the $Ag_2Te$–M NCs showed almost no mass variation when increasing temperature up to 500 °C. This represents further evidence of the organic-free surfaces characterizing the $Ag_2Te$–M NCs. The percentage of carbon remaining after annealing the $Ag_2Te$ NCs was measured by elemental analysis. A 2% of carbon was obtained from the analysis of the annealed $Ag_2Te$–OL. On the other hand, the carbon percentage obtained for $Ag_2Te$–M NCs was within the limit of our system resolution: <0.1%. In the same way, no nitrogen was detected, which points towards the role of $Ag^+$ ions instead of $NO_3^-$ as the stabilizing agent.

To validate the potential of the described procedure to prepare nanomaterials with enhanced performance, we characterized the thermoelectric properties of $Ag_2Te$ nanomaterials obtained from the bottom-up assembly of $Ag_2Te$ NCs. We produced and processed approximately 2 g of colloidal $Ag_2Te$ NCs. The organic ligands were displaced from 1 g of NCs using $AgNO_3$ ($Ag_2Te$–M). The other 1 g was left untreated ($Ag_2Te$–OL). Both samples were thoroughly purified, dried and annealed. The obtained $Ag_2Te$ nanopowders were consolidated into dense disk-shaped pellets with 10 mm diameter and 1 mm thickness. HP conditions (250 °C for 1 min) were carefully adjusted to maximize the pellet density, but minimize at the same time the crystal domain growth. The relative densities of the samples obtained in these conditions were around 92%. Fig. 5 displays a representative SEM image of the $Ag_2Te$ nanomaterials obtained. During annealing and hot press processes, the $Ag_2Te$ crystal domains underwent a factor 5 growth: from 11 nm to approximately 50 nm, as calculated from the XRD pattern using the Scherrer equation. No clear differences were obtained in this respect between $Ag_2Te$–M and $Ag_2Te$–OL nanomaterials. Fig. 2a displays the XRD pattern of the $Ag_2Te$ nanomaterial obtained after HP. The patterns obtained for both samples, $Ag_2Te$–M and $Ag_2Te$–OL, matched with the α-$Ag_2Te$ monoclinic phase (mP12, Hessite, JCPDS 34-0142). However, the XRD pattern of the $Ag_2Te$–OL nanomaterials (Fig. 2a) also displayed the presence of weak peaks associated with the Ag-poor $Ag_5Te_3$ hexagonal phase (JCPDS 47-1350). In the $Ag_2Te$–M samples, the transformation of the initial Ag-poor $Ag_{1.85}Te$ phase into the stoichiometric α-$Ag_2Te$ crystal structure is understood by the excess of Ag introduced during ligand displacement. The phase transition of the untreated $Ag_{1.85}Te$ nanoparticles into α-$Ag_2Te$ was accompanied by the formation of a small amount of a secondary Ag-poor phase.

We speculate the $Ag_2Te$–M samples to be slightly silver-rich due to the excess of Ag introduced during ligand displacement, and the $Ag_2Te$–OL samples to be slightly silver-poor, as the initially formed nanoparticles. We characterized the surface composition of the $Ag_2Te$ nanomaterials by means of XPS. From the XPS spectra, a slight excess of silver in the $Ag_2Te$–M

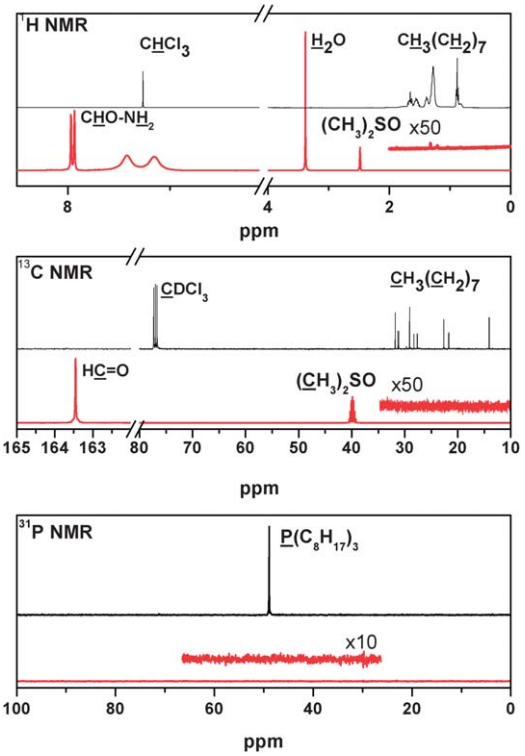


**Fig. 4** $^1$H-NMR, $^{13}$C-NMR and $^{31}$P-NMR spectra of the $Ag_2Te$–OL (top black spectra) and $Ag_2Te$–M nanocrystals (bottom red spectra).

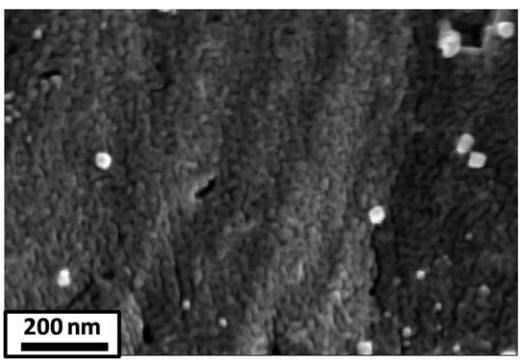


**Fig. 5** SEM micrograph of the $Ag_2Te$–M nanomaterial obtained after pressing the $Ag_2Te$–M nanoparticles using a hot press.

nanomaterial was observed. This excess also points towards the presence of $Ag^+$ ions at the NC surface after the organic ligand displacement.

Fig. 6 displays the electrical conductivity ($\sigma$), Seebeck coefficient ($S$), thermal conductivity ($\kappa$) and dimensionless thermoelectric figure of merit ($ZT$) of $Ag_2Te$–M and $Ag_2Te$–OL nanomaterials.

Significantly higher electrical conductivities were systematically measured for $Ag_2Te$–M when compared to $Ag_2Te$–OL. As displayed in Fig. 6a, above one order of magnitude enhancements were obtained when displacing the organic ligands from the NC surface before assembly. We associate this large increase of electrical conductivity with the absence of residual carbon at the NC surface. The slight excess of silver in the $Ag_2Te$–M nanomaterials may also contribute to the increase in charge carrier density. Besides, a marked decrease of electrical conductivity was observed for both samples in the temperature range between 400 K and 450 K. $Ag_2Te$ undergoes a phase transformation at around 420 K from the low-temperature monoclinic α-$Ag_2Te$ to a high-temperature cubic β-$Ag_2Te$ (F23, JCPDS 01-076-0137). Fig. 2b shows the evolution of the $Ag_2Te$ XRD pattern with temperature. A relatively sharp and reversible phase transition was clearly visible from this evolution. The electrical conductivity decrease was also associated with this phase transition. At temperatures above the phase transition the electrical conductivity of the $Ag_2Te$–M slightly decreased, which is consistent with the complete ionization of the shallow donor states introduced by the excess of silver. On the other hand, the $Ag_2Te$–OL materials displayed an increase of electrical conductivity with temperature, which we associate with the increase of the charge carrier concentration by the ionization of Ag vacancies acting as deep acceptor levels.[31,51]

The temperature evolution of the Seebeck coefficient (Fig. 6b) also displayed a jump at around 420 K, which we associate with the $Ag_2Te$ phase transition. For $Ag_2Te$–OL, the phase transition was accompanied by a change from n-type to p-type conductivity, as noticed by the sign inversion of the Seebeck coefficient, from negative to positive values. In contrast, in $Ag_2Te$–M, the Seebeck coefficient was negative in all the temperature range studied. $Ag_2Te$ electrical conductivity strongly depends on composition. While Ag-rich samples generally show n-type conductivity, Ag-poor $Ag_2Te$ shows p-type conductivity.[31] This is consistent with the excess and shortage of Ag in $Ag_2Te$–M and $Ag_2Te$–OL nanomaterials, respectively.

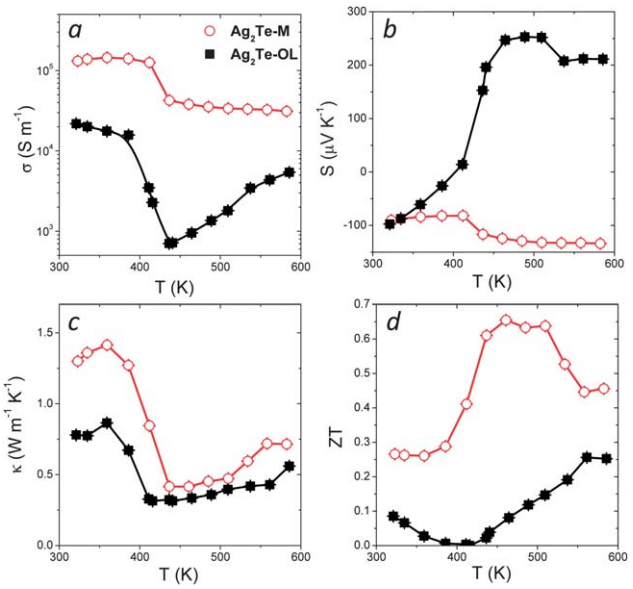


**Fig. 6** Electrical conductivity ($\sigma$), Seebeck coefficient ($S$), thermal conductivity ($\kappa$) and thermoelectric figure of merit ($ZT$) of $Ag_2Te$–OL (■) and $Ag_2Te$–M (○) nanomaterials.

$Ag_2Te$–M nanomaterials displayed higher thermal conductivities than $Ag_2Te$–OL samples. The lower thermal conductivities obtained from $Ag_2Te$–OL could be also associated with the presence of carbon at the $Ag_2Te$–OL interfaces. Carbon layers may enhance phonon scattering efficiency due to acoustic impedance mismatch. The thermal conductivity of both nanomaterials also underwent a strong variation with the crystallographic phase transition at around 400 K. Exceptionally low thermal conductivities, 0.3 $W\,m^{-1}\,K^{-1}$, were obtained at around this temperature. These very low thermal conductivities were associated with the combination of a high structural disorder at around the phase transition temperature and the high density of crystal interfaces characterizing nanomaterials. Both structural disorder and crystal interfaces effectively blocked phonon propagation, thus reducing thermal conductivity. At temperatures above the phase transition, a slight increase of thermal conductivity associated with the re-ordering of the silver and tellurium ions into the high temperature β-$Ag_2Te$ was obtained. At even higher temperatures, the electronic contribution to the thermal conductivity would explain the further increase of thermal conductivity.

Fig. 6d displays the dimensionless thermoelectric figure of merit for both $Ag_2Te$ nanomaterials: $Ag_2Te$–M and $Ag_2Te$–OL. $Ag_2Te$–M samples were characterized by much larger figures of merit than $Ag_2Te$–OL. A factor 6 enhancement of the thermoelectric figure of merit was reached in the middle temperature range where $Ag_2Te$–M had its maximum $ZT$. This improvement was mainly related to the much higher electrical conductivities of $Ag_2Te$–M compared to $Ag_2Te$–OL. Thermoelectric figures of merit up to $ZT = 0.66$ at 450 K were obtained for the $Ag_2Te$–M nanomaterial. This value is slightly higher than the best results previously obtained for pure $Ag_2Te$.[35] This improvement is related to the lower thermal conductivities of the nanomaterials produced here, which result from their reduced crystal domains.

## Conclusions

We presented a simple, general and scalable strategy to remove electrically insulating organic ligands from the surface of colloidal nanocrystals. The process uses a metal salt solution and renders the NCs soluble in polar solvents for relatively short periods of time, but long enough to allow their purification and assembly/deposition to produce technologically useful macroscopic nanomaterials.

The potential of the detailed approach was demonstrated by producing thermoelectric $Ag_2Te$ nanomaterials with up to a

 

6-fold enhancement of their thermoelectric figure of merit. The procedure reported here can be used to improve the performance of NC-based materials and devices in a wide range of applications.

## Acknowledgements

This research was supported by the European Regional Development Funds (ERDF, "FEDER Programa Competitivitat de Catalunya 2007–2013"). This work was also supported by the Spanish MICINN projects MAT2010-15138, MAT2010-21510, and CSD2009-00050. M. I. thanks the Spanish MICINN for her PhD grant. A. S. thanks the Catalan Government, Agència de Gestió d'Ajuts Universitaris i de Recerca (AGAUR), for financial support through the Beatriu i Pinos program.

## References

1 Y. Yin and A. P. Alivisatos, *Nature*, 2004, **437**, 664–670.
2 M. Ibáñez, P. Guardia, A. Shavel, D. Cadavid, J. Arbiol, J. R. Morante and A. Cabot, *J. Phys. Chem. C*, 2011, **115**, 7947–7955.
3 W. Li, A. Shavel, R. Guzman, J. Rubio-Garcia, C. Flox, J. Fan, D. Cadavid, M. Ibáñez, J. Arbiol, J. R. Morante and A. Cabot, *Chem. Commun.*, 2011, **47**, 10332–10334.
4 M. Ibáñez, R. Zamani, W. Li, A. Shavel, J. Arbiol, J. R. Morante and A. Cabot, *Cryst. Growth Des.*, 2012, **12**, 1085–1090.
5 M. Ibáñez, J. Fan, W. Li, D. Cadavid, R. Nafria, A. Carrete and A. Cabot, *Chem. Mater.*, 2011, **23**, 3095–3104.
6 D. V. Talapin, J.-S. Lee, M. V. Kovalenko and E. V. Shevchenko, *Chem. Rev.*, 2010, **110**, 389–458.
7 E. H. Sargent, *Nat. Photonics*, 2012, **6**, 133–135.
8 M. Ibáñez, D. Cadavid, R. Zamani, N. García-Castelló, V. Izquierdo-Roca, W. Li, A. Fairbrother, J. D. Prades, A. Shavel, J. Arbiol, A. Pérez-Rodríguez, J. R. Morante and A. Cabot, *Chem. Mater.*, 2012, **24**, 562–570.
9 T. Herranz, X. Deng, A. Cabot, J. Guo and M. Salmeron, *J. Phys. Chem. B*, 2009, **113**, 10721–10727.
10 W. U. Huynh, J. J. Dittmer and A. P. Alivisatos, *Science*, 2002, **295**, 2425–2427.
11 M. V. Kovalenko, M. Scheele and D. V. Talapin, *Science*, 2009, **324**, 1417–1420.
12 M. V. Kovalenko, M. I. Bodnarchuk, J. Zaumseil, J.-S. Lee and D. V. Talapin, *J. Am. Chem. Soc.*, 2010, **132**, 10085–10092.
13 M. V. Kovalenko, B. Spokoyny, J.-S. Lee, M. Scheele, A. Weber, S. Perera, D. Landry and D. V. Talapin, *J. Am. Chem. Soc.*, 2010, **132**, 6686–6695.
14 M. V. Kovalenko, M. I. Bodnarchuk and D. V. Talapin, *J. Am. Chem. Soc.*, 2010, **132**, 15124–15126.
15 J.-S. Lee, M. V. Kovalenko, J. Huang, D. S. Chung and D. V. Talapin, *Nat. Nanotechnol.*, 2011, **6**, 348–352.
16 A. Dong, X. Ye, J. Chen, Y. Kang, T. Gordon, J. M. Kikkawa and C. B. Murray, *J. Am. Chem. Soc.*, 2011, **133**, 998–1006.
17 E. L. Rosen, R. Buonsanti, A. Llordes, A. M. Sawvel, D. J. Milliron and B. A. Helms, *Angew. Chem., Int. Ed.*, 2012, **51**, 684–689.
18 A. Nag, M. V. Kovalenko, J.-S. Lee, W. Liu, B. Spokoyny and D. V. Talapin, *J. Am. Chem. Soc.*, 2011, **133**, 10612–10620.
19 A. T. Fafarman, W. Koh, B. T. Diroll, D. K. Kim, D.-K. Ko, S. J. Oh, X. Ye, V. Doan-Nguyen, M. R. Crump, D. C. Reifsnyder, C. B. Murray and C. R. Kagan, *J. Am. Chem. Soc.*, 2011, **133**, 15753–15761.
20 W. Koh, S. R. Saudari, A. T. Fafarman, C. R. Kagan and C. B. Murray, *Nano Lett.*, 2011, **11**, 4764–4767.
21 H. Zhang, B. Hu, L. Sun, R. Hovden, F. W. Wise, D. A. Muller and R. D. Robinson, *Nano Lett.*, 2011, **11**, 5356–5361.
22 A. Nag, D. S. Chung, D. S. Dolzhnikov, N. M. Dimitrijevic, S. Chattopadhyay, T. Shibata and D. V. Talapin, *J. Am. Chem. Soc.*, 2012, **134**, 13604–13615.
23 J. Tang, K. W. Kemp, S. Hoogland, K. S. Jeong, H. Liu, L. Levina, M. Furukawa, X. Wang, R. Debnath, D. Cha, K. W. Chou, A. Fischer, A. Amassian, J. B. Asbury and E. H. Sargent, *Nat. Mater.*, 2011, **10**, 765–771.
24 D. Zhitomirsky, M. Furukawa, J. Tang, P. Stadler, S. Hoogland, O. Voznyy, H. Liu and E. H. Sargent, *Adv. Mater.*, 2012, **24**, 6181–6185.
25 Z. Ning, Y. Ren, S. Hoogland, O. Voznyy, L. Levina, P. Stadler, X. Lan, D. Zhitomirsky and E. H. Sargent, *Adv. Mater.*, 2012, **24**, 6295–6299.
26 R. Harpeness, O. Palchik, A. Gedanken, V. Palchik, S. Amiel, M. A. Slifkin and A. M. Weiss, *Chem. Mater.*, 2002, **14**, 2094–2102.
27 T. Sakuma and S. Saitoh, *J. Phys. Soc. Jpn.*, 1985, **54**, 3647–3648.
28 P. F. Taylor and C. Wood, *J. Appl. Phys.*, 1961, **32**, 1–3.
29 C. Wood, V. Harrap and W. M. Kane, *Phys. Rev.*, 1961, **121**, 978–982.
30 R. Dalven, *Phys. Rev. Lett.*, 1966, **16**, 311–312.
31 R. Dalven and R. Gill, *J. Appl. Phys.*, 1967, **38**, 753–756.
32 M. Fujikane, K. Kurosaki, H. Muta and S. Yamanaka, *J. Alloys Compd.*, 2005, **387**, 297–299.
33 M. Fujikane, K. Kurosaki, H. Muta and S. Yamanaka, *J. Alloys Compd.*, 2005, **393**, 299–301.
34 J. Schneider and H. Schulz, *Z. Kristallogr.*, 1993, **203**, 1–15.
35 J. Capps, F. Drymiotis, S. Lindsey and T. M. Tritt, *Philos. Mag. Lett.*, 2010, **90**, 677–681.
36 C. Xiao, J. Xu, K. Li, J. Feng, J. Yang and Y. Xie, *J. Am. Chem. Soc.*, 2012, **134**, 4287–4293.
37 S. K. Bux, J.-P. Fleurial and R. B. Kaner, *Chem. Commun.*, 2010, **46**, 8311.
38 P. Vaqueiro and A. V. Powell, *J. Mater. Chem.*, 2010, **20**, 9577.
39 A. Shakouri, *Annu. Rev. Mater. Res.*, 2011, **41**, 399–431.
40 D. M. Rowe, *Thermoelectrics Handbook: Macro to Nano*, CRC PressINC, 2006.
41 K. Nielsch, J. Bachmann, J. Kimling and H. Böttner, *Adv. Energy Mater.*, 2011, **1**, 713–731.
42 M. G. Kanatzidis, *Chem. Mater.*, 2010, **22**, 648–659.
43 M. Zebarjadi, K. Esfarjani, M. S. Dresselhaus, Z. F. Ren and G. Chen, *Energy Environ. Sci.*, 2012, **5**, 5147.
44 C. J. Vineis, A. Shakouri, A. Majumdar and M. G. Kanatzidis, *Adv. Mater.*, 2010, **22**, 3970–3980.
45 M. Ibáñez, R. Zamani, A. LaLonde, D. Cadavid, W. Li, A. Shavel, J. Arbiol, J. R. Morante, S. Gorsse, G. J. Snyder and A. Cabot, *J. Am. Chem. Soc.*, 2012, **134**, 4060–4063.

46 Y. Zhao, J. S. Dyck and C. Burda, *J. Mater. Chem.*, 2011, **21**, 17049.
47 M. Ibáñez, D. Cadavid, U. A. Tamburini, R. Zamani, S. Gorsse, W. Li, A. Shavel, A. M. López, J. R. Morante, J. Arbiol and A. Cabot, *J. Mater. Chem. A*, 2013, **1**, 1421–1426.
48 M. Ibáñez, R. Zamani, W. Li, D. Cadavid, S. Gorsse, N. A. Katcho, A. Shavel, A. M. López, J. R. Morante, J. Arbiol and A. Cabot, *Chem. Mater.*, 2012, **24**, 4615–4622.
49 D. Cadavid, M. Ibáñez, S. Gorsse, A. M. López, A. Cirera, J. R. Morante and A. Cabot, *J. Nanopart. Res.*, 2012, **14**, 1328.
50 D.-K. Ko, J. J. Urban and C. B. Murray, *Nano Lett.*, 2010, **10**, 1842–1847.
51 J. Capps, B. Ma, T. Drye, C. Nucklos, S. Lindsey, D. Rhodes, Q. Zhang, K. Modic, S. Cawthorne and F. Drymiotis, *J. Alloys Compd.*, 2011, **509**, 1544–1549.

Journal of Materials Chemistry A

RSC Publishing

PAPER

View Article Online
View Journal | View Issue



Cite this: J. Mater. Chem. A, 2013, 1, 1421

# Colloidal synthesis and thermoelectric properties of $Cu_2SnSe_3$ nanocrystals

Maria Ibáñez,†[a] Doris Cadavid,†[b] Umberto Anselmi-Tamburini,[c] Reza Zamani,[bd] Stéphane Gorsse,[e] Wenhua Li,[b] Antonio M. López,[f] Joan Ramon Morante,[ab] Jordi Arbiol[dg] and Andreu Cabot*[ab]

Received 24th September 2012
Accepted 15th November 2012

DOI: 10.1039/c2ta00419d

www.rsc.org/MaterialsA

Copper-based selenides are attracting increasing interest due to their outstanding optoelectronic and thermoelectric properties. Herein a novel colloidal synthetic route to prepare $Cu_2SnSe_3$ nanocrystals with controlled size, shape and composition is presented. The high yield of the developed procedure allowed its up-scaling to the production of grams of colloidal $Cu_2SnSe_3$ nanocrystals. These nanocrystals were used as building blocks for the production of $Cu_2SnSe_3$ bulk nanostructured materials by spark plasma sintering. The thermoelectric properties of the prepared nanocrystalline $Cu_2SnSe_3$ pellets were characterized in the temperature range from 300 to 720 K. The obtained results show the bottom-up production of nanocrystalline materials from solution-processed nanocrystals to be a potentially advantageous alternative to conventional methods of production of efficient thermoelectric materials.

## Introduction

The numerous possibilities for chemical substitutions and structural modifications in ternary diamond-like chalcogenides allow a significant range in engineering their fundamental chemical and physical properties. Such ample chemical and structural freedom permits the use of ternary chalcogenides in multiple applications. Ternary diamond-like semiconductors of the family $I_2$–IV–$VI_3$ (I = Cu, Ag; IV = Ge, Sn; VI = S, Se, Te) find applications in the fields of photovoltaics,[1] Li-ion batteries,[2,3] thermoelectrics,[4] and in acousto-optic devices.[5]

In particular, $Cu_2SnSe_3$ (CTSe) is a p-type semiconductor with a direct band gap of 0.84 eV and a high optical absorption coefficient $>10^4$ $cm^{-1}$.[6–8] CTSe monocrystals are characterized by relatively high hole mobilities (870 $cm^2 V^{-1} s^{-1}$)[9] and a hole effective mass of $1.2m_e$.[8] CTSe has been reported to crystallize in a cubic sphalerite-like phase (space group $F\bar{4}3m$)[10,11] or in the monoclinic structure, the space group *Cc*, with a sphalerite superstructure.[8,12–14]

CTSe is an interesting candidate for acousto-optic applications in the IR region because of its low melting temperature (690 °C), relative low energy band gap, high mean atomic weight and high refractive indices.[8] It has been also extensively studied as an important ternary phase in the processing of $Cu_2ZnSnSe_4$, which is a potential low-cost solar cell absorber.[15,16]

Furthermore, like other copper-based ternary and quaternary selenides,[4,17–24] CTSe shows excellent thermoelectric properties. In CTSe the Cu–Se bond network stabilizes the structure and forms an electrically conductive framework. While Cu–Se bonds play the dominant role in controlling hole transport, Sn orbitals do not contribute much to the p-type carrier transport but allow tuning electrical conductivity by their partial substitution by a group III element.[17] At the same time, ionic substitutions create atomic mass fluctuations that promote phonon scattering, thus reducing thermal conductivities.[4,17,25] These properties have allowed the production of bulk CTSe with figures of merit up to 1.14 at 850 K and 0.41 at 716 K when doped with In or Mn atoms.[17,26]

Thermal conductivities can be further reduced by confining the material crystal domains to the nanoscale.[27–34] The ball-milling of crystalline ingots into small pieces and their posterior reconsolidation into bulk nanocrystalline materials by hot-pressing or spark plasma sintering is currently the most used approach in this direction.[35] Nevertheless, in the very last few years, the bottom-up processing of nanocrystalline materials from solution-processed nanoparticles is becoming a serious alternative to produce efficient thermoelectric nanomaterials.[23,24,30–32]

In this scenario, while a high degree of control over the solution-processing of binary chalcogenide nanocrystals exists,[36,37] the synthesis of ternary and quaternary nanocrystals

[a]Departament d'Electrònica, Universitat de Barcelona, 08028 Barcelona, Spain
[b]Catalonia Institute for Energy Research, IREC, 08930 Sant Adria del Besos, Barcelona, Spain. E-mail: acabot@irec.cat
[c]Dipartimento di Chimica, Universita' di Pavia, V.le Taramelli, 16, 27100 Pavia, Italy
[d]Institut de Ciència de Materials de Barcelona, ICMAB-CSIC, Campus de la UAB, Bellaterra, 08193, Spain
[e]CNRS, Université de Bordeaux, ICMCB, 87 avenue du Docteur Albert Schweitzer, 33608 Pessac Cedex, France
[f]Departament d'Enginyeria Electrónica, Universitat Politècnica de Catalunya, EPSEVG, Av. Victor Balaguer s/n, 08800 Barcelona, Spain
[g]Institució Catalana de Recerca i Estudis Avançats (ICREA), 08010 Barcelona, Spain
† These authors contributed equally.

with sufficient control over their physical, structural and chemical properties still represents an important challenge.[38] Furthermore, while the literature on the production, characterization and application of CTSe thin films[39–41] and nanocrystals[42–45] is minimal, there is still no report on the characterization of the thermoelectric properties of nanocrystalline CTSe.

Herein, a new colloidal synthesis route to prepare CTSe nanocrystals with unprecedented control over their size and shape is presented. The high yield of the reported procedure allowed its up-scaling to the production of grams of colloidal CTSe nanocrystals. These nanocrystals were used for the production of CTSe nanostructured materials by spark plasma sintering. Besides, the thermoelectric properties of these nanocrystalline materials were characterized and the obtained results are reported here.

## Experimental

### Chemicals

Copper(I) chloride (reagent grade, 97%), 1-octadecene (ODE, 90%), oleic acid (OA, tech. 90%) and hexadecylamine (HDA, tech. 90%) were purchased from Aldrich. Tin(IV) chloride pentahydrate (98%) was purchased from Acros. Selenium(IV) oxide (99.8%) and tri-*n*-octylphosphine (TOP, 97%) were purchased from Strem. *n*-Octadecylphosphonic acid (ODPA) was purchased from PCI Synthesis. Chloroform, isopropanol and ethanol were of analytical grade and obtained from various sources. All chemicals were used as received without further purification.

All syntheses were carried out using standard airless techniques: a vacuum/dry argon gas Schlenk line was used for the syntheses and an argon glove-box for storing and handling air and moisture-sensitive chemicals.

### Synthesis of $Cu_2SnSe_3$ nanocrystals

Copper(I) chloride (50 mg, 0.5 mmol), tin(IV) chloride pentahydrate (88 mg, 0.25 mmol), HDA (1230 mg, 5 mM), and ODPA (33 mg, 0.1 mmol) were dissolved in 10 ml ODE. The solution was heated under argon flow to 200 °C and maintained at this temperature for 1 h to remove low-boiling point impurities. Afterwards, the mixture was heated to the reaction temperature (285 °C). A selenium solution (4 ml, 3 mM), obtained by dissolving selenium(IV) oxide in ODE or TOP under argon atmosphere at 180 °C, was rapidly injected through a septum into the reaction flask. Following the injection, the temperature dropped to around 260 °C and then it slowly recovered to 285 °C. The solution was kept at a temperature between 260 °C and 285 °C for 5 min and then quickly cooled down. The formation of CTSe nanocrystals could be qualitatively followed by the color change of the mixture from an initial light yellow to green and eventually to the black color of the solution containing the CTSe nanocrystals. 3 ml of oleic acid were added to the mixture during the cooling at ~70 °C to replace the weakly bonded HDA. The crude solution was mixed with 10 ml of chloroform and sonicated at 50 °C for 5 minutes. The CTSe nanoparticles were isolated by centrifugation at 4000 rpm for 5 minutes. The black precipitate was redispersed in chloroform (~20 ml) and sonicated again at 50 °C for 5 minutes. Then the product was additionally precipitated by adding isopropanol (~10 ml) and centrifuging. Finally, the nanocrystals were re-dispersed in chloroform (~5 ml) and stored for their posterior use.

The same synthesis procedure was scaled up for the production of grams of nanoparticles. In the scaled-up procedure, 8 times larger amounts of all precursor, surfactant and solvent were used.

### Spark plasma sintering (SPS)

For thermoelectric characterization, CTSe nanocrystals were carefully washed and dried out from solution under an argon atmosphere. Afterward, the obtained CTSe nanopowder was heated to 500 °C for 2 hours under an Ar flow inside a tube furnace. The annealed material was compacted into pellets (15 mm diameter; 2 mm thickness) using a home-made spark plasma sintering (SPS) system. The set up of the equipment was based in a graphite die, two plungers that were in direct contact with the specimen, a set of spacers, and the bottom and up electrodes. The die, the plungers and spacers were made of conductive graphite. The electrical power was supplied by applying a voltage difference between the electrodes, so that the current intensity flowed through the entire assembly. The die was loaded in the equipment and the temperature was increased with a heating rate of 200 °C $min^{-1}$. Once the sample reached the designated temperature the pressure was rapidly increased up to 92 MPa. The sample was held under these conditions for 5 minutes and then the pressure was quickly released and the power was turned off.

### Thermoelectric characterization

The Seebeck coefficient was measured by using a static DC method. Electrical resistivity data were obtained by a standard four-probe method. Both Seebeck coefficient and electrical resistivity were measured simultaneously in a LSR-3 LINSEIS system in the range from room temperature up to 720 K, under helium atmosphere.

Thermal conductivities were obtained from flash diffusivity measurements, using the mass density and the Dulong–Petit approximation for the specific heat capacity. The thermal conductivity was calculated as $\kappa = DC_p d$, where $D$ is the thermal diffusivity, $C_p$ is the heat capacity, and $d$ is the density.

## Results and discussion

Fig. 1 shows representative TEM micrographs of the CTSe nanoparticles obtained by the above detailed procedure using either TOP:Se (Fig. 1a) or ODE:Se (Fig. 1b) as the Se source. The introduction of Se in coordination with TOP resulted in nanoparticles with relatively good size distribution and polyhedral geometry. However, the presence of TOP in the final solution limited the chemical stability of the produced nanoparticles, which slowly re-dissolved. On the other hand, the introduction of Se in ODE not only resulted in nanoparticles with both

 

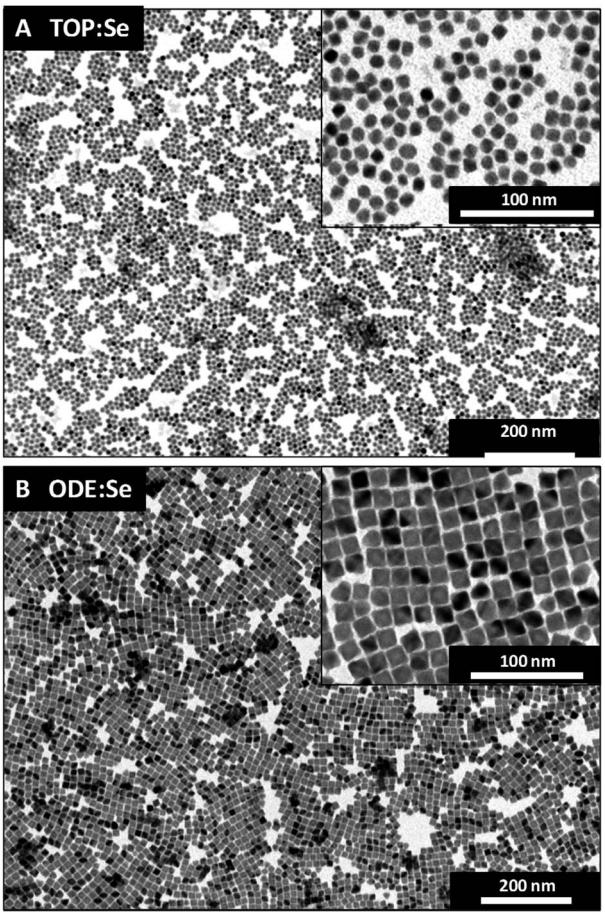


**Fig. 1** TEM micrographs of $Cu_2SnSe_3$ nanoparticles obtained using TOP:Se (a) and ODE:Se (b) as the Se sources.

excellent size and shape distributions, but at the same time, the final nanoparticles remained stable in solution for long periods of time. Moreover, the synthesis procedure yield was significantly improved with the use of ODE:Se instead of TOP:Se. Using ODE:Se, reaction yields well above 90% were obtained. Therefore, ODE:Se was the Se source used to prepare the CTSe nanoparticles for the following thermoelectric characterization.

Fig. 2 shows a HRTEM micrograph and the corresponding indexed power spectrum of a CTSe nanoparticle. HRTEM characterization of the nanocrystals showed them to be highly crystalline and to have a cubic structure (S.G.: $F4\bar{3}m$).[11] The calculated cell parameters and the indexation of the power spectrum frequencies were in good agreement with a cubic cell composed of $[Cu_2SnSe_3]$ tetrahedrons with Cu and Sn atoms randomly occupying the same positions in an occupancy ratio corresponding to $Cu_{0.667}/Sn_{0.333}$.[10]

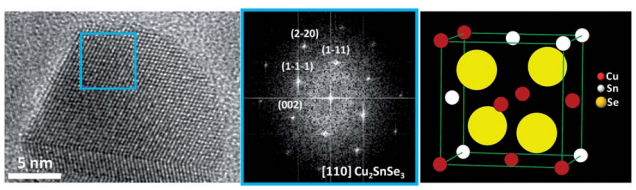


**Fig. 2** HRTEM and indexed power spectrum of a $Cu_2SnSe_3$ nanoparticle. A scheme of the cubic $Cu_2SnSe_3$ crystal structure with the space group $F4\bar{3}m$ is also shown.

XRD analysis of the obtained CTSe nanoparticles confirmed their cubic structure. Fig. 3 shows the XRD patterns of CTSe nanoparticles with 12 nm crystal domain sizes. No secondary phase was detected from the XRD characterization of the materials produced. The chemical composition of the nanocrystals obtained was very close to the required stoichiometry as determined from EDX and ICP analysis. At the same time, single particle analysis of the nanocrystals composition showed the three elements to be present in all nanoparticles and the composition to be highly homogeneous from particle to particle across the whole sample.

For thermoelectric characterization, the synthesis procedure was up-scaled for the production of nanoparticles at the gram scale. Right after synthesis, the nanoparticles were thoroughly washed by means of multiple precipitation and redispersion steps. The final dried powder was not soluble anymore in organic solvents, which proved the large extent of removal of the surface ligands used to control the nanoparticle size, shape and solubility during synthesis. The final nanopowder was annealed at 500 °C in an argon atmosphere to remove any remaining organic ligand or synthesis/washing byproduct. The annealing process did not appreciably modify the nanoparticle composition or crystal domain size, as observed from the XRD patterns (Fig. 3). The annealed nanopowder was then consolidated into nanocrystalline pellets by means of spark plasma sintering. For this process, a homemade system was used. Sintering temperatures in the range from 400 °C to 600 °C and different times and pressures were carefully tested to optimize the pellet density while preventing the crystal domain growth and the modification of the material composition and crystal phase. All sintering processes were performed under vacuum. Particles from the exact same batch, having an average crystal domain size of 12 nm and the stoichiometric composition were used for all the optimization tests. Finally, the sintering time was set to 5 min and the uniaxial sintering pressure to 92 MPa. Under these

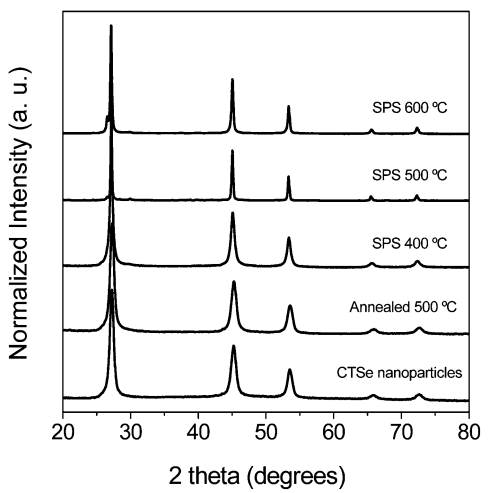


**Fig. 3** XRD patterns of $Cu_2SnSe_3$ nanoparticles, before and after an annealing treatment at 500 °C and after spark plasma sintering at 400 °C, 500 °C and 600 °C.

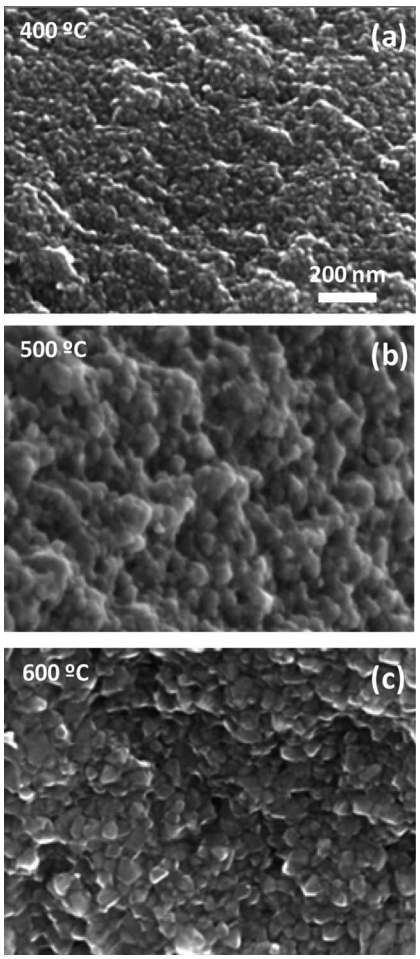


**Fig. 4** SEM micrographs of the nanocrystalline $Cu_2SnSe_3$ pellets obtained by spark plasma sintering at 400 °C (a), 500 °C (b) and 600 °C (c).

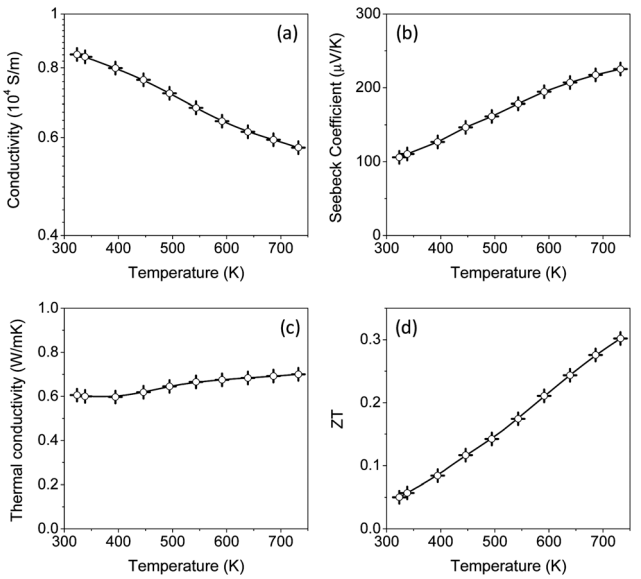


**Fig. 5** Temperature dependence of the electrical conductivity (a), Seebeck coefficient (b), thermal conductivity (c) and thermoelectric figure of merit ZT (d) of a representative nanocrystalline $Cu_2SnSe_3$ pellet obtained by the spark plasma sintering at 400 °C of solution-processed $Cu_2SnSe_3$ nanocrystals.

conditions, sintering temperatures of 400 °C, 500 °C and 600 °C resulted in an increase of the crystal domain size from the original 12 nm to 15 nm, 25 nm and 30 nm, respectively. These values were calculated from the fitting of the XRD patterns using Scherrer's equation. The highest processing temperatures resulted in a slight loss of Sn and the formation of CuSe as a secondary phase, as concluded from the XRD characterization of the material (Fig. 3). Fig. 4 shows SEM micrographs of the final nanocrystalline pellets produced by spark plasma sintering at different processing temperatures.

For thermoelectric characterization, two pellets 15 mm in diameter and 2 mm thick were produced using the optimized spark plasma sintering conditions (92 MPa, 400 °C, 5 min). In these conditions, the relative density of the obtained pellets was approximately 90%.

The thermoelectric properties of the nanocrystalline CTSe were measured in the temperature range from 300 K to 720 K. Fig. 5 shows the electrical conductivity, Seebeck coefficient, thermal conductivity and thermoelectric figure of merit of the nanocrystalline CTSe pellets produced. Electrical conductivities up to 8450 S $m^{-1}$ were obtained from nanocrystalline CTSe. These relatively high values prove the large extent of removal of the surface ligands used in the solution-processing of the material. These values were just 30% lower than those obtained from bulk CTSe produced by the reaction of the constituent elements at high temperatures and over long periods of time. These 30% lower electrical conductivities are explained in part by the scattering of charge carriers at the high density of grain boundaries and structural defects. On the other hand, the relatively lower pellet densities obtained by the bottom-up assembly of the nanocrystals most probably also played an important role in the electrical conductivity decrease. An estimation of the electrical conductivity that would be measured from a 100% dense sample can be obtained using a Maxwell–Eucken expression:[30,46,47]

$$\sigma_{100} = \sigma_P \frac{1+\beta P}{1-P}$$

where $\sigma_{100}$ is the electrical conductivity in the 100% dense medium, $P$ is the degree of porosity in the range between 0 and 1, and $\beta$ is an empirical parameter related to the pore geometry, which we fixed to 2.[47] This equation yielded electrical conductivities up to 11 200 S $m^{-1}$. The remaining 10% reduction of electrical conductivity when compared to bulk CTSe must be associated with charge carrier scattering at crystal interfaces.

The electrical conductivity of the CTSe nanocrystalline pellets decreased with the temperature in the whole range tested. This metallic-like character was probably associated with the thermal activation of an acceptor level at temperatures below 300 K. Above this temperature, the combination of the empty impurity band and the decrease of the hole mobility with temperature explain the observed metallic-like behavior. The same evolution of the electrical conductivity with temperature has been previously observed in bulk crystalline materials, what discards a major role of interfaces in this characteristic behavior.[17,26]

 

The positive Seebeck coefficients measured from nanocrystalline CTSe demonstrated the p-type character of the obtained materials. While a relatively large range of values has been reported, the Seebeck coefficients measured here from nanocrystalline CTSe were slightly lower than the best values obtained previously for pure CTSe bulk materials.[4,17,26]

On the other hand, the thermal conductivities of nanocrystalline CTSe measured in this work were significantly lower than those previously reported for bulk CTSe. Even correcting for the slightly larger porosity of the materials characterized here, the thermal conductivity of the nanocrystalline materials was between a factor of 2 and 4 lower than those obtained previously. This strong decrease of thermal conductivity must be associated with phonon scattering at the very high density of interfaces present in nanocrystalline CTSe.

These characteristics finally resulted in thermoelectric figures of merit up to 0.3 at 730 K. This value is very close to the best figures of merit reported for undoped CTSe and it might be notably improved with the introduction of controlled amounts of dopants. When comparing with current solid state methods, requiring long annealing treatments ($t$ > 100 h) at high temperature ($T$ > 500 °C),[8,17] it should be kept in mind that while the bottom-up processing of nanocrystalline CTSe from colloidal CTSe nanocrystals allowed obtaining thermoelectric materials with relatively high figures of merit, it also represents an important advantage in terms of processing time and energy consumption. Moreover, the high versatility of the processes reported here should allow a rapid and facile screening of the materials composition and structural properties to further optimize the figure of merit.

## Conclusions

A new colloidal synthetic route for the production of CTSe nanoparticles was detailed. The use of ODE:Se instead of TOP:Se as the Se source was demonstrated to result in stable nanoparticles with unprecedented size and shape distributions and very high production yields. The reported procedure was up-scaled to the production of grams of CTSe colloidal nanocrystals. The potential of these nanoparticles for the bottom-up production of nanocrystalline materials by means of spark plasma sintering was further demonstrated. The obtained nanocrystalline CTSe was characterized by figures of merit comparable to those obtained from bulk materials, but using considerably less time-consuming and energy-intensive processes. The introduction of doping elements in the CTSe structure, *e.g.* incorporating In or Mn salts in the initial precursor solution, is expected to allow a further improvement of the thermoelectric figures of merit reported here.

## Acknowledgements

The research was supported by the European Regional Development Funds (ERDF, "FEDER Programa Competitivitat de Catalunya 2007–2013"). This work was also supported by the Spanish MICINN Projects MAT2008-05779, MAT2008-03400-E/MAT, MAT2010-15138, MAT2010-21510, CSD2009-00050 and ENE2008-03277-E/CON. M. I. thanks the Spanish MICINN for her Ph.D grant. A. S. thanks the Catalan Government, Agència de Gestió d'Ajuts Universitaris i de Recerca (AGAUR), for financial support through the Beatriu i Pinos program. A. C. thanks the Spanish MICINN for financial support through the Ramón y Cajal program.

## Notes and references

1 P. A. Fernandes, P. M. P. Salomé and A. F. d. Cunha, *J. Phys. D: Appl. Phys.*, 2010, **43**, 215403.
2 B. Qu, H. Li, M. Zhang, L. Mei, L. Chen, Y. Wang, Q. Li and T. Wang, *Nanoscale*, 2011, **3**, 4389–4393.
3 B. Qu, M. Zhang, D. Lei, Y. Zeng, Y. Chen, L. Chen, Q. Li, Y. Wang and T. Wang, *Nanoscale*, 2011, **3**, 3646–3651.
4 E. J. Skoug, J. D. Cain and D. T. Morelli, *J. Alloys Compd.*, 2010, **506**, 18–21.
5 L. K. Samanta, *Phys. Status Solidi A*, 1987, **100**, K93–K97.
6 Y.-T. Zhai, S. Chen, J.-H. Yang, H.-J. Xiang, X.-G. Gong, A. Walsh, J. Kang and S.-H. Wei, *Phys. Rev. B: Condens. Matter Mater. Phys.*, 2011, **84**, 075213.
7 G. H. Chandra, O. L. Kumar, R. P. Rao and S. Uthanna, *J. Mater. Sci.*, 2011, **46**, 6952–6959.
8 G. Marcano, C. Rincón, L. M. De Chalbaud, D. B. Bracho and G. Sánchez Pérez, *J. Appl. Phys.*, 2001, **90**, 1847–1853.
9 L. I. Berger and V. D. Prochukhan, *Ternary Diamond-Like Semiconductors*, Consultants Bureau, New York, 1969.
10 L. S. Palatnik, Y. F. Komnik, E. K. Belova and L. V. Adroschenko, *Kristallografiya*, 1961, **6**, 960–964.
11 B. B. Sharma, R. Ayyar and H. Singh, *Phys. Status Solidi A*, 1977, **40**, 691–696.
12 G. E. Delgado, A. J. Mora, G. Marcano and C. Rincón, *Mater. Res. Bull.*, 2003, **38**, 1949–1955.
13 L. D. Gulay, M. Daszkiewicz, T. A. Ostapyuk, O. S. Klymovych and O. F. Zmiy, *Acta Crystallogr., Sect. C: Cryst. Struct. Commun.*, 2010, **66**, i58–i60.
14 G. Marcano, L. M. De Chalbaud, C. Rincón and G. Sánchez Pérez, *Mater. Lett.*, 2002, **53**, 151–154.
15 A. Shavel, J. Arbiol and A. Cabot, *J. Am. Chem. Soc.*, 2010, **132**, 4514–4515.
16 A. Shavel, D. Cadavid, M. Ibáñez, A. Carrete and A. Cabot, *J. Am. Chem. Soc.*, 2012, **134**, 1438–1441.
17 X. Shi, L. Xi, J. Fan, W. Zhang and L. Chen, *Chem. Mater.*, 2010, **22**, 6029–6031.
18 M. L. Liu, F. Q. Huang, L. D. Chen and I. W. Chen, *Appl. Phys. Lett.*, 2009, **94**, 202103.
19 C. Sevik and T. Cagin, *Appl. Phys. Lett.*, 2009, **95**, 112105.
20 S. Schorr, *Thin Solid Films*, 2007, **515**, 5985–5991.
21 J. Y. Cho, X. Shi, J. R. Salvador, G. P. Meisner, J. Yang, H. Wang, A. A. Wereszczak, X. Zhou and C. Uher, *Phys. Rev. B: Condens. Matter Mater. Phys.*, 2011, **84**, 085207.
22 J. Y. Cho, X. Shi, J. R. Salvador, J. Yang and H. Wang, *J. Appl. Phys.*, 2010, **108**, 073713.
23 M. Ibáñez, D. Cadavid, R. Zamani, N. García-Castelló, V. Izquierdo-Roca, W. Li, A. Fairbrother, J. D. Prades, A. Shavel, J. Arbiol, A. Pérez-Rodríguez, J. R. Morante and A. Cabot, *Chem. Mater.*, 2012, **24**, 562–570.

24 M. Ibáñez, R. Zamani, A. Lalonde, D. Cadavid, W. Li, A. Shavel, J. Arbiol, J. R. Morante, S. Gorsse, G. J. Snyder and A. Cabot, *J. Am. Chem. Soc.*, 2012, **134**, 4060–4063.
25 T. Irie, *Jpn. J. Appl. Phys.*, 1966, **5**, 854–859.
26 H. Sun and D. T. Morelli, *J. Electron. Mater.*, 2012, **41**, 1125–1129.
27 M. Zebarjadi, K. Esfarjani, M. S. Dresselhaus, Z. F. Ren and G. Chen, *Energy Environ. Sci.*, 2012, **5**, 5147–5162.
28 C. J. Vineis, A. Shakouri, A. Majumdar and M. G. Kanatzidis, *Adv. Mater.*, 2010, **22**, 3970–3980.
29 J. R. Szczech, J. M. Higgins and S. Jin, *J. Mater. Chem.*, 2011, **21**, 4037–4055.
30 M. Scheele, N. Oeschler, I. Veremchuk, K. G. Reinsberg, A. M. Kreuziger, A. Kornowski, J. Broekaert, C. Klinke and H. Weller, *ACS Nano*, 2010, **4**, 4283–4291.
31 M. Ibáñez, R. Zamani, W. Li, D. Cadavid, S. Gorsse, N. A. Katcho, A. Shavel, A. M. López, J. R. Morante, J. Arbiol and A Cabot, *Chem. Mater.*, DOI: 10.1021/cm303252q.
32 D. Cadavid, M. Ibáñez, S. Gorsse, A. M. López, A. Cirera, J. R. Morante and A Cabot, *J. Nanopart. Res.*, DOI: 10.1007/s11051-012-1328-0.
33 S. Gorsse, P. Bellanger, Y. Brechet, E. Sellier, A. Umarji, U. Ail and R. Decourt, *Acta Mater.*, 2011, **59**, 7425–7437.
34 S. Gorsse, P. Bauer Pereira, R. Decourt and E. Sellier, *Chem. Mater.*, 2010, **22**, 988–993.
35 Y. Lan, A. J. Minnich, G. Chen and Z. Ren, *Adv. Funct. Mater.*, 2010, **20**, 357–376.
36 M. Ibáñez, P. Guardia, A. Shavel, D. Cadavid, J. Arbiol, J. R. Morante and A. Cabot, *J. Phys. Chem. C*, 2011, **115**, 7947–7955.
37 W. Li, A. Shavel, R. Guzman, J. Rubio-Garcia, C. Flox, J. Fan, D. Cadavid, M. Ibáñez, J. Arbiol, J. R. Morante and A. Cabot, *Chem. Commun.*, 2011, **47**, 10332–10334.
38 M. Ibáñez, R. Zamani, W. Li, A. Shavel, J. Arbiol, J. R. Morante and A. Cabot, *Cryst. Growth Des.*, 2012, **12**, 1085–1090.
39 G. S. Babu, Y. B. K. Kumar, Y. B. K. Reddy and V. S. Raja, *Mater. Chem. Phys.*, 2006, **96**, 442–446.
40 D.-H. Kuo, W.-D. Haung, Y.-S. Huang, J.-D. Wu and Y.-J. Lin, *Thin Solid Films*, 2010, **518**, 7218–7221.
41 D. H. Kuo, W. D. Haung, Y. S. Huang, J. D. Wu and Y. J. Lin, *Surf. Coat. Technol.*, 2010, **205**, S196–S200.
42 X. Chen, X. Wang, C. An, J. Liu and Y. Qian, *J. Cryst. Growth*, 2003, **256**, 368–376.
43 B. Li, Y. Xie, J. Huang and Y. Qian, *Solid State Ionics*, 1999, **126**, 359–362.
44 J. Jeong, H. Chung, Y. C. Ju, J. Moon, J. Roh, S. Yoon, Y. R. Do and W. Kim, *Mater. Lett.*, 2010, **64**, 2043–2045.
45 M. E. Norako, M. J. Greaney and R. L. Brutchey, *J. Am. Chem. Soc.*, 2012, **134**, 23–26.
46 L. Yang, J. S. Wu and L. T. Zhang, *J. Alloys Compd.*, 2004, **364**, 83–88.
47 J. Adachi, K. Kurosaki, M. Uno and S. Yamanaka, *J. Alloys Compd.*, 2007, **432**, 7–10.

 